



# **Measuring the Muon Neutrino Magnetic Moment in the NOvA Near Detector**

Róbert Králik

*Supervisor:* Dr. Lily Asquith

*A thesis submitted in fulfilment of the requirements for the degree of  
Doctor of Philosophy to the*

School of Mathematical and Physical Sciences  
University of Sussex

In Brighton, United Kingdom

September 16, 2024

I hereby declare that I carried out this thesis independently, and only with the cited sources, literature and other professional sources.

I also declare that this thesis has not been and will not be, submitted in whole or in part to another University for the award of any other degree.

*Brighton, United Kingdom,*

*September 16, 2024*

---

Róbert Králik

# Acknowledgements

School of Mathematical and Physical Sciences, University of Sussex

DOCTORAL THESIS

---

Measuring the Muon Neutrino Magnetic Moment in the NOvA Near  
Detector

---

by Róbert Králik

**ABSTRACT**

Measuring an enhanced neutrino magnetic moment would be a clear indication of physics beyond the Standard Model (BSM), shedding light on the correct BSM theory or the potential Majorana nature of neutrinos. It would manifest in the NOvA near detector as an excess of neutrino-on-electron elastic scattering interactions at low electron recoil energies. Leveraging an intense and highly pure muon neutrino beam, along with the finely segmented liquid scintillator detector technology specifically designed for electromagnetic shower separation, enables NOvA to achieve a potentially world-leading sensitivity in probing the effective muon neutrino magnetic moment. This analysis, based on neutrino data collected between 2014 and 2021, corresponding to an exposure of  $13.8 \times 10^{20}$  protons-on-target, yields a result consistent with the Standard Model-only hypothesis with a p-value of 0.31. An upper limit on the effective muon neutrino magnetic moment is set at  $\mu_{\nu_\mu} < 19.1 \times 10^{-10} \mu_B$  at 90% confidence level. Despite facing statistical limitations stemming from the low cross section of the signal process, systematic uncertainties have a significant impact on this result. To address these challenges, the NOvA Test Beam experiment focuses on mitigating some of the largest systematic uncertainties within NOvA by investigating particle interactions and energy deposition in a small-scale replica NOvA detector. This thesis describes the calibration of the NOvA Test Beam detector, which is a crucial step in analysing the Test Beam data before they can be utilised to reduce NOvA systematic uncertainties.

Keywords: neutrino NOvA electromagnetic testbeam calibration

# Preface

This preface outlines the structure of this thesis and clarifies my contributions to the research presented in each chapter.

Chapter 1 provides a literature review of the current theoretical and experimental landscape of neutrino physics, with emphasis on neutrino interactions, oscillations, and mass generation mechanisms.

Chapter 2 introduces the NOvA experiment, primarily relying on publicly available sources, with internal NOvA documentation referenced only when greater technical detail was necessary. Throughout, I aimed to ensure proper attribution to my colleagues' contributions while prioritising publicly accessible resources whenever possible. My contribution to this chapter includes analysing hadron production data from the NA61 experiment, which will be used in the future upgrades of the neutrino beam prediction in NOvA, as discussed in Sec. 2.4.

Chapter 3 covers the calibration of the NOvA Test Beam detector, a technical project I undertook to reduce systematic uncertainties within the NOvA experiment. This chapter is divided into three sections:

1. Section 3.1 describes the design and construction of the NOvA Test Beam detector, conducted by my colleagues within the NOvA Test Beam experiment.
2. Section 3.2 presents the data-based simulation of cosmic muons used for calibration, originally created by my colleague which I significantly improved. My contributions include enhancing event selection, implementing energy and charge assignment, and producing and validating the resulting simulation samples.
3. Section 3.3 focuses on the Test Beam detector calibration itself, based on the calibration framework used for the other NOvA detectors. I adapted the Test Beam detector calibration to work with fibre brightness bins and recreated the Test Beam fibre brightness map and the threshold and shielding corrections. Ultimately, I completed and validated the first full calibration of the NOvA Test Beam detector.

Chapter 4 details the measurement of the effective muon neutrino magnetic moment. This analysis was initially suggested to me by my colleague, Matt Strait. The data and simulation samples, including the enhanced and the systematically shifted simulation samples, were created by my colleagues, together with the radiative correction weight. My contributions include assisting in the development of the enhanced  $\nu_e$ CCMEC sample and the neutrino magnetic moment weight, eliminating the need for a dedicated simulation. I also developed the event selection and investigated the effect of systematic uncertainties using tools and methods adapted from other NOvA analyses. Additionally, I implemented statistical analysis, customizing a fitting framework originally developed for the NOvA light dark matter analysis.

Finally, chapter 5 concludes with a summary of the findings of this thesis.

# Contents

<b>Acknowledgements</b>	<b>ii</b>
<b>Preface</b>	<b>iv</b>
<b>List of Figures</b>	<b>ix</b>
<b>List of Tables</b>	<b>xiv</b>
<b>1 Theory of neutrino physics</b>	<b>1</b>
1.1 Neutrino production . . . . .	2
1.2 Neutrino interactions . . . . .	4
1.3 Neutrino oscillation . . . . .	6
1.4 Neutrino mass . . . . .	11
<b>2 The NOvA experiment</b>	<b>13</b>
2.1 The neutrino beam for NOvA . . . . .	13
2.2 The NOvA detectors . . . . .	16
2.3 Readout and data acquisition . . . . .	18
2.4 Simulation . . . . .	20
2.5 Data processing and event reconstruction . . . . .	23
2.6 Detector calibration . . . . .	26
2.6.1 Scale . . . . .	29
2.6.2 Threshold and shielding correction . . . . .	29
2.6.3 Relative calibration . . . . .	30
2.6.4 Absolute calibration . . . . .	33
2.7 Energy estimation . . . . .	34
2.8 Systematic uncertainties . . . . .	34
<b>3 NOvA Test Beam detector calibration</b>	<b>38</b>
3.1 The NOvA Test Beam experiment . . . . .	39
3.2 Data-based simulation of cosmic muons . . . . .	44
3.2.1 Reconstruction and selection of cosmic data events . . . . .	44

3.2.2	Energy correction, charge assignment and smearing . . . . .	49
3.2.3	Validation . . . . .	54
3.2.4	Summary . . . . .	59
3.3	NOvA Test Beam detector calibration . . . . .	61
3.3.1	Fibre brightness . . . . .	61
3.3.2	Threshold and shielding corrections . . . . .	63
3.3.3	Simulation . . . . .	68
3.3.4	Period 2 data . . . . .	72
3.3.5	Period 3 data . . . . .	80
3.3.6	Period 4 data . . . . .	88
3.3.7	Absolute calibration results . . . . .	94
3.3.8	Validation . . . . .	97
3.3.9	Summary . . . . .	107
<b>4</b>	<b>Measuring the muon neutrino magnetic moment</b>	<b>111</b>
4.1	Theory of the neutrino magnetic moment . . . . .	113
4.1.1	Neutrino electric and magnetic dipole moments . . . . .	115
4.1.2	Measuring the neutrino magnetic moment . . . . .	118
4.2	Analysis overview . . . . .	124
4.3	Event selection . . . . .	127
4.3.1	Data collection quality . . . . .	128
4.3.2	Reconstruction quality . . . . .	128
4.3.3	Pre-selection . . . . .	132
4.3.4	Fiducial and containment cuts . . . . .	136
4.3.5	Multivariate analysis cuts . . . . .	138
4.4	Systematic uncertainties . . . . .	154
4.5	Statistical analysis . . . . .	157
4.5.1	Treatment of systematic uncertainties . . . . .	159
4.5.2	Hypothesis testing and confidence limits . . . . .	159
4.6	Results . . . . .	161
4.7	Summary . . . . .	163
<b>5</b>	<b>Conclusion</b>	<b>167</b>

<b>Acronyms</b>	<b>169</b>
<b>Bibliography</b>	<b>173</b>
<b>A Test Beam calibration validation plots</b>	<b>195</b>
A.1 Distributions for stopping muons . . . . .	195
A.2 Distributions for through-going muons . . . . .	205

# List of Figures

1.1	Neutrino interaction vertices in the SM . . . . .	2
1.2	Muon neutrino CC cross sections based on the interaction types . . . . .	5
2.1	The schematic of the NuMI beam facility . . . . .	14
2.2	NuMI neutrino beam components in the NOvA near detector . . . . .	15
2.3	The NOvA off-axis beam concept . . . . .	15
2.4	NOvA detectors . . . . .	16
2.5	NOvA Avalanche Photo Diodes . . . . .	18
2.6	NOvA Front End Board . . . . .	19
2.7	NOvA reconstruction of a single electron . . . . .	24
2.8	NOvA detectors event topologies . . . . .	25
2.9	Tricell condition for calibration hits in NOvA . . . . .	28
2.10	Fibre Brightness bins for the NOvA calibration . . . . .	29
2.11	Example attenuation fit for NOvA relative calibration . . . . .	31
2.12	Example LOWESS correction for NOvA relative calibration . . . . .	32
2.13	Example distributions for the NOvA absolute calibration . . . . .	33
3.1	Comparison of Test Beam detector to the Near and Far Detectors . . . . .	39
3.2	Scintillator oils used in the Test Beam detector . . . . .	42
3.3	Removing Test Beam beam spill . . . . .	45
3.4	Track start and $\text{Cos}_Z$ cut for data-based simulation selection . . . . .	47
3.5	Tracking algorithms for the data-based simulation selection . . . . .	49
3.6	Comparison of the $\text{Cos}_Z$ and track length distributions between tracking algorithms for the data-based simulation selection . . . . .	50
3.7	Event selection for the data-based simulation . . . . .	52
3.8	Energy correction for through-going muons for the data-based simulation . . . . .	53
3.9	Data-Simulation comparison of angular distributions . . . . .	56
3.10	Data-Simulation comparison of angular and track length distributions . . . . .	57
3.11	Data-Simulation comparison of track start X and Y distributions . . . . .	58
3.12	Data-Simulation comparison of track start Z distribution . . . . .	59

3.13 Comparison of simulation to a re-simulation validation sample . . . . .	60
3.14 Example of failed attenuation fits used for the Test Beam fibre brightness file . . . . .	62
3.15 Fibre Brightness map for the Test Beam detector . . . . .	63
3.16 Example threshold and shielding correction for Test Beam detector .	64
3.17 Map of the threshold and shielding correction across the Test Beam detector . . . . .	65
3.18 The relative gain variation as a function of the ‘pixel number’ (left) and cell number (right). . . . .	67
3.19 Plane-Cell distribution of hits for the simulation sample . . . . .	69
3.20 Uncorrected energy response along $w$ , cell and plane for simulation .	70
3.21 Map of fitted response at cell centre for simulation . . . . .	71
3.22 Example attenuation fits for simulation . . . . .	72
3.23 Plane-Cell distribution of tricell hits for period 2 data . . . . .	73
3.24 Uncorrected energy response along $w$ , cell and plane for period 2 data	75
3.25 Map of fitted response at cell centre for period 2 data . . . . .	76
3.26 Attenuation fits for standard cells in period 2 data . . . . .	77
3.27 Attenuation fits for underfilled cells in period 2 data . . . . .	78
3.28 Attenuation fits for cells with readout issues in period 2 data . . . .	79
3.29 Attenuation fits for cells with large fluctuations in period 2 data . .	81
3.30 Plane-Cell distribution of hits for the period 3 data sample . . . . .	82
3.31 Uncorrected energy response along $w$ , cell and plane for period 3 .	83
3.32 Map of fitted response at cell centre for epochs 3a, 3b and 3c data .	84
3.33 Attenuation fits for re-filled cells in period 3 data . . . . .	85
3.34 Attenuation fits for cells with faulty readout in period 3 data . . . .	86
3.35 Attenuation fits for cells with large fluctuations in period 3 data . .	86
3.36 Map of fitted response at cell centre for epochs 3d and 3e data . . .	87
3.37 Attenuation fits for dead channels in period 3 data . . . . .	89
3.38 Attenuation fits for cells with mixed scintillators in period 3 data . .	90
3.39 Corrected map of fitted response at cell centre for epochs 3d and 3e data	90
3.40 Plane-Cell distribution of hits for the period 4 data sample . . . . .	91
3.41 Uncorrected energy response along $w$ , cell and plane for period 4 .	92

3.42	Map of fitted response at cell centre for period 4 data . . . . .	93
3.43	Attenuation fits for cells with mixed oils in period 4 data . . . . .	94
3.44	Reconstructed and true energy responses of stopping muons . . . . .	96
3.45	Validation plots for stopping muons along w . . . . .	99
3.46	Validation plots for stopping muons across cells . . . . .	100
3.47	Validation plots for stopping muons across planes . . . . .	101
3.48	Validation plots for stopping muons along time . . . . .	103
3.49	Selection of stable runs from the period 4 Test Beam data . . . . .	104
3.50	Removing edge hits for validation with through-going muons . . . . .	105
3.51	Validation plots for through-going muons as a function of w, cell and plane . . . . .	106
3.52	Map of corrected energy deposition for through-going cosmic muons in data . . . . .	107
3.53	Map of corrected energy deposition for through-going cosmic muons in simulation . . . . .	108
4.1	Effective coupling of neutrinos with one photon electromagnetic field. . . . .	113
4.2	Neutrino-on-electron elastic scattering diagram . . . . .	118
4.3	Electron recoil energy versus recoil angle . . . . .	119
4.4	Comparison of the neutrino magnetic moment and the Standard Model cross sections . . . . .	121
4.5	Ratio of the neutrino magnetic moment and the Standard Model cross sections . . . . .	123
4.6	Vertex reconstruction quality cut . . . . .	130
4.7	Prong and hits reconstruction quality cuts . . . . .	131
4.8	Low calorimetric energy cut for reconstruction quality . . . . .	133
4.9	Number of hits cut for pre-selection . . . . .	134
4.10	Length of the longest prong cut for pre-selection . . . . .	135
4.11	$E\theta^2$ cut for pre-selection . . . . .	137
4.12	Vertex x containment cut . . . . .	139
4.13	Vertex y containment cut . . . . .	140
4.14	Vertex z containment cut . . . . .	141
4.15	Hit minimum x containment cut . . . . .	142

4.16	Hit maximum x containment cut . . . . .	143
4.17	Hit minimum y containment cut . . . . .	144
4.18	Hit maximum y containment cut . . . . .	145
4.19	Hit minimum z containment cut . . . . .	146
4.20	Hit maximum z containment cut . . . . .	147
4.21	Shower E fraction and number of hits cuts . . . . .	151
4.22	Reconstructed energy and $E\theta^2$ cuts . . . . .	152
4.23	NuoneID and EPi0ID cuts . . . . .	153
4.24	Background composition of final selection . . . . .	154
4.25	Summary of systematic uncertainties . . . . .	155
4.26	Neutrino flux systematic uncertainty . . . . .	156
4.27	Detector systematic uncertainties . . . . .	157
4.28	Final prediction and data comparison . . . . .	162
4.29	Distribution of the minimum log likelihood ratio as a function of the neutrino magnetic moment . . . . .	164
A.1	Energy deposition of stopping muons along cells . . . . .	196
A.2	Calibration variables of stopping muons along cells . . . . .	197
A.3	Energy deposition of stopping muons across cells . . . . .	198
A.4	Calibration variables of stopping muons across cells . . . . .	199
A.5	Energy deposition of stopping muons across planes . . . . .	200
A.6	Calibration variables of stopping muons along planes . . . . .	201
A.7	Energy deposition of stopping muons as a function of time . . . . .	202
A.8	Calibration variables of stopping muons as a function of time . . . . .	203
A.9	Distribution of calibration variables of stopping muons . . . . .	204
A.10	Validation plots for through-going muons along w . . . . .	205
A.11	Validation plots for through-going muons along w . . . . .	206
A.12	Validation plots for through-going muons across cells . . . . .	207
A.13	Validation plots for through-going muons across cells . . . . .	208
A.14	Validation plots for through-going muons across planes . . . . .	209
A.15	Validation plots for through-going muons across planes . . . . .	210
A.16	Validation plots for through-going muons along angle from the x axis	211
A.17	Validation plots for through-going muons along angle from the x axis	212

A.18 Validation plots for through-going muons along angle from the y axis	213
A.19 Validation plots for through-going muons along angle from the y axis	214
A.20 Validation plots for through-going muons along angle from the z axis	215
A.21 Validation plots for through-going muons along angle from the z axis	216

# List of Tables

2.1	Models and tunes used in the NOvA simulation of neutrino interactions.	22
3.1	Test Beam detector data taking periods. . . . .	40
3.2	Overview of the event selection for the data-based simulation . . . . .	51
3.3	Summary of relative calibration results for period 2 . . . . .	76
3.4	Description of Test Beam period 3 epochs . . . . .	80
3.5	Summary of relative calibration results for the combined epochs 3a, 3b and 3c . . . . .	85
3.6	Summary of relative calibration results for the combined epochs 3d and 3e . . . . .	88
3.7	Summary of relative calibration results for period 4 . . . . .	94
3.8	Summary of absolute calibration results . . . . .	95
4.1	Overview of the simulation samples and analysis weight used for the different signal and background components. . . . .	127
4.2	Event selection summary . . . . .	129
4.3	Event selection cutflow table for the reconstruction quality cuts . . .	132
4.4	Event selection cutflow table for the pre-selection . . . . .	136
4.5	Event selection cutflow table for the containment cuts . . . . .	148
4.6	Multivariate analysis cutflow table . . . . .	150
4.7	Interactions contributing to the SM background . . . . .	154

# CHAPTER 1

## Theory of neutrino physics

Neutrinos were first theoretically proposed by Wolfgang Pauli [1, 2] as very light electrically neutral particles with a half-integer spin and a possible magnetic moment [3]. They formed a crucial part of Enrico Fermi's successful theory of  $\beta$  decays [4, 5], which solidified their importance in particle physics even before their first experimental detection. Fermi's theory developed into the Standard Model (SM) of particle physics [6–8], which in its current form contains three generations of fermions. Each generation involves two leptons: one charged lepton and one neutrino, which has no mass, nor magnetic moment.

The SM is mathematically described by a Lagrangian, in which neutrinos are represented by a two-component left-handed chiral fields  $\nu_{\alpha L}$ , where  $\alpha = e, \mu, \tau$  denotes the three neutrino generations, also called flavours [9–11]. Neutrino fields form weak isospin doublets  $L_\alpha = \begin{pmatrix} \nu_{\alpha L} \\ \alpha_L \end{pmatrix}$  with their associated left-handed charged lepton fields  $\alpha_L$ . Unlike for the charged leptons, there is no right-handed chiral neutrino singlet field in the SM. This means that neutrinos cannot obtain a mass term, since the fermion mass terms arise from the Higgs mechanism [12–14] via the Yukawa coupling of the fermion and the Higgs fields<sup>1</sup> [15], which requires a combination of left-handed and right-handed chiral fields [16]. Additionally, since neutrinos are massless in the SM, all the neutrinos are left-handed helicity particles, and all the antineutrinos ( $\bar{\nu}$ ) are right-handed helicity antiparticles. Therefore, neutrinos and antineutrinos are mutually related not only by a charge conjugation, but by a combined Charge conjugation - Parity (CP) symmetry:  $\nu \xleftrightarrow{CP} \bar{\nu}$ .

The interaction terms for neutrinos can be separated into two parts, describing the Charged Current (CC) interactions with the  $W_\mu$  gauge field and the Neutral Current (NC) interaction with the  $Z_\mu$  gauge field, which are coupled to the  $W^\pm$  and  $Z^0$  gauge

---

<sup>1</sup>Further discussion about possible neutrino mass terms in Sec. 1.4

bosons respectively. Neglecting the non-neutrino components, the two neutrino interaction terms are [16]

$$\mathcal{L}_{\text{CC}}^{\text{SM}} = -\frac{g_w}{\sqrt{2}} \sum_{\alpha=e,\mu,\tau} \bar{\nu}_{\alpha L} \gamma^\mu \alpha_L W_\mu^+ + \text{h.c.} \quad (1.1)$$

$$\mathcal{L}_{\text{NC}}^{\text{SM}} = -\frac{g_w}{2 \cos(\theta_W)} \sum_{\alpha=e,\mu,\tau} \bar{\nu}_{\alpha L} \gamma^\mu \nu_{\alpha L} Z_\mu^0. \quad (1.2)$$

Here  $g_w$  is the weak coupling constant,  $\theta_W$  is the Weinberg angle and  $\gamma^\mu$  ( $\mu = 0, 1, 2, 3$ ) are the four Dirac gamma matrices. The  $\bar{\nu}_{\alpha L}$  denotes the Dirac adjoint of  $\nu_{\alpha L}$  and **h.c.** the hermitian conjugate. These two terms describe all the possible **SM** neutrino interaction vertices. Figure 1.1 shows the **CC** and the **NC** interaction of neutrinos and antineutrinos and, in case of the **CC** diagram, can also be flipped around the vertical axis to show the production of neutrinos from the weak interaction (or decays) of leptons. They can also be rotated 90° to either show the annihilation, or the production of the neutrino-lepton (for **CC**), or neutrino-antineutrino (for **NC**) pairs.

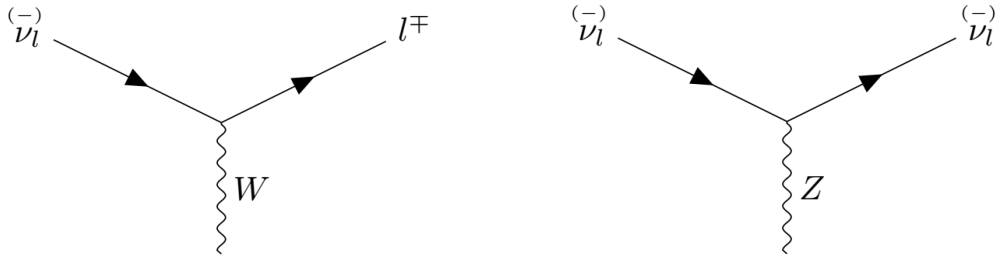


Figure 1.1: Neutrino interaction vertices in the **SM** via the weak charged currents (left) and the neutral currents (right).

## 1.1 Neutrino production

Some of the most common neutrino and antineutrino production channels include nucleon transitions via **CC** weak interactions. Specifically, the transition of a neutron into a proton, either as the decay of a free neutron, or as the  $\beta^-$  decay for neutrons bound in nucleus, produces an electron and an electron antineutrino:

$$n \rightarrow p + e^- + \bar{\nu}_e. \quad (1.3)$$

The study of the electron spectrum from  $\beta^-$  decay was the reason Pauli proposed the existence of the neutrino [1]. Additionally, this channel is an abundant source of  $\bar{\nu}_e$  from nuclear reactors, which were the first artificial sources of neutrinos, significantly increasing the flux of high energy neutrinos compared to the naturally occurring sources, thus enabling the first ever detection of a neutrino [17–19].

Similarly, the production of an electron neutrino together with a positron via the transition of a proton into a neutron can occur inside the nucleus either as the  $\beta^+$  decay:

$$p \rightarrow n + e^+ + \nu_e, \quad (1.4)$$

or via the electron capture:

$$p + e^- \rightarrow n + \nu_e. \quad (1.5)$$

This channel occurs in stars and in the first phase of supernovae [16]. However, most supernovae neutrinos are created via a thermal pair production via **NC** interaction

$$e^- + e^+ \rightarrow \nu_\alpha + \bar{\nu}_\alpha \quad (1.6)$$

producing neutrinos and antineutrinos of all flavours. Neutrino pair production via the decay of  $Z^0$  was studied in great detail [20], since the magnitude of the  $Z^0$  decay width depends on the number of neutrino flavours ( $N_\nu$ ) that can couple to  $Z^0$ , with the current best fit  $N_\nu = 2.9840 \pm 0082$  [21]. Therefore, there should be exactly three light active neutrino flavours.

An abundant source of  $\nu_\mu$  and  $\bar{\nu}_\mu$  is the decay of pions and muons

$$p + X \rightarrow \pi^\pm \rightarrow \mu^\pm + \nu_\mu (\bar{\nu}_\mu) \quad (1.7)$$

$$\mu^\pm \rightarrow e^\pm + \bar{\nu}_\mu (\nu_\mu) + \nu_e (\bar{\nu}_e), \quad (1.8)$$

which naturally occurs in Earth's atmosphere from the interaction of cosmic ray protons. It is notable, that if all the muons decay by the time they reach Earth's surface, the ratio of  $(\nu_\mu + \bar{\nu}_\mu) : (\nu_e + \bar{\nu}_e)$  should be exactly 2:1. The same process is also used in the modern accelerator-based neutrino sources, which use protons from accelerators with desired energies, impinge them onto a fixed target, and focus the resulting hadrons (mostly  $\pi$ ) to achieve a highly pure and precise source of  $\nu_\mu$  or  $\bar{\nu}_\mu$  [22, 23].

Heavier hadrons, such as kaons and charmed particles, can be produced from accelerated protons and other particles, either from natural or artificial origins. These hadrons then also produce neutrinos, including  $\nu_\tau$  and  $\bar{\nu}_\tau$  if their energies are high enough [24, 25].

## 1.2 Neutrino interactions

The interaction of neutrinos with matter can either be categorized based on the target, which is generally either an atomic electron or a nucleus, or the neutrino energy.

Neutrino-electron interactions occur either via elastic scattering, which result in a neutrino and an electron, or via the inverse muon (or tau) decay, which contains a muon (or tau) in the final state. Both of these interactions at the lowest order involve only free leptons and are very well understood theoretically. The elastic scattering has no energy threshold and can occur for any neutrino. On the other hand, due to the large difference between  $m_e$  and  $m_\mu/m_\tau$ , the inverse muon decay has an energy threshold of  $E_{\nu_\mu} > 10.92 \text{ GeV}$ , and the inverse tau decay  $E_{\nu_\tau} > 3 \text{ TeV}$  [16, 26].

Neutrino-nucleus interactions can be, to an extent, approximated by the interaction of a neutrino with quasi-free nucleons inside the nucleus [27]. These interactions can be separated into different interaction channels based on what happens to the nucleon and therefore on the resulting particles. The interaction channels depend on the neutrino incident energy, as illustrated on the case of  $\nu_\mu$  CC interactions in Fig. 1.2.

At lower energies, neutrino-nucleon interactions result in the production of either a nucleon together with a neutrino in the case of NC elastic scattering, or a nucleon with a charged lepton in the case of CC Quasi-Elastic (QE) interactions. The CCQE interaction of an antineutrino on a proton

$$\bar{\nu}_\alpha + p \rightarrow n + \alpha^+ \quad (1.9)$$

is called the inverse  $\beta$  decay and was used for the first ever detection of neutrinos (specifically  $\bar{\nu}_e$  from a nuclear reactor) [17, 18]. Together with the interaction of a neutrino on a neutron

$$\nu_\alpha + n \rightarrow p + \alpha^- \quad (1.10)$$

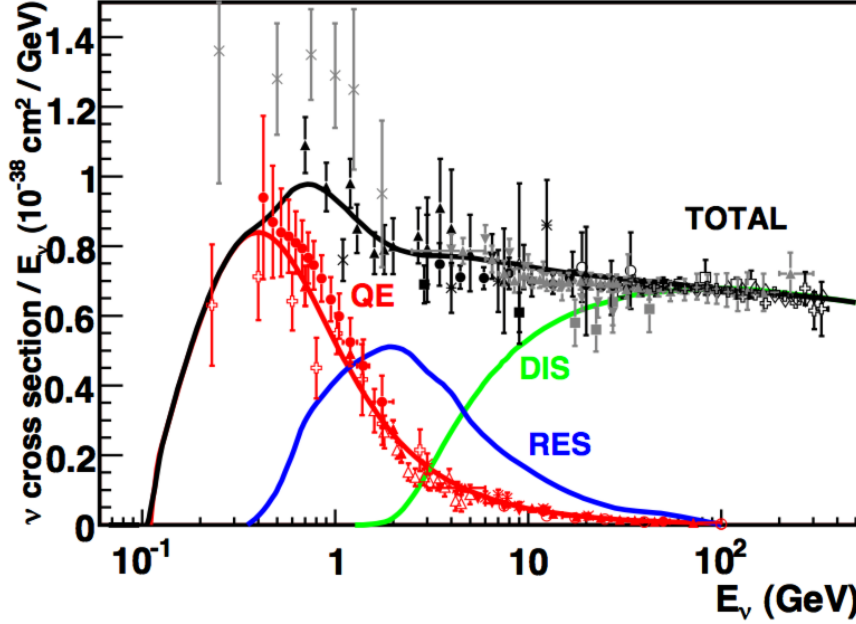


Figure 1.2: Neutrino CC cross sections on an isolated nucleon divided by the neutrino energy based on the interaction types: Quasi-Elastic (QE), Resonant baryon production (Res) and Deep Inelastic Scattering (DIS). Figure is from [28] and compares the measured data [27] and the prediction provided by the NUANCE generator [29].

they serve as fundamental processes for neutrino detection [24, 30, 31]. There is no low energy threshold for the  $\nu_e$  CCQE interaction, however, there is a threshold for  $\bar{\nu}_e$ :  $E_{\bar{\nu}_e} \gtrsim 1.8$  MeV and for the other neutrino and antineutrino flavours:  $E_{\nu_\mu} \gtrsim 110$  MeV and  $E_{\nu_\tau} \gtrsim 3.5$  GeV.

At higher energies, neutrinos can transfer enough energy to the outgoing nucleon to excite it into a resonant baryon, which then decays back into the original nucleon and into one or more additional particles. This Resonant baryon production (Res) has a threshold of about 270 MeV for  $\nu_\mu$  and can be distinguished by the presence of an additional  $\pi$  on top of the CCQE products, or, at higher energies, even of multiple additional  $\pi$ 's or other hadrons. Increasing the neutrino incident energy even higher means that neutrinos can start probing the quark contents of the individual nucleons in the Deep Inelastic Scattering (DIS), as can be seen in Fig. 1.2.

Even though the approximation of nuclei as collections of quasi-free nucleons is useful, it has been shown [32] there are important nuclear effects that have to be considered. For example the Fermi motion of nucleons and their binding inside the nucleus, or Pauli's exclusion principle resulting in nucleon energy levels [33]. Another important example is the two particle - two hole (2p2h) interaction [34–36],

which occurs when neutrinos interact with a correlated pair of nucleons and can significantly increase the [QE](#) cross section [33]. The [2p2h](#) interaction often occurs via the Meson Exchange Current (MEC), where the meson effectively propagates the interaction between the two correlated nucleons. Furthermore, the products of all of the aforementioned interactions can re-interact inside of the nucleus in Final State Interactions (FSIs), which can alter the particle content observed in the detector.

Additionally, if the total energy transferred to the nucleus is small neutrinos can interact with the entire nucleus coherently, where the contributions from each individual nucleon are added together. At low energies, neutrinos can interact via the Coherent Elastic  $\nu$ -Nucleus Scattering (CEvNS) [37], which results in the excitation of the nucleus. At higher energies, neutrinos can interact via the Coherent  $\pi$  (COH $\pi$ ) production, which produces a single  $\pi$  without transferring much momentum to the nucleus. In case of the [NCCOH \$\pi\$](#)  production the produced  $\pi$  is neutral and for the [CCCOH \$\pi\$](#)  there is an additional charged lepton and the produced  $\pi$  is positive (negative) for (anti)neutrinos. As the produced  $\pi$  receives most of the transferred momentum from the neutrinos, it generally travels in the same direction as the initial neutrino and can be difficult to distinguish, especially from  $e$  and  $\gamma$  signals in a detector [33].

### 1.3 Neutrino oscillation

The idea that neutrinos can oscillate originates as a possibility of transitions between neutrinos and antineutrinos [38, 39], analogically to the already known oscillations of  $K^0 \leftrightarrow \overline{K^0}$ . This was adapted to the oscillations between different neutrino flavours [40, 41], by considering that the flavour neutrino states  $\nu_\alpha$ , which are the eigenstates of weak interactions described in Eq. 1.1 and 1.2, are not identical to the mass neutrino states  $\nu_k$ , which are the eigenstates of the vacuum Hamiltonian  $\mathcal{H}_0$ :

$$\mathcal{H}_0 |\nu_k\rangle = E_k |\nu_k\rangle, k = 1, 2, 3, \dots, \quad (1.11)$$

with energy  $E_k$ . Instead, the neutrino flavour and mass eigenstates are related as

$$|\nu_\alpha\rangle = \sum_k U_{\alpha k}^* |\nu_k\rangle, \quad (1.12)$$

where  $U$  is the Pontecorvo-Maki-Nakagawa-Sakata (PMNS) matrix, named after the authors [16, 42].  $U$  is defined as unitary, which makes the inverse relation simply

$$|\nu_k\rangle = \sum_{\alpha} U_{\alpha k} |\nu_{\alpha}\rangle. \quad (1.13)$$

Using the Schrödinger equation

$$i \frac{d}{dt} |\nu_k(t)\rangle = \mathcal{H} |\nu_k(t)\rangle, \quad (1.14)$$

the evolution of massive neutrino states in vacuum ( $\mathcal{H} = \mathcal{H}_0$ ) can be described by plane waves

$$|\nu_k(t)\rangle = e^{-iE_k t} |\nu_k\rangle. \quad (1.15)$$

The energy of a neutrino state with mass  $m_k$  and momentum  $\vec{p}$

$$E_k = \sqrt{\vec{p}^2 + m_k^2} \quad (1.16)$$

can be approximated as

$$E_k \xrightarrow{m^2 \ll p^2 \approx E^2} E + \frac{m_k^2}{2E}, \quad (1.17)$$

assuming small neutrinos masses and for ultra-relativistic neutrinos [16]. Additionally, as it is generally easier to measure the distance neutrinos travel ( $L$ ), rather than the time ( $t$ ), and given the notation  $c \equiv 1$ , where  $c$  is the speed of light in vacuum, it is common to interchange  $L \leftrightarrow t$ .

Given the orthogonality of neutrino states,  $\langle \nu_k | \nu_j \rangle = \delta_{kj}$  and  $\langle \nu_{\alpha} | \nu_{\beta} \rangle = \delta_{\alpha\beta}$ , and using Eq. 1.15, 1.12 and 1.13, the amplitude of the oscillation (transition) from  $\nu_{\alpha} \rightarrow \nu_{\beta}$  over the ‘baseline’  $L$  can be written as

$$A_{\nu_{\alpha} \rightarrow \nu_{\beta}}(L) \equiv \langle \nu_{\beta} | \nu_{\alpha}(L) \rangle = \sum_k U_{\alpha k}^* U_{\beta k} e^{-iE_k L} \quad (1.18)$$

and the probability as

$$P_{\nu_{\alpha} \rightarrow \nu_{\beta}}(L) = |A_{\nu_{\alpha} \rightarrow \nu_{\beta}}(L)|^2 = \sum_{k,j} U_{\alpha k}^* U_{\beta k} U_{\alpha j} U_{\beta j}^* e^{-i(E_k - E_j)L}. \quad (1.19)$$

Using Eq. 1.17 and by defining the neutrino mass splitting (also called the mass

squared difference) as

$$\Delta m_{kj}^2 \equiv m_k^2 - m_j^2, \quad (1.20)$$

the oscillation probability can be expressed as

$$P_{\nu_\alpha \rightarrow \nu_\beta}(L) = \sum_{k,j} U_{\alpha k}^* U_{\beta j} U_{\alpha j} U_{\beta k}^* e^{-i \frac{\Delta m_{kj}^2 L}{2E}}. \quad (1.21)$$

So far no assumption has been made as to the specific number of neutrino mass or flavour states. However, as was described above in Sec. 1.1, from the decay of  $Z^0$  we know there are probably exactly three active neutrino flavour states,  $\nu_e$ ,  $\nu_\mu$  and  $\nu_\tau$ . Consequently, it is common to also consider exactly three neutrino mass states. This is often called the three neutrino paradigm. Therefore, the **PMNS** matrix can be written as [16]:

$$U = \begin{pmatrix} U_{e1} & U_{e2} & U_{e3} \\ U_{\mu 1} & U_{\mu 2} & U_{\mu 3} \\ U_{\tau 1} & U_{\tau 2} & U_{\tau 3} \end{pmatrix} = \\ = \begin{pmatrix} 1 & 0 & 0 \\ 0 & c_{23} & s_{23} \\ 0 & -s_{23} & c_{23} \end{pmatrix} \begin{pmatrix} c_{13} & 0 & s_{13} e^{-i\delta} \\ 0 & 1 & 0 \\ -s_{13} e^{i\delta} & 0 & c_{13} \end{pmatrix} \begin{pmatrix} c_{12} & s_{12} & 0 \\ -s_{12} & c_{12} & 0 \\ 0 & 0 & 1 \end{pmatrix}, \quad (1.22)$$

where  $c_{ij} \equiv \cos \theta_{ij}$  and  $s_{ij} \equiv \sin \theta_{ij}$ . The matrix is parametrized using three mixing angles  $\theta_{12}$ ,  $\theta_{13}$ , and  $\theta_{23}$  and one phase<sup>2</sup>, often denoted  $\delta_{CP}$ . This phase describes a possible **CP** symmetry violation in neutrino oscillations, which would result in a difference between the neutrino and antineutrino oscillation probabilities.

When neutrinos pass through matter, their evolution changes due to coherent elastic **CC** and **NC** scattering. However, since the **NC** scattering affects all neutrino flavours equivalently, it does not have any effect on neutrino oscillations. Additionally, as electrons are the only charged leptons present in matter, only the relative difference between the **CC** interactions of  $\nu_e$  and of the other flavours needs to be considered. The effective interaction potential of neutrinos passing through matter

---

<sup>2</sup>If neutrinos are Majorana particles, they can have two additional phases, which however do not enter into neutrino oscillation probabilities

with an electron density  $N_e$  can be written as

$$V_{CC} = \pm \sqrt{2} G_F N_e. \quad (1.23)$$

Here  $G_F$  is the Fermi coupling constant and the plus or minus sign is for neutrinos or antineutrinos respectively. The electron density (and therefore the interaction potential) can change along the neutrino path, as it does in the Sun, which can resonantly increase the probability of oscillations, as described by the Mikheyev-Smirnov-Wolfenstein (MSW) effect [43, 44]. However, in accelerator based experiments, where neutrinos only pass through the surface of the Earth, the  $N_e$  can be approximated as a constant.

The effect of neutrinos passing through matter on oscillation probabilities can be expressed as shifts to mixing angles and to mass squared differences, proportional to the  $V_{CC}$ . Since the matter effect differs for neutrinos and antineutrinos, it needs to be carefully considered especially for the  $\delta_{CP}$  measurement, which relies on the comparison of neutrino to antineutrino oscillations [16].

The first experimental signs of neutrino oscillations appeared as an apparent deficit of solar neutrinos compared to their predicted flux [30]. However, due to low confidence in the prediction of the solar neutrino flux, no conclusion could have been drawn. Similarly, experiments measuring atmospheric neutrinos [45–48] saw a disagreement between the measurement and the prediction for the  $\nu_\mu : \nu_e$  fraction of the atmospheric neutrino flux. This *atmospheric neutrino anomaly* was finally resolved by the Super-Kamiokande (SK) experiment [49], reporting the first experimental evidence for neutrino oscillations. The *solar neutrino anomaly* was resolved shortly after by the Sudbury Neutrino Observatory (SNO) experiment [50], which compared the NC rate, unaffected by neutrino oscillations, to the rate of CC neutrino interactions. This was proof that solar neutrinos oscillate without reliance on the model of the Sun. This result also confirmed the importance of accounting for the matter effect in neutrino oscillations, especially for the oscillation of solar neutrinos, due to the large matter density in the Sun.

The difference between the frequency of solar neutrino oscillations and that observed in atmospheric neutrinos proves that there are at least two mass splittings governing neutrino oscillations. As a result, there must be at least three separate

neutrino mass states, with at least two of them possessing non-zero masses. This is in direct contradiction to the SM and is to-date the only laboratory-based observation of physics Beyond Standard Model (BSM) [51].

Currently, the three neutrino paradigm of oscillations between three neutrino flavour states via three neutrino mass states is well established [52, 53]. The magnitudes of both the neutrino mass splittings and of two mixing angles,  $\theta_{12}$  and  $\theta_{13}$ , are measured within 3%. The third mixing angle  $\theta_{23}$  is measured to be close to the maximum mixing value of 45°. However, there are three main questions yet to be determined for neutrino oscillations [51]:

1. What is the sign of the larger neutrino mass splitting? Is the electron neutrino made up of the lightest neutrino mass states (normal ordering), or the heaviest (inverted ordering)?
2. Is  $\theta_{23} < 45^\circ$  or  $\theta_{23} > 45^\circ$ ? These two options determine the  $\nu_\mu : \nu_\tau$  relative contributions to the neutrino mass states and are also referred to as the upper and the lower octant respectively.
3. Is there CP violation in neutrino oscillations? What is the value of  $\delta_{CP}$ ? If neutrinos oscillate differently than antineutrinos, this could be an important part of the matter-antimatter asymmetry in the Universe.

All three of these questions are jointly investigated in the current Long Baseline (LBL) accelerator neutrino oscillation experiments, namely the NuMI Off-axis  $\nu_e$  Appearance (NOvA) [54] and the Tokai to Kamioka (T2K) [55] experiments. Both use precise  $\nu_\mu$  and  $\bar{\nu}_\mu$  beams, affected by the matter effect, and compare the rates of  $\nu_\mu$  and  $\bar{\nu}_\mu$  disappearance and  $\nu_e$  and  $\bar{\nu}_e$  appearance to constrain neutrino oscillation parameters [51]. The same methods will be used in the next generation LBL neutrino oscillation experiments, namely the Deep Underground Neutrino Experiment (DUNE) [56] and the Hyper-Kamiokande (HK) [57] experiment, which should give the final answers to all three neutrino oscillation questions [51].

## 1.4 Neutrino mass

The absolute values of neutrino masses are currently not known and cannot be directly measured in neutrino oscillation experiments. However, results from experiments measuring the kinematic distribution of  $\beta$  decays [58], or from cosmology [59], currently set a limit for each neutrino mass to  $< 1 \text{ eV}$ . This is several orders of magnitude smaller than the charged fermion masses, suggesting that **BSM** theories which introduce neutrino masses should have a different mechanism for their generation than the one used for the other fermions [52]. Furthermore, in order to introduce neutrino masses into the **SM**, it is necessary to either add new fields, break the renormalizability of the **SM** Lagrangian, or do both [42]. Also, massive neutrinos can no longer be described by Weyl spinors

The most straight-forward solution, often called the *minimally extended SM*, is to add the missing right-handed chiral neutrino fields, which would enable neutrino mass generation through Yukawa couplings with the Higgs field. These right-handed fields would however be singlets under all the **SM** gauge symmetries and would therefore not participate in any of the **SM** interactions. Neutrinos created by these fields are called *sterile* and could potentially mix with the *active* neutrinos via neutrino oscillations. There are however a few issues with the minimally extended **SM**. Since the mass generation mechanism is the same as for the charged fermions, there is no theoretical explanation for the relative smallness of neutrino masses. There is also currently no experimental confirmation of oscillations between active and sterile neutrinos [52], although there are some possible indications [60, 61]. Additionally, having to add new fields by hand makes the **SM** an incorrect description of reality even at low energies. This is an issue, as it is generally believed that **SM** is at least a good low energy effective theory of a more complex general theory and only breaks down at some New Physics (NP) threshold value  $\Lambda_{NP}$  [62].

Adding new non-renormalizable terms to the **SM** Lagrangian, which are suppressed by this **NP** scale as  $1/\Lambda_{NP}$ , would maintain the renormalizability (and validity) of the **SM** at energies well below  $\Lambda_{NP}$  [62]. It is possible to create such a term using only the existing **SM** fields and preserving the **SM** gauge symmetries, which after spontaneous symmetry breaking generates neutrino mass terms. Additionally, three of the newly generated masses are also suppressed as  $1/\Lambda_{NP}$  and belong to

mostly left-handed (active) fields, while the rest are very large ( $\sim \Lambda_{NP}$ ) and belong to mostly sterile neutrinos, which are therefore also called Heavy Neutral Leptons (HNLs). This is called the see-saw mechanism [63] and provides a natural explanation for the smallness of neutrino masses. Furthermore, the large masses of HNL make them more likely to avoid experimental detection. However, neutrinos with masses produced by this mechanism all have to be Majorana particles [64].

If neutrinos are Majorana particles, they are equivalent to their own antiparticles (via charge conjugation). The particles described as antineutrinos in the previous sections are however still different to neutrinos, although for Majorana neutrinos they only differ by parity transformation. Therefore, Majorana neutrinos and antineutrinos can be seen as two different spin states of a two-state ‘Majorana particle’. This is in contrast to neutrinos being Dirac particles, which have four independent states (neutrino/antineutrino, each with two independent spin states), same as the other fermions and as in the minimally extended SM [16]. It is possible for neutrinos to be Majorana particles as they have no electric charge. However, all the other additive quantum numbers, including the total lepton number, must vanish for Majorana neutrinos as well. This means that Majorana neutrinos can effectively annihilate with each other, violating the total lepton number by two units.

A sure way of finding out whether neutrinos are Majorana particles or not is an observation of a neutrino-less double  $\beta$  decay [62]. This is currently a subject of an extensive experimental investigation without a concrete conclusion [52]. Neutrinos being Majorana particles does not affect neutrino oscillations, however, other measurements could probe the nature of neutrinos, or possible theories BSM, such as the measurements of the possible neutrino magnetic moment [51].

## CHAPTER 2

# The NOvA experiment

The NOvA [65] experiment is a long-baseline neutrino oscillation experiment based at the Fermi National Accelerator Laboratory (Fermilab) [66]. NOvA receives an off-axis  $\nu_\mu$  and  $\bar{\nu}_\mu$  beam from Fermilab’s Neutrinos from the Main Injector (NuMI) neutrino source (Sec. 2.1) and measures  $\nu_e$  or  $\bar{\nu}_e$  appearance and  $\nu_\mu$  or  $\bar{\nu}_\mu$  disappearance between its two highly active and finely segmented detectors (Sec. 2.4) [67].

The capability to measure both  $\nu_e$  and the  $\bar{\nu}_e$  appearance, coupled with a significant matter effect induced by its long baseline, allows NOvA to address some of the most important questions in neutrino physics to date, such as the neutrino mass ordering, the octant of  $\theta_{23}$ , and the possible CP symmetry violation in the neutrino sector [54, 67–70]. NOvA data also enables measurements of  $\theta_{13}$ ,  $\theta_{23}$  and  $|\Delta m_{32}^2|$  [67], measurements of neutrino differential cross sections in the Near Detector (ND) [71–74], constraints on possible sterile neutrino models [75, 76], monitoring for supernova neutrino activity [77, 78], searches for magnetic monopoles [79], and constraints on the neutrino electromagnetic properties (this thesis). Using two functionally identical detectors mitigates the dominant systematic uncertainties of neutrino oscillation measurements, described in Sec. 2.8.

NOvA started taking data in February 2014 and is expected to run through 2026 [80], or until Fermilab begins redirecting its efforts towards the startup of the upcoming DUNE experiment [81].

### 2.1 The neutrino beam for NOvA

The neutrino beam for NOvA comes from the Fermilab-based NuMI neutrino source [82]. The schematic description of NuMI is shown in Fig. 2.1, starting on the left hand side with 120 GeV protons from the Main Injector (MI), part of the Fermilab accelerator complex. The proton beam is divided into 10  $\mu\text{s}$  long pulses, with  $\sim 5 \times 10^{13}$

Protons On Target (POT) per spill every  $\sim 1.3$  s long cycle time, resulting in a proton beam power of  $\sim 800$  kW (current record 959 kW [83]), with upgrades currently underway to surpass 1 MW [84].

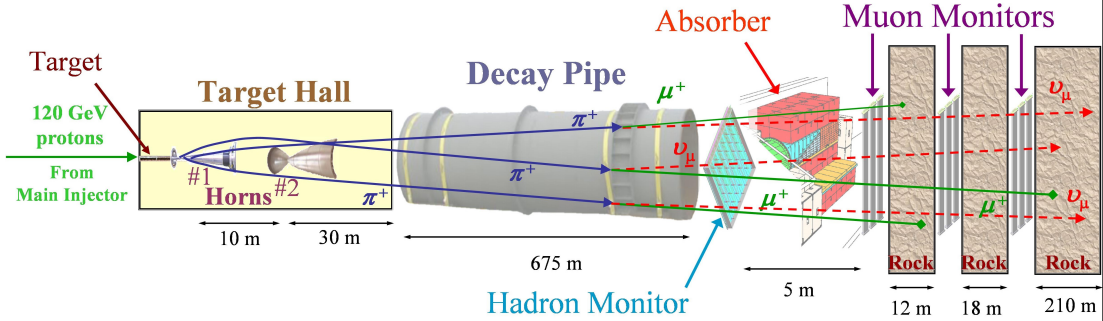


Figure 2.1: The NuMI neutrino beam starts on the left hand side with protons from the MI impinged on a graphite target producing mainly pions and kaons. These are then focused and charge-selected by two focusing horns, after which they decay inside the decay pipe into a high-purity  $\nu_\mu$  or  $\bar{\nu}_\mu$  beam. The residual hadrons are stopped and monitored in the hadron absorber and the remaining muons are recorded with muon monitors and absorbed inside the rock. Figure from [82].

The proton beam passes through a collimating baffle before hitting a  $\sim 1.2$  m-long (equal to about two interaction lengths) graphite target [85], producing hadrons, predominantly pions and kaons [82]. These are then focused and selected by two parabolic magnetic ‘horns’. The focused hadrons pass through a 675 m-long decay pipe filled with helium to create a low density environment for hadrons to propagate and decay in flight into either neutrinos or antineutrinos. High energy hadrons that do not decay in the decay pipe are absorbed within a massive aluminium, steel, and concrete hadron absorber and monitored with a hadron monitor. The leftover muons are ranged out in dolomite rock after the absorber and monitored using three muon monitors. The hadron and muon monitors are ionization chambers, used to monitor the quality, location and relative intensity of the beam.

Using a positive current inside the horns focuses positively charged particles, which then decay into neutrinos, and removes negatively charged particles. Reversing the horn current focuses negatively charged particles, which decay into antineutrinos, and defocuses positively charged particles. The neutrino mode is therefore called Forward Horn Current (FHC) and the antineutrino mode is called Reverse Horn Current (RHC). The composition of the neutrino beam for both these modes at the NOvA ND is shown in Fig. 2.2, displaying the very high purity of the  $\nu_\mu$  or  $\bar{\nu}_\mu$

component in the **FHC** ro **RHC** beam respectively [82].

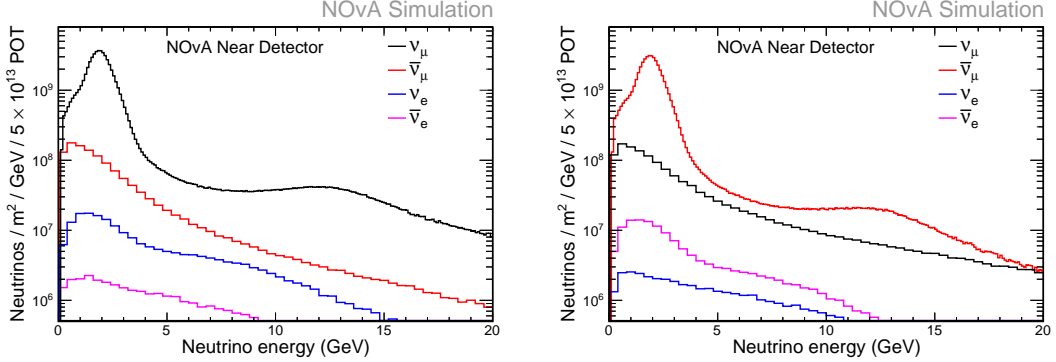


Figure 2.2: The components of the neutrino beam at the **NOvA ND** per one **NuMI** spill in the **FHC** regime shown on the left and the **RHC** regime on the right. The  $\nu_\mu$  ( $\bar{\nu}_\mu$ ) composition in the **FHC** (**RHC**) regime is 93.8% (92.5%), with a wrong sign contribution of 5.3% (6.6%) and only 0.9% (0.9%) contamination by  $\nu_e$  ( $\bar{\nu}_e$ ), showing the high purity of  $\nu_\mu$  and  $\bar{\nu}_\mu$  in the neutrino beam for **NOvA**. Beam composition values calculated for neutrinos with energies between 1 – 5 GeV. Figures are from internal **NOvA** repository [86].

The resulting neutrino beam energy distribution is peaked at  $\sim 7$  GeV with a wide energy band. However, thanks to the kinematics of the dominant pion decay, by placing the **NOvA ND** and Far Detector (FD) 14.6 mrad ( $\approx 0.8^\circ$ ) off the main **NuMI** beam axis, **NOvA** achieves a narrow band neutrino flux peaked at 1.8 GeV [54, 87], as can be seen in Fig. 2.3. Using an off-axis neutrino flux increases the neutrino beam around 2 GeV about 5-fold compared to the on-axis flux and narrow-band peak enhances background rejection for the  $\nu_e$  appearance analysis [87].

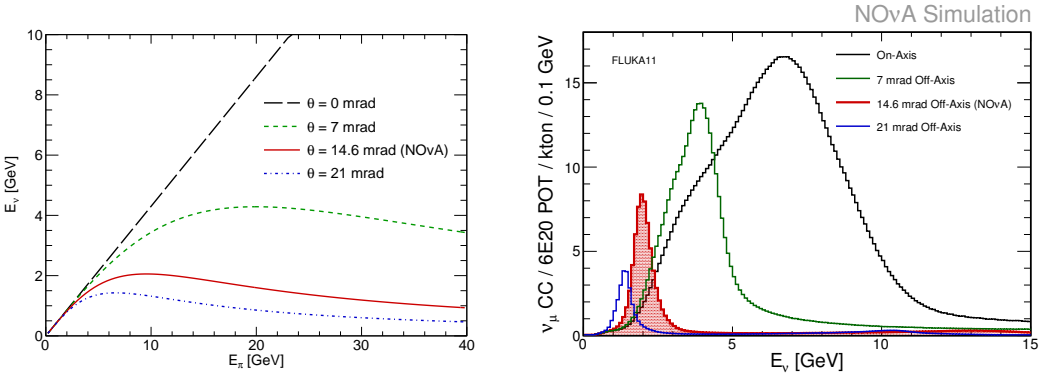


Figure 2.3: (Left) Dependence of the neutrino energy on the parent pion's energy and (right) neutrino energy distribution for an on-axis beam and three different off-axis beam designs. The case for **NOvA** is shown in red and results in a narrow neutrino energy distribution around 2 GeV, with limited dependence on the parent pion's energy. Figure from [87]

## 2.2 The NOvA detectors

The two main NOvA detectors are the ND, located in Fermilab  $\sim 1$  km from the NuMI target and  $\sim 100$  m under ground, and the FD, located  $\sim 810$  km from Fermilab at Ash River in north Minnesota, partially underground with a rock overburden [87]. NOvA also operated a detector prototype called Near Detector on the Surface (NDOS), which was used for early research and development of detector components and analysis [68]. Additionally, NOvA operated a Test Beam detector, described in detail in Sec. 3.1.

The scales of the ND and FD are shown in Fig. 2.4.

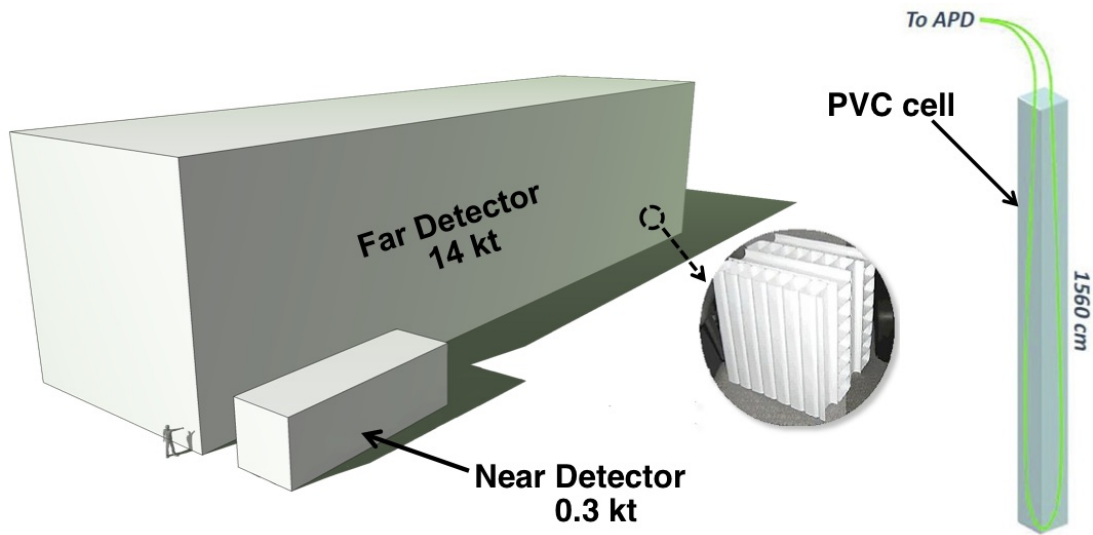


Figure 2.4: Schematic description of the scale and composition of the NOvA ND and FD. The inset shows a photo of the orthogonal planes made out of PVC cells. An example of a FD cell containing liquid scintillator and a looped WLS fibre attached to an APD is shown on the right [88].

All NOvA detectors are highly segmented, highly active, functionally identical tracking calorimeters made up of Polyvinyl chloride (PVC) cells filled with liquid scintillator. Each cell is a long rectangular cuboid with depth of 5.9 cm and width of 3.8 cm (with some variations), with cell length extending to the full width/height of each detector, which is  $\sim 4.1$  m for the ND and  $\sim 15.6$  m for the FD [87]. An example of a FD cell is shown on the right of Fig. 2.4.

Cells are connected side-by-side into a 16 cell-wide extrusions with 3.3 mm-wide walls between cells and 4.9 mm-wide walls on the outsides of the extrusions. The first and last cell of each extrusion are  $\sim 3$  mm narrower than the rest of the cells. Two extrusions are connected side-by-side to form a 32 cell-wide module, with each

module having a separate readout (see Sec. 2.3). In the **FD**, 12 modules are connected side-by-side to form one plane of the detector. In the **ND** only 3 modules make up a plane. Planes are positioned one after another, alternating between vertical and horizontal orientation, and grouped into diblocks, each containing 64 planes. The **FD** contains 14 diblocks, totalling 896 planes, whereas the **ND** contains 3 diblocks totalling 192 planes. The **ND** also contains a Muon Catcher region, positioned right after the active region, consisting of 22 planes of the normal **NOvA** detector design, 2 modules high and 3 modules wide, sandwiched with 10 steel plates to help range out muons mainly from the  $\nu_\mu$  charged current interactions [68, 87].

The **NOvA** coordinate system is centred with  $(0, 0, 0)$  in the centre of the first plane, relative to the beam direction. The x axis runs from left to right when facing the detector, y axis from bottom to top and z axis runs perpendicular to the planes along the beam direction.

Each cell is filled with a liquid scintillator consisting of mineral oil with 4.1% pseudocumene as the scintillant [89]. Each cell contains a single wavelength shifting fibre with double the length of the cell, looping at one end and connecting to the readout at the other. The **PVC** walls of the cells are loaded with highly reflective titanium dioxide, with light typically bouncing off the **PVC** walls  $\sim 8$  times before being captured by the Wavelength Shifting (WLS) fibre [87].

The final dimensions of the **FD** are  $15.6\text{ m} \times 15.6\text{ m} \times 60\text{ m}$  with a total mass of 14 kT and for the **ND** the dimensions are  $3.8\text{ m} \times 3.8\text{ m} \times 12.8\text{ m}$  with a mass of about 0.3 kT [80]. The active volume, consisting only of the liquid scintillator without the **PVC** structure, makes up about 70% of the total detector volume [87].

The **NOvA** detectors are specifically designed for electromagnetic shower identification, with a radiation length of 38 cm, which amounts to  $\sim 7$  planes for particles travelling perpendicular to the detector planes [68]. This is particularly useful to distinguish electrons from  $\pi^0$ s.

We can calculate the minimum energy an electron needs to have to cross one cell (5.9 cm) of the **NOvA** detector by using the measured scintillator density  $0.86\text{ g/cm}^3$  [90], which gives us the required range of  $\sim 5\text{ g/cm}^2$ . Comparing this to measured values for the electron range [91] in the continuous slowing down approximation in a Polyethylene (approximation of the **NOvA** scintillator [92]), gives us an estimate of

the lowest detectable electron energy as  $E_e \gtrsim 10$  MeV.

## 2.3 Readout and data acquisition

The signal from the WLS fibres is read out by an Avalanche Photodiode (APD), converting the scintillation light into electrical signal, with a high quantum efficiency of  $\sim 85\%$  and a gain of 100 [87]. An example APD is shown in Fig. 2.5. Both ends of each fibre correspond to a single readout channel and are connected to one of the 32 pixels on the APD, organized in four rows of 8 pixels, with each APD reading out signal from one module. To maximise the signal to noise ratio, the APDs are cooled to  $-15^\circ\text{C}$  by a thermoelectric cooler, with heat carried away by a water cooling system.

The combination of the APD quantum efficiency and the light yield, determined by the PVC reflectivity and the scintillator and WLS fibre responses, result in a signal requirement of at least 20 Photo Electron (PE) in response to minimum ionizing radiation at the far end of the FD cell.

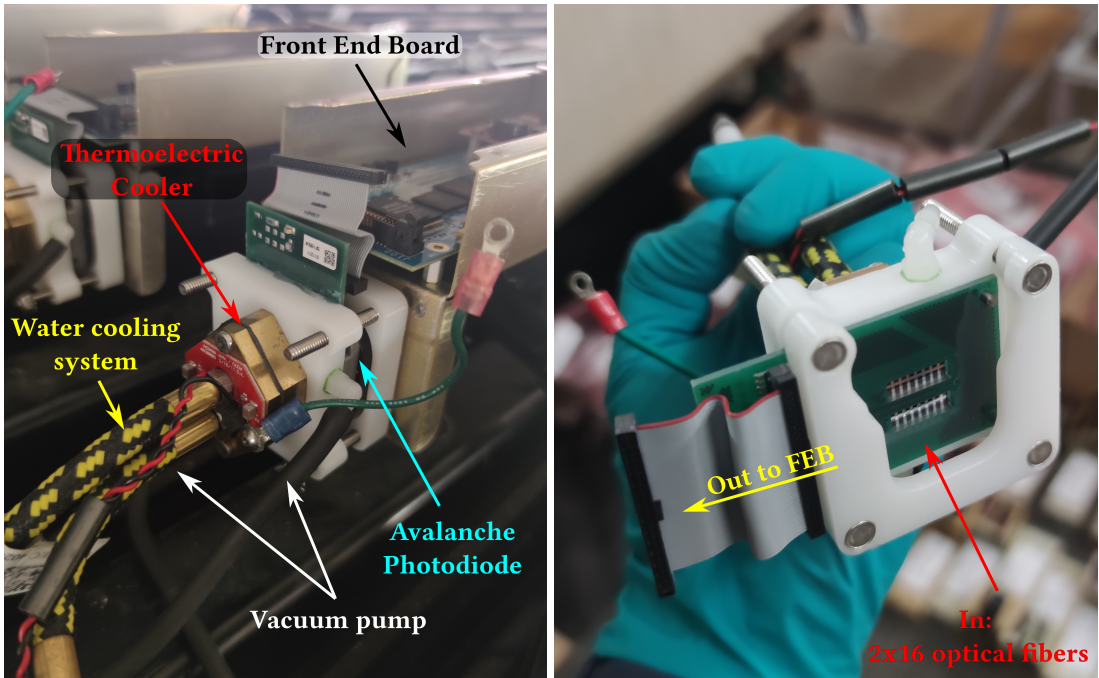


Figure 2.5: The modules with APDs for NOvA mounted on top of the detector on the left picture, and shown from the bottom on the right. The individual components of the module are described. The left picture shows a disconnected ribbon cable and ground cable, which are normally connected to the front end board.

Each APD is connected to a single Front End Board (FEB), shown in Fig. 2.6. The FEB amplifies and integrates the APD signal, determines its amplitude and arrival

time, before passing it to the Data Acquisition (DAQ) system. On the FEB the APD signal is first passed to a custom NOvA Application-Specific Integrated Circuit (ASIC), which is designed to maximize the detector sensitivity to small signals. ASICs amplify, shape and combine the signal, before sending it to an Analog-to-Digital Converter (ADC). The combined noise from the APD and the amplifier is equivalent to about 4 PEs, which, compared to an average PE yield from the far end of the FD cell of 30, results in a good signal and noise separation [87]. The digitized data from an ADC is sent to a Field Programmable Gate Array (FPGA), which extracts the time and amplitude of the ADC signals, while subtracting noise based on a settable threshold. The FPGAs employ multiple correlated sampling methods to reduce noise and improve time resolution of the signal [93].

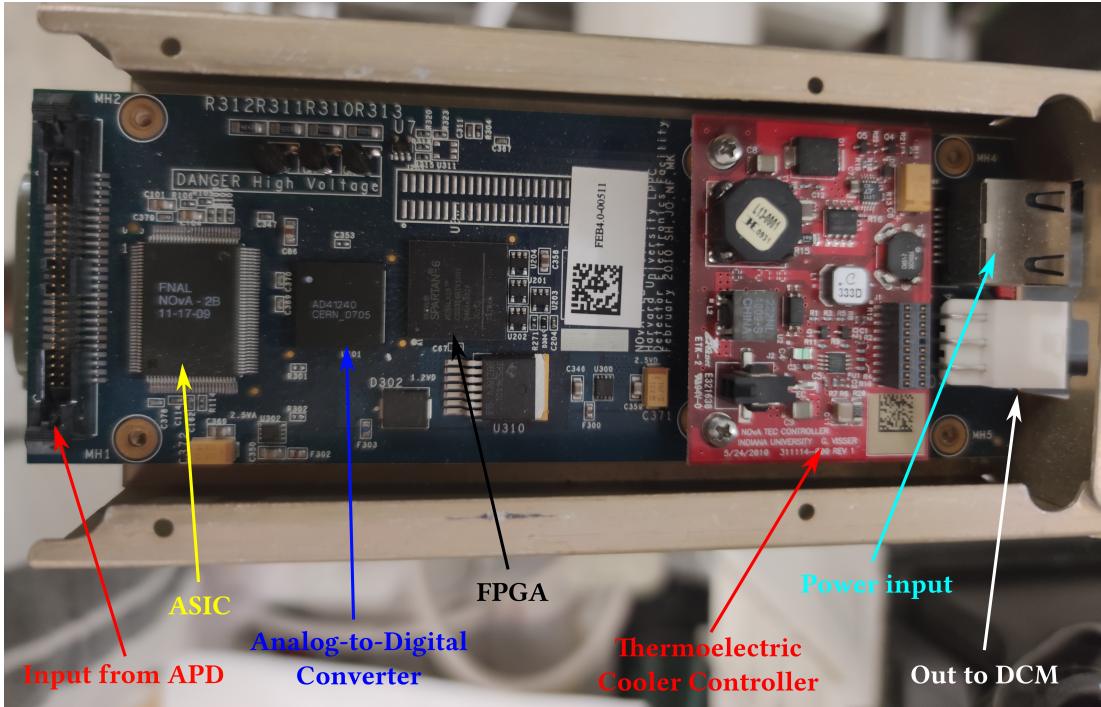


Figure 2.6: An example of a NOvA FEB with individual components labelled.

All of the NOvA front end electronics (APDs and FEBs) are operated in a continuous readout mode, without requiring any external triggers [87]. Due to higher detector activity during beam spills, the ND FEBs work at a higher frequency of 8 MHz, whereas the FD FEBs suffice with 2 MHz sampling frequency [93].

Data from up to 64 FEBs are concentrated in a Data Concentration Module (DCM), which concatenates and packages the data into 5 ms time slices, before sending it to the buffer nodes. DCMs are also connected to the timing system and pass a single

unified timing measurement to the [FEBs](#) to maintain synchronization across the detector [93].

The buffer nodes cache the data for at least 20 seconds while receiving information from the trigger system. Each trigger uses a time window based either on the time of the [NuMI](#) beam spill, on a periodic interval for monitoring and for the readout of cosmic events, or on one of the activity-based data-driven triggers [93]. Data that fall within any of the trigger windows are sent to a data logger system, where they are merged to form events, before being written to files for offline processing and sent to an online monitoring system. Files are organized based on a unique combination of run and subrun numbers, with runs corresponding to data taking periods with constant detector conditions and limited to either 64 subruns or 24 hours. Subruns are delineated either by a 2 GB file size constraint or a 1-hour timeout limit [94].

The detectors are continuously monitored to ensure data stability and quality. Subruns with suboptimal detector conditions or with events failing basic quality criteria are flagged as ‘bad’ and recorded in a ‘bad runs list’ [94]. Additionally, individual readout channel are assessed on a per-subrun basis, with those with too high or too low hit rates marked as ‘bad’ [95]. Both the ‘good runs’ list and the ‘bad channel’ maps are used to inform event processing and during simulation to emulate real detector conditions.

## 2.4 Simulation

To extract neutrino oscillation parameters, or to test a hypothesis, [NOvA](#) uses a series of simulations to make predictions according to various physical models [96]. The simulation chain can be divided into four parts: simulation of the neutrino beam, simulation of neutrino interactions within the [NOvA](#) detectors, simulation of cosmic particles interacting in the [NOvA](#) detector and simulation of the detector and readout response.

To simulate the neutrino beam, [NOvA](#) uses a simulation based on the GEANT4 v9.2.p03 [97] Monte Carlo (MC) event generator with a detailed model of the [NuMI](#) beamline [98], as described in Sec. 2.1. The simulation starts with the 120 GeV/c [MI](#) protons interacting within the long carbon target and producing hadrons, mainly

$\pi$ ,  $K$  and secondary protons. This is followed by transport and possible further interaction of hadrons within the focusing system, until finally ending with hadron decays producing the neutrino beam.

To account for the inherently imprecise theoretical models used in GEANT4, **NOvA** uses the Package to Predict the Flux (**PPFX**) to incorporate external measurements of yields and cross sections of hadron interactions inside the target and the other **NuMI** materials into the neutrino beam prediction [99]. The current version of **PPFX** is limited by the results available during its creation and only corrects the most frequent interactions while assigning conservative systematic uncertainties to the rest (see Sec. 2.8). For the most common  $\pi$ ,  $K$  and  $p$  production, **PPFX** uses the NA49 measurements [100–102] of 158 GeV/c protons interacting on a thin (few percent of interaction length) carbon target. To expand the kinematic coverage, **PPFX** uses a few data points from Barton et al [103] for the  $\pi$  production and  $K/\pi$  ratios from the Main Injector Particle Production (MIPP) [104] experiment for the production of  $K$ . These results have to be scaled to the 20 – 120 GeV/c incident proton moment seen throughout **NuMI** using the FLUKA [105, 106] **MC** generator.

There are two new experiments that measure the production and interaction of hadrons on various targets and incident energies, specifically designed to improve the prediction of neutrino beams. The most impactful measurements from the NA61 experiment are of the 120 GeV/c protons on a thin carbon target [107–109], of the hadron incident interactions on various materials [110], and of the 120 GeV/c protons on a **NuMI** replica target [111]. Additionally, the Fermilab-based EMPHATIC experiment [112] is currently analysing a broad range of hadron production and secondary and tertiary interaction measurements for neutrino beam prediction with a significant involvement of **NOvA** and **DUNE** collaborators. Inclusion of the results from both of these measurement is currently under way and will significantly improve the neutrino beam prediction in **NOvA** [111].

The output of the neutrino beam simulation is passed to the simulation of neutrino interactions inside the detectors, which is done with the GENIE v3.0.6 [113] neutrino **MC** generator. GENIE allows users to choose the particular models for different types of neutrino interactions and particle propagation within the nucleus, as well as possible tunes to external measurements. The four main interaction modes in GENIE are

the [QE CC](#) scattering, the [Res](#), the [DIS](#), and the [COH \$\pi\$](#)  production. The special case of the [2p2h](#) interaction via [MEC](#) and the [FSI](#) inside a nucleus are also considered. The initial state of the nucleus is represented by a local Fermi gas in the [QE](#) and [2p2h](#) models, while a global relativistic Fermi gas is used for all other processes. All of these are set by the Comprehensive Model Configuration (CMC), which is currently N1810j0000 for [NOvA](#). Additionally, [NOvA](#) adds a costume tune to the [NOvA](#)  $\nu_\mu$ [CC](#) data for a better constraint of the [CCMEC](#) interactions. [NOvA](#) also uses a set of external  $\pi$  interaction measurements to constrain the [FSI](#) model. Table 2.1 shows the list of models and tunes for different interaction modes in [NOvA](#) [54].

Table 2.1: Models and tunes used in the [NOvA](#) simulation of neutrino interactions.

Interaction	Model	Tune
<a href="#">CCQE</a>	València [114]	External $\nu - D$ data [115]
<a href="#">CCMEC</a>	València [116, 117]	<a href="#">NOvA</a> $\nu_\mu$ <a href="#">CC</a> data
<a href="#">Res &amp; COH<math>\pi</math></a>	Berger-Sehgal [118, 119]	External $\nu - A$ data
<a href="#">DIS</a>	Bodek-Yang [120, 121]	External $\nu - A$ data
<a href="#">FSI</a>	Semi-classical cascade [122]	External $\pi - {}^{12}C$ data

Since the [FD](#) is on the surface [NOvA](#) also uses a simulation of cosmic rays generated with the [MC](#) Cosmic-Ray Shower Generator (CRY) [123]. The simulated cosmic muons are also used to calibrate [NOvA](#) detectors [99].

Particles that are created from neutrino interactions and cosmic rays are propagated through the [NOvA](#) detectors using the GEANT4 v10.4.p02 [97], which outputs the energy deposited in the scintillator. This is then passed to a custom [NOvA](#) software of the light model [99], which calculates the amount of scintillation light produced for the deposited energy based on a Poisson distribution. The scintillation light production is parametrized using the Birks-Chou model [124], which corrects for the recombination in organic scintillators at high deposited energies. The scintillator light yield and the inherent production of the Cherenkov light, which can affect the light readout, are tuned to [NOvA](#) data [72]. The light collection by the [WLS](#) fibres, its transport to the [APDs](#), and the [APD](#) response use a parametrized simulation, as the [NOvA](#) cells and their readout are generally the same across the detectors [99]. The simulation of the readout electronics is done by another custom [NOvA](#) parametrized model, which accounts for random noise in the readout electronics and outputs true events in the same format as the real data.

Due to the high neutrino rate in the **ND**, there are neutrinos interacting in the surrounding rock creating particles, mainly muons, that make it to the detector and act as background. However, since only a few ‘rock muons’ make it into the detector, it would be very time consuming to run a simulation which includes the rock around the **ND** for every neutrino. Instead, **NOvA** creates a separate simulation that includes the surrounding rock and then overlays these results into the nominal **NOvA** simulation chain to match the **NuMI** neutrino rate [99].

## 2.5 Data processing and event reconstruction

Both data and simulation events for all **NOvA** detectors are passed through the same event reconstruction and particle identification algorithms. The reconstruction was specifically developed with the  $\nu_e$  appearance search in mind, focusing on identifying the  $\nu_e$ **CC** signal against the  $\nu_\mu$ **CC** and **NC** backgrounds. Each **NOvA** detector has to deal with different challenges, with multiple neutrinos interacting during one beam spill in the **ND**, and a large cosmic background in the **FD** [125].

The output from the **DAQ** system for each channel is called a *raw hit*. Hits are grouped into 550  $\mu\text{s}$ -long windows and passed to an offline reconstruction chain [125]. Reconstruction starts by grouping hits into *slices* based on their proximity to other hits in both time and space [126]. Slices are designed to ideally contain only a single neutrino interaction event.

For events that produce hadronic and electromagnetic showers, reconstruction first identifies straight lines through major features using a modified Hough transform [127], representing particle directions. These lines are passed to the Elastic Arms algorithm [128] to identify *vertex* candidates from their intersection points. Hits are then clustered into *prongs*, which are collections of hits with a start point, based on the vertex, and a direction, using a k-means algorithm called FuzzyK [129, 130]. Here ‘fuzzy’ means that each hit can belong to multiple prongs. Prongs are first created separately for each view (also called 2D prongs) and then, if possible, view-matched into 3D prongs (from here on referred to as prongs) [125]. Figure 2.7 shows an example of a simulated electron shower, where the reconstructed vertex is shown as a red cross and the prong as a red shaded area. The prong groups together all the hits that

are part of the shower, while removing the background hits, shown in grey.

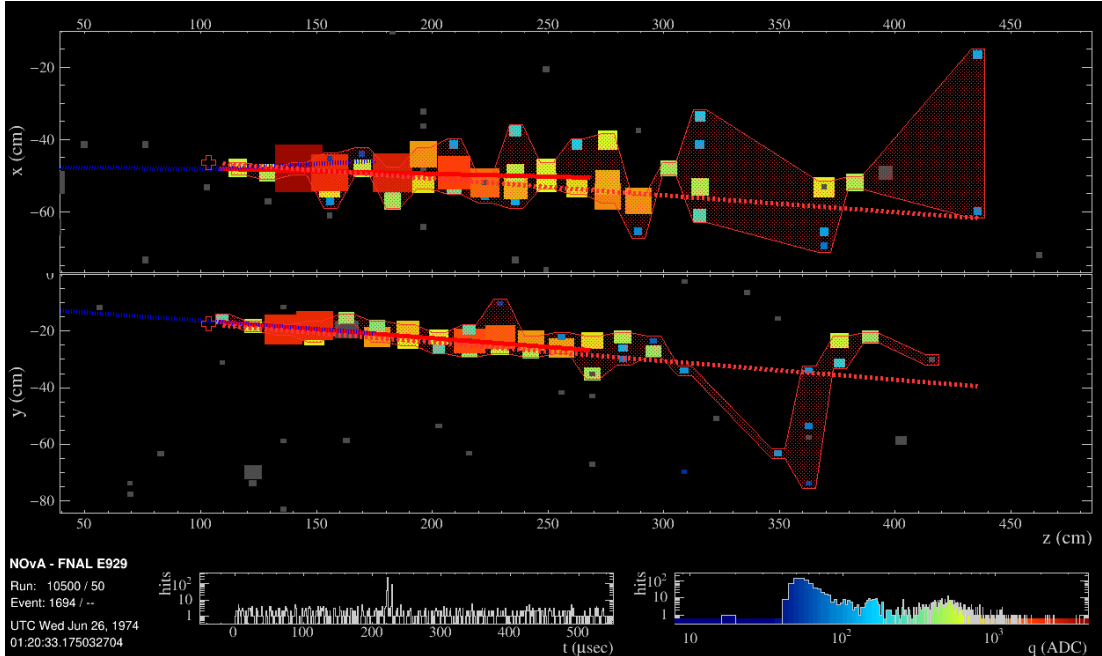


Figure 2.7: Reconstruction of a simulated single electron event in the **NOvA** ND. The red cross is the reconstructed vertex, the shaded area shows the cluster of hits into a prong and the dotted red line shows the estimated shower direction. The blue dotted line shows the true direct of the scattering neutrino and the solid red line the true momentum of the scattered electron. Figure from internal **NOvA** database [131].

For particles that are represented by tracks rather than showers (especially muons), the reconstruction takes the slice hits and forms ‘Kalman tracks’ based on a Kalman filter [132]. In addition to the start point and the direction, which exist also for prongs, tracks also contain information on the vector of trajectory points that make up the track and on the end point - and therefore on the track length. A parallel tracking algorithm takes in the Elastic Arms vertex and the Fuzzy-K prongs and forms Break Point Fitter (BPF) tracks [133, 134], using a model of Coulomb scattering and energy loss. BPF tracks also contain an information on the particle 4-momenta based on various particle assumptions, most notably the muon assumption. For cosmic particles, mostly muons, **NOvA** uses another track reconstruction algorithm, called ‘window cosmic track’ [135]. It uses a sliding 5 plane-long window, in which it fits a straight line to the recorded hits. The window starts from the end of the detector and then slides forward and repeats the fitting process until all hits are processed. This way it accounts for possible Coulomb scattering of cosmic muons. The intersection of each cosmic track with the edge of the detector (or extrapolation of the track to the edge

of the detector) is reconstructed as the ‘cosmic ray vertex’.

To identify individual particles and remove backgrounds, NOvA uses several Machine Learning (ML) algorithms, outputs of which are used in combination with the information from classical reconstruction algorithms for Particle Identification (PID). The most common topologies for particles interacting in NOvA detectors are shown in Fig. 2.8. Muons are easily identifiable as single long tracks which decay into an electron (or positron) if stopping inside of the detector. Both electrons and  $\pi^0$ ’s produce electromagnetic showers, but thanks to the low-Z composition and high granularity of the detector, there is a gap between the interaction vertex and the electromagnetic shower for the  $\pi^0$ .

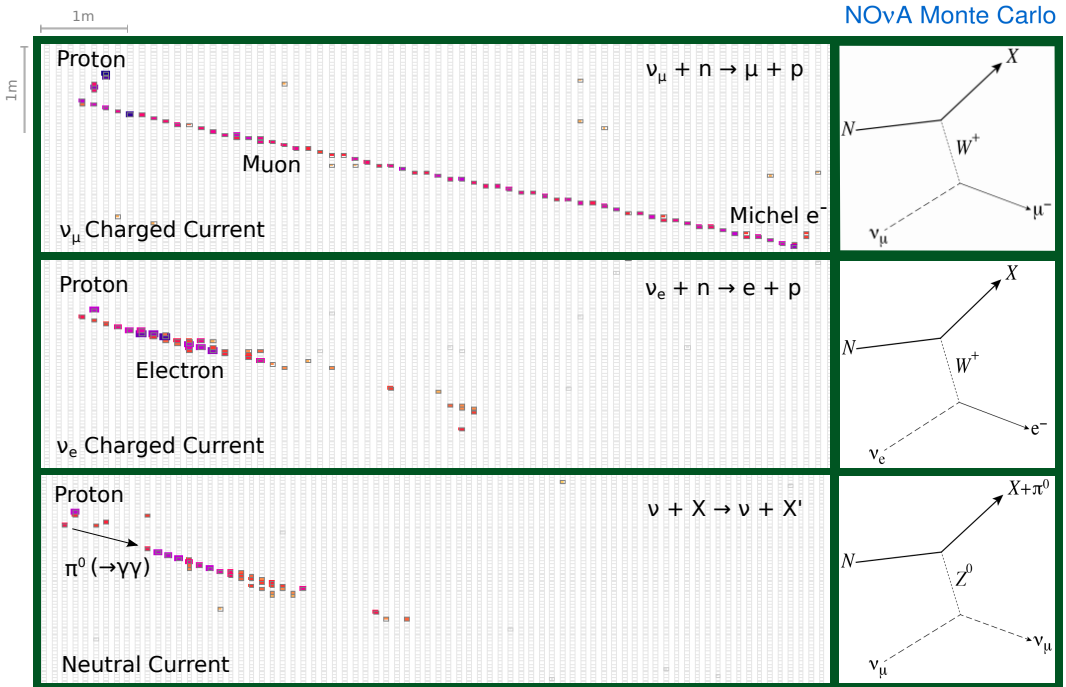


Figure 2.8: Different event topologies as seen in the NOvA detectors with corresponding Feynman diagrams [125]. Each event is a simulated 2.15 GeV neutrino interacting in a NOvA detector producing a 0.78 GeV proton and a second 1.86 GeV particle depending on the interactions type. The figure shows only one view and the colouring represents the deposited energy.

One of the ML algorithms that NOvA employs is a Convolutional Neural Network (CNN) based on the GoogLeNet [136] architecture named Convolutional Visual Network (CVN) [137]. When it is applied to identify entire events it is called *EventCVN* and uses slice hits to classify interactions into one of the five categories:  $\nu_e$ ,  $\nu_\mu$ ,  $\nu_\tau$ , NC, or cosmic. The same architecture, but applied to the Fuzzy-K prongs, is called

*ProngCVN* [138], and is used to identify what particles the prongs most likely correspond to. This assignment is useful in calculation of prong energy, as described in Sec. 2.7. Another [ML](#) algorithm is specifically designed for identifying muons and is based on a Boosted Decision Tree (BDT). It is called Reconstructed Muon Identifier (ReMID) [132] and uses the reconstructed Kalman tracks as inputs.

## 2.6 Detector calibration

The energy deposited within [NOvA](#) detectors is represented by the peak [ADC](#) values for each cell the particle passed through, obtained from the readout electronics, as described in Sec. 2.3. The conversion of the peak [ADC](#) values into physical units of energy requires calibrating the [NOvA](#) detectors [139], while accounting for the attenuation of light along the [WLS](#) fibres, or for differences between individual cells. The purpose of calibration is to calculate a conversion factor from  $\text{ADC} \rightarrow \text{MeV}$  for every part of the detector, so that the same energy deposited anywhere and at any time, is recorded as the same value of the reconstructed energy.

[NOvA](#) uses cosmic ray muons for calibration due to their abundance in the [NOvA](#) detectors and their consistent energy deposition. To calculate the absolute energy scale, [NOvA](#) selects a subsample of muons stopping inside of the detectors when they are almost exactly Minimum Ionising Particle (MIP) and therefore have a well understood energy deposition. The cosmic muons are collected using a periodic trigger with the same length as the beam trigger, whilst removing events with timestamps overlapping with the beam spill window. The simulation of cosmic muons is created using the [CRY](#) [123] [MC](#) generator, as outlined in Sec. 2.4.

Cosmic muon tracks are reconstructed using the window cosmic track algorithm described in Sec. 2.5. The selection of well reconstructed cosmic tracks requires that at least 80% of all hits from the reconstructed slice contribute to the track [92]. Each track must have at least 2 hits in both the x and y views and the difference in the number of planes the track crossed between the views must be at most 10% of the total number of planes. Also, the plane where each track starts or stops in one view must be within 3 planes of the start or stop plane in the other view. Additionally, since tracks that do not cross many planes tend to not be reconstructed very well, the

extent of each track in the z direction must be at least 70 cm and tracks must have at least 20% of their total track direction in the z axis. Tracks with on average more than 6 cells per plane and with path lengths through the cell larger than 10 cm are removed for the same reason. Furthermore, all the reconstructed tracks must start at most 10 cm from the edge inside of the detector and stop at most 10 cm outside of the detector. Lastly, tracks with trajectory points far away from each other are also removed. The selection of stopping muons for the absolute energy scale relies on identifying Michel electrons, which are produced by decaying muons at the end of their tracks, as can be seen on the top panel of Fig. 2.8.

Since the energy deposited in a cell is proportional to the distance the particle travels through the cell, the input variable for calibration is the deposited energy divided by the path length through the cell  $PE/cm$ . To ensure the path length is well calculated, all hits used in calibration must satisfy the so-called ‘tricell’ condition, shown in Fig. 2.9. This means that for each calibration hit, there must be a corresponding hit in both of the surrounding cells in the same plane for the same track. The path length can then be calculated simply from the height of the cell and the angle of the reconstructed track. In case there is a bad channel in a neighbouring cell (right side of Fig. 2.9), this channel is ignored and the tricell condition looks one cell further [139]. If the tricell condition fails, the hit can still pass the ‘z tricell’ condition, which is a longitudinal equivalent of the tricell condition and requires a hit in both the neighbouring planes in the same view and with the same cell number. The ‘z tricell’ hits are saved separately and may be used if there are no hits satisfying the original tricell condition. This is especially useful for the cells on the edge of the detector, which fail the tricell condition due to only having one neighbouring cell.

The calibration conversion factor from the signal recorded by the detector readout to the deposited energy can be expressed by as

$$E_{dep} \text{ [MeV]} = \text{Signal [ADC]} \times S_d \times TS_{d,i}^{\text{CALIB}} \times R_{d,i}(t) \times A_d(t). \quad (2.1)$$

The calibration scale therefore consists of four separate and complementary factors: the Scale ( $S_d$ ), the Threshold and Shielding correction ( $TS_{d,i}$ ), the Relative calibration ( $R_{d,i}(t)$ ) and the Absolute calibration ( $A_d(t)$ ), all described below. Each part is calculated for each detector separately, as indicated by the subscript  $d$ . The threshold

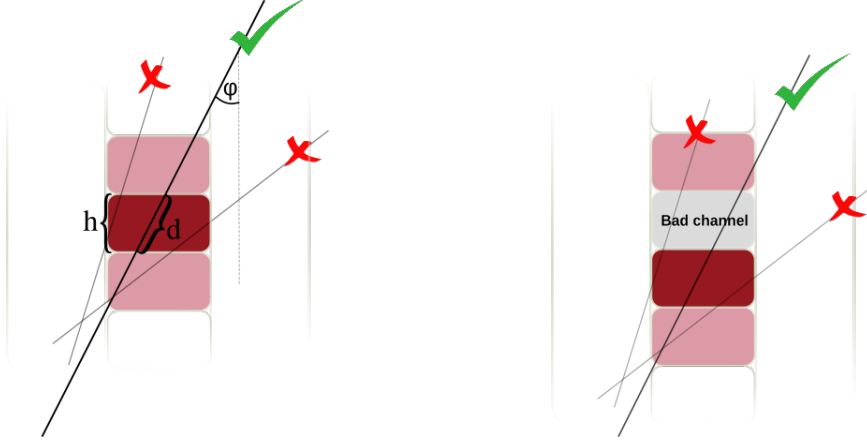


Figure 2.9: Illustration of the tricell condition. Only the hits with two surrounding hits in the same plane are used in the [NOvA](#) calibration, as shown on the left plot. This is to ensure a good quality of the path length ( $d$ ) reconstruction, which is calculated from the known cell height ( $h$ ) and the reconstructed track angle ( $\varphi$ ). In case the hit is next to a bad channel, as shown on the right plot, the bad channel is ignored and the tricell condition requires a hit in the next cell over.

and shielding correction is only used during calibration and is omitted when applying the calibration results. The relative and absolute calibrations are calculated for each time period separately to account for possible changes in the energy deposition throughout the time, possibly caused by the ageing of the scintillator oil, or of the readout electronics. The time periods are either determined by a fixed time interval, or by running conditions separated by significant changes to the readout or the [DAQ](#) systems, including the summer shutdown.

The threshold and shielding correction and the relative calibration calculate a calibration factor for each position within the detector to account for variations caused by the attenuation of light as it travels through the [WLS](#) fibres, or by differences between individual cells. This is expressed with a subscript  $i$  in Eq. 2.1. For data, the position of a hit in the detector is described by the plane number, cell number and the position within the cell ( $w$ ).  $w$  is calculated as the projection of the cosmic track to the central cell axis and its value is equivalent to the x axis (y axis) coordinate of the projection for the horizontal (vertical) cells, with the 0 value at the centre of the cell [139].

For simulation, the calibration does not use the plane number to determine the position within a detector, as by construction all detector planes should have the same readout. This significantly reduces the requirements for the number of events that

need to be simulated, reconstructed, and calibrated, especially for the FD with 896 planes. However, in reality there are some variations in the detector response between individual planes, caused by different *brightness* qualities of the fibres, zipped or twisted fibres, different qualities of the scintillator, possible air bubbles, and potentially other factors. To include these differences in simulation without having to simulate every cell individually, all the cells are divided into 12 equally populated Fibre Brightness (FB) bins based on the uncorrected average response in the center of that cell, as shown in Fig. 2.10. These FB bins describe the relative differences in the detector response between individual cells [140].

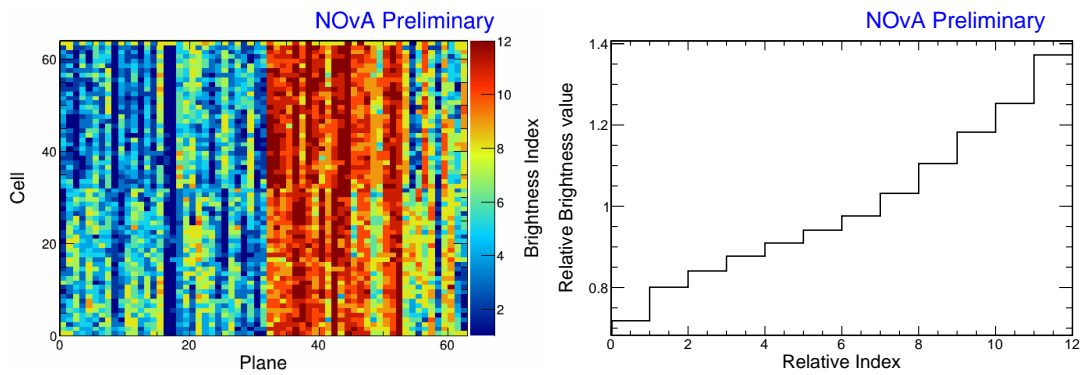


Figure 2.10: Distribution of the NOvA detector cells into 12 brightness bins (left plot), each representing a relative difference in energy response (right plot) due to different brightnesses of the fibres, scintillators, or readout. This is an example from the NOvA Test Beam detector, described in Sec. 3.1, where the left side of the detector (planes 1-32) has clearly lower response relative to the right side of the detector (planes 33-64).

### 2.6.1 Scale

The scale calibration factor from Eq. 2.1 is a simple conversion from the peak ADC value into the number of PEs. This factor only depends on the APD gain (which was different in the beginning of NOvA data taking) and on the FEB type (different between detectors, as described in Sec. 2.3).

### 2.6.2 Threshold and shielding correction

The threshold and shielding correction accounts for two assumptions, which hold true in most cases in NOvA, but fall short for some hits at the bottom of the detector, or far away from the readout, especially for the FD [139].

The first assumption is that the **ADC** response to the photon signal is linear, which is mostly true except close to the **APD** threshold. Energy deposited far away from the readout may produce photons that get attenuated enough to be shifted below the threshold. However, due to natural fluctuations of the number of photons created by the energy deposition, the same deposited energy may also produce photons that would make it over the threshold, therefore making it appear that the actual deposited energy was higher than in reality, introducing a bias to the calibration. The threshold correction is calculated using simulation, as the ratio between the mean of the Poisson distribution of the true number of the created **PE** ( $\text{PE}_{\text{Poisson}\lambda}$ ) and the number of the ‘reconstructed’ **PE** seen by the **APD** ( $\text{PE}_{\text{Reco}}$ ).

The second assumption is that the spectrum of cosmic muons is uniform within each detector. Again, this is generally true, but breaks down in the **FD**, which is big enough for the top of the detector to shield the bottom of the detector and therefore affect the energy distribution. The shielding correction is calculated from simulation as a ratio between the expected deposited energy if the particle was a **MIP** ( $E_{\text{MIP}}$ ), which is estimated from simulation for the **NOvA** scintillator as  $E_{\text{MIP}} = 1.78 \text{ MeV/cm}$  and the true deposited energy ( $E_{\text{true}}$ ).

The total threshold and shielding correction is calculated for simulated events in each cell, **FB** bin and  $w$  as

$$TS_i = \frac{\text{PE}_{\text{Poisson}\lambda}}{\text{PE}_{\text{Reco}}} \frac{E_{\text{MIP}}}{E_{\text{true}}}. \quad (2.2)$$

To ensure that the correction changes smoothly across each cell position, the final correction is calculated as a fit to the mean correction value along  $w$  in each cell and **FB** bin.

### 2.6.3 Relative calibration

The main goal of the relative calibration is to correct for the attenuation of the scintillator light as it travels through the **WLS** fibre to the readout. The attenuation in each cell is estimated by performing an ‘attenuation fit’ to the mean response in **PE/cm**, as shown in Fig. 2.11. The relative calibration scale is then calculated as the ratio between the average response in **PE/cm** across the entire detector (can differ between

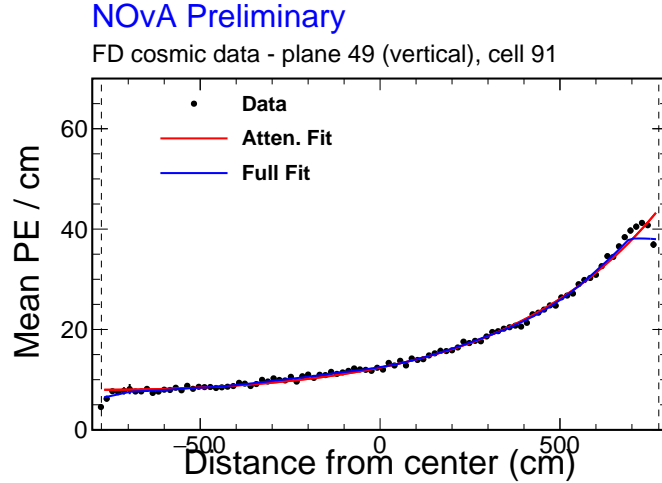


Figure 2.11: Example attenuation fit for a single cell in the NOvA FD across its full length, as shown by dashed vertical lines. The red line shows the initial exponential fit and the blue line shows the full fit after the LOWESS correction, both described in text. Figure from [141].

detectors) and the result of the attenuation fit in each particular position within the detector. The response after applying the relative calibration scale is expressed as Corrected Photo Electronss (PECorrs). Since the relative calibration scale is calculated for each cell independently, it effectively corrects for the relative differences between detector cells as well as for the attenuation. Therefore, the resulting distribution of PECorr/cm should be uniform across the detector, especially along the plane, cell and  $w$  [139].

The first step to do the attenuation fit is to create ‘attenuation profiles’ for each cell. Attenuation profiles are profile histograms of mean detector response over the path length through the cell, in the units of  $PE/cm$ , along the position within the cell. An example attenuation profile is shown in Fig. 2.11 as black dots. The threshold and shielding correction described in Sec. 2.6.2 is applied to the attenuation profiles before doing the attenuation fit, which consists of two steps.

1. The first step is a three-parameter exponential fit according to

$$y = C + A \left( \exp \left( \frac{w}{X} \right) + \exp \left( -\frac{L+w}{X} \right) \right), \quad (2.3)$$

where  $y$  is the fitted response,  $L$  is the length of the cell and  $C$ ,  $A$  and  $X$  are the fitted parameters representing the background, attenuation scale and atten-

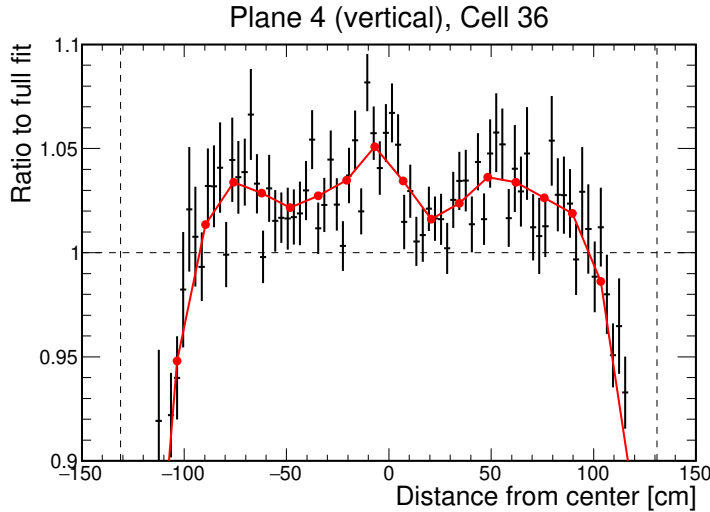


Figure 2.12: Example LOWESS correction for the residual differences after the exponential part of the attenuation fit of the NOvA relative calibration. This is an example for a single cell in the NOvA Test Beam detector with black points showing the residual differences and red line the LOWESS correction, both described in text.

uation length respectively. An example of the exponential fit is shown as a red curve in Fig. 2.11.

2. The second step is the smoothing out of residual differences between the exponential fit and the original distribution with the Locally Weighted Scatter plot Smoothing (LOWESS) method, shown in Fig. 2.12. The residual differences get evened out by creating a smooth distribution of 20 locally weighted points across the length of each cell. The result of the LOWESS correction is then combined with the exponential fit into the full attenuation fit, shown as a blue line in Fig. 2.11.

Even after applying the LOWESS correction, there are sometimes large differences between the attenuation fit and the fitted response. This is usually caused by a small number of events in that cell, common for cells at the edge of the detector. To ensure a good quality of the attenuation fit, the total  $\chi^2$  between the attenuation fit and the fitted response is calculated and only cells with the final  $\chi^2 \leq 0.2$  are counted as *calibrated*. Cells with  $\chi^2 > 0.2$  are ignored in further processing and marked as *uncalibrated*.

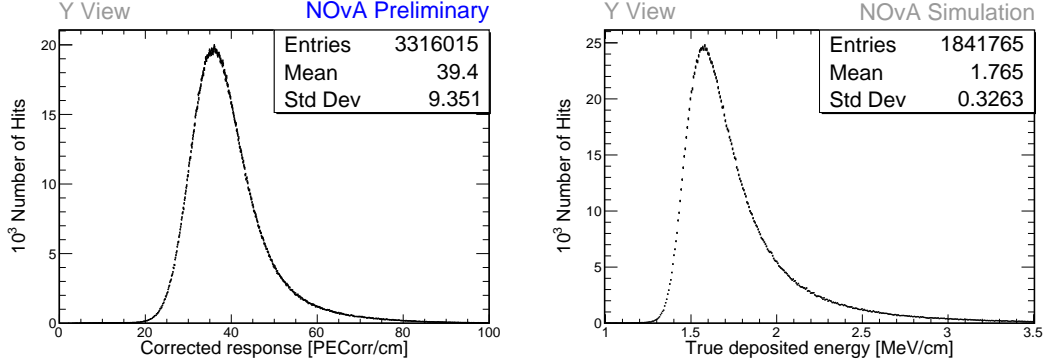


Figure 2.13: The absolute energy scale is calculated as the ratio between the simulated mean true deposited energy (right) and the mean reconstructed energy response (left) for selected stopping muons in each view and each data period or simulation.

#### 2.6.4 Absolute calibration

The absolute calibration only uses hits from muons stopping inside of the detector, in a track window 1 – 2 m from the end of their tracks. This is when they are approximately MIP and their energy deposition is well understood. Additionally, hits at the edges of each cell are removed to mitigate the effects at the end of the WLS fibres and the lower number of events at the edge of the detector [92].

First, the relative calibration results are applied to the selected stopping muon hits to get a distribution of the corrected detector response in *PECorr*/cm, as shown on the left of Fig. 2.13. The mean of this distribution is called the *reconstructed Muon Energy Unit* (MEU) and is calculated separately in each of the two views, and in each time period or version of simulation. Analogously, the mean of the true deposited energy in MeV/cm from simulation, shown on the right of Fig. 2.13, is called the *true MEU*. The absolute energy scale (the absolute calibration scale) is then the ratio between the true and the reconstructed MEU value, where both the MEU values are taken as a simple average over the two views

$$\text{Absolute Energy Scale} = \frac{\text{MEU}_{\text{True}} \text{ [MeV/cm]}}{\text{MEU}_{\text{Reco}} \text{ [PECorr/cm]}}. \quad (2.4)$$

The values of the absolute energy scales for each data period and simulation, as well as the results of the attenuation fit, are saved in a set of lookup tables, which are then used any time a hit is recorded in the NOvA detector and processed and reconstructed with the NOvA algorithms described above.

## 2.7 Energy estimation

The deposited energy from detector calibration (Sec. 2.6) is only the first step in estimating the neutrino energy ( $E_\nu$ ) required for the main [NOvA](#) analyses.

For the  $\nu_\mu$  disappearance analysis, the  $\nu_\mu$  energy is measured as the sum of the muon energy and the energy of the hadronic shower [54]. The muon energy is identified from the length of its track, without the need of the calibration results. The energy of the hadronic shower is estimated from simulation as a fit to the 2D distribution of the true  $\nu_\mu$  energy minus the reconstructed muon energy, versus the visible (not corrected for the dead material) deposited energy of the hadronic system [138].

For the  $\nu_e$  appearance analysis, the  $\nu_e$  energy is calculated using a quartic fit to the 2D distribution of the electromagnetic versus the hadronic calorimetric energies, both corrected for the energy deposition in the dead material (PVC cells) [138]. The dead material correction is currently just a simple scaling of the deposited energy from calibration for all particles and is calculated from the measurement of the  $\pi^0$  mass peak in the [NOvA ND](#). This correction is correct only for electromagnetic showers and is not directly applicable to hadronic showers. The fit to determine the  $\nu_e$  energy keeps the normalization of both the electromagnetic and the hadronic energies free, so the exact value of the dead material correction is not important. It is however used in other, non-neutrino oscillation analyses.

## 2.8 Systematic uncertainties

There are several known unknowns that can affect the results of [NOvA](#) measurements, represented by systematic shifts of predictions. The impact of systematic uncertainties is assessed by varying prediction independently for each systematic shift and passing all predictions through the same analysis procedures as the nominal (non-shifted) sample. The nominal and systematically shifted predictions are then compared to determine the systematic uncertainty on the measured parameters. This approach inherently accounts for the effects of systematic uncertainties on background composition, event selection, reconstruction, and other aspects of the analysis.

The primary sources of systematic uncertainties in [NOvA](#) include the simulations of neutrino flux, neutrino interaction, and detector modelling, all explained in Sec. 2.4,

as well as the detector calibration procedure. Other sources of systematic uncertainties are relevant only to specific analyses and are not discussed here. In **NOvA**, the 3-flavour [54] and the sterile [76] neutrino oscillation analyses use the **ND** data to constrain the **FD** prediction by fitting the **ND** prediction to data, significantly reducing the effect of the neutrino beam and neutrino interaction systematic uncertainties. On the other hand, these are the leading sources of systematic uncertainties for the **ND**-only analyses, such as the cross section analyses [71–74], or the neutrino magnetic moment analysis. Detector calibration and modelling uncertainties are significant across all **NOvA** measurements.

The systematic uncertainty on the neutrino beam prediction arises from two sources: hadron production and beam focusing [99]. Hadron production uncertainties are estimated using the multi-universe technique within the **PPFX** (see Sec. 2.4), which involves creating 100 alternative universes where inputs from external measurements of hadron production cross-sections are varied within their respective uncertainties. Beam focusing uncertainties are contained in 20 parameters accounting for uncertainties in horn and target positions, horn current, beam position on the target, beam spot size, and the effect of Earth’s magnetic field in the beam pipe. Since all these uncertainties can be correlated, particularly in an off-axis detector such as **NOvA**, a Principal Component Analysis (PCA) is performed to estimate the bin-to-bin covariances in true energy for each neutrino flavour, detector and beam mode [142]. PCA reduces the number of required neutrino flux systematic uncertainty parameters from  $20 \times 100$  to only 8 “*principal components*” (each with positive and negative shifts) for the **ND** analyses, or 5 principal components for the **ND+FD** analyses. Additionally, principal components are uncorrelated by construction and ordered by the scale of their effect on the neutrino beam prediction.

Neutrino interaction-related systematic uncertainties involve 77 adjustable parameters, most of which are provided directly by GENIE [113] to account for the theoretical uncertainties of the prediction [54]. These include knobs to adjust the axial and vector masses of **QE** and **Res** interactions,  $\pi$  angular distribution in the **Res** $\pi$  production, parameters of the Bodek-Yang **DIS** model, or branching ratios for the radiative and single  $\eta$  resonance decays. Additionally, **NOvA** developed its own set of systematic uncertainties [143], either based on its own measurements, or on

discrepancies observed in other experiments. For example, the **NOvA MEC** tune has associated uncertainties based on its dependence on the transferred four momentum or on the neutrino energy. Furthermore, a discrepancy between data on the **Res** interactions at low transfer energies and their prediction in the **NOvA ND** motivated a conservative 100 % one-sided systematic uncertainty, allowing for a complete suppression of **Res** events with low energy transfers.

For the long-range dependence of **CCQE** interactions **NOvA** adapted a theory-based systematic uncertainty developed outside **NOvA** and **GENIE** [144, 145]. Several data-simulation discrepancies in external experiments motivated additional systematic uncertainties, such as for the **DIS** interactions at high neutrino energies [146], for the distance that a parton travels before hadronization in **DIS** interactions [147], for **COH $\pi$**  production [148], or for the **FSI** model [149]. Lastly **NOvA** applies a 2 % systematic uncertainty on the ratio of  $\nu_e$ **CC** and  $\nu_\mu$ **CC** cross sections to account for their potential differences due to radiative corrections or second class currents [150].

Systematic uncertainties on the simulation of the detector response arise mainly from the light model tuning described in Sec. 2.4. This includes the uncertainty on the overall normalization of the amount of light produced by deposited energy and an additional uncertainty for the Cherenkov light contribution. The Cherenkov light uncertainty is calculated by profiling over various Cherenkov scaling factors during the light model tune and using the  $3\sigma$  confidence interval around the best fit value as the Cherenkov systematic uncertainty. This results in a  $\pm 6.2$  % systematic uncertainty on the predicted amount of Cherenkov light. The light level systematic uncertainty is determined in the same way by profiling over the overall light level scaling factor, resulting in a  $\pm 5$  % uncertainty.

There are three systematic uncertainties arising from the calibration procedure: the absolute energy scale, the calibration shape and the detector ageing uncertainty. Measurements of some "standard candle" processes, mainly in the **ND**, are used to set the systematic uncertainty on the absolute energy scale, calculated as the data-simulation difference. These standard candles include beam muons, beam protons, rock muons, Michel electrons and the  $\pi^0$  mass peak. Their combined results lead to a 5 % systematic uncertainty on the absolute energy scale [151]. The calibration shape uncertainty accounts for the residual variations in the relative energy depo-

sition along the cell, especially on cell edges. The shape and size of the calibration shape systematic uncertainty is determined by a fit to a ratio of data and simulation, resulting in a steep rise at cell edges, where the uncertainty is up to 30 %, while being fixed to 0 % in the cell centre [152]. Lastly, the detector ageing uncertainty is implemented as time-dependent decrease of the overall light level scaling by 4.5 % per year, with a corresponding increase in the overall calibration scale to compensate [153].

## CHAPTER 3

# NOvA Test Beam detector calibration

The NOvA Test Beam experiment [154] is a sub-experiment designed to enhance NOvA’s sensitivity to neutrino oscillation measurements by improving the understanding of particle interactions and energy deposition within the NOvA detectors. Initial studies [155] showed that, only by improving the detector calibration, the Test Beam experiment has the potential to reduce the total systematic uncertainty in the measurement of the three flavour oscillation parameters by about 10%.

The NOvA Test Beam experiment consists of a scaled down version of the NOvA detectors placed in a test beam. Using a test beam allows for the study of the response of tagged single particles with known momenta and positions within a NOvA detector. Additionally, this setup enables the determination of the energy resolution and the absolute energy scale without the use of simulation. Furthermore, it permits the comparison of responses between beam muons and cosmic ray muons, study of fibre attenuation, and validation of the NOvA calibration process. The Test Beam detector is equipped with a combination of the ND and FD readout electronics and filled with a range of NOvA scintillator oils, enabling a comparison of their respective performance and particle responses [156]. All these advantages require, or benefit from, the calibration of the Test Beam detector, which follows the same calibration procedure as the standard NOvA detectors (Sec. 2.6).

In this chapter I introduce the NOvA Test Beam experiment in Sec. 3.1, focusing on the Test Beam detector and especially on the aspects that could impact its calibration. Section 3.2 describes the new data-based simulation of cosmic muons that I developed for the Test Beam detector calibration, while Sec. 3.3 discusses the calibration of the Test Beam detector itself.

### 3.1 The NOvA Test Beam experiment

The NOvA Test Beam experiment [157] consists of a scaled down version of the NOvA ND and FD, shown in Fig. 3.1, and a series of beamline detectors to measure and identify a range of particles from the MCenter beamline in the Fermilab Test Beam Facility (FTBF) [158].

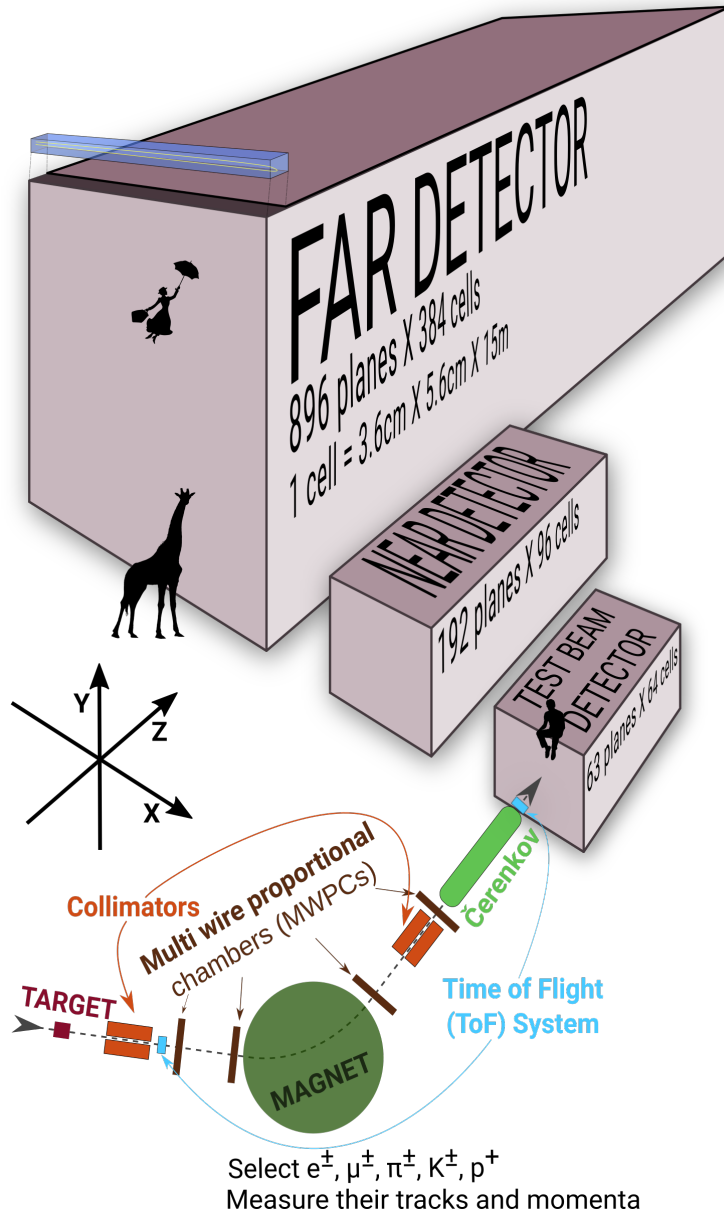


Figure 3.1: Comparison of Test Beam detector scale to the NOvA ND and FD (and a man, giraffe, or Mary Poppins). Also shown are the Test Beam beamline detectors and components (not to scale), with arrows showing the direction of the beam. The three black arrows show the orientation of the detector coordinate system.

The operation of the Test Beam detector started with commissioning runs in June

2019 and ran, with an exception of regular summer shutdowns, until July 2022, after which it was decommissioned. The Test Beam data taking is divided into *periods*, which are defined in Tab. 3.1. Period 1 only lasted for about a month and with only a half-filled detector, as explained below. It was therefore only used for detector commissioning and will not be used in any of the Test Beam physics analysis, or in the calibration.

Table 3.1: Test Beam detector data taking periods.

Period 1	June 3 <sup>rd</sup> 2019	-	July 6 <sup>th</sup> 2019
Period 2	December 5 <sup>th</sup> 2019	-	March 20 <sup>th</sup> 2020
Period 3	January 12 <sup>th</sup> 2021	-	June 27 <sup>th</sup> 2021
Period 4	November 30 <sup>th</sup> 2021	-	July 10 <sup>th</sup> 2022

Majority of the Test Beam detector and its instrumentation is identical to the other **NOvA** detectors, with a few exceptions that could have an impact on the calibration. We are going to identify and discuss these differences in this section.

## Beamline

The beam for the Test Beam experiment originates from the same 120 GeV Main Injector protons used in **NuMI**, extracted once a minute in a continuous 4.2 s spill [154]. The protons are impinged on a copper target producing mostly protons and pions, which are then directed towards a second target, producing the tertiary beam of particles used in the Test Beam detector. As can be seen in Fig. 3.1, two collimators are used to direct the tertiary beam and a magnet to select the desired momentum. Particle tracking is done using the four Multiwire Proportional Chambers (MWPCs) and particle identification is done with a combination of Time of Flight (ToF) detectors and a Cherenkov detector set for electron detection.

## Detector parameters

The **NOvA** Test Beam detector consists of two 31-plane blocks, each beginning and ending with a vertical plane, with an additional horizontal plane glued in-between them to preserve the alternating pattern [159]. Each plane consists of 2 modules side-by-side, both made up of 32 cells. Each cell is 2.6 m long with an inner (without the

PVC) depth and width of 5.9 cm and 3.8 cm respectively, same as for the other **NOvA** detectors. This brings the final dimensions of the Test Beam detector to 63 planes  $\times$  64 cells, or  $2.6 \times 2.6 \times 4.1 \text{ m}^3$ .

The 63 planes are numbered from 0 to 62, with even numbers corresponding to vertical planes and odd numbers to horizontal planes. Cells are numbered 0 to 63, going from bottom to top for horizontal planes and left to right, when facing the front of the detector, for vertical planes.

The detector coordinate system is illustrated in Fig. 3.1. It is centred with  $(0, 0, 0)$  in the centre of the first plane [160]. The x axis runs left to right when facing the front of the detector, y axis from bottom to top, and z axis goes along the beam direction from front to the back of the detector. Position within each cell ( $w$ ) is aligned with the x (y) axis for the horizontal (vertical) cells, with  $w = 0$  centred in the middle of each cell. The exact geometry of the Test Beam detector was measured in several alignment surveys and is saved in gdml files [161].

In the past we encountered an issue when trying to align the Test Beam detector with the beamline measurements by rotating the detector. This broke several assumptions within the Test Beam geometry [160] and manifested as uncalibrated cells in the back of the detector [162]. This was fixed by realigning both the detector and the beamline separately, based on the last alignment survey, measured during the decommissioning of the detector.

## Scintillator

Test Beam used a combination of the leftover **ND** and **FD** production scintillator oils and the oil drained from the **NOvA NDOS** test detector. The used scintillator oils also differ in the way they were stored since the **ND** and **FD** filling, or the **NDOS** draining, which apparently impacted its quality. These factors have a significant effect on the energy deposition within them. The distribution of individual scintillator oils and the relative difference in their energy response can be seen in Fig. 3.2.

There are four distinct samples of **NOvA** scintillator oil used in the Test Beam detector:

1. Mixed **ND** production oil and **NDOS**-drained oil stored in a tanker and four tanks outside in Fermilab [163];

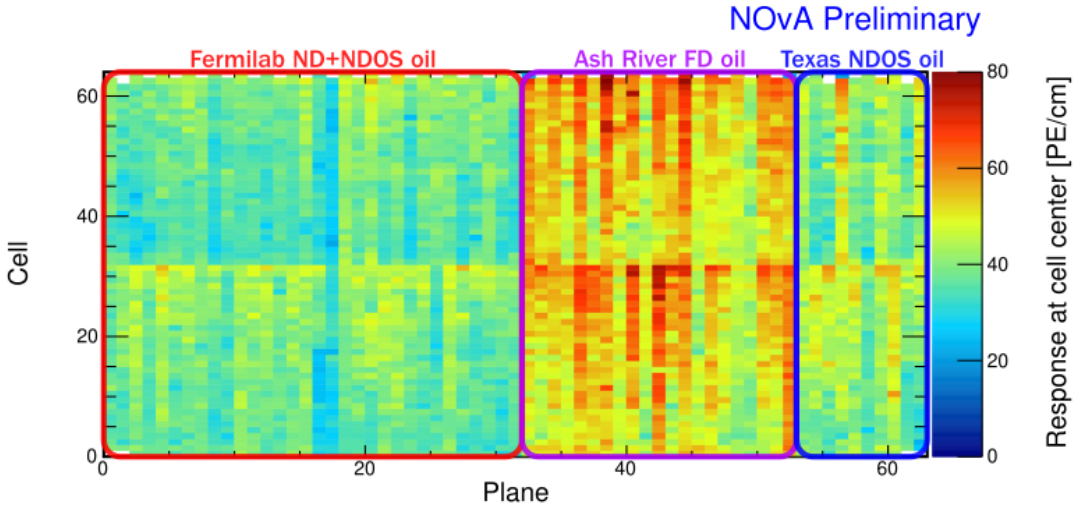


Figure 3.2: Uncorrected energy response in the centre of cells across the Test Beam detector showing a clear distinction between different scintillator oils, labelled with coloured boxes and descriptions.

2. Separate **ND** production oil and **NDOS**-drained oil stored underground in barrels at the MiniBooNE<sup>1</sup> cavern [155];
3. **FD** production oil stored inside in Ash River in ‘totes’ under several layers of black plastic [165];
4. **NDOS**-drained oil stored mainly inside at Texas A&M University and University of Texas at Austin [166, 167].

The original plan [168] was to only use the tanker/tank scintillator (sample #1). First tests showed acceptable results and the tanker oil was used to fill out almost the entirety of the first block of the detector (first 32 planes) [163]. However, when the oil from tank #2 was loaded into the tanker, it became extremely cloudy and unusable, possibly due to contamination with water accumulated at the bottom of the tanks. The rest of the first block was therefore topped up with high quality scintillator from **NDOS** (sample #2). This is labelled as ‘Fermilab **ND+NDOS** oil’ in Fig. 3.2.

The first 21 planes of the second block (planes 32 to 52) were filled with the **FD** production scintillator shipped in from Ash River (sample #3) [169]. These planes were again topped up with the **ND+NDOS** scintillator (sample #2).

The last 10 planes (planes 53 to 62) [169] were filled with the ‘Texas’ scintillator (sample #4), which has higher light yield than the one from the tanker, but lower than

---

<sup>1</sup>MiniBooNE [164] is a Fermilab experiment located close to the NOvA ND

the Ash River one [166].

In total, the Test Beam detector is filled with 5418 gallons of scintillator oil with a weight of approximately 28.6 tons [159].

## Readout

The Test Beam detector uses in total 126 [FEBs](#), each reading out signal from 32 cells [159]. The readout is located on the top and right side (when looking at the front) of the detector. 118 [FEBs](#) are version 4.1, same as in the [FD](#), and 8 [FEBs](#), located in pairs on planes 16, 17, 48 and 49, are version 5.2, same as in the [ND](#). As was described in Sec. 2.3, the [ND FEBs](#) are designed to read out data at a faster rate than the [FD FEBs](#) and using a mix of [FEB](#) types allows us to study the difference in their response and to validate both versions in the same environment [170].

## Environment

The enclosure that housed the Test Beam detector was made up of a concrete platform covered by a metal semi-cylindrical roof. Therefore, unlike the [ND](#) and [FD](#), the Test Beam detector did not have any overburden to shield it from cosmic particles, affecting their rate and energies inside the detector. The temperature and humidity were controlled by a humidity, ventilation and air conditioning control system and monitored by a range of sensors. The temperature was kept to around 20 °C and within the range of 18 – 22 °C, except for about three months in the beginning of Period 3 data taking, when it was kept to within 16 – 20 °C. The readout electronics were turned off when the dew point reached 10 °C to limit humidity related noise in the [FEBs](#).

## Underfilled cells issue

The Test Beam detector is slightly tilted around the z axis by about 0.7° towards the readout. This caused the top cells of both modules of all the horizontal planes (cells 31 and 63) to be underfilled, creating an air bubble on the left side of the detector and severely affecting the energy response in those cells [170]. This was fixed [171] during the period 3 running by adding extensions to the filling ports and overfilling the horizontal cells with the [ND+NDOS](#) scintillator (sample #2 from the scintillator

description). More details on this issue and its effects and on how it was handled in calibration are detailed in Sec. 3.3.5.

## 3.2 Data-based simulation of cosmic muons

The standard **NOvA** calibration procedure described in Sec. 2.6 uses the **CRY MC** generator (see Sec. 2.4) to create the simulated cosmic ray sample for calibration. However, **CRY** proved to be inefficient, generating particles failing to hit the detector, resulting in wasted processing resources and disk space. Moreover, the momentum and angle distributions in **CRY** are not well suited to the **NOvA** sites, potentially impacting the calibration accuracy.

To overcome these challenges, I developed and implemented a data-based simulation that eliminates the need for the **CRY MC** generator. Instead, I use a subset of the cosmic data sample used in calibration, pulling information on the muon vertex position, direction and momentum, to use, after some corrections and smearing, as inputs to the detector simulation to create a new simulated cosmic ray sample.

This approach results in a near-perfect efficiency, ensuring that almost every simulated muon contributes to the final calibration sample, thus saving processing time, file size, and storage. Additionally, the simulated muon distributions are inherently consistent with the distributions from data. Given that the calibration chain itself is a time and computing intensive process, the reduction in the number of simulation files and in their sizes has significant benefits downstream of the file generation.

### 3.2.1 Reconstruction and selection of cosmic data events

It is important to choose a data sample that represents the detector in an ideal state, with as few known issues as possible. For Test Beam, we chose the period 4 data sample (see Tab. 3.1), as the other periods had complications such as faulty **FEBs**, or underfilled cells. We only used half of period 4 data by skipping every other sub-run to limit the number of simulated events to that necessary for a successful calibration.

We designed the reconstruction and selection criteria so that the majority of the simulated cosmic muons make it into the final simulation calibration sample. Therefore, we employed a similar process to that used to create the data calibration samples.

Additionally, we require all distributions of the selected events to be well-understood and to resemble those of the data calibration samples.

### Remove beam spills

The first step is to remove beam spill events based on their time relative to the time of the beam spill. For Test Beam the beam spill is 4.2 s long and we remove all events within a 5 s window from the start of the beam spill, as shown in Fig. 3.3. This should leave us with mostly cosmic events.

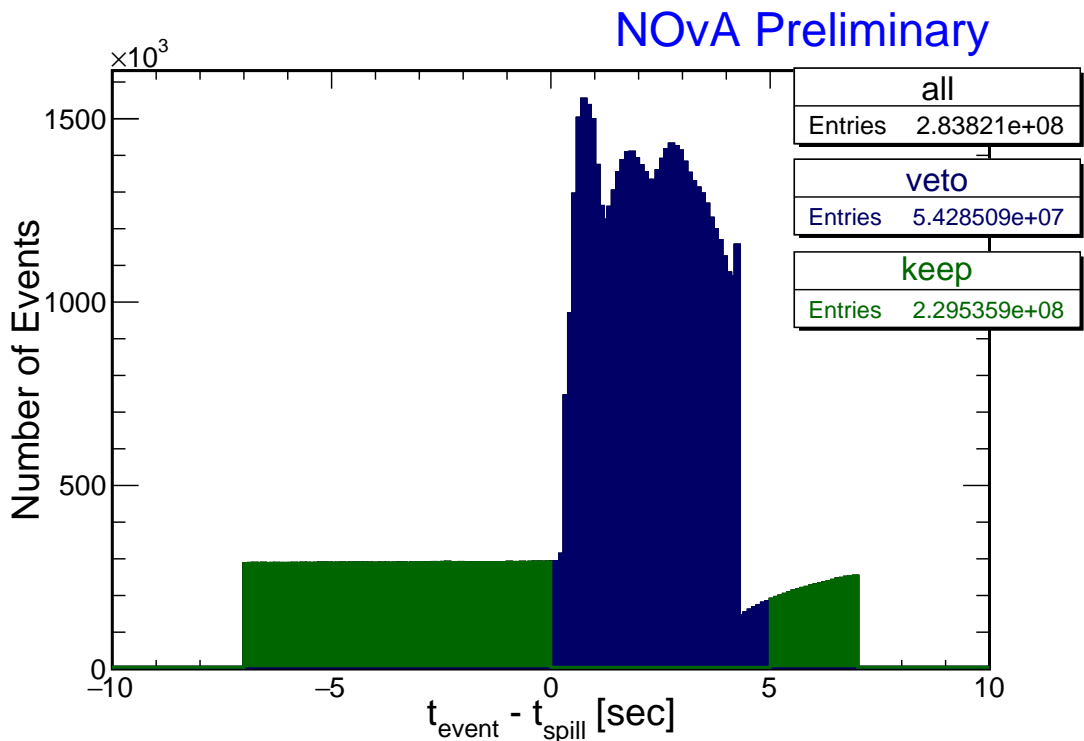


Figure 3.3: Test Beam beam spill events removed (blue) from the calibration samples. The remaining events (green) should mostly consist of cosmic particles. This example and the numbers of entries are for the full period 4 Test Beam sample.

### Reconstruction

To use data events in simulation, we need to reconstruct their vertex positions and their initial 4-momenta. We use the standard reconstruction methods from NOvA, described in Sec. 2.5. First we take the raw hits and group them into slices. Then we reconstruct cosmic tracks using the window cosmic track algorithm (used for calibration samples). Since we also require the 4-momentum information we have to use the BPF tracking algorithm to identify muons and assign their momenta. BPF

requires vertex and prong input information, which we get from a cosmic ray vertex and FuzzyK prong algorithms respectively. The first three steps are identical to the full reconstruction applied to both data and simulation to produce the calibration samples. Since we do not need a 4-momentum information for calibration, we do not need to use cosmic ray vertex, FuzzyK vertex, or the **BPF** to create calibration samples.

## Selection

After the reconstruction process, we proceed to select events based on their slice and **BPF** track properties. The overview of all selection criteria and their corresponding cut values are listed in Tab. 3.2. In detail, the following conditions are used to select cosmic muon events for the data-based simulation:

1. We only use successfully reconstructed 3D **BPF** tracks with the muon assumption;
2. As we aim to select cosmic events originating outside the detector, we apply a cut based on the distance of each track's start position from the edges of the detector. This cut has a negligible impact on the **BPF** tracks, as indicated by the minimal difference between the red and the dotted azure lines in Fig. 3.4;
3. We remove all events whose track is parallel to the beam direction, by requiring the angle from the z axis (parallel to the beam) to be  $|\text{Cos}_Z| \leq 0.98$ . Figure 3.4 demonstrates the presence of events peaked at track lengths of approximately 410 cm and 200 cm, which correspond to the total and half length of the detector, respectively (or alternatively lengths of both blocks and of a single block). These events are strictly parallel to the beam direction and are likely remnants of beam events. Applying a cut on  $\text{Cos}_Z$  effectively removes these events without affecting the rest of the data. This cut might only be needed for the Test Beam detector and not for the **ND** and **FD**, as it is likely these are particles scattered from the Test Beam beamline, or from the secondary beam.
4. To ensure that only events contributing to the final calibration sample are simulated, we use a selection based on the cuts used to select events for the data calibration samples (described in Sec. 2.6 and listed as Calibration sample selec-

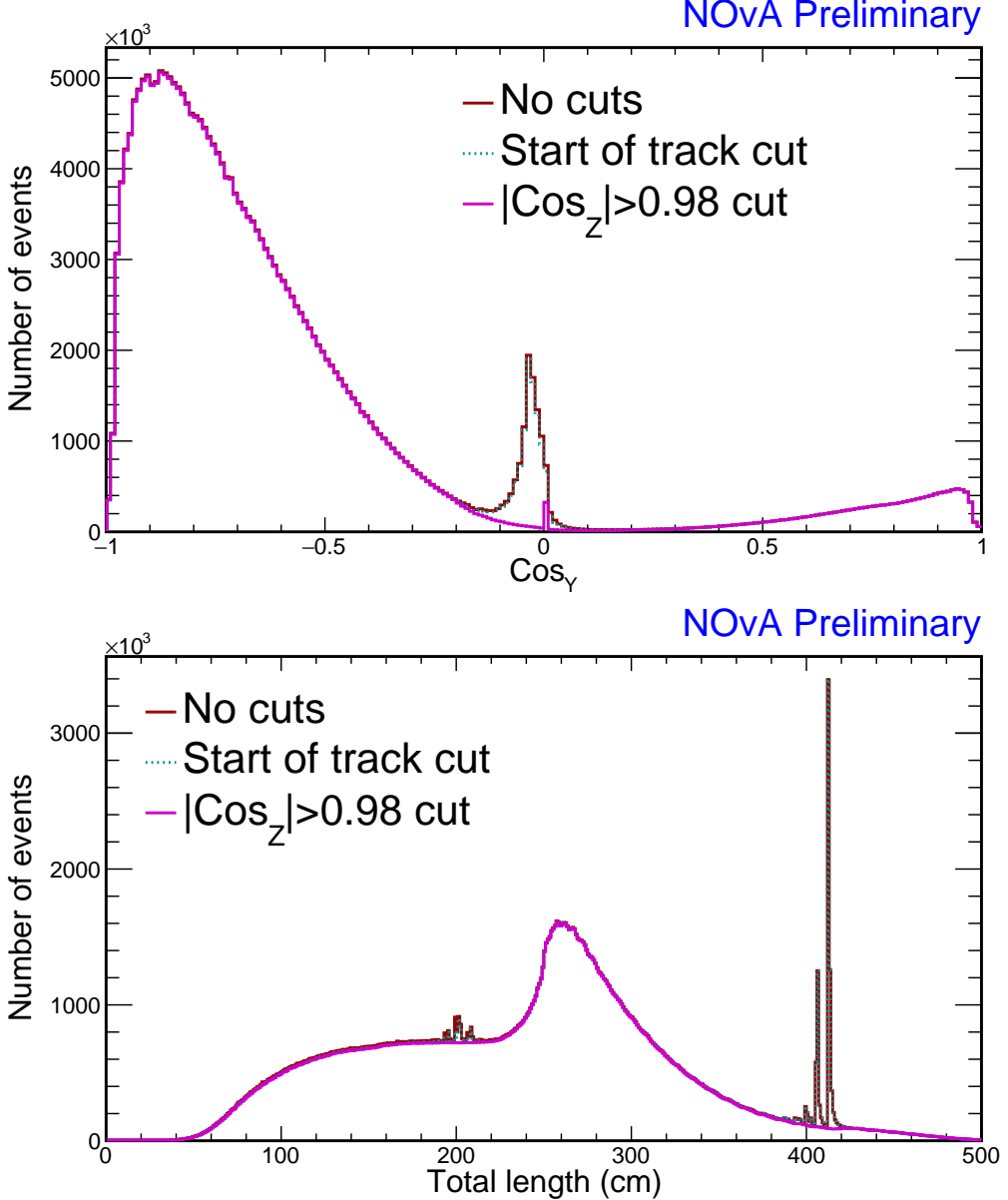


Figure 3.4: Impact of the cuts on the track start and on the maximum track angle from the z axis ( $\text{Cos}_Z$ ) on the Test Beam data for the data-based simulation of cosmic muons. Top plot shows distribution of the angle from the y axis and bottom of the total track length, both made from the period 4 Test Beam data.

tion in Tab. 3.2). We call these cuts the **calibration cuts**. However, there are two caveats we need to consider when applying the calibration cuts:

- (a) First, to create calibration samples, we apply the selection on tracks from the **window cosmic track** algorithm instead of the **BPF** algorithm, which yield different distributions as depicted in Fig. 3.5. Notably, the **BPF** tracks have a hard cut-off at the detector edges, whereas the window cosmic tracks are allowed to start beyond these limits. Also, as can be seen in the

bottom plot of Fig. 3.6, the **BPF** tracks have a rugged distribution in  $\text{Cos}_Z$ , which is not present for window cosmic tracks. The origin of this shape is not exactly known, but it is likely caused by the detector structure, as shown in Fig. 3.6. We concluded that the rugged shape should not have any impact on the resulting simulation. However given these differences between the tracking algorithms, applying the calibration cuts on the **BPF** tracks could mistakenly remove events that would pass the same selection when applied to the window cosmic tracks.

- (b) Second, each reconstruction algorithm has intrinsic deficiencies that can lead to misreconstructions. Therefore, applying the full calibration cuts on misreconstructed events may remove them, even though they would have passed if they were reconstructed correctly and hence they should have been included in the simulation. These events would then be missing from the resulting simulation sample, introducing a bias.

To address these concerns, we loosened the full calibration cuts to create a ‘buffer’ around the selected events, allowing for fluctuations of the reconstruction algorithms while maintaining track quality. This way, events that would have been removed based on the calibration cuts applied to their reconstructed **BPF** tracks, but kept based on the calibration cuts applied to their window cosmic tracks, now have a chance to make it into the final selection and therefore calibration sample. The differences between the full calibration cuts and the employed loosened calibration cuts applied to the **BPF** tracks are listed in Tab. 3.2 and shown in Fig. 3.7. There we also show the data calibration sample, which was created by applying the full calibration cuts on window cosmic tracks.

During the selection process, we determine whether the muon is stopping inside the detector or passing through, based on the end position of the reconstructed track. For Test Beam we say it is a stopping muon if its track ends at least 20 cm from any edge of the detector. For the **ND** and **FD** this is 50 cm. This information assists in correcting the energy of through-going muons, as outlined in the following Sec. 3.2.2.

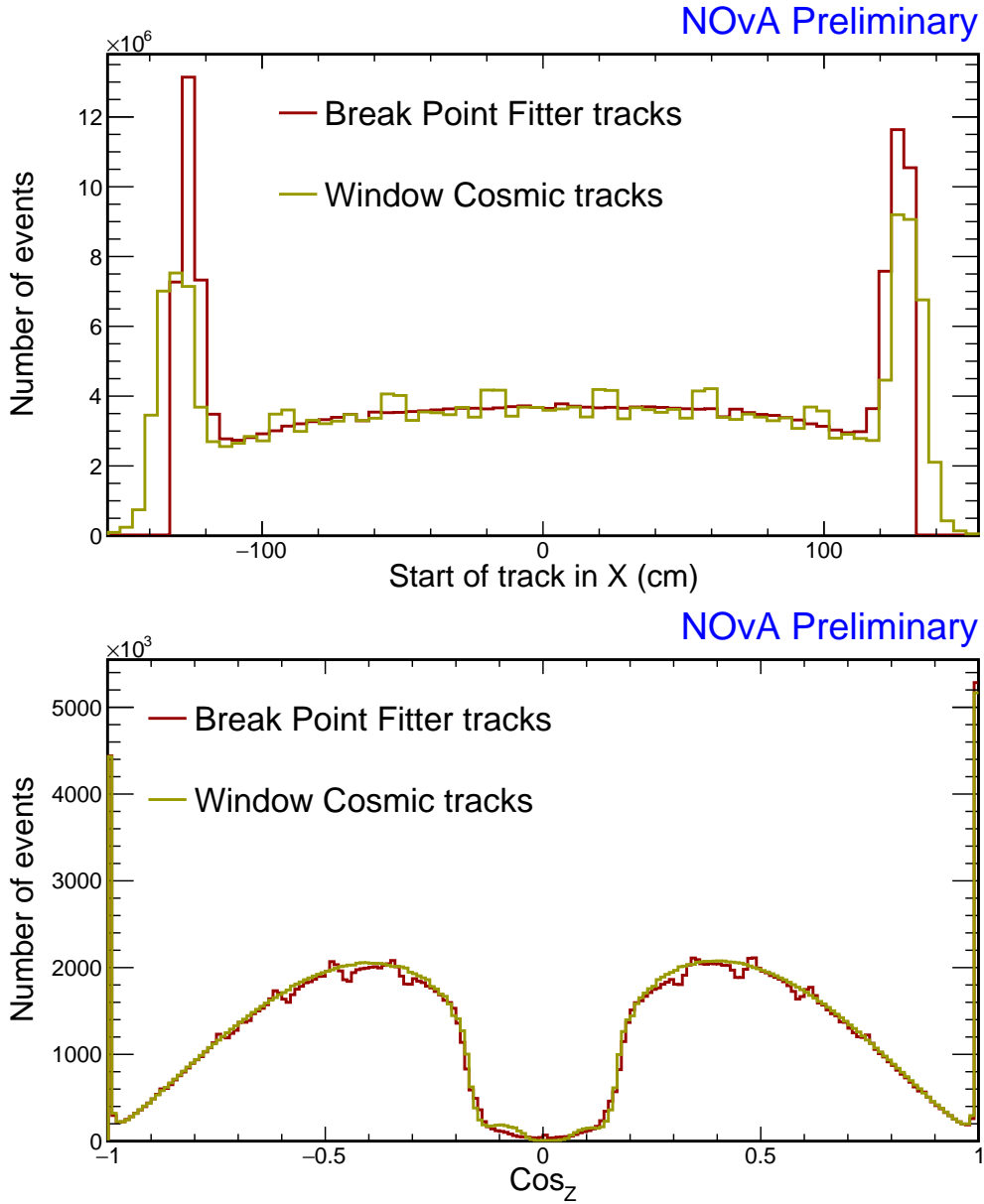


Figure 3.5: Difference between the tracks reconstructed with the BPF and with the window cosmic track algorithms. Top plot shows the distribution of the start of track along the x axis and bottom plot shows the distribution of the angle from the z axis, both for the period 4 Test Beam data (with removed beam spill) without applying any selection.

### 3.2.2 Energy correction, charge assignment and smearing

Once we have the kinematic information for the selected events, we perform several tasks to get the final sample of cosmic muons for the data-based simulation. This includes correcting energies of the through-going muons, assigning a charge to each muon event, and smearing and converting the information into the correct format required by the generator.

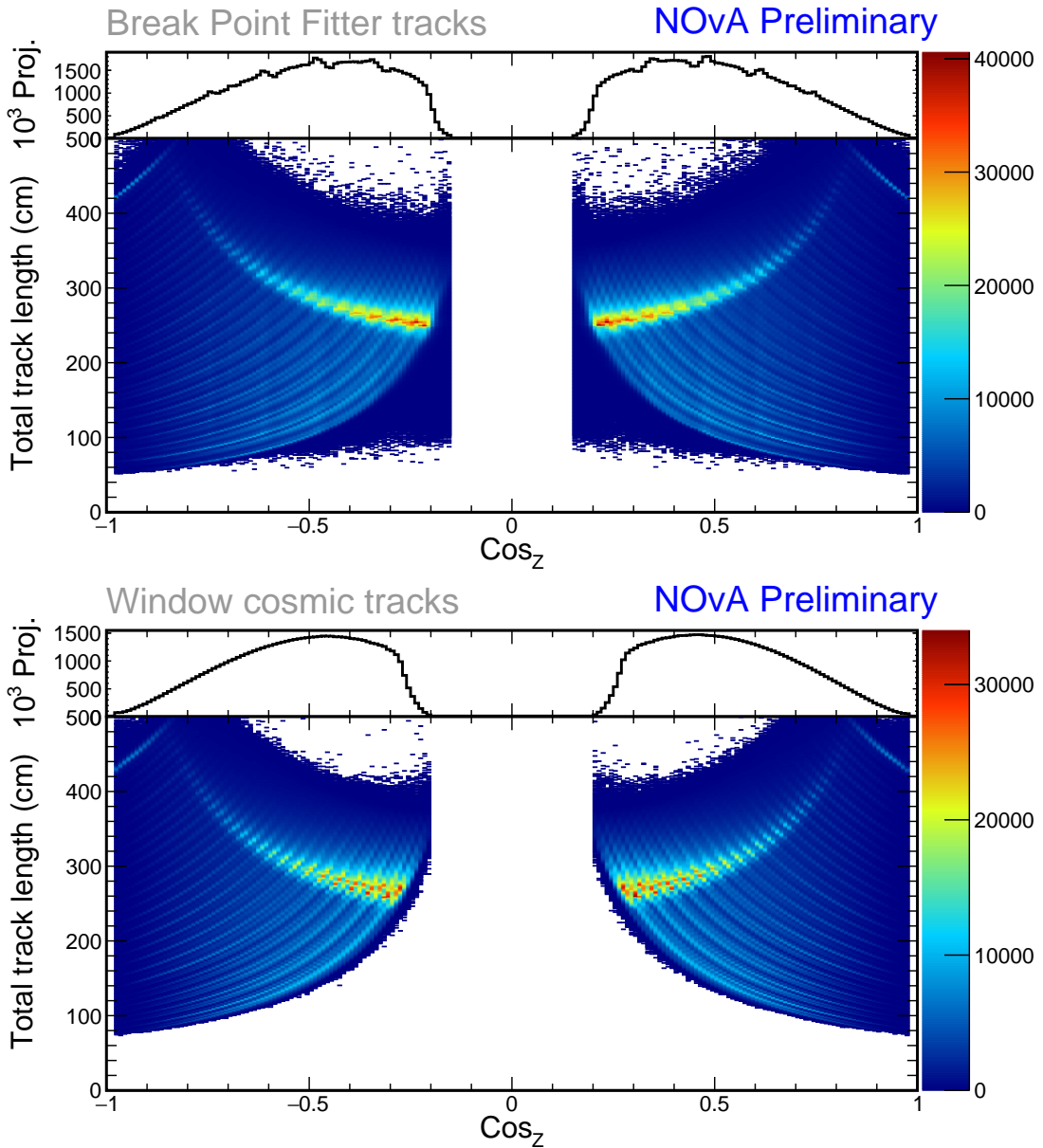


Figure 3.6: Comparison of the angle from the z axis ( $\text{Cos}_Z$ ) and the total track length distributions between the **BPF** tracks (top) and window cosmic tracks (bottom). Top parts of both plots show the 1D  $\text{Cos}_Z$  distributions, scaled by  $1/10^3$ . The top plot is created with loose calibration cuts and the bottom plot with full calibration cuts per Tab. 3.2, although this difference in selection shouldn't matter. These plots are investigating the origin of the rugged shape in the  $\text{Cos}_Z$  distribution of **BPF** tracks, as can be seen in the top part of the top plot. The long curved light blue/green lines in the 2D plots correspond to constant values of  $|\text{Cos}_Z| \times \text{Tot. length} \equiv \text{Tot. length}_Z$ , equal to the extent of the track length in the z direction, and are distinct from each other due to the structure of the detector (segmentation into planes). It is clear that the **BPF** tracks are peaked more sharply in  $\text{Tot. length}_Z$  than the window cosmic tracks, which are more spread out. This discrepancy could cause the resulting shape in the  $\text{Cos}_Z$  distribution of **BPF** tracks.

Table 3.2: Event selection of cosmic muons used for the data-based simulation (in green under Loose selection) and comparison to the Full selection cuts used to create the calibration samples (described in Sec. 2.6) in blue. The last two rows are not used for Test Beam, but are employed for the ND and FD.

Cut	Selection	
	Full	Loose
Calibration sample selection	Muon assumption and 3D track from BPF	
	Max. track start distance from edge	50 cm
	Max. $Cos_Z$	0.98
	Min. number of hits in X or Y	2
	Min. difference between $Stop_Z$ and $Start_Z$	70 cm
	Min. $Cos_Z$	0.2
	Min. frac. of slice hits in track in each view	0.8
	Max. number of cells per plane in each view	6
	Max. difference in X-Y for first (last) plane	3
	Max. plane asymmetry	0.1
	Max. step size to median step size ratio	3
	Max. vertex distance from edge	10 cm
	Max. track end distance from edge	10 cm

## Energy correction

Through-going muons do not deposit all of their energy inside the detector. Therefore we cannot reliably calculate their initial energies from the reconstructed information, but we can estimate an energy that could leave the same track. In general, the energy spectrum of cosmic muons can be approximately described by a power law  $E^{-\alpha}$ , with  $\alpha \approx 2.7$  [52, 172]. The expectation value for the ‘true’ initial energy of through-going muons can be therefore calculated as

$$\langle E \rangle = \frac{\int_{E_R}^{E_C} E \cdot E^{-\alpha}}{\int_{E_R}^{E_C} E^{-\alpha}} = \left( \frac{\alpha - 1}{\alpha - 2} \right) \left( \frac{E_C^{2-\alpha} - E_R^{2-\alpha}}{E_C^{1-\alpha} - E_R^{1-\alpha}} \right), \quad (3.1)$$

where  $E_R$  is the reconstructed energy we got from the BPF.  $E_C$  is the critical energy chosen conservatively to be 300 GeV, as we do not expect muons with higher energies to be selected due to large showers along their paths. We use this corrected initial energy for all muons that do not stop inside the detector, as identified during selection described in Sec. 3.2.1. Figure 3.8 shows the corrected energy distribution of our selected events and demonstrates that the choice of the critical energy does not significantly change the correction.

This corrected energy is however **not** a good representation of the true energy

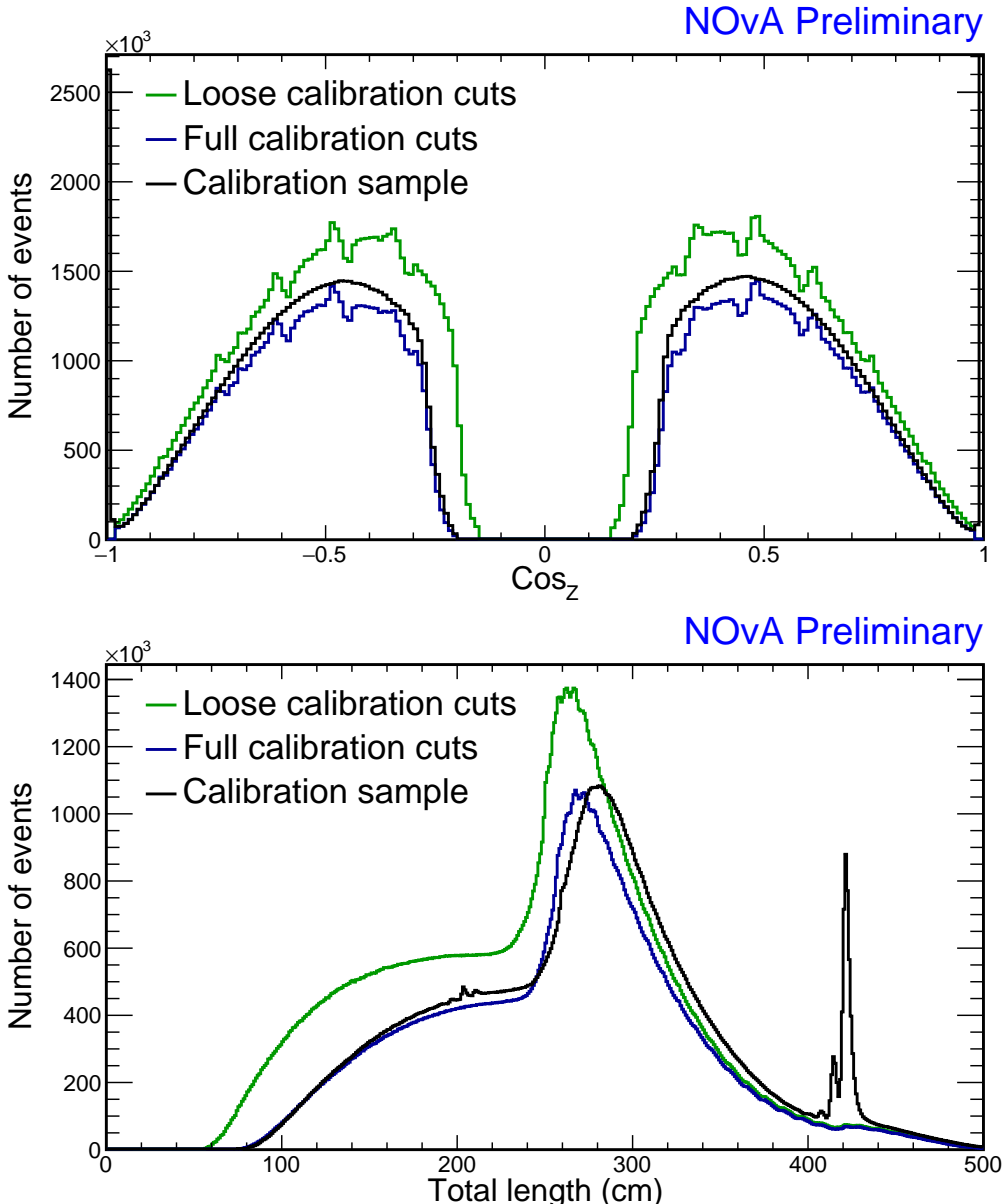


Figure 3.7: Comparison of full and loose event selections for the data-based simulation as per Tab. 3.2 and of the corresponding data calibration sample in black. As described in text, the loose calibration cuts applied to the **BPF** tracks (green) were used for simulation to mitigate the discrepancy between applying the full calibration cuts to the **BPF** tracks (blue) and the window cosmic tracks (black). All of the distributions are made from the period 4 Test Beam data.

spectrum of cosmic muons at surface level and getting a correct energy distribution from data would require a much more dedicated effort. The corrected energy would also be different for different **NOvA** detectors, since the reconstructed energy is calculated from the track length. For example, the corrected energy of cosmic muons when entering the detector would be larger for the bigger **ND** than for Test Beam, even though the **ND** is underground.

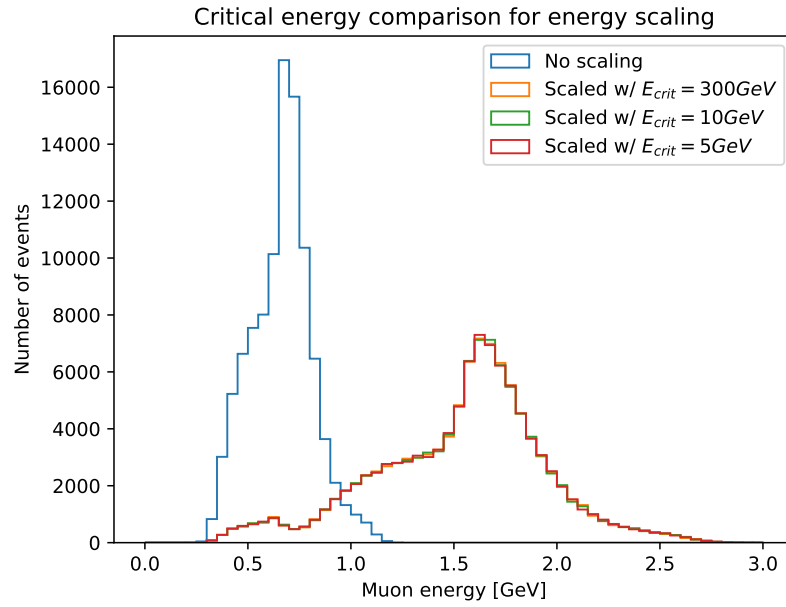


Figure 3.8: The effect of energy correction for through-going muons with various critical energies. No significant difference can be seen when using different critical energies.

However, since this simulation is intended to be used for calibration, where we use through-going muons only for relative calibration, we do not need a perfect representation of the cosmic muon energy spectrum. Not including more energetic cosmic muons into the simulation does bias the energy deposition towards lower values, but this is corrected for during absolute calibration which only uses stopping muons, for which we assume we reconstruct their energy well from BPF.

If someone were to use this simulation for something other than calibration, it would be necessary to rethink the energy correction, either by changing the energy estimation from track based algorithms to energy deposition, or by including information from external sources. It would also be necessary to include angular dependence for the energy correction as described in the PDG [52].

### **Smearing**

The reconstructed distributions in data are influenced by the detector structure, reconstruction efficiencies and other effects that can bias the simulation. To avoid this influence, we smear the reconstructed values by randomly varying

- the total momentum within 2%,

- the azimuthal angle uniformly,
- the polar angle within 4 mrad,
- and the x, y and z vertex positions within the width or depth of the cell respectively.

### Charge assignment

We need to tell the detector simulation whether to simulate a muon or an anti-muon. However we do not reconstruct the charge of the muons, so we have to randomly assign it based on a statistical distribution from external measurements. The probability that a muon has a positive charge can be expressed as [172]

$$P_+ \simeq 0.539 + \frac{x}{34.5} - \left(\frac{x}{9.48}\right)^2 + \left(\frac{x}{8.27}\right)^3, \quad (3.2)$$

where  $x$  is the logarithm of the total momentum in GeV.

### Production of the simulation

We save the vertex positions, the four momenta and the assigned charge into a text file, that is then fed into the same detector and readout simulation chain, as was described for the ND and FD in Sec. 2.4. We use the fibre brightness map that is used in calibration (see Sec. 2.6) to inform the simulation about the real detector conditions. Since we want the simulated detectors to be functional copies of the ideal versions of the real detectors, it is important to provide a correct brightness file without any defects. For this simulation we use the fibre brightness map described in Sec. 3.3.1.

#### 3.2.3 Validation

To validate whether the newly created simulation works as expected, we create the simulation calibration sample using the reconstruction and selection of cosmic muons for calibrations described in Sec. 2.6. We then compare this to the equivalent data calibration sample, created from the same data that was used to seed the simulation. Additionally, we use the newly simulated events as ‘fake data’ and pass them through the same reconstruction, selection and simulation processes as were used to create

the first iteration, hence creating a ‘re-simulation’ sample. This is used to validate the stability of the simulation process.

The data-simulation comparisons are shown in Fig. 3.9-3.12. The data and simulation calibration samples are shown in black and pink solid lines respectively. Both are equivalent to applying the full calibration cuts to the window cosmic tracks, as described in Sec. 3.2.1. For comparison, we are also showing distributions of the **BPF** tracks with full and loose calibration cuts in blue and green dashed lines respectively. We are expecting that the distributions of the simulation calibration sample (pink) match the distributions of the data calibration sample (black), without being affected by the different shape of the **BPF** tracks (dashed lines).

It can be seen that the distributions of the new simulation calibration sample resemble those of the data **BPF** tracks with full calibration cuts applied (blue dashed lines) more closely than those of the data calibration sample. This indicates that the simulated window cosmic tracks have similar properties to the data **BPF** tracks, meaning that the differences between the tracking algorithms have an impact on the resulting simulation. Therefore, loosening the calibration cuts did not help with mitigating these differences as expected. However, there were in total four versions of simulation created, with varying event selections and smearing applied, including using full calibration cuts and with different loosened calibration cut values. It is clear that it is unlikely we can mitigate the differences between the window cosmic tracks and the **BPF** tracks simply by changing the event selection or smearing and it would require adapting (or developing) a different reconstruction algorithm for the simulation. Due to the time and effort required for such a task, and due to the relative similarity between the simulation and data calibration samples, we decided to proceed with the reconstruction, selection, and correction as described above.

Figures 3.9 and 3.10 show the effect of removing the beam-like events with a  $|\cos_Z| < 0.98$  cut as described in Sec. 3.2.1. While we applied this cut to the data events used to create the simulation (green dashed lines), it is not included in the selection process for the calibration samples. This means that we were successful in removing these undesirable events from the new simulation. This can be seen by the wide peaks at  $\cos_{X/Y} = 0$  in Fig. 3.9 which are present for the data calibration sample, by not for the simulation. Additionally, sharp peaks in the total track length and

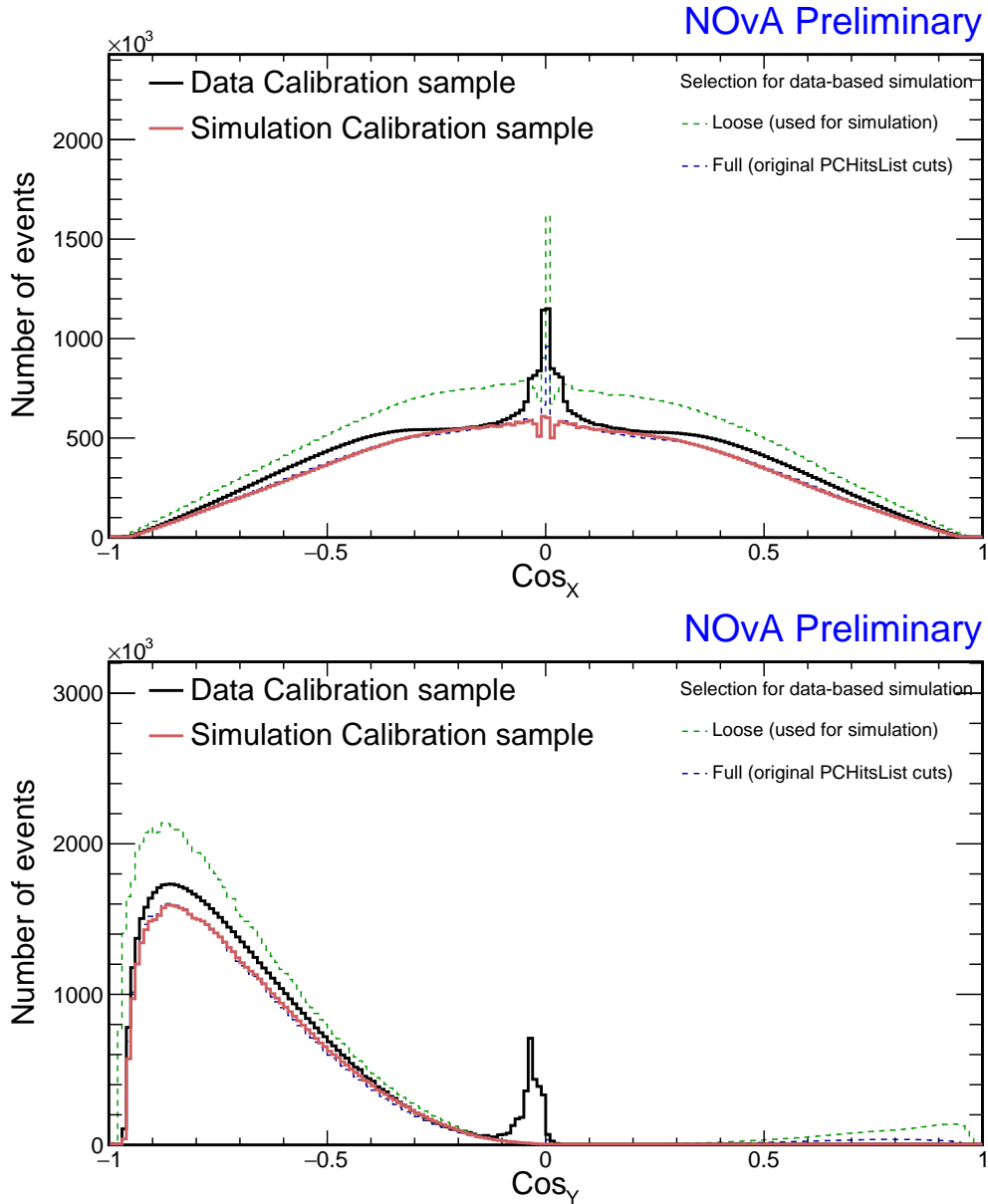


Figure 3.9: Comparison of the angle from the x axis (top) and y axis (bottom) between the data (black) and simulation (pink) calibration samples, as detailed in the text. Additionally, the distributions of data with full (blue) and loose (green) selections applied to the BPF tracks are shown, where the loose selection was used to create the simulation.

in the edges of the angle from the z axis distributions in Fig. 3.10 further illustrate this distinction.

The effect of smearing of vertex positions and four momenta is visible in the top plot of Fig. 3.10 and in Fig. 3.12. Here, the rugged distributions of the data used for simulation (green dashed lines) appears smoother for the simulation calibration sample (pink solid lines). However, comparisons of track start positions in Fig. 3.11 and

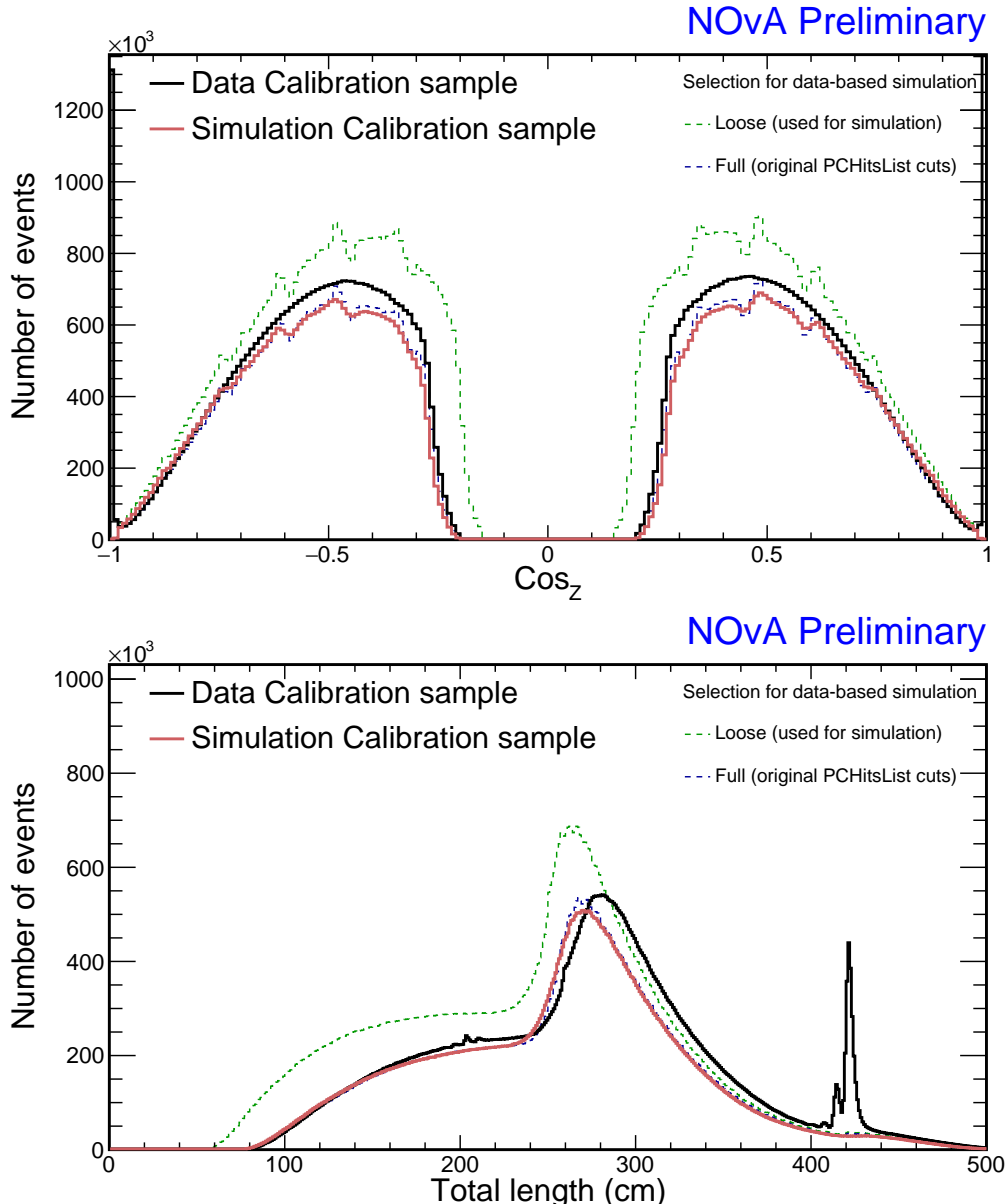


Figure 3.10: Comparison of the angle from the z axis and total track length between the data (black) and simulation (pink) calibration samples, as detailed in the text. Additionally, the distributions of data with full (blue) and loose (green) selections applied to the BPF tracks are shown, where the loose selection was used to create the simulation.

3.12 show that the simulated events start further away from the detector edge compared to data. While this is likely also a result of smearing, we anticipate it will not impact the calibration of the simulated detector.

After adding the distributions for the re-simulation calibration sample, shown as solid brown lines Fig. 3.13, we can see that the track start positions are shifted even further towards the inside of the detector. This would support the hypothesis that

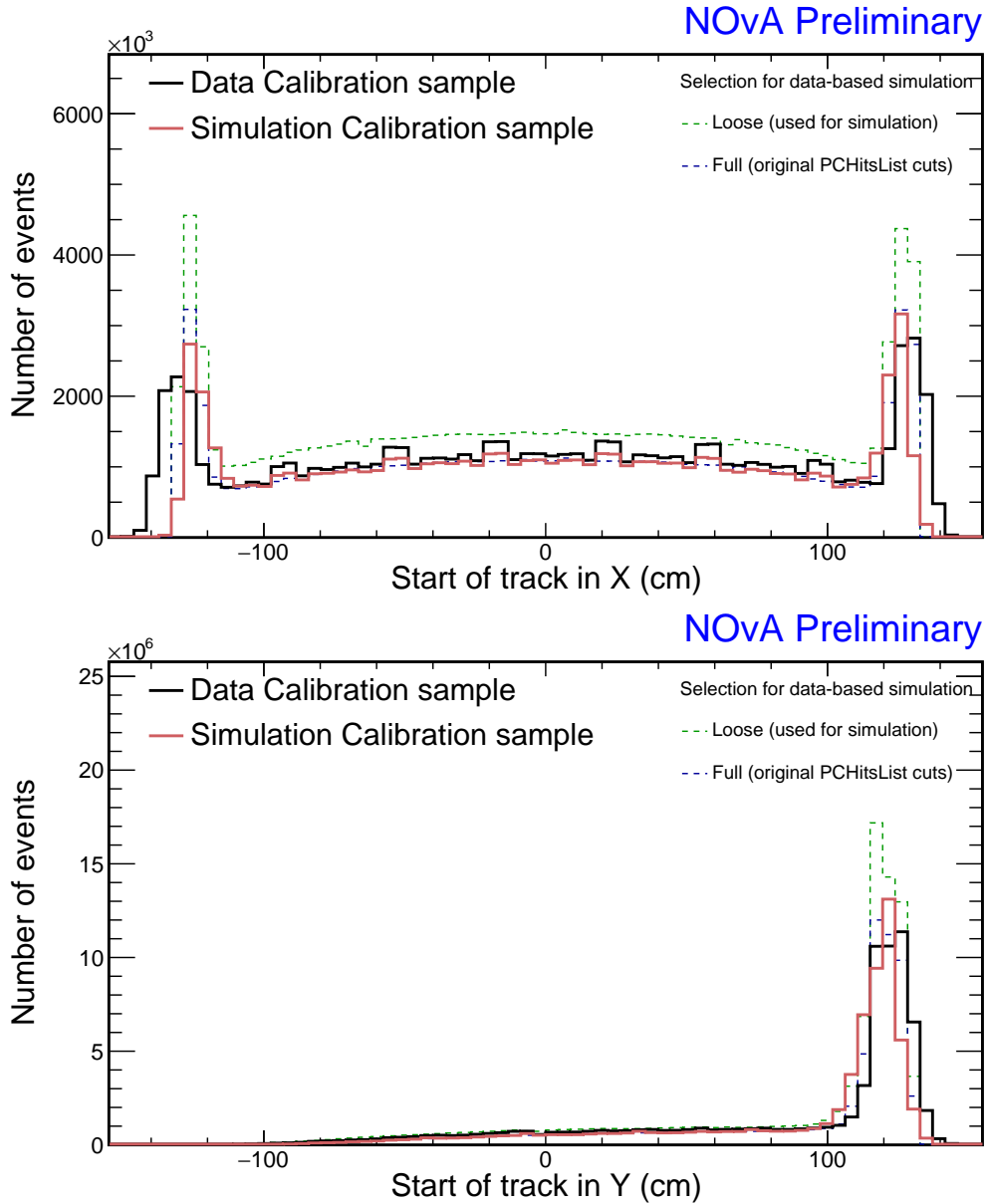


Figure 3.11: Comparison of the x (top) and y (bottom) track start position between the data (black) and simulation (pink) calibration samples, as detailed in the text. Additionally, the distributions of data with full (blue) and loose (green) selections applied to the BPF tracks are shown, where the loose selection was used to create the simulation.

this effect is caused by smearing and is also likely related to the loss of events with longer track lengths, as shown in Fig. 3.13, since if tracks start a few centimetres later in the detector their tracks would get shorter by the same amount. Since there are only minimal discrepancies between the simulation and the re-simulation, we conclude that the reconstruction, selection and correction processes used to create the simulation do not significantly bias the simulation, which is self-consistent.

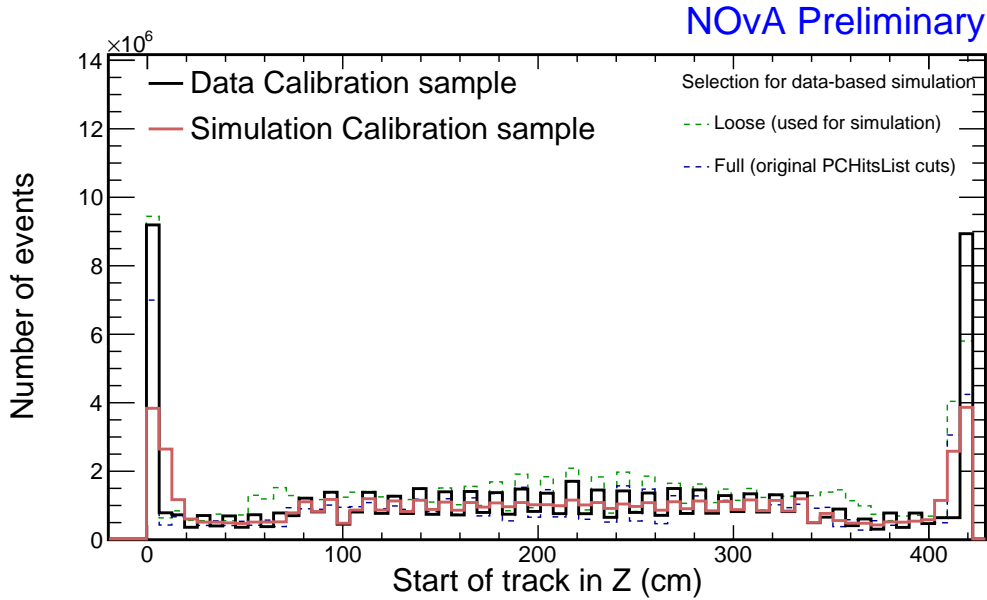


Figure 3.12: Comparison of the z track start position between the data (black) and simulation (pink) calibration samples, as detailed in the text. Additionally, the distributions of data with full (blue) and loose (green) selections applied to the **BPF** tracks are shown, where the loose selection was used to create the simulation. Each bin corresponds to a single detector plane and the shape of the distribution is caused by the fact that cosmic rays are naturally more vertical and therefore more likely to be detected by horizontal than vertical planes.

### 3.2.4 Summary

I have successfully developed a new simulation of cosmic muons intended for Test Beam calibration. The reconstruction, selection, and correction processes were designed to minimize the number of simulated events, resulting in an efficient and concise simulation while avoiding a significant bias, particularly in the applicability to the calibration procedures.

While the simulation achieved its objectives, there are possible improvements that could be introduced to refine it. Using a different track reconstruction algorithm than the **BPF**, more consistent with the window cosmic track algorithm, could make the simulation calibration sample more alike the data calibration sample. Additionally, developing a more sophisticated energy correction procedure, potentially involving external measurements of energy distribution of cosmic muons, would enable simulation of through-going muons with accurate incident energies.

Looking ahead, there are plans to use the data-based simulation approach for cosmic muons in the **NOvA ND** and **FD**. While the primary motivation is again detector

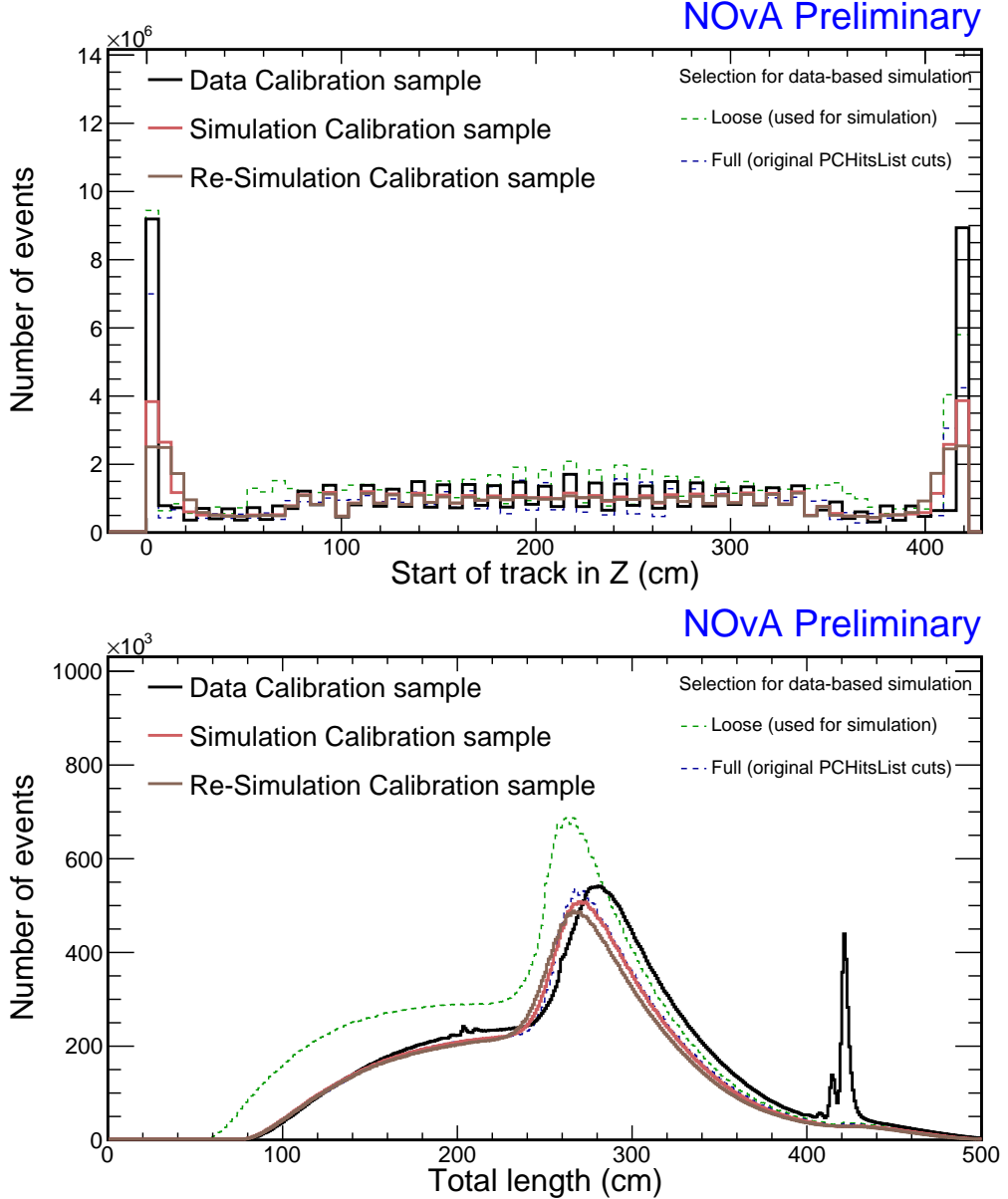


Figure 3.13: Comparison of the z track start position and total track length between the re-simulated events (brown), which use simulation as ‘fake data’ for the second iteration of the same simulation process, and the data (black) and simulation (pink) events. Additionally, the distributions of data with full (blue) and loose (green) selections applied to the BPF tracks are shown, where the loose selection was used to create the simulation.

calibration, there is potential for broader applications in cosmic ray studies. However, using the simulation for a different detector would require re-validating the event selection process, especially with the inclusion of the calibration cuts missing for the Test Beam detector, as outline in Sec. 3.2.1 and showed shaded out in two bottom rows of Tab. 3.2.

### 3.3 NOvA Test Beam detector calibration

In this section I describe the details of the Test Beam detector calibration as it was finalized in June 2023. This version includes a new purpose-made simulation and all the measured Test Beam data, with the exception of the period 1 data.

The data calibration samples for Test Beam were created using the same procedures as the [ND](#) and [FD](#) calibration samples, described in Sec. 2.6. However, there are two cuts from the event election, that were not included for Test Beam during the processing of the data samples. This can be seen on Tab. 3.2, where the two bottom rows show the two excluded cuts. One cut contains the vertex close to the edge of the detector ensuring we only use cosmic events, the other contains the end of track close to the edge, ensuring we only use through-going muons for the relative calibration. Given that we remove beam events and that all the other cuts are designed to select cosmic events, the first cut has only a negligible effect on the final selection. Additionally, the stopping muons only make up a small fraction of the total cosmic muon events, rendering the second cut also negligible.

This section is organized as follows. I first describe the Test Beam versions of the fibre brightness map in Sec. 3.3.1 and the threshold and shielding correction in Sec. 3.3.2, as they were introduced in Sec. 2.6. I then go over the simulation sample and the three data samples (for periods 2, 3, and 4), showing distributions of hits selected for calibration and of the uncorrected energy deposition before calibration. I discuss considerations going into calibration, including splitting the individual periods into smaller samples, or describing issues that could affect the calibration results. Afterwards, I am showing a selection of attenuation fit results for each sample together with an overview of the relative calibration effects. Lastly, I discuss the absolute calibration results for all the samples combined, as well as the validation and conclusion of the Test Beam calibration.

#### 3.3.1 Fibre brightness

To divide the Test Beam detector into [FB](#) bins we use the attenuation fit results for Test Beam period 4 data (described in Sec. 3.3.6), as that is the best detector conditions data we have. Since we need the [FB](#) map in order to run the attenuation fits and we

need the attenuation fit results to create the **FB** map, we proceeded iteratively. We first run the attenuation fit with an older version of the **FB** map and use the results to create a new **FB** map, discussed here, which is then used in a new attenuation fit.

We are only using the attenuation fit results in the centre of each cell to create the **FB** map, therefore, we decided to allow some cells that failed the calibration condition ( $\chi^2 > 0.2$ ), to be still used for the creation of the **FB** map. Otherwise, all the officially uncalibrated cells are assigned an average response across the entire detector, resulting in a loss of information on their relative brightness. As can be seen in Fig. 3.14, some attenuation fits have  $\chi^2 > 0.2$ , even though they correctly represent the energy deposition in the centre of that cell. By carefully investigating all the uncalibrated Test Beam cells (doable for Test Beam, due to its small number of cells), we concluded that all the cells with  $\chi^2 < 0.7$  can be used to create the **FB** map, since the response in their centre is described reasonably well by their attenuation fits. We use this loosened calibration condition only to create the **FB** map and we keep the original condition for the actual calibration results.

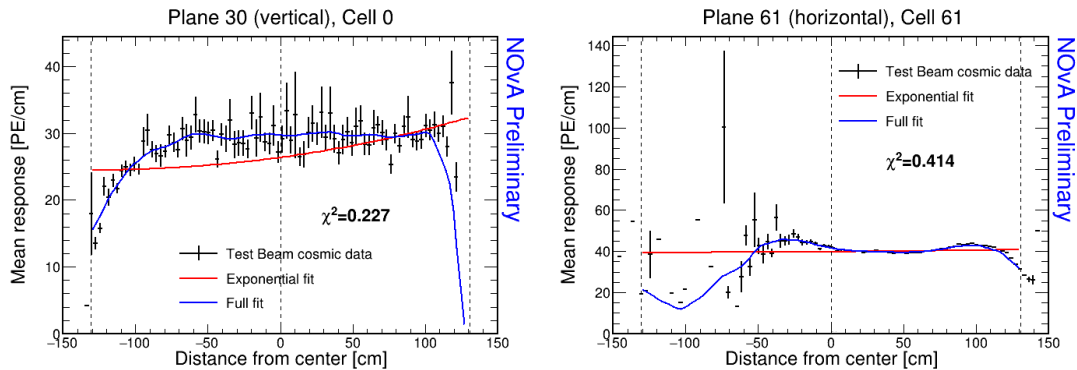


Figure 3.14: Examples of attenuation fits for two cells that fail the calibration condition, but the fit (blue line) still correctly represents the energy deposition in the centre of that cell (dashed vertical line in the middle). The total  $\chi^2$  between the data (black) and the attenuation fit for both plots are included.

The final distribution of relative **FB** values that are used to populate the **FB** bins for the Test Beam detector is shown in Fig. 3.15. The resulting map of **FB** bins and their corresponding relative brightnesses was shown in the previous chapter in Fig. 2.10.

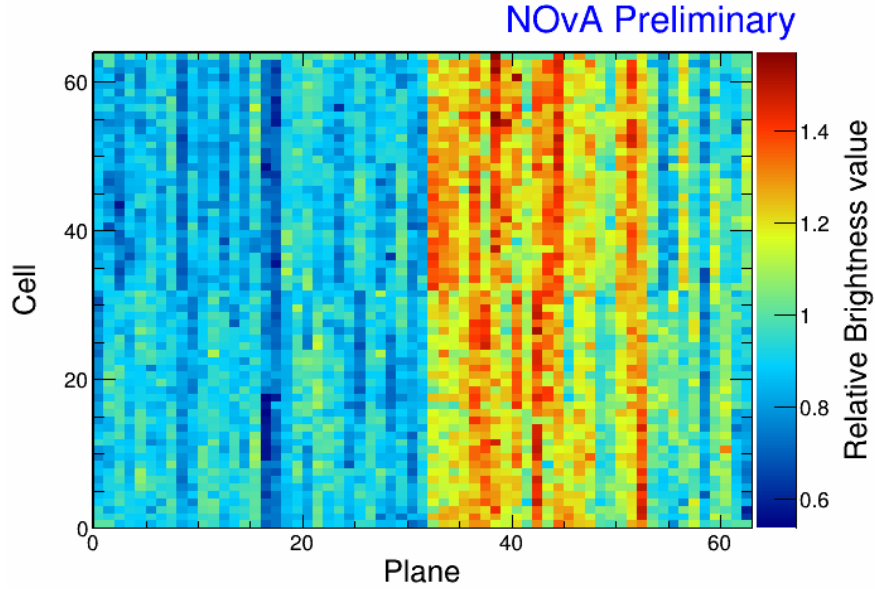


Figure 3.15: **FB** map representing relative differences in energy response due to different brightnesses of the fibres, scintillators, or readout. Create from the attenuation fit results of the NOvA Test Beam detector with a shifted calibration condition from  $\chi^2 < 0.2 \rightarrow 0.7$  to enable using the attenuation fits that are officially uncalibrated, but correctly represent energy deposition in cell centre. Otherwise, all the uncalibrated cells get assigned a mean detector response, represented by number 1 on this map.

### 3.3.2 Threshold and shielding corrections

The threshold and shielding correction is intended to mitigate biases arising from differences between cosmic events used for calibration and beam events. It is only used prior to the attenuation fits and is omitted when applying the results of the relative calibration, whether during the absolute calibration or for beam events. Additionally, it is derived exclusively from simulation.

We created a new threshold and shielding correction for the Test Beam detector using the new simulation described in Sec. 3.2. The correction is calculated for both views, across 12 **FB** bins, 64 cells, and 100  $w$  bins, where  $w \in (-130 \text{ cm}, 130 \text{ cm})$ . Two examples of the correction as a function of  $w$  are shown in Fig. 3.16, demonstrating an almost uniform behaviour along a cell. Relative variations of the correction in the X view range from 1 – 2 %, primarily concentrated at the edges of the cell. In the Y view, the correction exhibits sub-1 % variations. These trends are consistent across all the **FB** bins and views. Given that the threshold and shielding correction precedes relative calibration, the absolute value of the correction is irrelevant and only the relative variations along  $w$  and between cells matter.

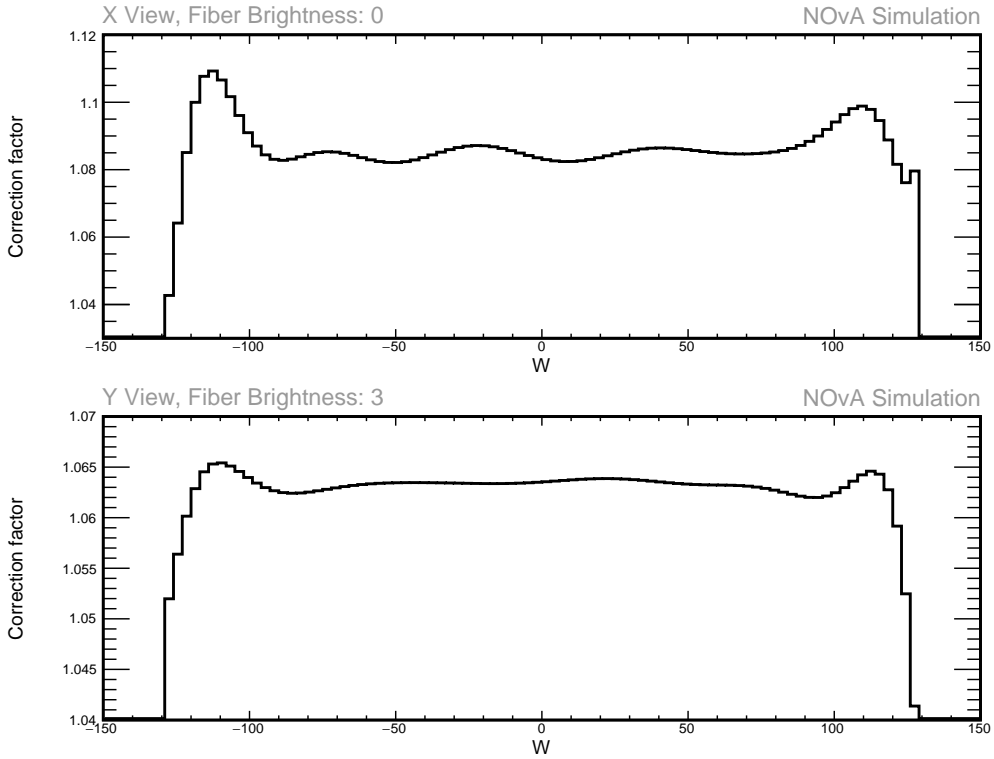


Figure 3.16: Examples of threshold and shielding corrections as a function of the position within a cell in X view (top) and Y view (bottom) for the Test Beam detector.

This uniformity of the distributions is expected, considering the relatively small size of the Test Beam detector compared to the FD, which prompted the investigation into threshold and shielding effects. The Test Beam detector's cell length of 2.6 m has only a negligible impact on the threshold saturation or on the energy distribution of cosmic muons, resulting in the uniformity of the threshold and shielding correction for Test Beam detector. The larger correction at cell edges is likely caused by lower event counts in those areas. However, since this relative sparsity of events also influences relative calibration due to large variation in the energy response, the relatively larger threshold and shielding correction at cell edges is not detrimental.

The distribution of the threshold and shielding correction across Test Beam detector's cells and planes, shown in the top of Fig. 3.17, demonstrates, that while the correction is expected to be generally uniform across the detector, there are notable variations between cells and planes forming a discernible pattern. These variations and their shape primarily stem from the threshold component of the correction, shown in the bottom of Fig. 3.17.

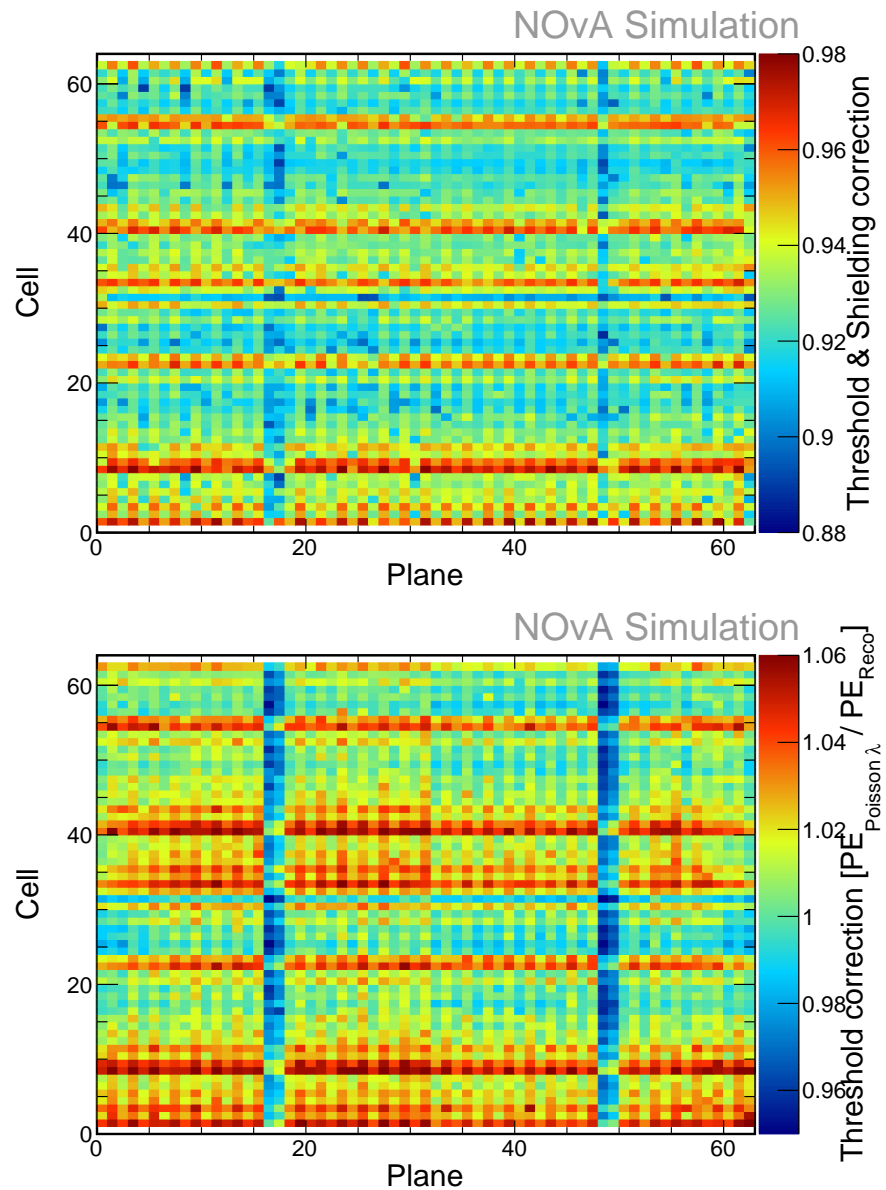


Figure 3.17: Map of the threshold and shielding correction (top) and only of the threshold part of the correction (bottom) as a function of the Test Beam detector's cell and plane number. Each bin shows the mean correction for all the simulated events in that cell.

The threshold part of the correction can be expressed as

$$\text{Threshold correction} = \frac{PE_{Poisson\lambda}}{PE_{Reco}}, \quad (3.3)$$

where  $PE_{Poisson\lambda}$  represents the mean of the Poisson distribution of the true deposited energy (in terms of  $PE_{True}$ ), and  $PE_{Reco}$  is the reconstructed number of PE from simulation. Both  $PE_{Poisson\lambda}$  and  $PE_{True}$  are direct outputs of the light model simulation, as detailed in Sec. 2.4. After the light model simulation,  $PE_{True}$  is passed through the readout simulation, which includes a PE-to-ADC function for calculating the peak ADC value. This value is then converted into  $PE_{Reco}$  using the ADC-to-PE scale described in Sec. 2.6. The observed shape in the threshold correction can thus be attributed to differences between  $PE_{True}$  and  $PE_{Poisson\lambda}$ , as well as to various effects introduced by the readout simulation. However, the differences between  $PE_{True}$  and  $PE_{Poisson\lambda}$  are marginal (below 1 %) and contribute minimally to the threshold correction. Therefore, the predominant influence on the observed pattern comes from the effects introduced by the readout simulation.

There are two prominent features in the threshold correction variations in Fig. 3.17. Firstly, the two blue vertical lines in planes 16-17 and 48-49. These planes are using the FEB version 5.2, used in the ND, instead of the FEB version 4.1, used in the FD and in all the other Test Beam planes, as explained in Sec. 3.1. Both the readout simulation and the ADC-to-PE scale do account for the expected disparity in the ADC/PE ratio between the two FEB versions. However, it is expected that FEBv5 would exhibit a lower response to the same energy compared to FEBv4. Therefore, for the same  $PE_{Poisson\lambda}$  values, the  $PE_{Reco}$  for FEBv5 should be smaller than that for FEBv4. Consequently, the FEBv5 planes should have a larger threshold correction compared to the FEBv4. However, as was shown in Fig. 3.17, the observed correction is contrary to this expectation, suggesting a potential error in the readout simulation regarding the handling of different FEB versions.

The second notable feature in Fig. 3.17 is the variation of the threshold correction across cells, which appears to be consistent across all planes, depicted by the presence of red horizontal lines. The origin of this dependency is in the APD structure, where each APD collects signal from 32 cells arranged in 4 rows of 8 APD pixels, as explained in Sec. 2.3. Manufacturing discrepancies [173] lead to relative gain variations among

the [APD](#) pixels, typically exhibiting either increasing or decreasing trend along each of the four rows. To incorporate these variations into the readout simulation, the mean relative gain across cells of every module (comprising 32 cells) is used in the [PE-to-ADC](#) function. Consequently, these variations are consistent across all modules in the simulated detector, despite their inherent randomness in actual data.

The distribution of the relative gain for each ‘pixel number’ is shown on the left of Fig. 3.18. However, it is important to note that ‘pixel number’ is a [NOvA](#) jargon and does not correspond directly to the [APD](#) pixel position or cell number; instead it denotes the purely technical routing of [APD](#) pixels to the [FEB](#) [174]. Therefore, the depicted distribution of gain variation on the left of Fig. 3.18 is incorrect and should instead describe the distribution with respect to the cell number rather than the ‘pixel number’. Simply translating ‘pixel numbers’ to cell numbers yields the distribution shown on the right of Fig. 3.18. Comparing this to the positions of the red horizontal lines in Fig. 3.17 demonstrates that this (incorrect) relative gain variation is responsible for the observed pattern in the threshold correction.

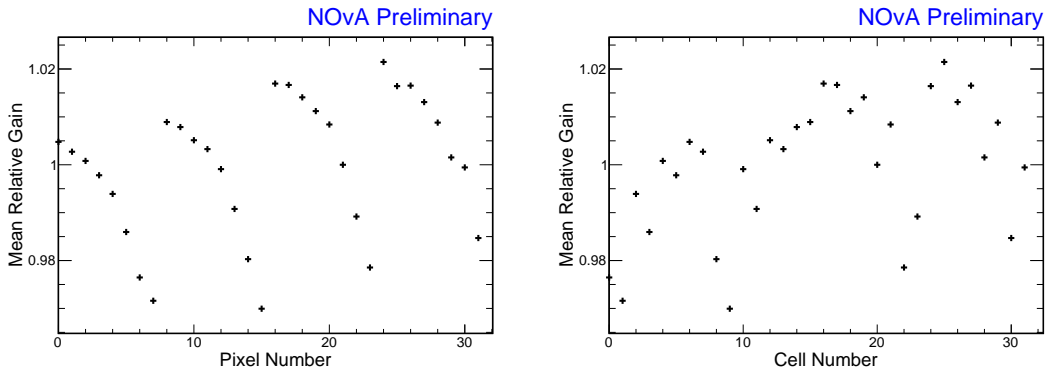


Figure 3.18: The relative gain variation as a function of the ‘pixel number’ (left) and cell number (right).

In summary, the threshold and shielding correction exhibits significant variations concentrated within specific planes and cells, arising from various effects in the readout simulation. However, it is evident that these effects are not limited to cosmic events and therefore should not be incorporated into the threshold and shielding correction. Given that these effects are corrected out for simulation before the attenuation fits, they are not accounted for in the relative calibration and therefore remain present for the absolute calibration and for beam events. Moreover, the two main effects outline above are not implemented into the simulation correctly, result-

ing in discrepancies between actual data and simulation. This means, that in data these variations are either not present or present in a different way than in simulation. Therefore, applying the simulation-based threshold and shielding corrections to data introduces new variations that would otherwise not exist for data. As a result, these new variations are incorporated into the attenuation fits for data, resulting in incorrect relative calibration results applied to both absolute calibration and beam events.

Several approaches can address these issues. For simulation-related discrepancies, the only viable solution is to rectify the identified faults and to remake the simulation, albeit this would be computationally very intensive. However, for data-related concerns, efforts are underway to devise a new data-driven threshold and shielding correction [175], eliminating any influence of simulation on the relative calibration of data. If a purely data-driven correction is not viable, there is another possible improvement to the threshold correction while still using simulation, which is to not use the  $PE_{Poisson\lambda}$  directly, but to pass it through the readout simulation in the same way as  $PE_{True}$  and create an alternative  $PE_{Poisson\lambda Reco}$ .

### 3.3.3 Simulation

The distribution of tricell hits from the simulated cosmic muon events selected for calibration, mapped across the Test Beam detector’s planes and cells, is shown in Fig. 3.19. As this is a simulated detector, we will use this ‘ideal conditions’ distribution of tricell hits to illustrate the main features, which are also present in all the data samples discussed below. We can clearly see the difference in the number of events between the vertical (even) and the horizontal (odd) planes. This is expected as cosmic muons are generally vertical and a single cosmic track often passes more horizontal planes than vertical planes. We can also see that due to the tricell condition there are no hits in cells 0 and 63, which are on the edge of the detector. These cells can still be calibrated by including hits from the ‘z tricell’ condition, which is not shown in the plot. The three clear horizontal lines of relatively lower response going across the detector correspond to pairs of cells 15 + 16, 31 + 32, and 47 + 48. Together with cells 0 and 63, they represent the first and the last cells of each 16 cell-wide extrusion, which makes up half of a module, which in turn makes up half of a Test Beam plane. As

was mentioned in Sec. 2.2, these cells are 3 mm narrower than the rest, resulting in fewer hits and a lower deposited energy. However, using the deposited energy divided by path length for calibration should compensate for this effect. Overall, Fig. 3.19 demonstrates that the tricell hits are distributed fairly uniformly in the centre of the detector, with the number of hits dropping off towards the front, back and corners of the detector. This is a result of the event selection applied to the cosmic tracks for calibration.

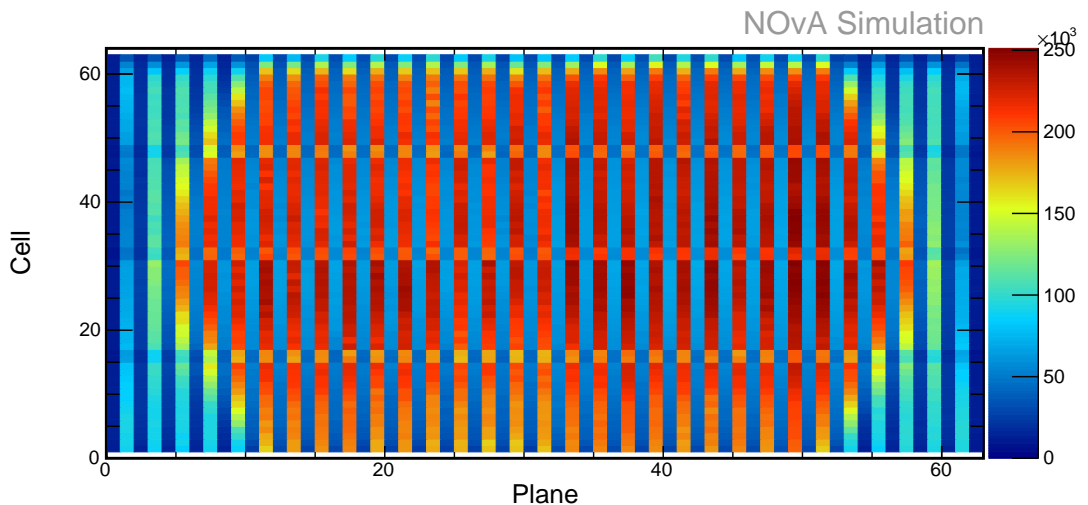


Figure 3.19: Distribution of tricell hits used for the calibration of the simulated Test Beam detector. Features are described in text.

The distributions of deposited energy per path length through the cell before the calibration in units of PE/cm as a function of  $w$ , cell and plane number, are shown in Fig. 3.20. These distributions should be uniform after applying the results of the calibration and can be used to identify the main features that will need to be corrected for during the calibration. The shallow rise of the energy response along  $w$  is caused by the attenuation of light along the [WLS](#) fibres. The drop in the response at the edges of the cell is caused by the fibres looping and connecting to the [APDs](#), while the larger statistical uncertainties at the edges of the cell reflect the lower number of hits passing the event selection including the tricell condition.

The rise of the response with the cell number, visible in the middle plots in Fig. 3.20, is due to the varying distance of cells to the readout. Since the [APDs](#) are located on one side of each module, light from cells on the opposite side has to travel along the [WLS](#) fibre for an additional module width, compared to the cells closer to the readout. Light undergoes additional attenuation along these so-called ‘pig tails’, causing

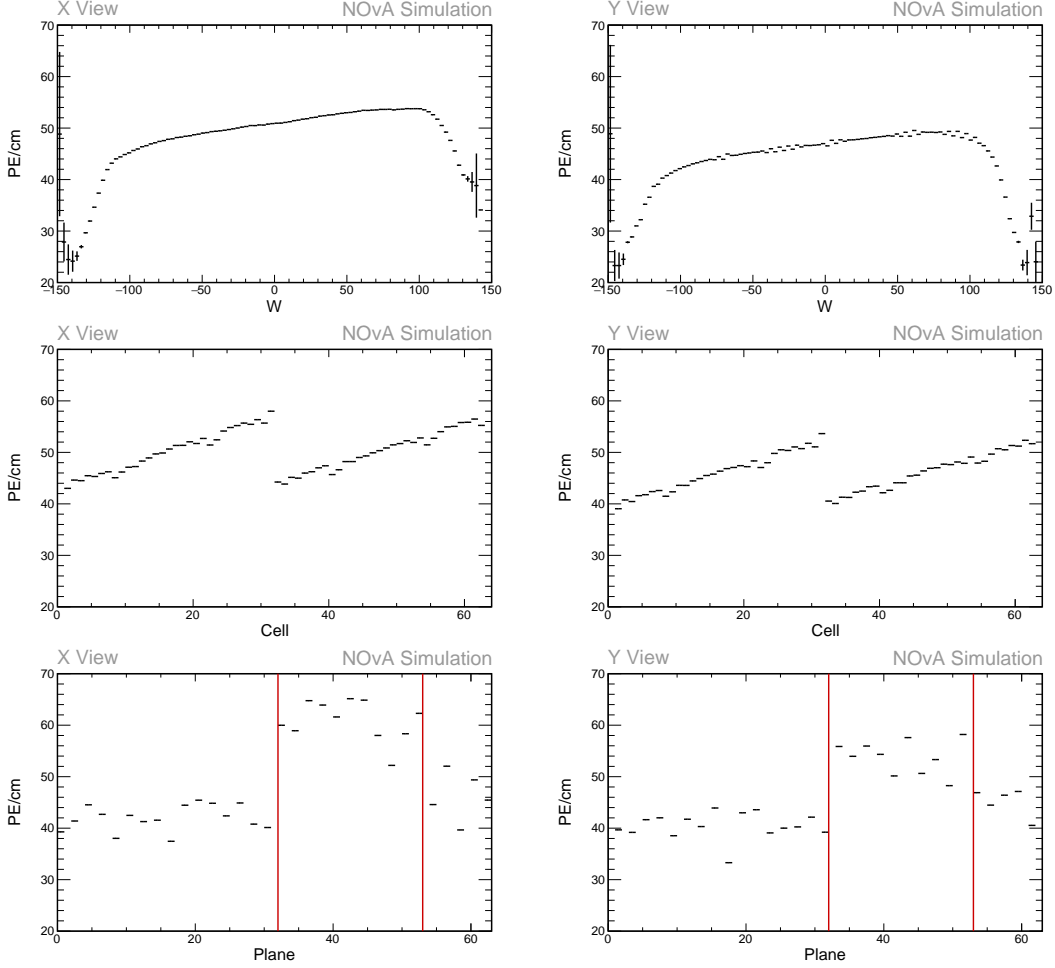


Figure 3.20: Uncorrected average energy response as a function of the position within a cell ( $w$  - top), cell number (middle), or plane number (bottom) for the Test Beam detector simulation of cosmic muon hits selected for calibration. Left side shows distributions for the X view (vertical) planes and right side for the Y view (horizontal) planes. Each plot is a profile histogram, with uncertainties representing statistical variations. Red lines on the bottom two plots depict the boundaries between different scintillators. Features explained in text.

the difference of the energy response. The additional variations across cells within a module, notably the relatively lower response in cells 0, 1, 9, 10, 23, 24, 31 and 32, is caused by including the relative gain differences into the simulation, as explained above in Sec. 3.3.2.

The uncorrected energy response as a function of plane number is shown in the bottom row of Fig. 3.20, illustrating large fluctuations between planes in both views. We can clearly identify the three distinctly different responses delineated by red lines, corresponding to the three scintillator variations used, as described in Sec. 3.1. Additionally, planes 16, 17, 48 and 49 use the FEBv5.2 instead of FEBv4.1, resulting in

a relatively lower response. All these variations between planes in simulation are caused by consolidating the planes and replacing possible discrepancies with the FB map (Sec. 3.3.1), which is used for simulation to emulate real detector conditions. The rest of the variations are caused by differences between readout electronics and individual cells, but are exacerbated by the FB binning, which groups otherwise smooth variations across planes into 12 discrete bins, thus amplifying them.

### Simulation relative calibration results

An overview of the attenuation fit results for simulation is shown in Fig. 3.21 as a map of average fitted response in the centre of each cell. Blank cells mark the uncalibrated cells which failed the calibration condition (attenuation fit  $\chi^2 > 0.2$ ). All the uncalibrated cells but one are on the edges of the detector, which is expected, as they have much fewer events that pass the calibration sample selection. There are 43 uncalibrated cells out of the total 4032 cells in the Test Beam detector, resulting in 1.07% of the simulated detector remaining uncalibrated.

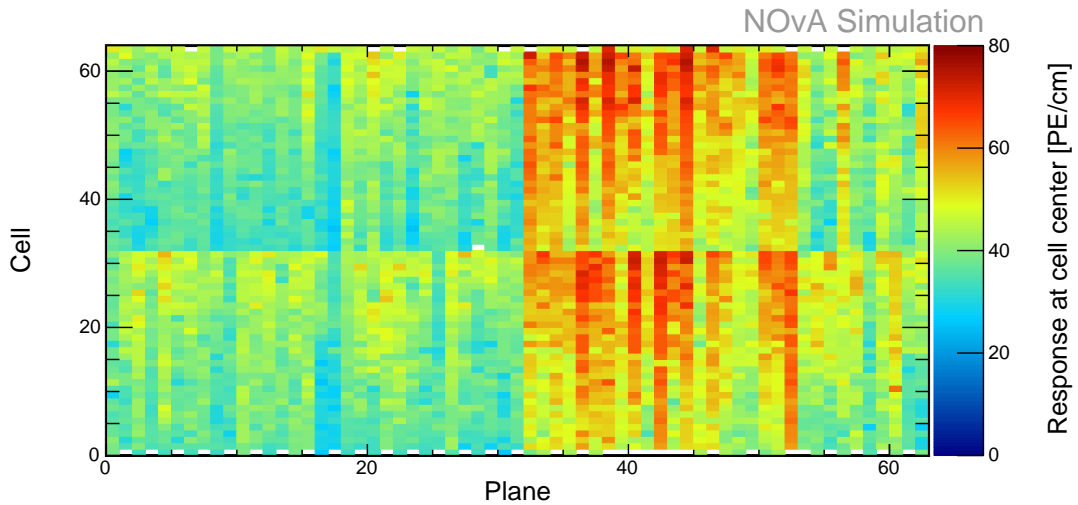


Figure 3.21: Overview of the attenuation fit results for the simulated Test Beam detector. Each cell represents the result of the attenuation fit to the energy response in the centre of that cell. The blank cells are uncalibrated as the attenuation fit did not satisfy the calibration condition.

For simulation, the attenuation fit is done for each FB bin and each cell separately. Examples of detector response for different cells in various FB bins are shown in Fig. 3.22. Here the red line shows the initial exponential fit and the blue line depicts the final attenuation fit after the LOWESS correction, as described in Sec. 2.6. The cells

on the edge of the detector failed the calibration conditions due to the low number of entries causing large fluctuation in the mean response.

There is only one cell in the middle of the detector that is left uncalibrated. This is the cell 32 in a vertical plane in FB bin 5, shown on the top right of Fig. 3.22, with  $\chi^2 = 0.227$ . Apparently, the reason the attenuation fit for this cell failed the calibration condition is the unusually high response with a large uncertainty in the right-most bin. It is unclear why this bin has such an elevated mean response, but since this only causes an issue for a single cell, we decided to ignore it and leave it uncalibrated.

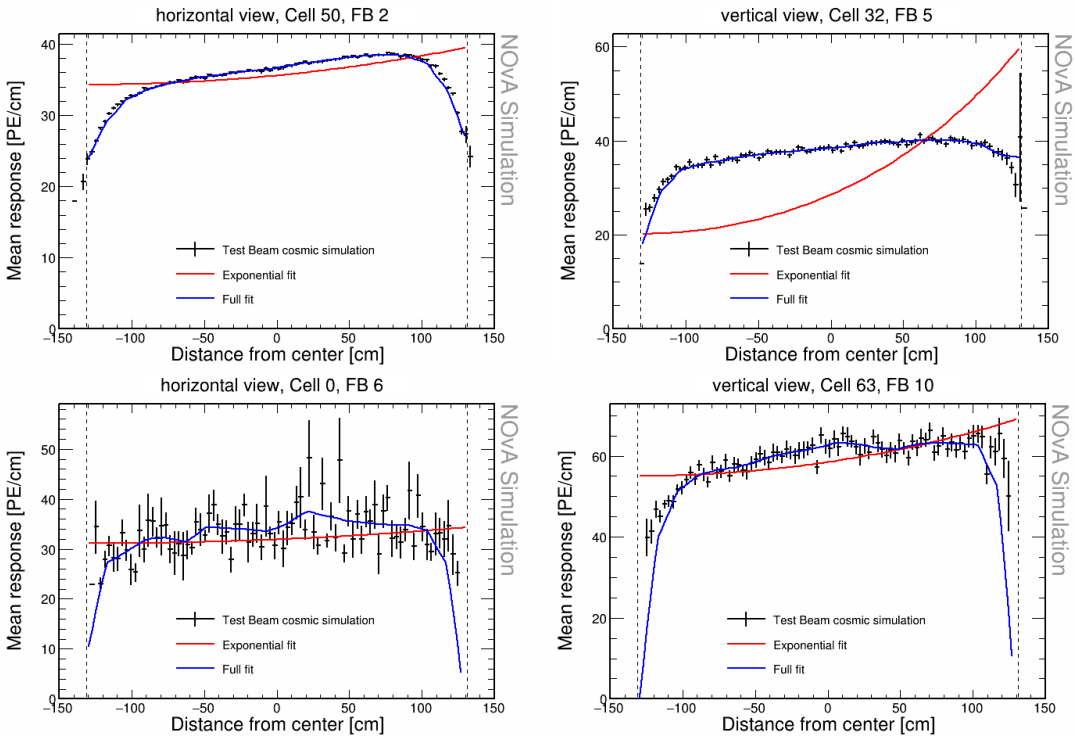


Figure 3.22: Attenuation fits for a selection of cells in various FB bins in the calibration of the Test Beam simulation. Top left is an example of a successful attenuation fit, top right is a failed fit due to statistical fluctuation in the last bin and the bottom plots show failed fits for cells on the edges of the detector.

### 3.3.4 Period 2 data

The distribution of cosmic muon tricell hits selected for calibration in Test Beam period 2 data is shown in Fig. 3.23. The issue with underfilled cells described in Sec. 3.1 was present throughout period 2. The underfilled cells were marked as bad channels and therefore ignored during production of calibration samples. This also visibly af-

fects the event count in the neighbouring cells to the underfilled cells, which have fewer calibration hits due to the tricell condition (see Sec. 2.6). However, since the underfilled cells 63 are also on the edge of the detector, labelling them as bad channels can't mitigate the effect on the neighbouring cells 62.

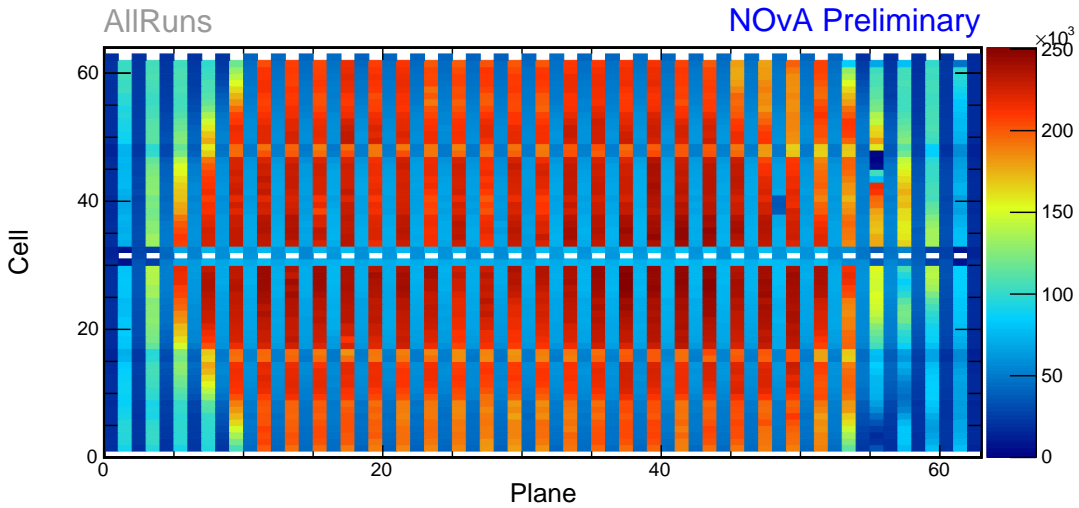


Figure 3.23: Distribution of tricell hits as a function of Test Beam detector cells and planes in the entire period 2 data calibration sample. The rows of empty cells 31 and 62 across all the horizontal planes are caused by the underfilled cells (and tricell condition), as explained in text. There are several areas with relatively fewer hits. Notably cells 38-40 in plane 48 and cells 45-47 in plane 55. Both of these spots comprise of three cells, pointing towards the middle cell being a dead channel (for a limited time) and the two surrounding cells being affected by the tricell condition. Additionally, the bottom half of planes 55 and 57 have noticeably lower number of hits than their top halves (one half corresponds to a single readout).

We can also observe areas with relatively fewer hits, likely due to channels that were dead for some time. This also affects their immediate neighbours due to the tricell condition. Additionally, there are planes that have noticeably fewer hits in one half than in the other, and since half of a plane corresponds to a single readout (one FEB and APD), which means an entire readout was faulty for a certain time.

Officially, period 2 is divided into six epochs labelled 2a - 2f, based on specific Test Beam detector running conditions. Generally, smaller calibration samples reduce time-dependent effects on calibration, such as detector ageing or temperature and humidity variations. However, smaller samples also increase the number of cells with issues in the attenuation fit (examples shown below). Therefore, it is important to choose an optimal calibration sample size to balance both concerns. Since individual epochs in period 2 do not contain enough events for a successful attenuation fit, and

variations between epochs are minimal, we decided to calibrate the entire period 2 together, without splitting it into any smaller calibration samples.

The epochs in period 2 mostly differ in the use of various [FEB](#) firmwares or in the presence of trigger studies. We compare the energy deposition during the individual epochs in Fig. 3.24. As can be seen, the difference between the energy response across the individual epochs is fairly small (within 2 %) and only in normalization, with the largest outliers seemingly epochs 2a and 2d. There is also no clear trend of energy response falling or raising with time (epoch labels are organized in time alphabetically).

The only noticeable variation of energy response across epochs in both normalization and shape can be seen on the distributions of the energy response as a function of planes, where the uncorrected response in plane 55 is noticeably higher than the rest of the period. The exact reason for this is unknown, although it is likely caused by a fault in one of the two [FEBs](#) that make up the plane readout.

## Period 2 relative calibration results

The results of the attenuation fit for period 2 are summarised in Fig. 3.25, showing the map of the fitted response at the centre of each cell, with blank bins representing cells that failed the calibration condition and are left uncalibrated. Summary of the relative calibration results is shown in Tab. 3.3. There are 199 cells that failed the calibration condition out of the total 4032 cells, constituting 4.94% of the detector left uncalibrated for period 2. The largest contribution to the uncalibrated cells are the peripheral cells on the edge of the detector, which contain too few events due to the tricell condition.

Most cells have the standard response, as discussed for simulation. However, some cells have one or more regions with a drop in the energy response, as shown in Fig. 3.26. These low regions are a real physical effect caused by zipped, or possibly even twisted, [WLS](#) fibres [176]. This effect is present in all the [NOvA](#) detectors. As can be seen, the attenuation fit is capable of fitting this irregular response and therefore the relative calibration corrects for this effect in data. However, zipped fibres are not included in simulation for any of the detectors, which could potentially cause discrepancy from data due to the [ADC](#) threshold. It was decided that this does not

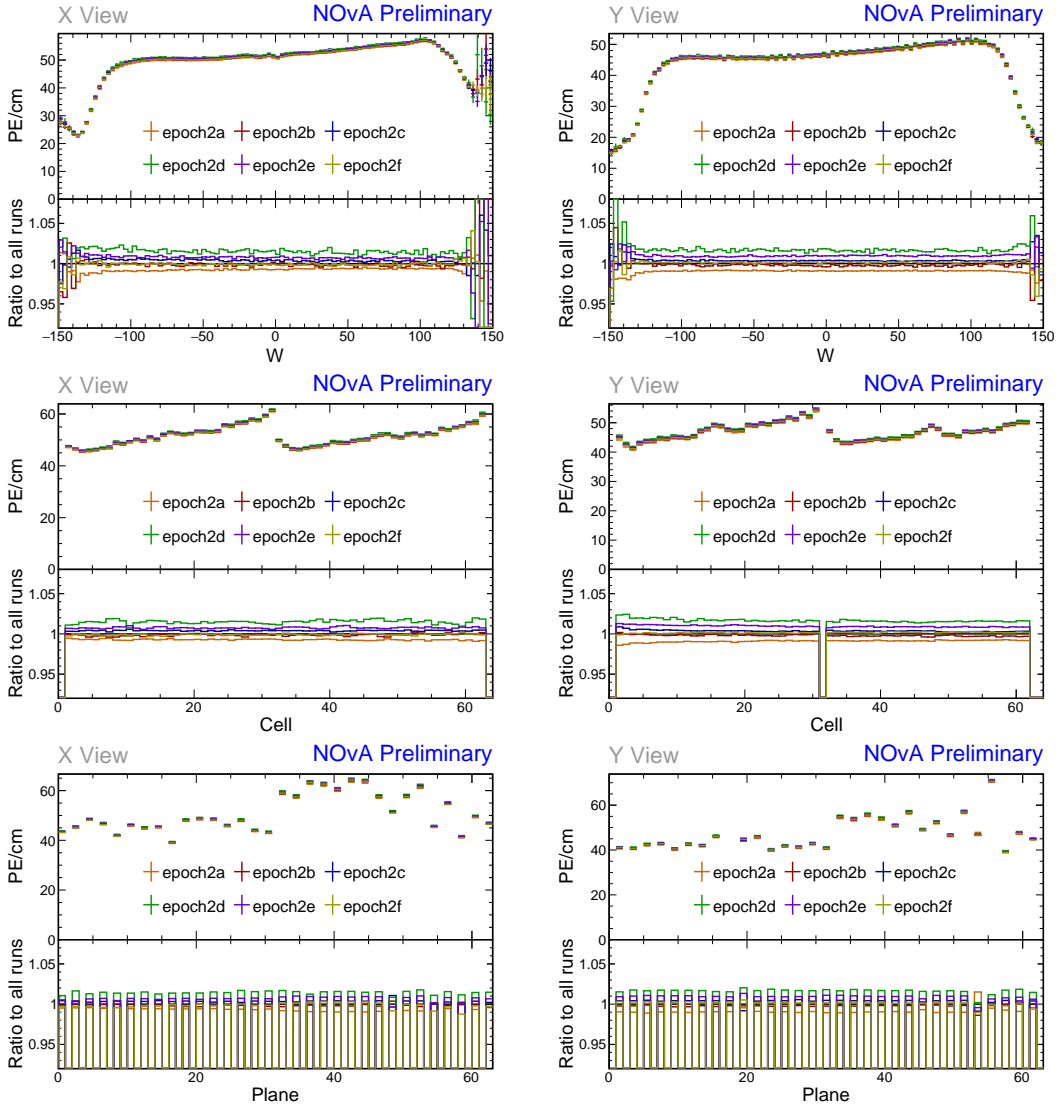


Figure 3.24: Uncorrected average energy response as a function of the position within a cell ( $w$  - top), cell number (middle), or plane number (bottom) for various epochs in the Test Beam detector period 2 data of cosmic muons hits selected for calibration. Left side shows distributions for the X view (vertical) planes and right side for the Y view (horizontal) planes. Each plot is a profile histogram, with uncertainties representing statistical variations. It is clear that there is no significant difference in shape between the various epochs. The one exception is plane 55, which has a visibly higher energy response than the rest of the planes, especially in epoch 2a, as can be seen in the bottom right plot.

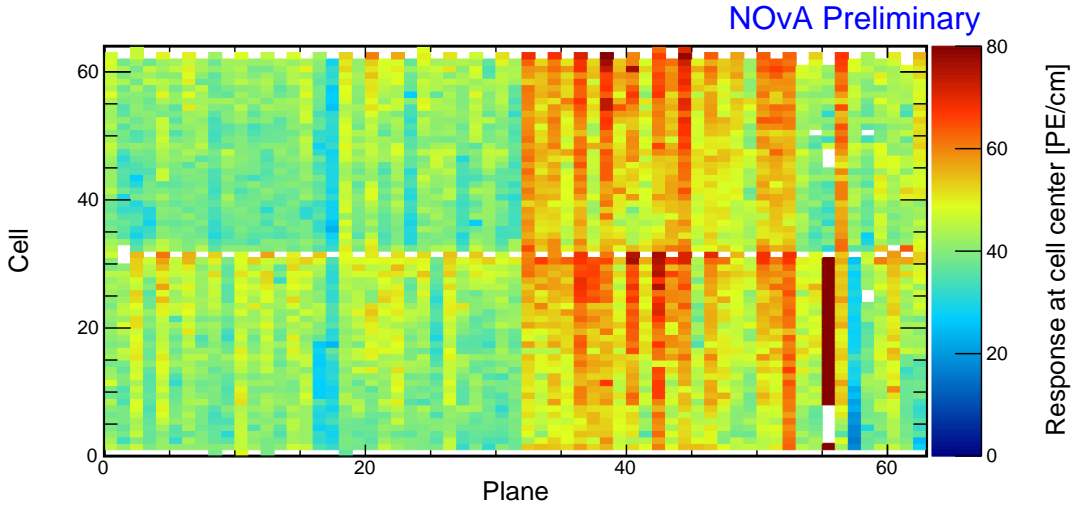


Figure 3.25: Overview of the attenuation fit results for the Test Beam detector period 2 data. Each cell represents the result of the attenuation fit to the energy response in the centre of that cell, with blank cells failing the calibration condition ( $\chi^2 > 0.2$ ). Cells 0 and 63, which are on the edges of the detector are mostly uncalibrated due to low statistics of calibration hits. Cell 31 and 63 in horizontal planes are underfilled, showing as rows of blank cells across the detector. This affects some of their neighbouring cells, such as cells 30 and 32 in plane 1, or cells 62 in all of the horizontal planes. Cells 0-31 for planes 55 and 57 have a visibly higher (plane 55) and lower (plane 57) energy response, caused by faulty FEBs, which for some time wrongly recorded scaled response. Cells 2-4 and 45-47 in plane 55 were dead for some time during period 2, resulting in failing the calibration condition. There are a few other uncalibrated cells, which are concentrated at the end of the detector (right hand side), which failed the calibration condition due to large fluctuations at cell edges.

Table 3.3: Summary of relative calibration results for period 2 with the uncalibrated cells divided into four categories based on the main reason of failure, all described in text.

<b>Calibration status</b>	<b>Number of cells</b>	<b>Detector proportion</b>
Calibrated	3833	95.06 %
Uncalibrated	121	3.00 %
	64	1.59 %
	9	0.22 %
	5	0.12 %

have a significant impact and it would not be worth the amount of work required to include all the zipped fibres into the simulation.

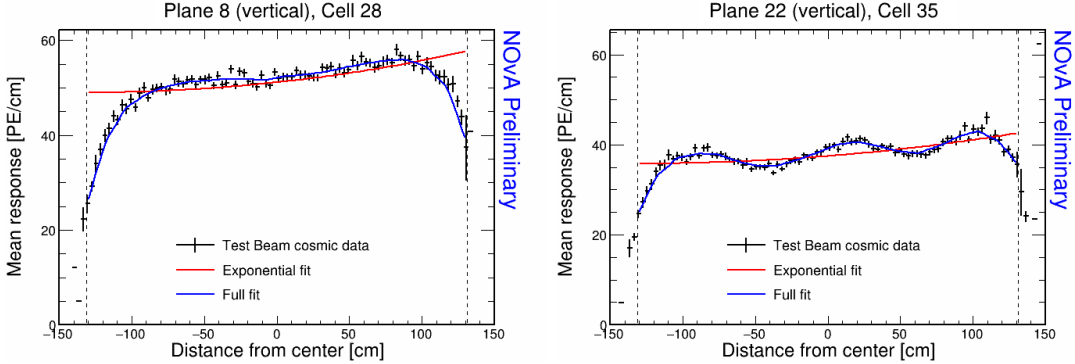


Figure 3.26: Attenuation fits for a selection of cells in period 2. Left plot shows an example of the standard energy deposition in the Test Beam and right plot shows the effect of zipped fibres.

The attenuation fits for the underfilled cells fail the calibration condition as expected. On the other hand, most of their neighbouring cells in the middle of the detector (cells 30 and 32) successfully pass the calibration condition despite having fewer events. This is thanks to the decision to label the underfilled cells as bad channels, as shown in Fig. 3.27. However, it appears that some cells neighbouring the underfilled cells near the edge of the detector have too few events to have satisfactory attenuation fits.

The effects of the issues with dead channels and with faulty readout electronics occurring during period 2, which were discussed above, can be clearly seen on the map of the attenuation fit results in Fig. 3.25 and on the attenuation fits themselves in Fig. 3.28. The (temporarily) dead channel in plane 55 contains too few events to pass the calibration condition. However, the channel in plane 48 was likely dead for a shorter duration, resulting in a successful attenuation fit, despite the lower number of hits compared to a standard cell. Cells corresponding to the entire readout affected have lower number of hits, resulting in some of them having attenuation fits failing the calibration condition. Furthermore, these cells have a strikingly different energy response, even  $3\times$  larger than the average in the case of plane 55. This is due to the corresponding [APDs](#) or [FEBs](#) incorrectly recording a scaled-up or scaled-down energy response than the real energy deposited in the detector. The cause for this scaled recorded response is not known. Since this effect is present for all data, not only for the cosmic muons used for calibration, it is important to correctly account

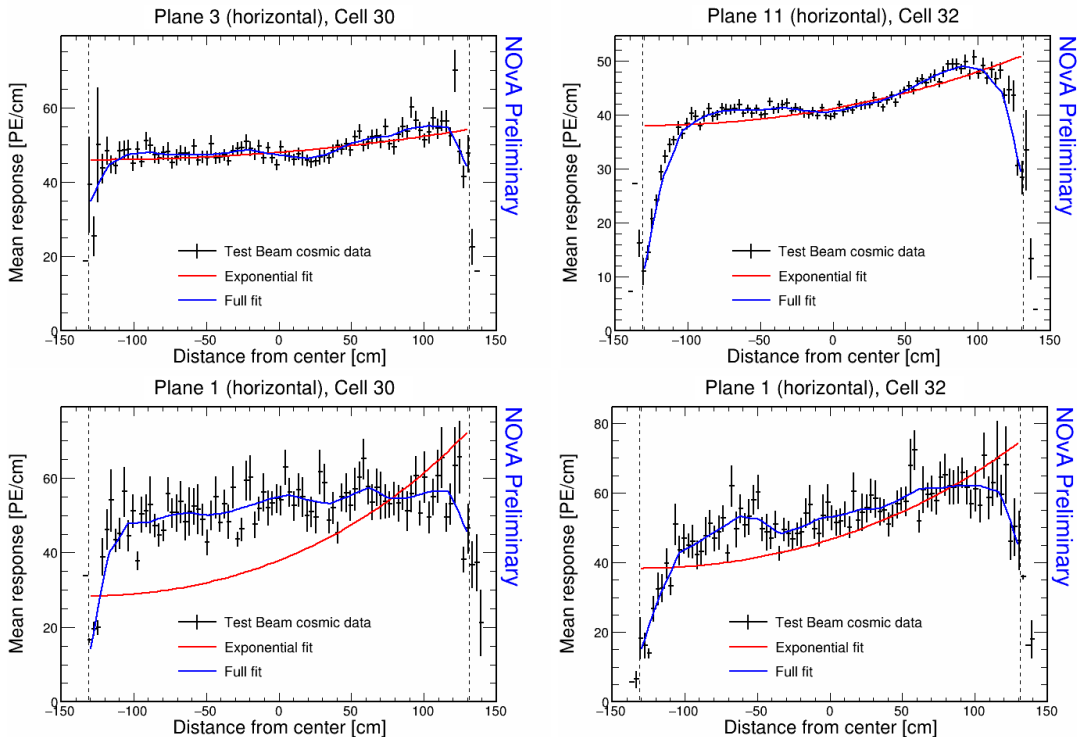


Figure 3.27: Fit to the energy response in period 2. Showing examples of cells neighbouring the underfilled cells which have fewer events and therefore larger fluctuations than the ‘usual’ Test Beam cell. Bottom two plots show examples of neighbouring cells to the underfilled cells, specifically in plane 1, which failed the calibration condition due to low statistics. This is a result of the combined effect of being a neighbour to the underfilled cell and on the edge of the detector.

for it in calibration. However, there is a reason for concern, as this issue can arise even if these FEBs (or possibly APDs) were only affected for a limited time out of the entire calibrated period. Since we are performing the attenuation fits on the average response across the entire calibrated period, if an FEB records a standard response for half of the time and  $7\times$  larger response for the second half, calibration is going to assume the response was  $4\times$  larger the entire time, which would be incorrect. However, since both of the affected planes are in the back of the detector, we decided to ignore this effect for period 2.

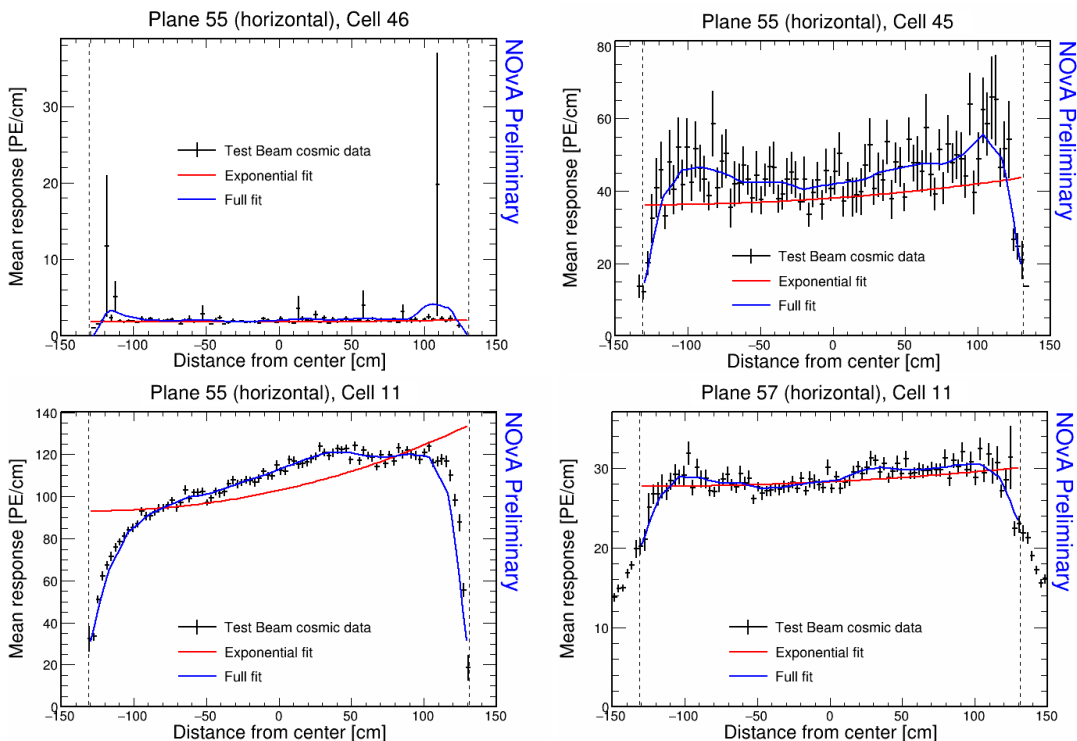


Figure 3.28: Fit to the energy response in period 2. Some channels were likely dead for some time, resulting with significantly less recorded events as shown on the top left plot. This also affect their neighbouring cells due to the tricell condition as shown on the top right. Planes 55 and 57, shown on the bottom left and bottom right plots respectively, correspond to one of the ‘faulty’ FEBs affected for some time. This results in a significantly different scale of energy response, which is much higher than the rest of the detector for plane 55, and smaller for plane 57.

An unexpected issue appeared for several cells located near the end of the Test Beam detector (relative to the beam). These cells have attenuation fits failing the calibration condition due to the unusually high response or a lack of events in histogram bins at the edges of the cell, as shown in Fig. 3.29. This is a combination of a real physical effect - caused by fewer hits at the edge of the detector, possibly also due

to the fibre loops and fibre ends - and of the choice of binning for the attenuation profiles. All attenuation profiles for all the **NOvA** detectors are created with 100 bins, extending beyond the physical dimensions of the detector. For example, in the Test Beam detector, the attenuation profiles range from  $-150\text{ cm}$  to  $150\text{ cm}$ , while the actual half-length of a Test Beam cell is  $131.07\text{ cm}$ . This means that the attenuation profile bins near the physical edges of the cell contain fewer hits from inside of the detector, resulting in larger fluctuations. Since the attenuation fits are limited to the physical cell boundaries, these bins with larger variations can skew their results. This effect can be addressed either by changing the binning of the attenuation profiles to better match the physical dimension of the cell, by loosening the calibration condition for hits on the edges of the cell, or using larger samples for the attenuation fits to reduce variations. However, since the affected uncalibrated cells are in the end of the detector, we decided to ignore them.

### 3.3.5 Period 3 data

The underfilled cells were refilled (or overfilled) during the period 3 data taking. This was the main motivation for dividing period 3 into individual epochs as shown in Tab. 3.4. Another major event that could impact calibration is the replacement of several faulty **FEBs**, which motivated the creation of epoch 3e.

Table 3.4: Test Beam period 3 epochs, their start dates and the reason for their separation.

Name	Start date	Reason for creating the epoch
Epoch 3a	January 12 <sup>th</sup> 2021	Underfilled cells
Epoch 3b	April 21 <sup>st</sup> 2021	Overfilling the back 9 horizontal planes and the 7th horizontal plane from the front
Epoch 3c	April 27 <sup>th</sup> 2021	Overfilling of the 15 front horizontal planes (except the 7th, which was already done) and the 14th horizontal plane
Epoch 3d	April 30 <sup>th</sup> 2021	Overfilling of the remaining 8 horizontal planes
Epoch 3e	May 12 <sup>th</sup> 2021	FEB swaps

The refilling of the underfilled cells can be clearly seen on the cell and plane distribution of hits in Fig. 3.30 and on the distribution of energy deposition across hori-

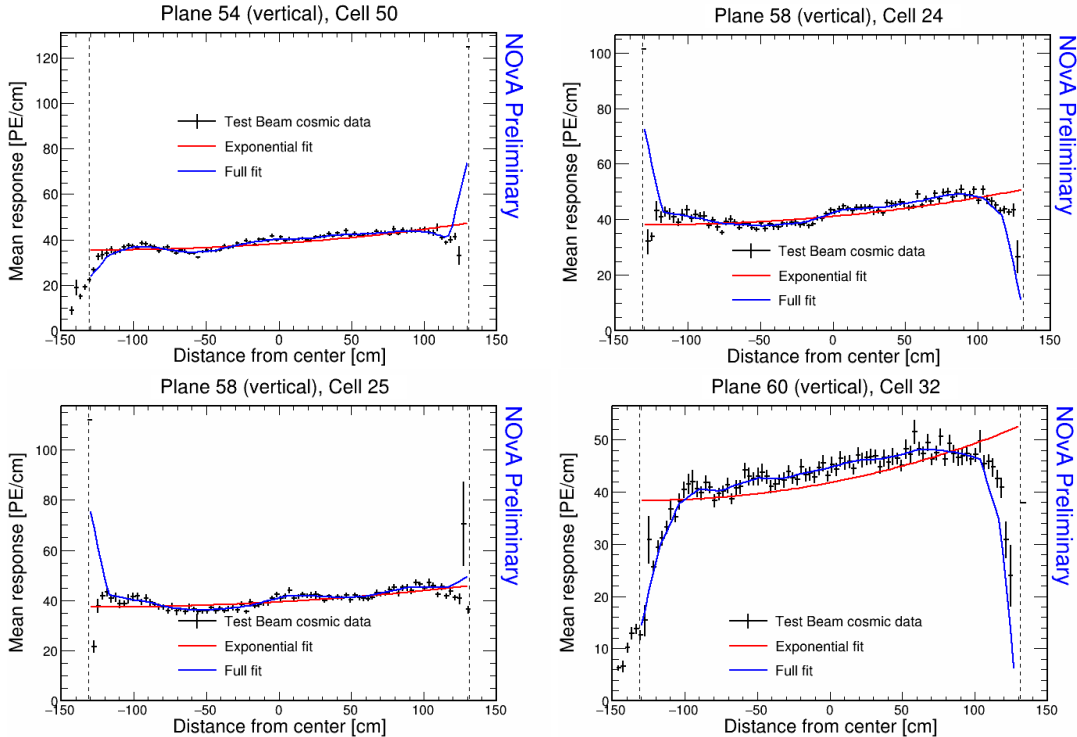


Figure 3.29: Fit to the energy response in period 2. Examples of cells that have an unusually high or low energy response at the edge of the cell, skewing the attenuation fits and resulting in them getting labelled as not calibrated. Cells shown on the two top plots and on the bottom left plot have a single bin on the edge of the fitted region (marked by dotted vertical lines) with noticeably higher average energy response. These anomalous bins typically only have a single entry that skews that attenuation fits and their  $\chi^2$  calculations. Cell 32 in plane 60, shown in the bottom right plot, has bins on the edge of the cell with no entries, resulting in the same effect as the other cells mentioned above.

zontal (Y view) cells in Fig. 3.31. The distributions of hits also shows a few channels that were dead for a certain time. Additionally, the energy deposition distributions show, that one of the FEBs was recording a scaled up/down energy response, similarly to the faulty FEBs in period 2. However, a can be seen in the distribution of hits, this particular faulty FEB recorded the same number of events as were recorded in the surrounding modules. This is one of the FEB that got replaced between epochs 3d and 3e and, as will be shown below, this is the FEB with the largest impact on the calibration out of the faulty FEBs replaced before the start of epoch 3e.

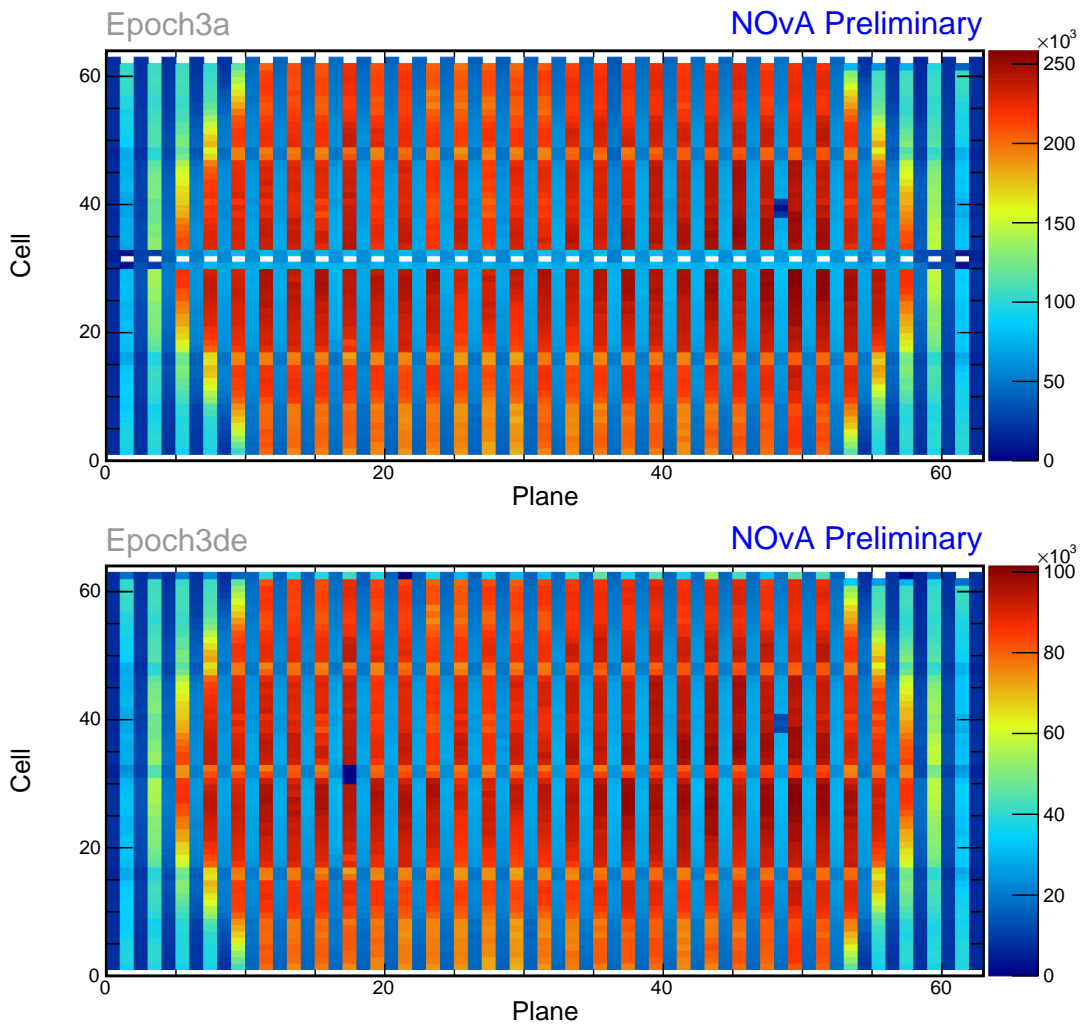


Figure 3.30: Distribution of events in the period 3 Test Beam data calibration sample. Comparison of the epoch 3a data before the refilling of the underfilled cells 31 and 63, clearly visible by a row of empty bins, and the combination of epochs 3d and 3e after the full refilling. There are also several cells that experienced readout issues, specifically cell 39 in plane 48 and cell 31 in plane 18.

From the aforementioned considerations, we decided to calibrate epochs 3a, 3b and 3c together, which are all the epochs containing any underfilled cells, and to

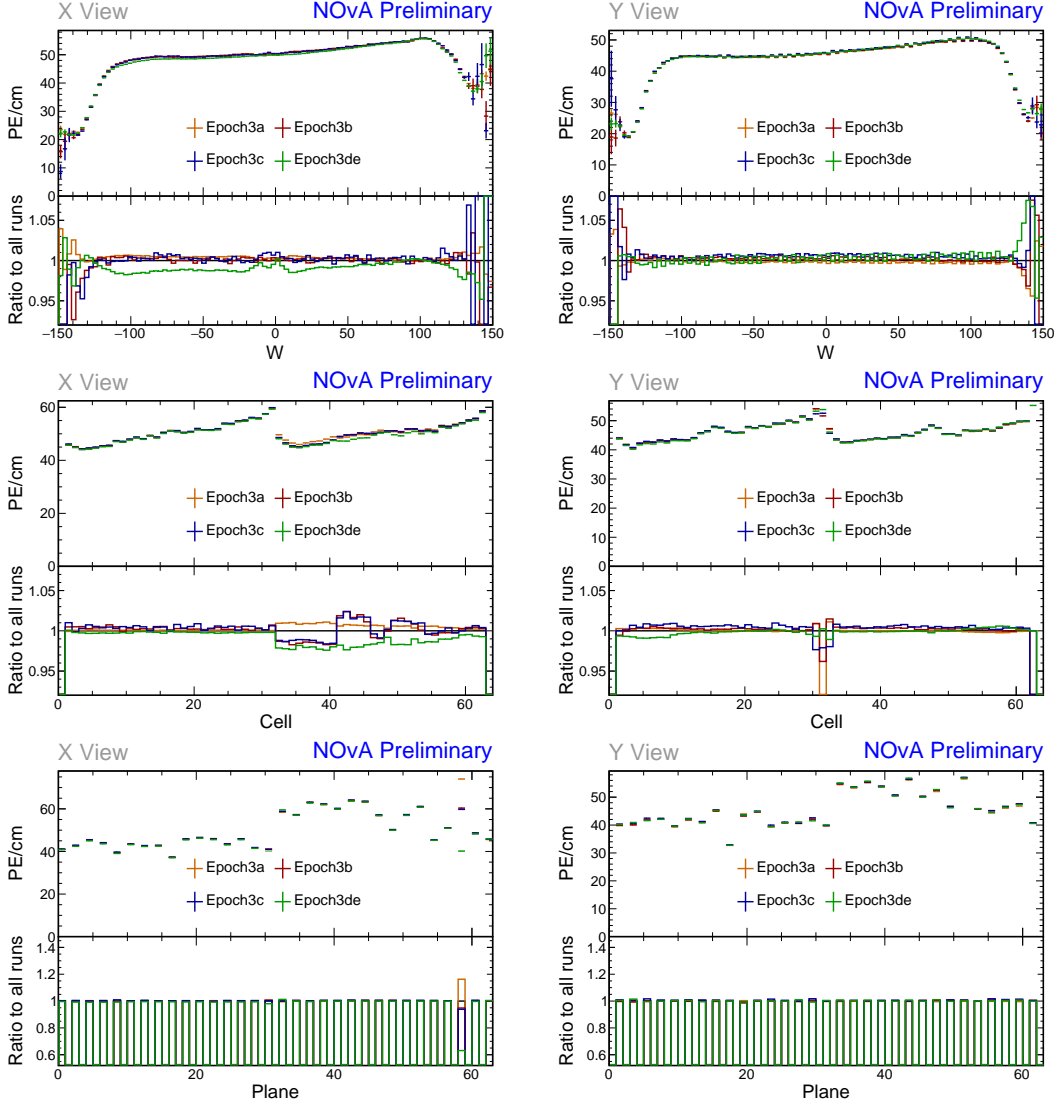


Figure 3.31: Uncorrected average energy response as a function of the position within a cell ( $w$  - top), cell number (middle), or plane number (bottom) for various epochs in the Test Beam detector period 3 data of cosmic muons hits selected for calibration. Left side shows distributions for the X view (vertical) planes and right side for the Y view (horizontal) planes. Each plot is a profile histogram, with uncertainties representing statistical variations. The effect of staged refilling of the underfilled cells between the epochs can be seen in the middle right plot, where epoch 3a (orange) has all no underfilled cells refilled, and epochs 3d and 3e (green) have all the cells filled to the top. Comparing the distributions of energy deposition in X view between the cell and plane plots, it can be seen that the top FEB/APD in plane 58, which correspond cells 32-63, was faulty throughout period 3. Specifically, that the energy response in this module was larger in epoch 3a, then got lower in epochs 3b and 3c, until getting significantly lower for epochs 3d and 3e.

separately calibrate epochs 3d and 3e together. The faulty FEB in the top of plane 58 is far enough in the back of the detector, that we didn't find it necessary to calibrate epochs 3d and 3e separately. Additionally, epochs 3b and 3c contain only few days worth of data, therefore they wouldn't have enough events for successful independent attenuation fits.

### Combined epochs 3a, 3b and 3c relative calibration results

The results of attenuation fits for the combined epochs 3a, 3b and 3c are summarised in Fig. 3.32, showing the map of the fitted response at the centre of each cell. There are 182 uncalibrated cells out of 4032, constituting 4.51% of the detector, as shown in Tab. 3.5.

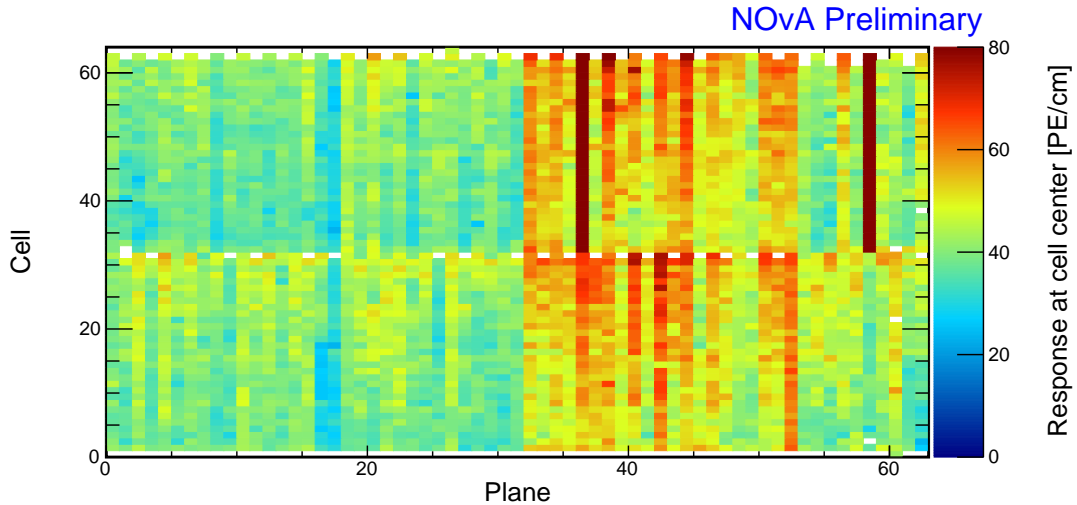


Figure 3.32: Overview of the relative calibration results for the Test Beam detector period 3, combined epochs 3a, 3b and 3c data. Each cell represents the result of the attenuation fit to the energy response in the centre of that cell. The blank bins represent uncalibrated cells. The rows of uncalibrated cells 31 and 62 are caused by the underfilled cells together with the tricell condition. The same effect affects cell 32 in plane 1. The two dark-red stripes correspond to two faulty FEBs in planes 36 and 58. There are five additional uncalibrated cells, specifically cell 2 in plane 58, cells 21 and 32 in plane 60, and cells 31 and 38 in plane 63, which are uncalibrated due to large fluctuations at cell edges.

We can see that some of the underfilled cells that have been refilled for epochs 3b or 3c, but were underfilled for epoch 3a, which makes up the majority of this calibrated data, are now calibrated thanks to including these two short epochs into the same attenuation fit. Example of energy deposition in such a cell is shown on the left side of Fig. 3.33. Same as in period 2, most of the neighbouring cells to the

Table 3.5: Summary of relative calibration results for the combined epochs 3a, 3b and 3c with the uncalibrated cells divided into four categories based on the main reason of failure, all described in text.

Calibration status	Number of cells	Detector proportion
Calibrated	3850	95.49 %
Uncalibrated	128	3.17 %
	49	1.22 %
	0	0.00 %
	5	0.12 %

underfilled cells are calibrated, except for cells on the edge of the detector due to lower statistics.

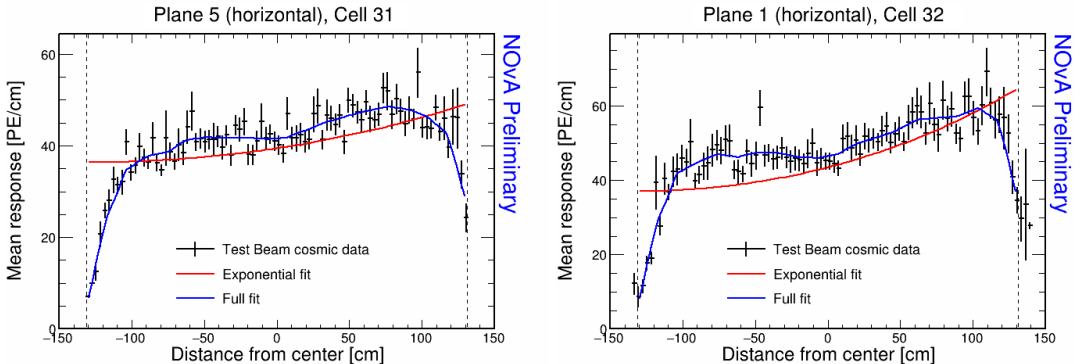


Figure 3.33: Fit to the energy response in epochs 3a, 3b and 3c. Some underfilled cells that have been refilled in epochs 3b and 3c are now calibrated as shown on the left plot. Cell 32 in plane 1 is the only neighbouring cell to the underfilled cell that didn't manage to get calibrated due to low number of events.

There is a couple of noticeably faulty FEBs with a scaled energy response, shown in Fig. 3.34. Besides the expected FEB in plane 58, which has about  $5\times$  larger response, there is also the FEB in plane 36, which has about  $2.5\times$  larger response compared to the average. This could mean that the FEB in plane 36 was faulty only for a limited time compared to the FEB in plane 58. This is a reason for concern, as the relative calibration correction for hits in this module, during the time when the FEB wasn't faulty, would be too large (and therefore the ‘corrected response’ would be too small). On the other hand, during the time when the FEB was faulty, the correction would be too small and hence the corrected response would be too large. Given that plane 36 is in the middle of the detector, there is a chance this might noticeably affect some Test Beam analysis results. Therefore, it is possible this issues might have to be mitigated

in the future, whether with an additional uncertainty, or by improving the calibration. It is currently difficult to address issues such as this in the NOvA calibration. However, there is currently an effort underway to split the inputs for calibration by cells, rather than by time, which would make solving these issues much simpler. For the time being, we decided to ignore these faulty FEBs.

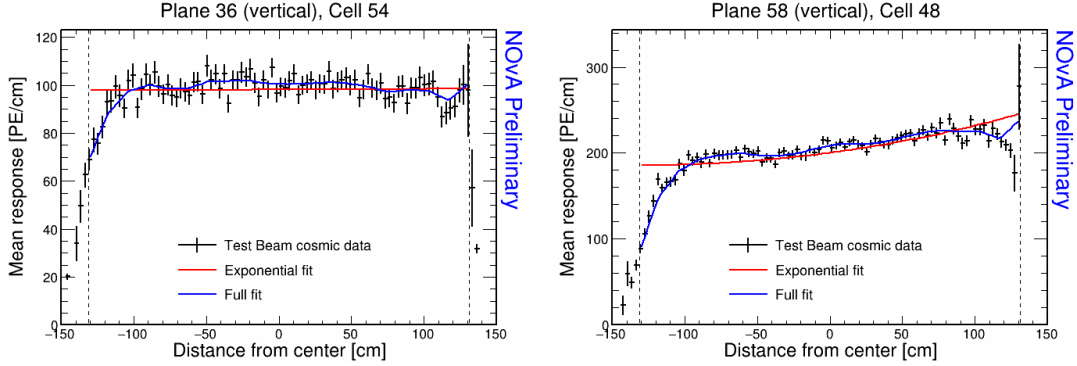


Figure 3.34: Fit to the energy response in epochs 3a, 3b and 3c. The most obvious faulty FEBs that have a significantly larger energy response than their neighbours.

Similarly to period 2, there are a few cells in the back of the detector that have a sharp rise in energy response at their edge, which causes their attenuation fit to fail the calibration condition. This can be seen in Fig. 3.35, where the significantly different mean responses at the edge bins is pulling the attenuation fit to incorrect values. Given this is concentrated in cells in the end of the detector, we decided to ignore this effect and leave these cells uncalibrated.

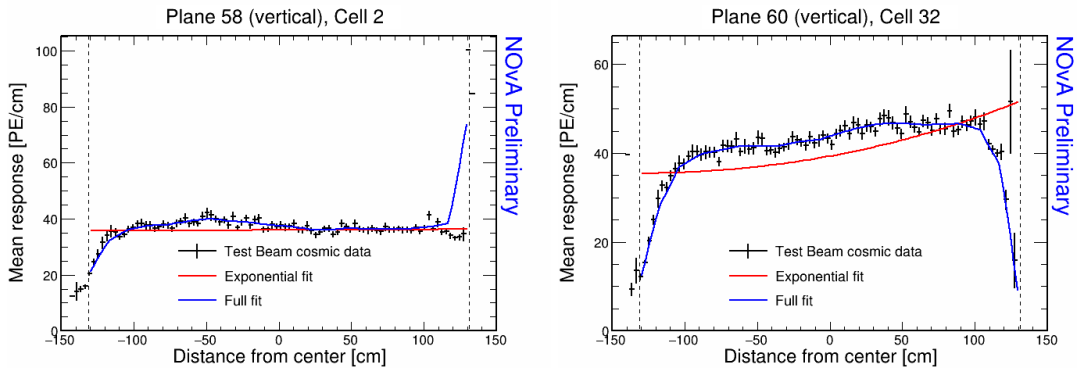


Figure 3.35: Fit to the energy response in epochs 3a, 3b and 3c. Some cells are not calibrated due to large fluctuations at one edge of the cells.

### Combined epochs 3d and 3e relative calibration results

The attenuation fits results for epochs 3d and 3e are shown in Fig. 3.36. There are 182 uncalibrated cells out of 4032 total cells, making up 4.51% of the detector. The uncalibrated cells are now however almost entirely concentrated at the edges of the detector. Summary of the relative calibration results is shown in Tab. 3.6.

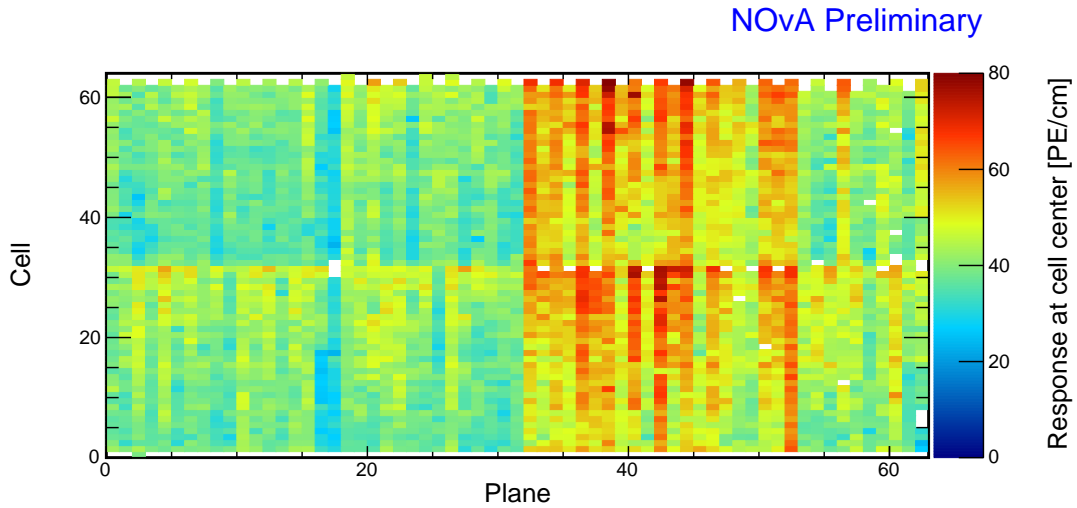


Figure 3.36: Overview of the relative calibration results for the Test Beam detector period 3, combined epochs 3d and 3e data. Each cell represents the result of the attenuation fit to the energy response in the centre of that cell. The blank cells are uncalibrated. The uncalibrated cells 30-32 in plane 17 and cells 5-7 in plane 63 are caused by a dead channel coupled with the effect of the tricell condition. The 8 previously underfilled cells 31 in planes 33, 35, 37, 41, 47, 49, 51 and 59 are uncalibrated due to the difference in the scintillator used for refilling, as described in text. There are 11 cells that are uncalibrated due to low number of events combined with the attenuation profile binning.

The expected effect of one of the two dead channels is shown in Fig. 3.37 together with some of the cells in the back of the detector, which have a rise or drop in energy deposition at their edge. This is similar to the effects seen in period 2 and epochs 3a+3b+3c and since it's again concentrated in the end of the detector, we ignore these cells and leave them uncalibrated.

Epochs 3d and 3e should have all the previously underfilled cells now refilled, but as can be seen in Fig. 3.36, there are several of these previously underfilled cells that are still uncalibrated. The energy deposition in these cells is shown in Fig. 3.38. Here we can see that these cells have a fairly large discrepancy between the left and right sides of the cell. This is caused by using different scintillator oils for the initial filling and for the refilling (or overfilling). Specifically, as was described in Sec. 3.1, these

Table 3.6: Summary of relative calibration results for the combined epochs 3d and 3e with the uncalibrated cells divided into four categories based on the main reason of failure, all described in text. Brackets show the number of cells that were originally calibrated (or uncalibrated, depending on the row) before the manual alteration of their  $\chi^2$  values, as described in text. Proportions are calculated from the final cell counts.

<b>Calibration status</b>	<b>Number of cells</b>	<b>Detector proportion</b>
Calibrated	3858 (3850)	95.68 %
Uncalibrated	Peripheral cells	3.13 %
	Underfilled cells	0.77 %
	Readout	0.15 %
	Binning	0.27 %

cells have been initially filled with the Ash River oil, or with the Texas oils, depending on the cell, which have a higher energy response compared to the NDOS oil that was used for their overfilling. These scintillator oils clearly did not mix properly, which caused a discrepancy in the energy deposition in different parts of the cells. This is a physical effect that should be accounted for in calibration, and, as we can see, the attenuation fits are actually performing reasonably well. Additionally, these cells are in the middle of the detector and leaving them uncalibrated would almost certainly have an impact on Test Beam analyses. The large  $\chi^2$  value of the attenuation fit is most likely caused only by the unusual shape of the distribution, which the fit is not designed for. Therefore, we decided to manually change the  $\chi^2$  values for these cells inside the csv tables (which hold the results of the attenuation fits), so that their  $\chi^2 < 0.2$  and these cells are officially considered calibrated when applying the calibration results, even if they originally weren't. The map of the 'corrected' distribution of the attenuation fit results for epochs 3d and 3e is shown in Fig. 3.39.

### 3.3.6 Period 4 data

The data collected during period 4 of the Test Beam run represent our best dataset, with nearly ideal detector conditions. There were a few commissioning runs in the very beginning of period 4, which uncovered some dead channels or faulty FEBs that were immediately fixed. These initial runs constitute epoch 4a, shown on the top of Fig. 3.40. Additionally, a few runs included studies where parts of the detector

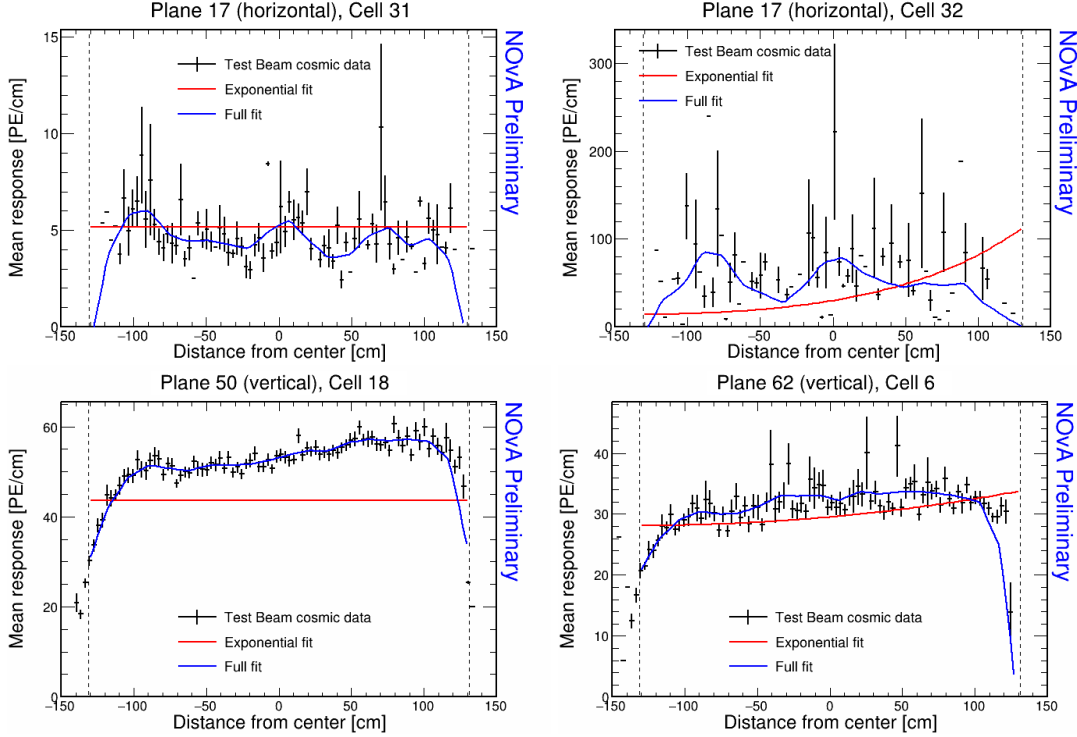


Figure 3.37: Fit to the energy response in epochs 3d and 3e. Top plots show the dead channel (left) and its immediate neighbour (right) affected by the tricell condition. Bottom plots show examples of cells with large fluctuations on their edges likely caused by low number of events combined with binning of attenuation profiles.

were masked to address FEB saturation issues [177], clearly visible in the middle of Fig. 3.40. The bottom part of Fig. 3.40 shows the remainder of period 4 data, which do not have any noticeable faults in their hit distribution across the detector.

Figure 3.41 shows, that the epoch 4a and the cell masking study had noticeable impacts on the energy deposition across the detector. Both of these special periods only span a short time and therefore contain very limited number of hits. We decided to ignore these runs and only calibrate the rest of period 4 data, using their results for all runs in period 4.

### Period 4 relative calibration results

Results of the attenuation fits for period 4 are summarised in Fig. 3.42 and Tab. 3.7. We can see that almost the entire detector is now calibrated, with only few exceptions on the edges of the detector and a single cell with an unusually high response at the edge (right plot of Fig. 3.43). We treated the formerly underfilled cells the same way as in epochs 3d and 3e, manually changing the  $\chi^2$  of their attenuation fits inside the csv

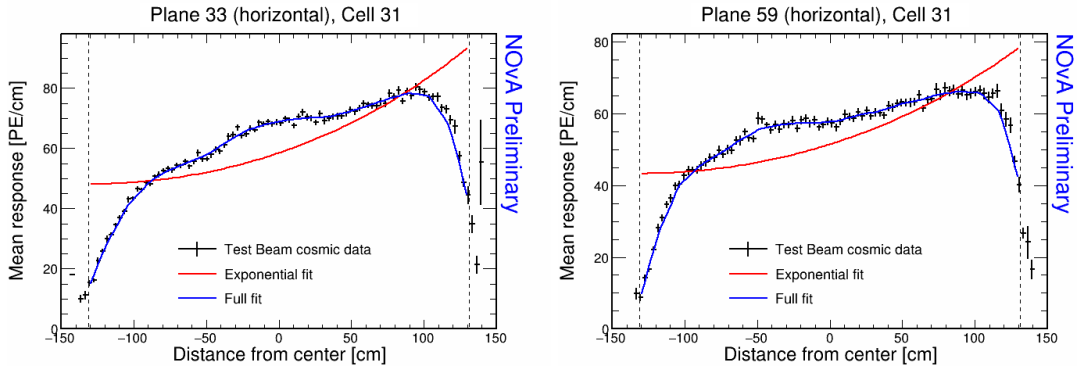


Figure 3.38: Fit to the energy response in epochs 3d and 3e. The scintillator oil used for refilling of the underfilled cells has lower energy response than the oil used for the initial filling. These oils didn't mix properly causing a different energy response in the left and right side of the cell.

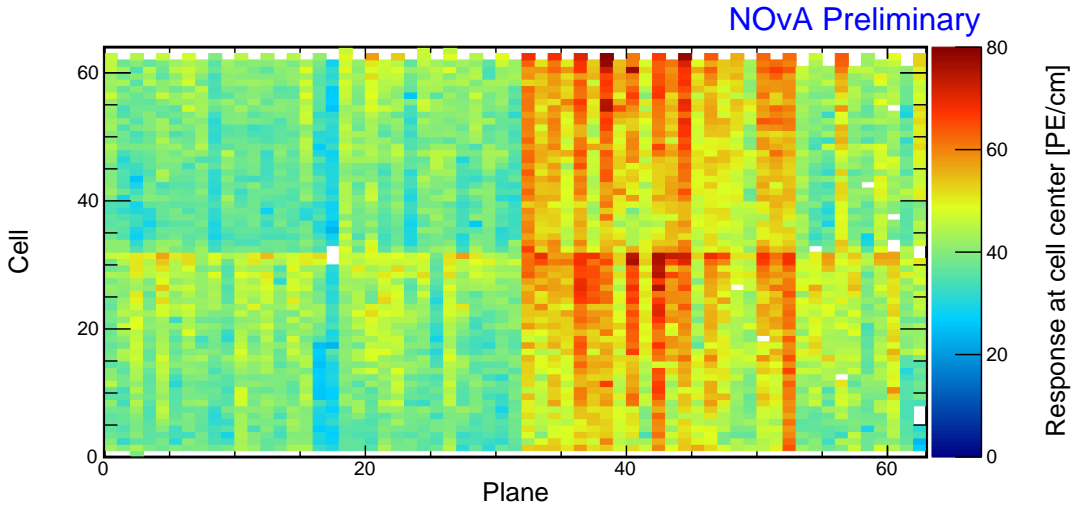


Figure 3.39: Overview of the final relative calibration results for the combined epochs 3d and 3e data after manually labelling the originally uncalibrated refilled cells as calibrated. Each cell represents the result of the attenuation fit to the energy response in the centre of that cell. The blank cells are uncalibrated and described in text.

files to  $< 0.2$ , therefore making them officially calibrated. There are 108 uncalibrated cells out of 4032, totalling 2.68% of the detector.

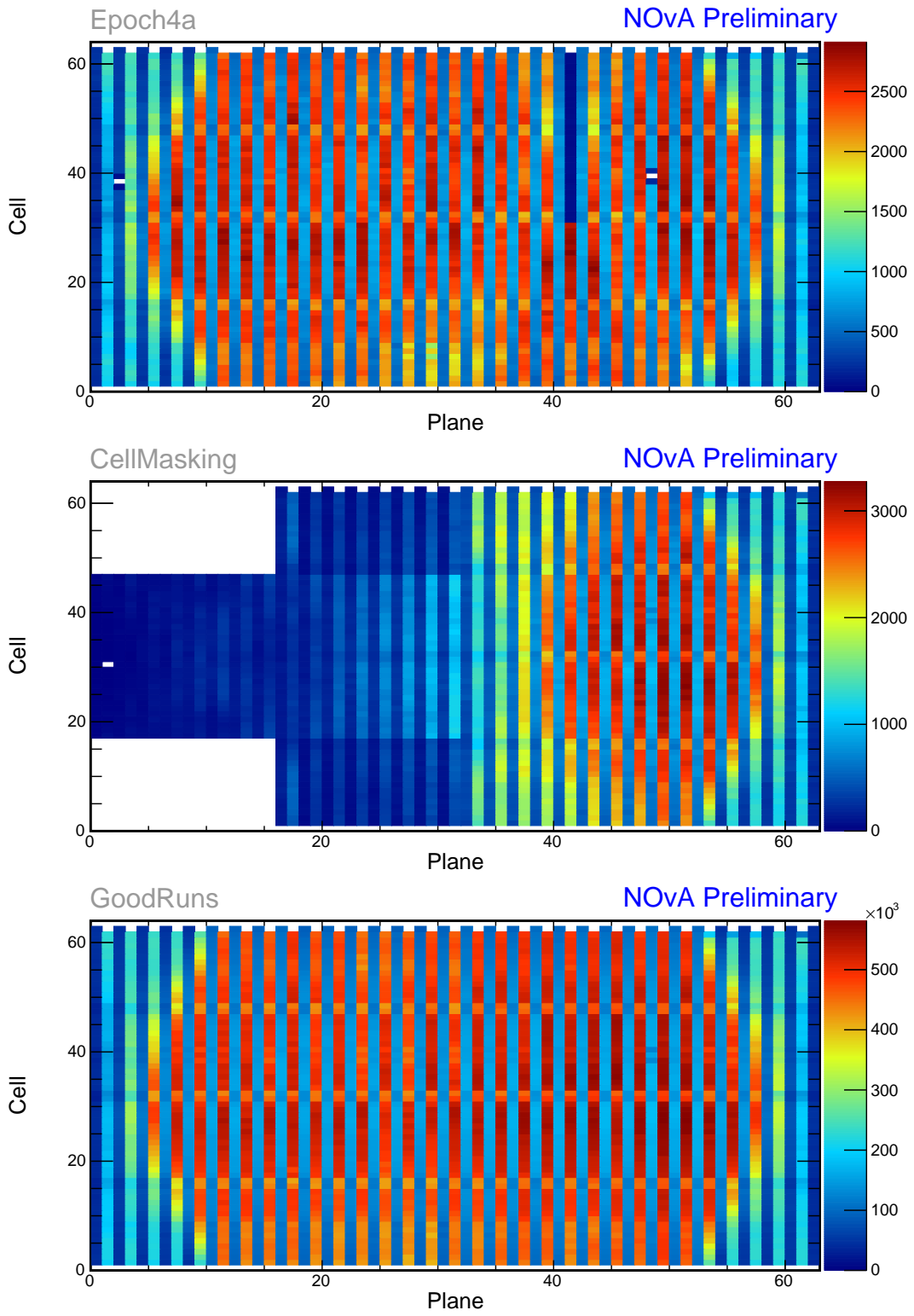


Figure 3.40: Distribution of events in the Test Beam period 4 data calibration sample. The top plot shows the first three commissioning runs with readout issues, the middle plot shows the status of the detector during the cell masking studies and the bottom plot shows the rest of the runs. Only the runs from the bottom plot (marked GoodRuns) are used for calibration.

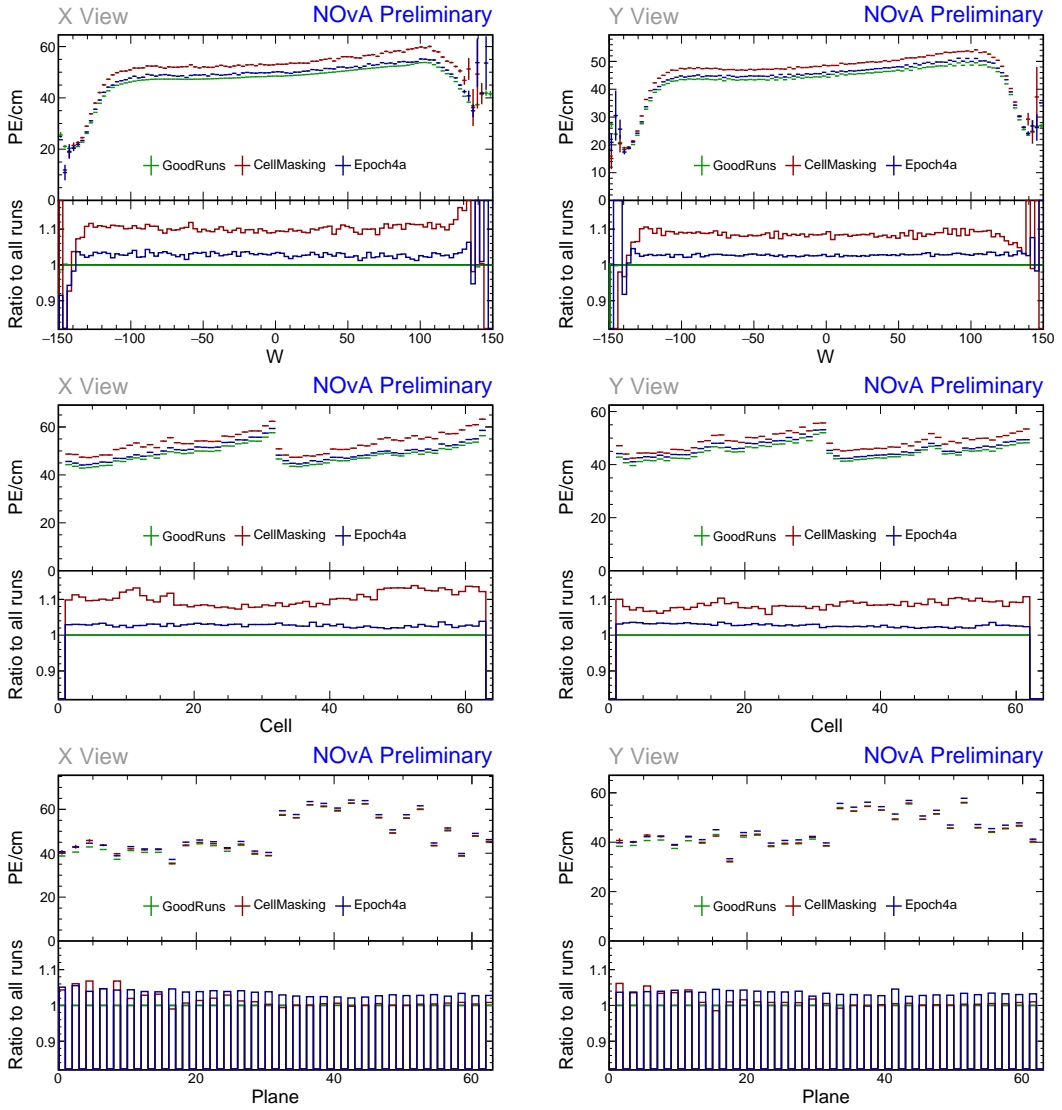


Figure 3.41: Uncorrected average energy response as a function of the position within a cell ( $w$  - top), cell number (middle), or plane number (bottom) for the Test Beam detector period 4 data of cosmic muons hits selected for calibration. Left side shows distributions for the X view (vertical) planes and right side for the Y view (horizontal) planes. Each plot is a profile histogram, with uncertainties representing statistical variations. The commissioning runs in epoch 4a and the runs during the cell masking studies have a visibly different energy deposition across all the shown variables compared to the rest of the period 4 runs.

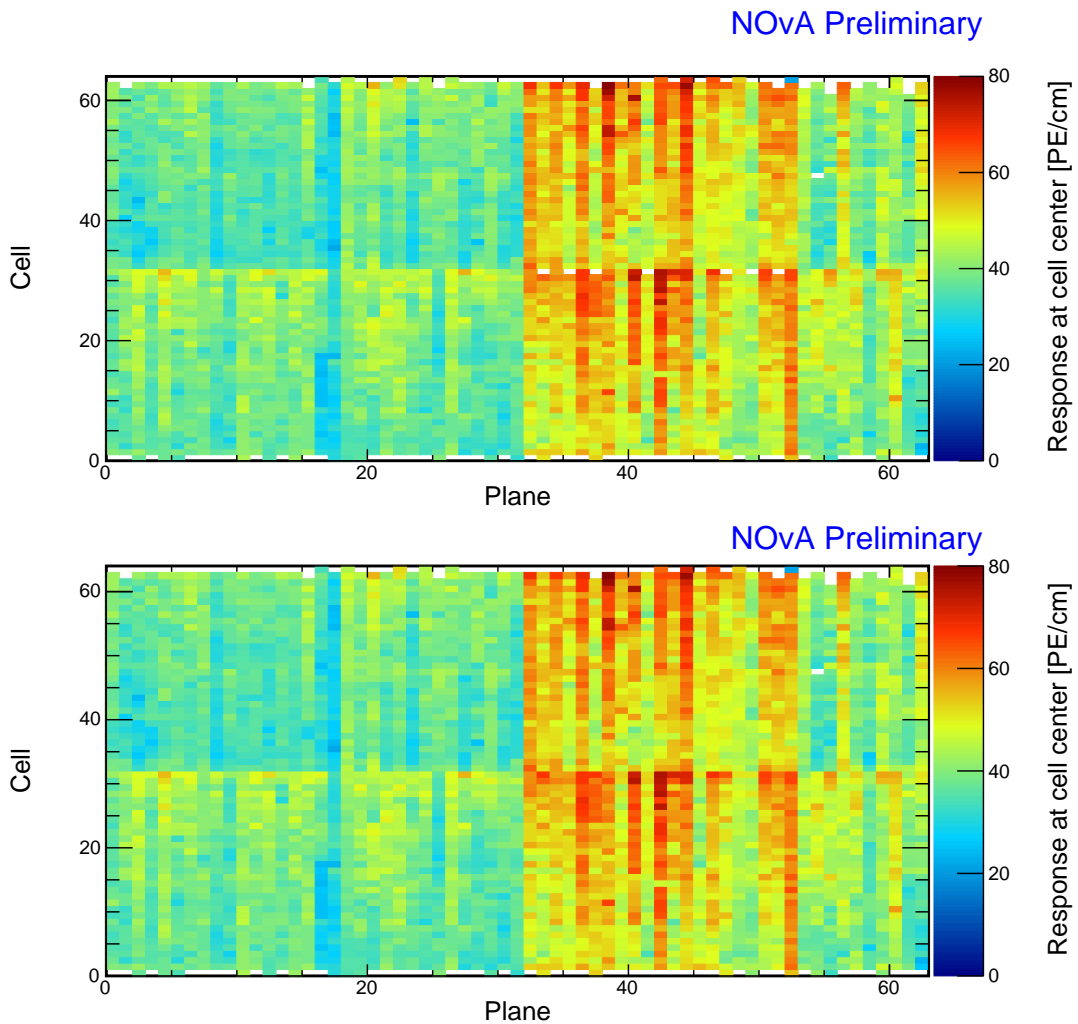


Figure 3.42: Overview of the relative calibration results for the Test Beam detector period 4 data. Top plot shows the results of the attenuation fit and bottom plot shows the final result for period 4 after manually labelling the originally uncalibrated refilled cells as calibrated. Each cell represents the result of the attenuation fit to the energy response in the centre of that cell. The blank cells are uncalibrated. The uncalibrated cells are concentrated on the edge of the detector, with a single cell 47 in plane 54 with an unusually high response at the edge of the cell. The 7 previously uncalibrated cells in the middle of the detector were artificially marked as calibrated after careful considerations.

Table 3.7: Summary of relative calibration results for period 4 with the uncalibrated cells divided into four categories based on the main reason of failure, all described in text. Brackets show the number of cells that were originally (un)calibrated before the manual alteration of their  $\chi^2$  values, as described in text. Proportions are calculated from the final cell counts.

Calibration status	Number of cells	Detector proportion
Calibrated	3924(3917)	97.32 %
Uncalibrated	97	2.41 %
	10(17)	0.25 %
	0	0.00 %
	1	0.02 %

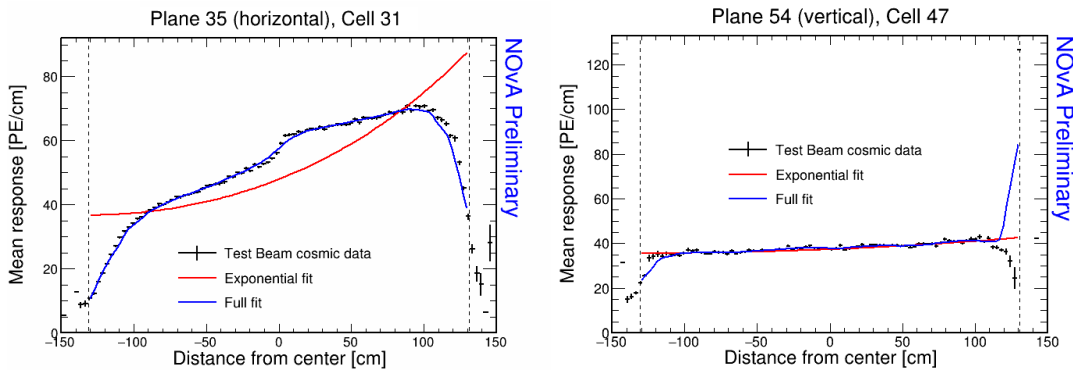


Figure 3.43: Fit to the energy response in period 4. Previously underfilled cells refilled with a scintillator of a different quality causing an unusual distribution of energy deposition (left). Unusually high energy response at the edge of the cell 47 (right).

### 3.3.7 Absolute calibration results

The results of the relative calibration (without the threshold and shielding correction) are applied to the stopping muon sample to calculate the absolute energy scale, which translates the energy response from  $\text{PECorr}$  to GeV, as described in Sec. 2.6. We apply the absolute calibration cuts to select minimum ionising muons, which represent a very well understood source of energy deposition. The absolute calibration cuts are mostly the same as for the other NOvA detectors, selecting hits 1 – 2 m from the end of their tracks and removing uncalibrated and wrongly reconstructed hits by requiring non-zero path lengths,  $\text{PE} > 0$ ,  $\text{PECorr} > 0$ , as well as  $\text{PECorr}/\text{cm} < 100$ . Additionally, we constrain  $w$  to a smaller allowed range:  $-80 < w < 80$  cm, reflecting the smaller Test Beam cell length, removing hits approximately 0.5 m from each side of the detector.

Distributions of reconstructed and true energy responses, for both views, and for each data and simulation sample, are shown in Fig. 3.44. The mean of each of these distributions constitute the  $\text{MEU}_{\text{Reco}}$  or  $\text{MEU}_{\text{True}}$  values for both views. We calculate the statistical uncertainty on the  $\text{MEU}$  values as the standard deviation of the corresponding distributions divided by the square root of the number of entries. To combine the result from the two views, we take the average over the view-dependent  $\text{MEU}$  values to obtain the final  $\text{MEU}$  value for each sample. This is the first time in the calibration chain where the two views, which were treated completely independently so far, are combined together. The uncertainties are added in the sum of squares. The total number of entries, the  $\text{MEU}$  values for each sample and view, as well as the combined  $\text{MEU}$  values with corresponding statistical uncertainties are shown in Tab. 3.8. Given the large number of entries in the energy response distributions, the statistical uncertainties on the  $\text{MEU}$  values are negligible (around 0.05%). This are however not the final uncertainties of the absolute energy scale used in NOvA. Instead, we use comparison to other standard candles, as was explained in Sec. 2.8.

Table 3.8: Summary of absolute calibration results.  $\text{MEU}_{\text{Reco}}$  values (top table), including the statistical uncertainty  $\sigma_{\text{MEU}_{\text{Reco}}}$ , are in units of  $\text{PECorr}/\text{cm}$  and  $\text{MEU}_{\text{True}}$  values (bottom table) are in units of  $\text{MeV}/\text{cm}$

Sample		X view		Y view		Combined	
		NHits	MEU	NHits	MEU	$\text{MEU}_{\text{Reco}}$	$\sigma_{\text{MEU}_{\text{Reco}}}$
Data	Period 2	2.322e+05	38.70	1.413e+06	39.40	39.05	0.02
	Epochs 3abc	2.638e+05	38.49	1.621e+06	39.40	38.94	0.02
	Epochs 3de	1.049e+05	38.63	6.725e+05	39.42	39.02	0.03
	Period 4	5.268e+05	38.63	3.316e+06	39.40	39.01	0.01
Simulation		2.829e+05	40.17	1.842e+06	39.93	40.05	0.02

$$\text{MEU}_{\text{True}} = 1.7722 \text{ MeV/cm} \quad \sigma_{\text{MEU}_{\text{True}}} = 0.0003 \text{ MeV/cm}$$

As expected, the comparison of the absolute calibration results in Fig. 3.44 and Tab. 3.8 demonstrates that the  $\text{MEU}$  values across the four data samples are consistent, particularly in the Y view, which has larger statistics. However, the  $\text{MEU}_{\text{Reco}}$  values are noticeably higher for simulation than for data, especially in the X view (vertical planes). This discrepancy is anticipated, as through-going muons in the new data-based simulation (Sec. 3.2) have incorrect (smaller) incident energies, leading to smaller mean deposited energies used in the attenuation fits and consequently larger relative calibration corrections. These larger corrections are then applied to the cor-

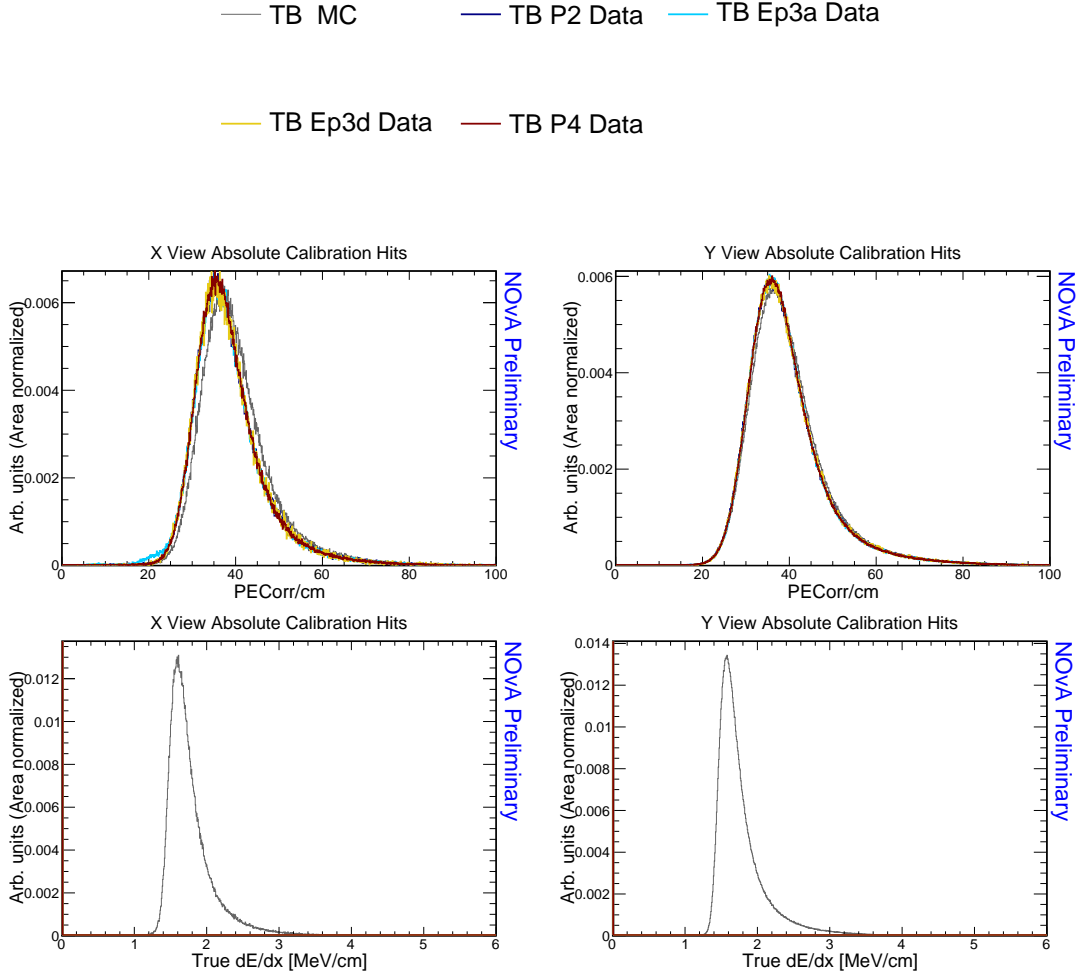


Figure 3.44: Distributions of the reconstructed (top) and true (bottom) energy response of stopping muons in the X (left) and Y (right) view within a  $1 - 2$  m track window from the end of their tracks. The mean of the reconstructed and true distributions of the response are the reconstructed and true MEU values respectively for the corresponding views.

rectly simulated stopping muons, resulting in higher  $\text{PECorr}$  and therefore larger  $\text{MEU}_{\text{Reco}}$ . Additionally, the true deposited energy, and therefore the  $\text{MEU}_{\text{True}}$ , which is also used for data, should be accurate.

There is a noticeable discrepancy of about 1% in the  $\text{MEU}_{\text{Reco}}$  values between the two views. Given the minimal statistical uncertainties and the consistency of results across the samples, this is unlikely to be a random effect. Additionally, the discrepancy between the two views is in a different direction for the data samples and for simulation. The actual reason for this discrepancy is unknown; it could be due to a real difference in the stopping muon distribution between the two views that is not accounted for, or a systematic difference in the calibration treatment of the two

views. This effect is observed in all [NOvA](#) detectors [178]. Since this means that the final result is technically incorrect for both views, one possible mitigation is to apply the absolute calibration results to each view separately. However, this contradicts the logic that stopping muons can serve as a standard candle, providing a single final calibration value.

### 3.3.8 Validation

The initial validation of the Test Beam detector calibration is performed using the same cosmic muons that were used in the calibration process. This step is essential to ensure that the calibration performs as intended and successfully unifies the energy deposition of cosmic muons across the detector (as a function of  $w$ , cell and plane) and throughout the Test Beam detector runtime. By analysing these validation results and investigating any residual differences, we assess the stability and quality of the calibration.

After the initial validation with cosmic muons, we apply the calibration results to beam events. For the [ND](#) and the [FD](#), we use a selection of standard candles, as described in Sec. 2.8, to evaluate the performance of the cosmic-based calibration on beam events and to assess the calibration systematic uncertainties. However, Test Beam offers a unique opportunity to validate the detector calibration directly with measurements from its beamline and to reassess and potentially reduce the systematic uncertainties associated with detector calibration in [NOvA](#). This is going to be one of the main results of the Test Beam experiment, therefore, we are focusing solely on the cosmic-based validation process.

The following section highlights the most important features observed during the validation, with additional plots provided in Appendix A for the reader’s convenience.

#### Validation with stopping muons

First, we examine the calibration effects on the same stopping muon hits as were used for the absolute calibration (Sec. 3.3.7), including all the absolute calibration cuts. These stopping muons, which have a very reliable and stable energy deposition, are used to compare the calibration performance amongst the various data and simulation samples. However, since we require hits to be within 1 – 2 m from the end

of the stopping muons' tracks, they are not evenly distributed across the detector, particularly absent in its bottom parts. This causes large statistical uncertainties and scattered distributions along  $w$  in the X view (for hits with  $w < 0$ ), and across cells in the Y view (for cells  $< 32$ ).

Figures 3.45-3.48 present the distributions of uncorrected (in PE/cm) and corrected (in MeV/cm) energy deposition as a function of  $w$ , cell number, plane number, and time. The uncorrected energy deposition distributions are displaying the same general attributes as were discussed for each sample in previous sections. As expected, the corrected energy deposition is generally uniform across all the studied variables. However, some residual variations can be noticed and are discussed below.

The distributions as a function of  $w$  (Fig. 3.45) illustrate the successful uniformity of energy deposition after applying calibration. Excluding the region affected by the lack of stopping muon hits, the corrected energy deposition for each sample is uniform within  $\pm 0.5\%$ . Additionally, all four data samples are consistent with each other, and the discrepancy between data and simulation is within  $\pm 1.5\%$ .

The distributions of uncorrected energy deposition as a function of  $w$  (top of Fig. 3.45) demonstrate a relative decrease in energy response over time, with period 4 data exhibiting a significantly smaller uncorrected energy response than period 2 data. This decrease, however, is corrected by calibration as expected.

The data-simulation discrepancy for the corrected energy deposition along  $w$  (bottom of Fig. 3.45) varies in the opposite direction between the X and Y views. This discrepancy arises from averaging the two view-dependent  $\text{MEU}_{\text{Reco}}$  values, which show opposite variation in simulation compared to data, as explained in Sec. 3.3.7. Ideally, there should be no data-simulation discrepancy after applying the full calibration results. Therefore, applying the view-dependent absolute calibration results separately to each view, which would likely resolve this issue, is worthwhile to consider.

The distributions of energy deposition across cells in Fig. 3.47 exhibit greater variability after calibration compared to the  $w$  dependence. This variability, particularly noticeable in the X view, is caused by issues with the threshold and shielding correction discussed in Sec. 3.3.2. The threshold and shielding correction is not applied to these distributions, just as it is not applied to the stopping muon sample for absolute calibration or to beam events, as it is not supposed to affect them. However, since the

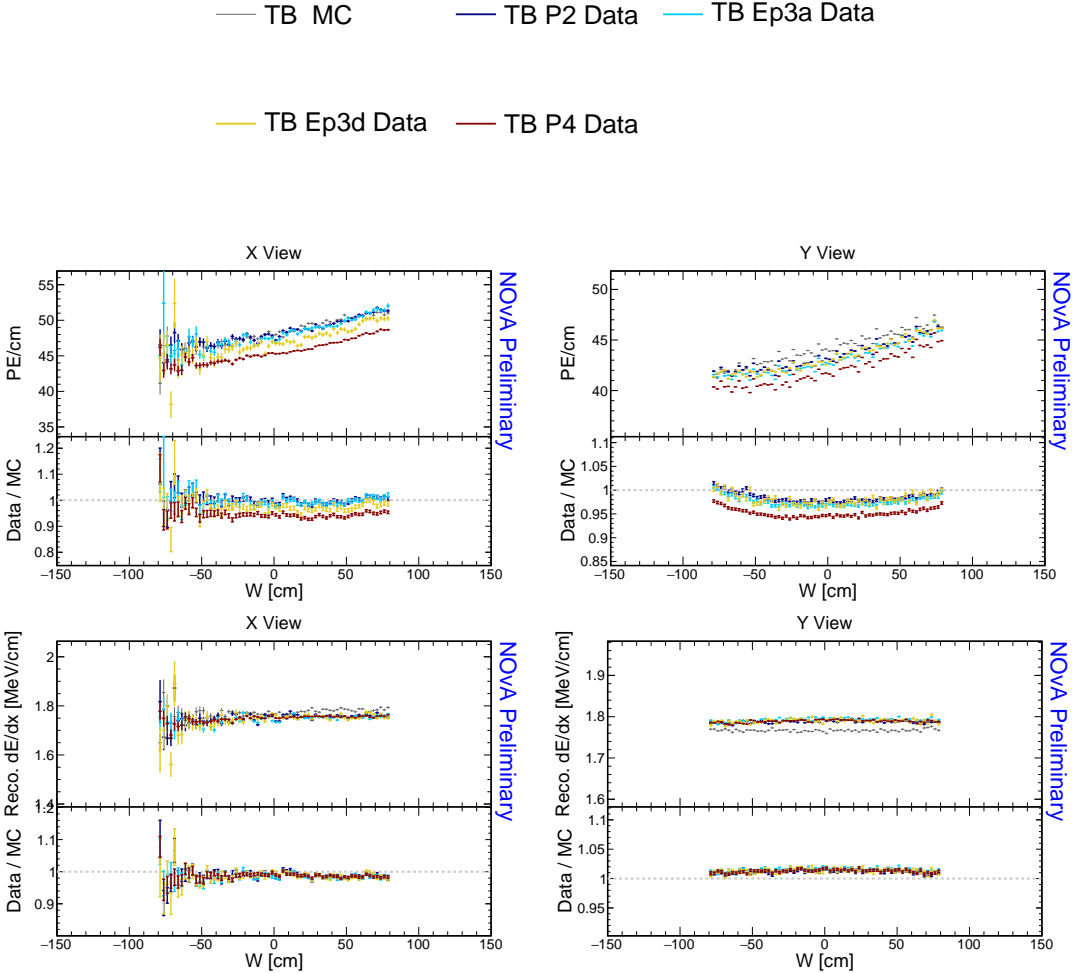


Figure 3.45: Distributions of uncorrected (top) and corrected (bottom) energy deposition for stopping MIP muons in the X view (left) and the Y view (right) as a function of the position within a cell. Bottom panel of each plot shows the ratio of the simulation sample (gray) and the four data samples, labelled at the top. Ep3a labels a combination of epochs 3a+3b+3c and Ep3d labels epochs 3d+3e. The left half ( $w < 0$ ) of the X view distributions has large statistical uncertainties due to the low number of stopping muons at the bottom of the detector. The discrepancy between the data and the simulation samples for the corrected energy depositions is explained in text.

incorrect threshold and shielding correction is applied during relative calibration, it is incorporated into the calibration results and consequently into the reconstructed deposited energy. The variability introduced by these faulty corrections is within  $\pm 3.5\%$ .

The distribution of corrected energy across cells in the Y view (bottom right of Fig. 3.46) additionally shows two cells with a noticeably lower energy response ( $\sim 2-4\%$ ) for period 2 and epochs 3a+3b+3c compared to the rest of the samples. Specifically, this is the cell 31, which was underfilled during period 2 and epoch 3a, and its

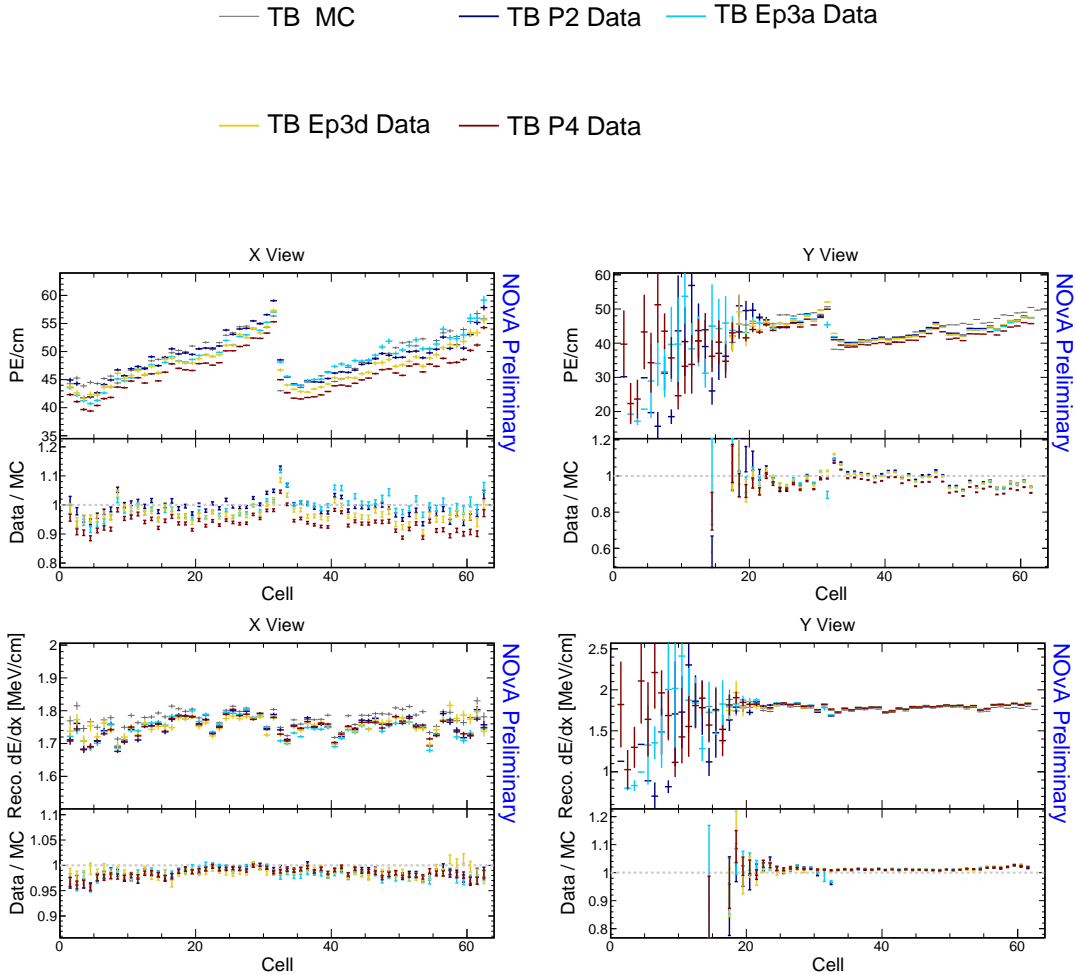


Figure 3.46: Distributions of uncorrected (top) and corrected (bottom) energy deposition for stopping MIP muons in the X view (left) and the Y view (right) as a function of the cell number. Bottom panel of each plot shows the ratio of the simulation sample (gray) and the four data samples, labelled at the top. Ep3a labels a combination of epochs 3a+3b+3c and Ep3d labels epochs 3d+3e. The left part (cell  $\lesssim 25$ ) of the Y view distributions has large statistical uncertainties due to the low number of stopping muons at the bottom of the detector. Features described in text.

neighbouring cell 32. The variation for the underfilled cell is expected. However, it is unclear why one of the neighbouring cells to the underfilled cells is miscalibrated.

The relative differences in the uncorrected energy response across planes (top of Fig. 3.47) between the three different data taking periods demonstrate that the decrease in energy deposition over time varies between planes. This variation is especially noticeable in the X view plot, but is equally present in the Y view planes. This effect is attributed to the differences in the quality of the scintillator oil used to fill the detector, as explained in Sec. 3.1. Additionally, it indicates scintillator ageing, which results in a decrease of the scintillation light produced per deposited energy

over time. Specifically, the ND+NDOS scintillator oil (planes 0-31) appears to have aged the most between periods 2 and 4, followed by the Texas NDOS oil (planes 53-62), while the Ash River oil (planes 32-52) aged the least. However, more quantitative studies are necessary to assess the ageing of the **NOvA** scintillator, as its details are currently not well understood.

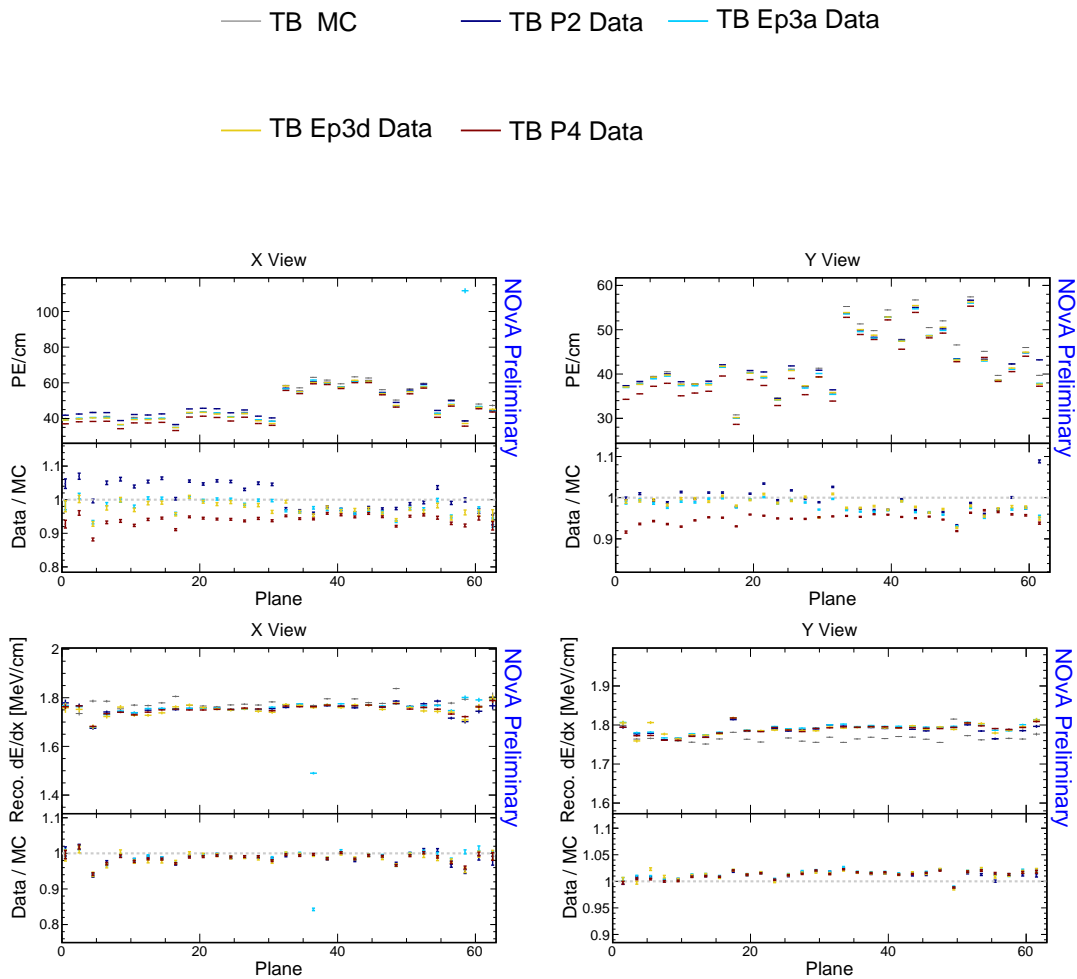


Figure 3.47: Distributions of uncorrected (top) and corrected (bottom) energy deposition for stopping **MIP** muons in the X view (left) and the Y view (right) as a function of the plane number. Bottom panel of each plot shows the ratio of the simulation sample (gray) and the four data samples, labelled at the top. Ep3a labels a combination of epochs 3a+3b+3c and Ep3d labels epochs 3d+3e. Features described in text.

The distribution of the corrected energy response across planes in the X view (bottom left of Fig. 3.47) reveals a significantly smaller response ( $\sim 16\%$ ) for epochs 3a+3b+3c in plane 36. This indicates that the relative calibration over-corrected the energy response due to through-going muons having an unusually high energy response (as shown in Fig. 3.34), but not the selected stopping muons. The most likely

explanation is that the affected **FEB** was ‘faulty’ only for a certain period. Consequently, the corrected energy response would be accurate for the period when the **FEB** was faulty, but would be under-estimated for the period when the **FEB** functioned normally.

We can observe the effect of different **FEB** versions in both the corrected and uncorrected energy response distributions across planes, shown in Fig. 3.47. Specifically, the **FEBv5** was used in planes 16, 17, 48 and 49, which is evident by the relatively larger corrected energy deposition, especially in the simulation and in the X view. Although this effect should be corrected during calibration, it is not, due to the incorrect incorporation of the variations between the **FEB** versions in the simulation and its impact on the threshold and shielding correction, as discussed in Sec. 3.3.2.

There are additional variations in the corrected energy deposition across planes (bottom of Fig. 3.47). In the X view, there is a significant ( $\sim 6\%$ ) drop in corrected energy response in planes 4 and 58, along with a smaller drop in some surrounding planes. The cause of this variation is unknown. However, it appears to be due to a discrepancy between through-going and stopping muons, as it disappears when analysing through-going muons, as explained below. In the Y view, the corrected response increases with planes within the first half of the detector. This effect is only observed in data and not in simulation. The origin of this slope is unclear, however it is also absent when examining variations for through-going muons.

The distributions of energy deposition over time (Fig. 3.48) reveal a complex dependency and significant variations. As shown, the calibration process currently only normalizes the mean of each calibrated sample, leaving time-dependent variations within the samples uncorrected. The uncorrected energy response is noticeably higher for period 2 compared to period 4, likely due to detector ageing, as previously discussed. However, there is no clear downward-going trend; the variations are larger than any consistent time-dependent pattern, except for the second half of period 4.

In the **ND** and **FD** calibration, these time-dependent variations are partially addressed by reducing the size of the calibration samples to month-long epochs. This approach reduces variations in the calibrated energy deposition but generally results in larger portions of the detector being uncalibrated. However, this did not have a significant effect on the rate of calibrated cells for the **ND** and **FD** [179] and in the fu-

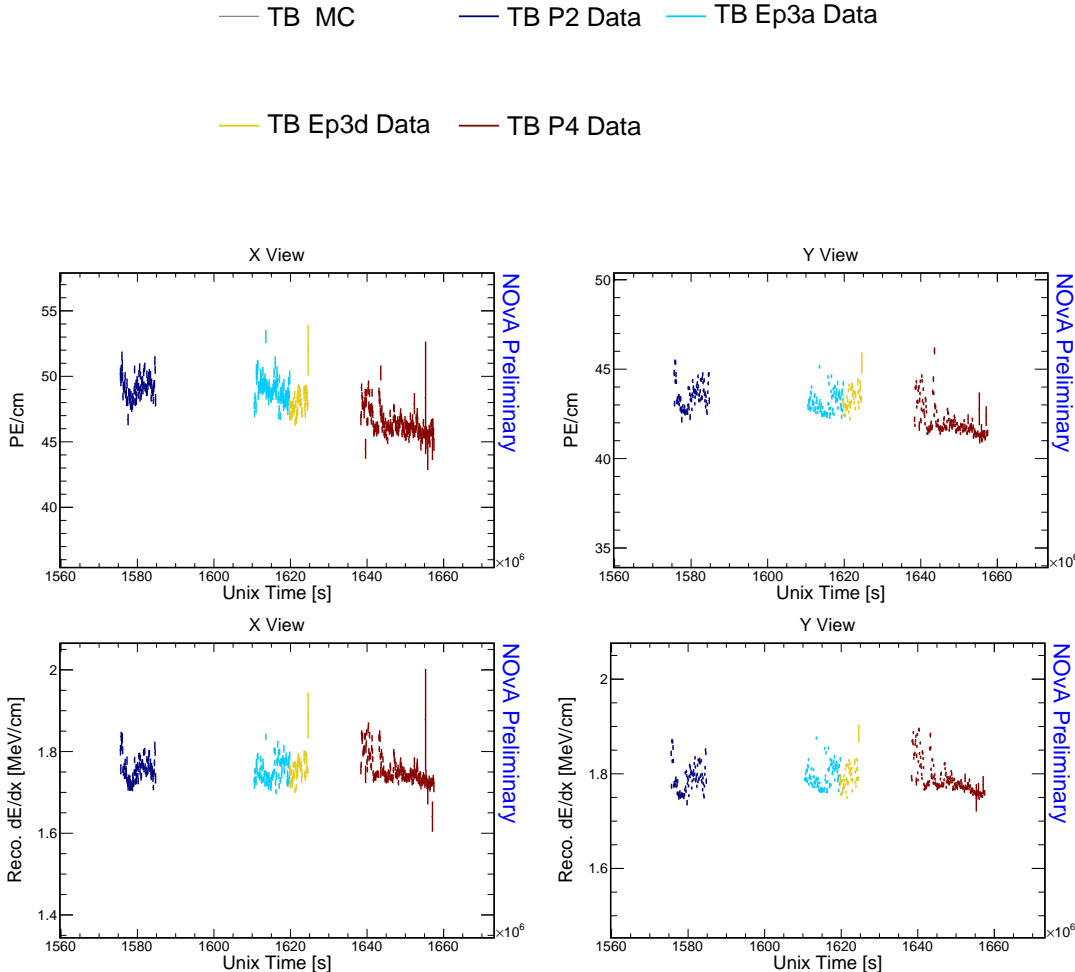


Figure 3.48: Distributions of uncorrected (top) and corrected (bottom) energy deposition for stopping MIP muons in the X view (left) and the Y view (right) as a function of the event UNIX time (which starts at the beginning of the NOvA data taking). Comparing the four data samples, labelled at the top. Ep3a labels a combination of epochs 3a+3b+3c and Ep3d labels epochs 3d+3e. Features described in text.

ture can be explored for Test Beam detector as well. The ND and FD typically exhibit smaller variations in energy response over time compared to the Test Beam detector due to the Test Beam detector’s less stable running conditions, such as larger fluctuations in temperature and humidity in the Test Beam hall.

The effect of these environmental factors on detector performance, along with scintillator and potential readout electronics ageing, are not well understood within NOvA. As these effects are more pronounced in the Test Beam detector and given the range of scintillator oils and readout electronics used, separating the effects of the individual factors is challenging and is currently the focus of ongoing studies [180].

## Validation with through-going muons

To validate the calibration performance without the limitations imposed by stopping muons, we examine the effects of calibration on through-going muons, which were also used for the relative calibration. Unlike for the stopping muon sample, we apply the threshold and shielding corrections for the through-going muons to truly verify the validity of the relative calibration process. Since the simulated through-going muons have incorrect incident energies, this validation focuses solely on variations in shape rather than scale.

Considering the variability of detector performance over time, we use through-going muons collected during ‘stable runs’ in period 4, as depicted in Fig. 3.49. This period was selected by visually inspecting the time dependence of corrected energy deposition and choosing runs that correspond to seemingly stable energy deposition.

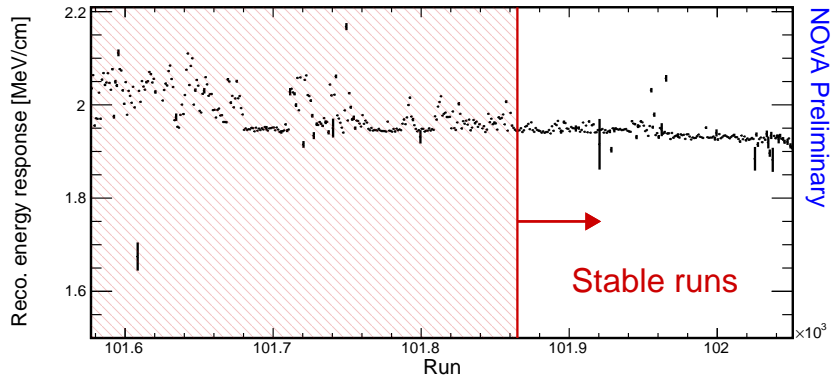


Figure 3.49: Selection of stable runs from the period 4 Test Beam data. Showing the reconstructed energy response as a function of the run number for through-going cosmic muons. Shaded red area shows rejected runs.

Furthermore, Fig. 3.50 shows significant variation of energy deposition at cell edges. This issue is addressed by the calibration shape systematic uncertainty discussed in Sec. 2.8. Therefore, for this validation study we ignore the edge variations, using the same  $w$  limit as for the stopping muon sample:  $-80 < w < 80$  cm.

With the aforementioned constraints, we expect uniform distributions with limited variations. Residual variations should be scattered throughout the detector without any particular pattern, indicating potential errors in the calibration process. It is worth noting that investigating these distributions without applying the threshold and shielding correction led to the discovery of the issues discussed in Sec. 3.3.2. Any

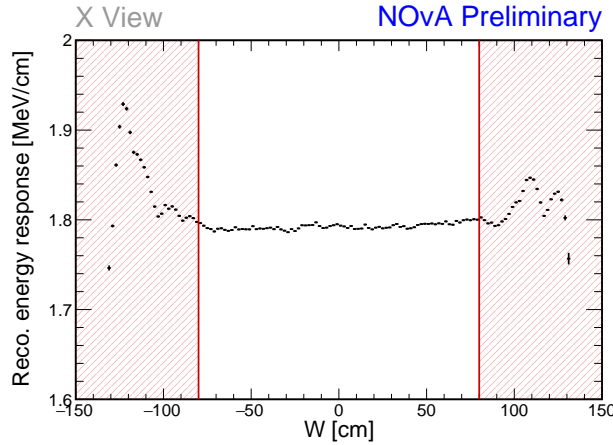


Figure 3.50: Removing edge hits for validation with through-going muons. Showing only events from the stable runs of the period 4 Test Beam cosmic data.

remaining variations point to potential systematic uncertainties in the calibration process.

Figure 3.51 displays individual distributions of corrected energy response as a function of  $w$ , plane, and cell number for both data and simulation. For through-going muons with the threshold and shielding correction applied, the calibration procedure works as expected, with residual variations around  $\pm 0.2\%$  for the  $w$  and cell dependence. However, for plane dependence, these residual variations are larger: approximately  $\pm 0.5\%$  in data and up to  $\pm 1\%$  in simulation. Additionally, maps of corrected energy deposition as a function of both plane and cell numbers, along with their 1D projections, are shown in Fig. 3.52 for data and in Fig. 3.53 for simulation. These plots demonstrate that the final residual variations for calibration reach approximately 1% in data and 4% in simulation.

In the distributions for data, we observe a clear effect of the different scintillators used, which is related to varying levels of detector ageing among the scintillators, as previously discussed. This effect is particularly noticeable in this validation sample due to the selection of events from ‘stable runs’, while the relative calibration was calculated for the entire period 4. Therefore, calibration scales the deposited energy with respect to the mean deposited energy for the full period 4. Consequently, planes 0-31 appear to have the lowest relative corrected response in Fig. 3.51 and 3.52 because the corresponding ND+NDOS scintillator oil aged the most compared to the mean. This issue could be addressed by splitting period 4 into smaller epochs for calibration.

For simulation, the relative calibration is performed in bins of  $w$  for each cell and

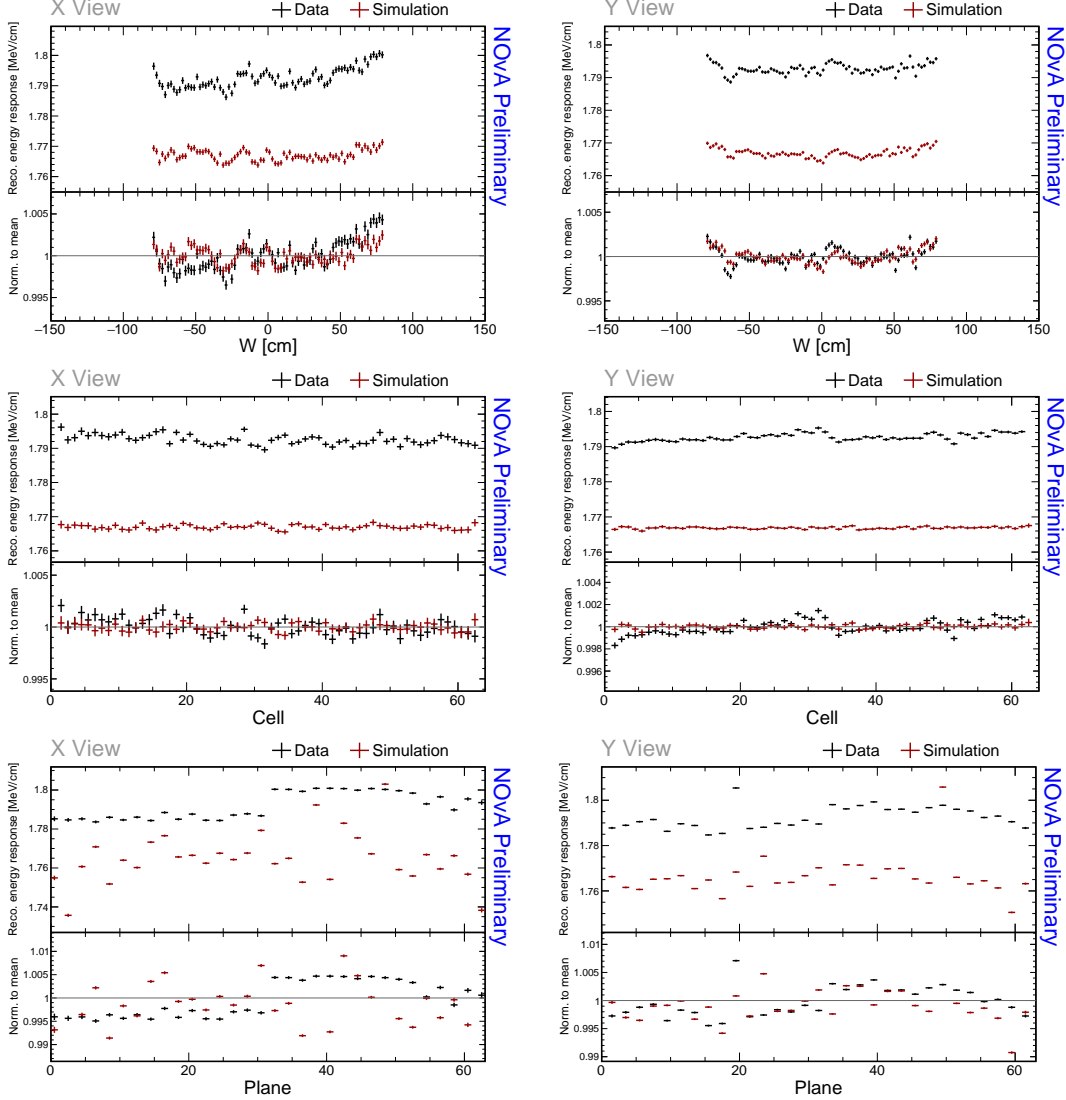


Figure 3.51: Distributions of through-going cosmic muons with  $w \in (-80, 80)$  cm as a function of  $w$ , cells and planes for stable runs in the Test Beam period 4 data (black) and data-based simulation (red). Bottom panel of each plot shows the ratio between the value for each bin and the mean across the entire y axis, calculated separately for data and simulation.

each **FB** bin but importantly not for each plane. As a result, the relative calibration in simulation does not specifically correct for plane dependence, leading to larger variations between planes.

Furthermore, one half of plane 19 in data shows a corrected energy response approximately 0.7 % higher than the rest. This is due to a faulty **FEB** that was likely malfunctioning for a brief period. Since this study aims to examine purely the residual variations from the calibration procedure, cells corresponding to this **FEB** can be ignored. Additionally, planes 48 and 49 in simulation, which correspond to **FEBv5**,

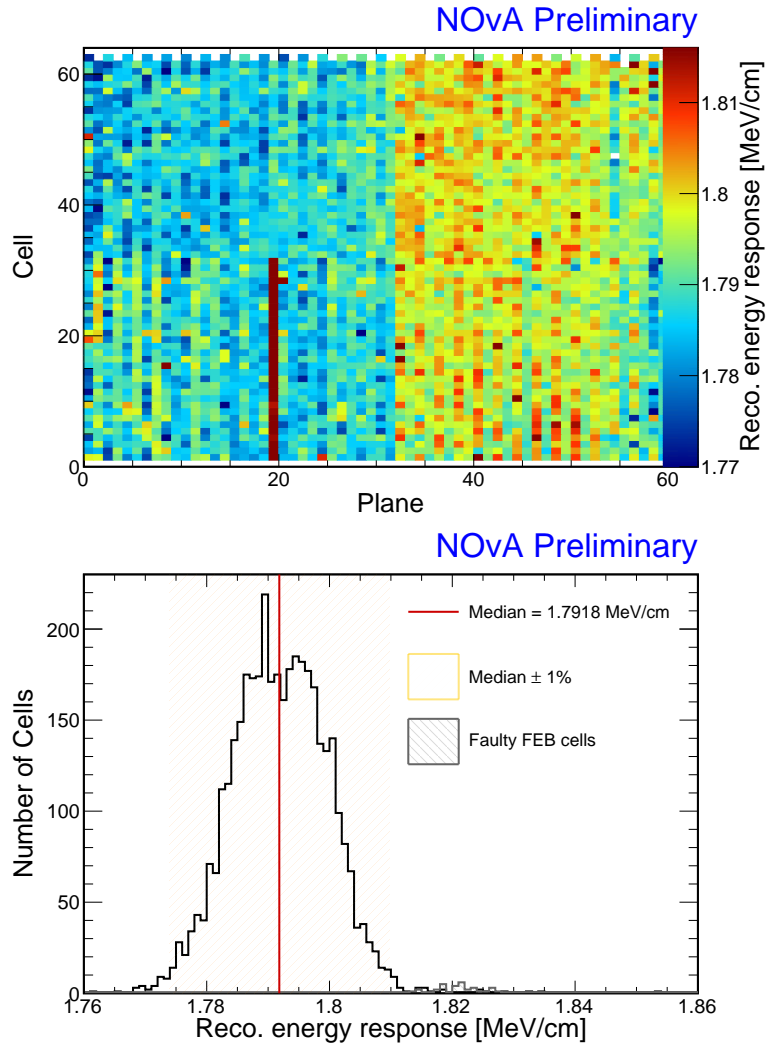


Figure 3.52: Top: Map of corrected energy deposition for through-going cosmic muons with  $w \in (-80, 80)$  cm as a function of cell and plane numbers for stable runs in the Test Beam period 4 data. Bottom: Projection of each bin from the map. Red line shows the median value of the projection and red shaded area shows the  $\pm 1\%$  range of the median value. Gray shaded bins show the excluded bins corresponding to faulty FEB, visible as a stark red line in plane 19 on the map. Additional features explained in text.

display a corrected energy response about 2 – 2.2 % higher than the rest. This discrepancy arises from the incorrect accounting for different FEB versions in simulation, combined with consolidating the planes into FB bins.

### 3.3.9 Summary

We have successfully calibrated the NOvA Test Beam detector in four independent Test Beam data samples and in simulation. This is a critical step in order to analyse the Test Beam data, enabling crucial improvements to our understanding of the detector

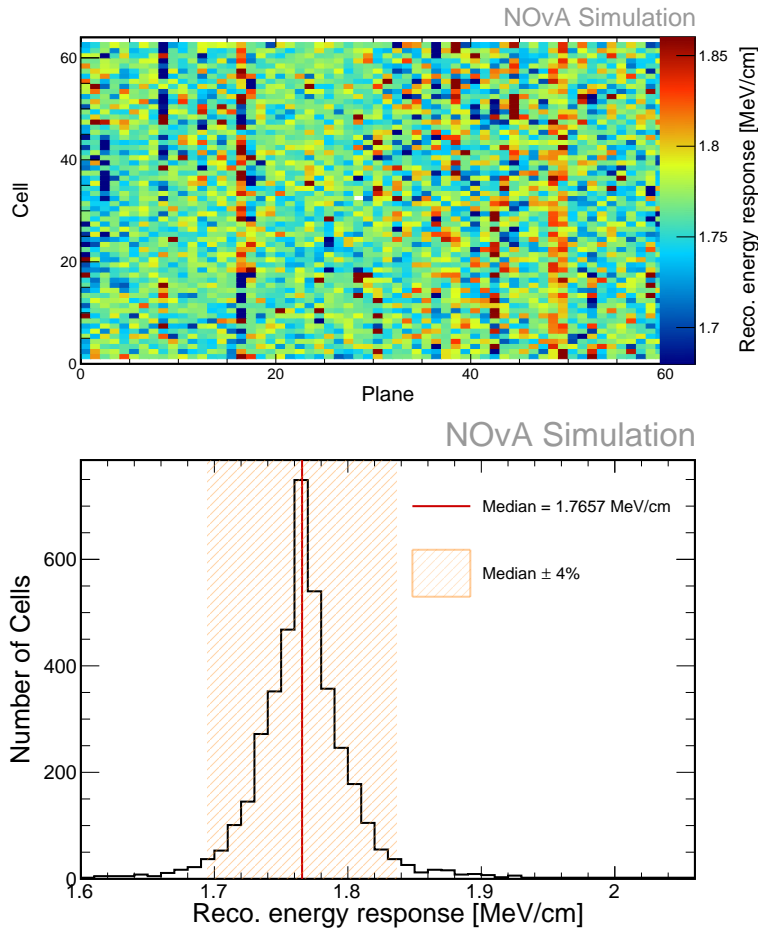


Figure 3.53: Top: Map of corrected energy deposition for through-going cosmic muons with  $w \in (-80, 80)$  cm as a function of cell and plane numbers for stable runs in the Test Beam data-based simulation. Bottom: Projection of each bin from the map. Red line shows the median value of the projection and red shaded area shows the  $\pm 4\%$  range of the median value. Additional features explained in text.

response and particularly of the calibration for all the NOvA detectors.

Each calibrated sample contains only a few uncalibrated cells, mainly concentrated on the periphery of the detector. Most of the other uncalibrated cells failed the calibration condition due to unavoidable circumstances, such as underfilled cells, or dead channels. However, several improvements could increase the number of calibrated cells or otherwise improve the calibration performance. Some of the improvements could benefit not only the Test Beam detector but all the NOvA detectors.

Several issues discovered during the Test Beam calibration that will enhance calibration and simulation for all the NOvA detectors include the problems found with the threshold and shielding correction and with the readout simulation, described in Sec. 3.3.2. Ongoing work aims to address these issues by improving the logic of

the threshold and shielding correction or basing it entirely on data. Additionally, plans are in place to remove the relative gain variation from the simulation, as the **FB** map used during simulation already sufficiently describes the relative gain variations, making the current treatment redundant.

One of the most common issues that could be resolved is the faulty **FEBs**, which often malfunctioned only for a limited period. This is particularly concerning, as cells belonging to faulty **FEBs** usually pass the calibration condition; however, if the corresponding **FEB** was faulty only for a limited period, the calibration results for those cells would be incorrect. This issue is currently difficult to address because the inputs for the relative calibration are organized by run and subrun numbers instead of by cells, making it impossible to calibrate cells corresponding to a single **FEB** separately from the rest. However, ongoing work is adapting both the input files and the calibration procedures to enable calibrating individual cells separately.

The time dependence of energy deposition in the Test Beam detector discussed in Sec. 3.3.8 is currently being studied and could help explain several contributions to the time-dependency seen in all **NOvA** detectors. Specifically, the Test Beam can study the environmental effects on energy deposition, as well as the ageing of different scintillators and electronics. The first results indicate that the **NOvA** scintillator oils age differently based on their quality.

Addressing the time-dependent variations in the energy deposition in Test Beam could include splitting the calibrated periods into smaller samples, similarly to the **ND** and **FD**. However, this approach risks insufficient statistics for attenuation fits in various cells. This could in turn be addressed by tuning the binning of the attenuation profiles to better fit the real cell dimensions that are actually being fitted in the attenuation fits.

Another technical improvements to the calibration results could stem from manually altering the  $\chi^2$  value of cells that have attenuation fits which visibly looks all right, to below 0.2. This would officially rendering these cells calibrated, similarly to how it was done for some cells in epochs 3d+3e and period 4. However, this would require manually going over all the uncalibrated cells, which is only really possible for the Test Beam detector and only for larger calibrated samples. Reducing the size of the calibrated sample would make this extremely impractical.

Lastly, there is a possible improvement to the data-simulation discrepancy, by applying the absolute calibration results to each view independently. This would however have to be seriously considered, as the stopping muon sample used for calibration should technically not have any variation between the views and therefore this might introduce bias when applying the calibration results to beam data.

Overall, the calibration of the NOvA Test Beam detector was successful and represents a significant advancement, with ongoing efforts aimed at further refining the process and addressing the identified issues to improve calibration accuracy and reliability across all [NOvA](#) detectors. Part of the ongoing work also aims to quantify the correctness of the Test Beam calibration, devising a concrete systematic uncertainty.

## CHAPTER 4

# Measuring the muon neutrino magnetic moment

In this analysis, I aim to detect a potential signal of the effective muon neutrino magnetic moment in the [NOvA ND](#). This signal would manifest as an excess of neutrino-on-electron ( $\nu$ -on-e) elastic scattering interactions at low electron recoil energies, proportional to the value of the effective neutrino magnetic moment, over the [SM](#) background. If no significant excess is observed, I will establish an upper limit on the effective muon neutrino magnetic moment.

Detecting the neutrino magnetic moment ( $\mu_\nu$ ) would provide definitive evidence of new [BSM](#) physics, and measuring its value would help identify the appropriate [BSM](#) theory. As current and planned experiments can only detect an anomalously large neutrino magnetic moment, observing such a signature would strongly suggest that neutrinos are Majorana particles and would have significant implications for astrophysics and cosmology [51].

The best model-independent experimental results on the neutrino magnetic moment come from experiments searching for dark matter using xenon-based detectors. These highly sensitive detectors detect solar neutrinos, which are part of the background in dark matter searches but can be reanalysed for other purposes. In 2020, the XENON1T experiment observed [181] a low energy excess of solar neutrinos, which could correspond to a signal from an anomalously large effective magnetic moment within  $\mu_{\nu_\odot} \in (0.14, 0.29) \times 10^{-10} \mu_B$  at 90 % Confidence Level (C.L.), where  $\nu_\odot$  marks solar neutrinos. However, this result was disfavoured by the follow-up XENONnT experiment in 2022 [182], which saw no excess and set the current world-leading limit on neutrino magnetic moment at  $\mu_{\nu_\odot} < 0.063 \times 10^{-10} \mu_B$  at 90 % C.L.. Other solar neutrino experiments also reported null results regarding neutrino magnetic moment [183, 184], placing less stringent limits on its value. Given some basic assumptions [184, 185] this limit for solar neutrinos would correspond to a limit on muon neutrino

effective magnetic moment of  $\mu_{\nu_\mu} < 0.137 \times 10^{-10} \mu_B$ . However, the relationship between effective magnetic moments of different neutrino flavours may be non-trivial, especially in the context of possible new **BSM** physics, and studying muon neutrinos remains an important endeavour [186].

The best results for  $\nu_\mu$  and  $\bar{\nu}_\mu$  come from accelerator-based stopped pion neutrino sources [187, 188], which also do not observe any low energy excess and provide an upper limit on the effective muon neutrino magnetic moment of  $\mu_{\nu_\mu} < 6.8 \times 10^{-10} \mu_B$  at 90 % **C.L.** [187]. Stopped pion neutrino sources provide well-understood beams made up of  $\nu_\mu$ ,  $\bar{\nu}_\mu$  and  $\nu_e$  with energies up to 52.8 MeV. Slightly looser limits come from pion decay-in-flight accelerator-based measurements (similar to **NOvA**) [189, 190], which provide a limit of  $\mu_{\nu_\mu} < 8.5 \times 10^{-10} \mu_B$  at 90 % **C.L.**.

Thanks to the very intense and highly pure beam of muon neutrinos and antineutrinos, and a detector designed for the reconstruction and identification of events with electrons in the final state, **NOvA** is well-positioned to provide a highly competitive, and possibly even world-leading, measurement (or limit) of the effective muon neutrino magnetic moment. A previous analysis of **NOvA ND** data for a measurement of the effective muon neutrino magnetic moment was presented in a thesis [191], providing a (statistics-only) limit of  $\mu_{\nu_\mu} < 15.8 \times 10^{-10} \mu_B$  at 90 % **C.L.**

Additionally,  $\nu$ -on-e elastic scattering interactions are used in various other analyses in **NOvA**, specifically in efforts to constrain the neutrino beam prediction [192, 193] and in the search for Light Dark Matter (LDM) [194]. These analyses developed various tools and methods that can be utilized in the search for a neutrino magnetic moment.

In this chapter, I will provide an overview of the theory of neutrino electromagnetic interactions in Sec. 4.1, focusing on the effective neutrino magnetic moment and its implications for  $\nu$ -on-e measurements and other theoretical considerations. In Sec. 4.2, I will discuss the analysis strategy, the signal and background definition, as well as the data and simulation samples and the analysis weights. Following this, in Sec. 4.3 I will explain the selection of events for this analysis, while in Sec. 4.4 I will address the relevant systematic uncertainties and in Sec. 4.5 the statistical methods employed to analyse the results. I will present the results of this analysis in Sec. 4.6 and summarise them in Sec. 4.7.

## 4.1 Theory of the neutrino magnetic moment

As was described in Sec. 1, neutrinos in the SM are massless and electrically neutral particles. However, even SM neutrinos can have electromagnetic interaction through loop diagrams involving charged leptons and the W boson, covered by the neutrino charge radius [51].

In general BSM theories, considering interactions with a single photon as shown on Fig. 4.1, neutrino electromagnetic interactions can be described by an effective interaction Hamiltonian [195]

$$\mathcal{H}_{em}^{(\nu)}(x) = \sum_{k,j=1}^N \bar{\nu}_k(x) \Lambda_\mu^{kj} \nu_j(x) A^\mu(x). \quad (4.1)$$

Here  $\nu_k(x)$ ,  $k = 1, \dots, N$ , are neutrino fields in the mass basis with  $N$  neutrino mass states,  $\Lambda_\mu^{kj}$  is a general vertex function and  $A^\mu(x)$  is the electromagnetic field.

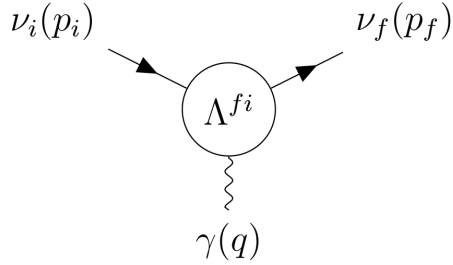


Figure 4.1: Effective coupling of neutrinos with one photon electromagnetic field.

The vertex function  $\Lambda_\mu^{fi}(q)$  is generally a matrix and, in the most general case consistent with the SM gauge invariance [196, 197], can be written in terms of linearly independent products of Dirac matrices ( $\gamma$ ) and only depends on the four momentum of the photon ( $q = p_f - p_i$ ):

$$\begin{aligned} \Lambda_\mu^{fi}(q) = & \mathbb{F}_1^{fi}(q^2) q_\mu + \mathbb{F}_2^{fi}(q^2) q_\mu \gamma_5 + \mathbb{F}_3^{fi}(q^2) \gamma_\mu + \mathbb{F}_4^{fi}(q^2) \gamma_\mu \gamma_5 + \\ & \mathbb{F}_5^{fi}(q^2) \sigma_{\mu\nu} q^\nu + \mathbb{F}_6^{fi}(q^2) \epsilon_{\mu\nu\rho\gamma} q^\nu \sigma^{\rho\gamma}, \end{aligned} \quad (4.2)$$

where  $\mathbb{F}_i^{fi}(q^2)$  are six Lorentz invariant form factors and  $\delta$  and  $\epsilon$  are the Dirac delta and the Levi-Civita symbols respectively.

Applying conditions of hermiticity  $(\mathcal{H}_{em}^{(\nu)\dagger} = \mathcal{H}_{em}^{(\nu)})$  and of the gauge invariance

of the electromagnetic field, the vertex function can be rewritten as

$$\Lambda_\mu^{fi}(q) = (\gamma_\mu - q_\mu q^2/q^2) \left[ \mathbb{F}_Q^{fi}(q^2) + \mathbb{F}_A^{fi}(q^2) q^2 \gamma_5 \right] - i\sigma_{\mu\nu} q^\nu \left[ \mathbb{F}_M^{fi}(q^2) + i\mathbb{F}_E^{fi}(q^2) \gamma_5 \right], \quad (4.3)$$

where  $\mathbb{F}_Q^{fi}$ ,  $\mathbb{F}_M^{fi}$ ,  $\mathbb{F}_E^{fi}$  and  $\mathbb{F}_A^{fi}$  are hermitian matrices representing the charge, dipole magnetic, dipole electric and anapole neutrino form factors respectively. It is clear that the vertex function only depends on the square of the four momentum of the photon  $q^2$ . In coupling with a real photon ( $q^2 = 0$ ) these form factors become the neutrino charge and magnetic, electric and anapole moments respectively. Additionally, the neutrino charge radius corresponds to the second term in the expansion of the charge form factor [195].

The above expression can be simplified [198] as

$$\Lambda_\mu^{fi}(q) = \gamma_\mu \left( Q_{\nu_{fi}} + \frac{q^2}{6} \langle r^2 \rangle_{\nu_{fi}} \right) - i\sigma_{\mu\nu} q^\nu \mu_{\nu_{fi}}, \quad (4.4)$$

where  $Q_{\nu_{fi}}$ ,  $\langle r^2 \rangle_{\nu_{fi}}$ , and  $\mu_{\nu_{fi}}$  are the neutrino charge, effective charge radius (also containing anapole moment), and an effective magnetic moment (also containing electric moment) respectively. This is possible thanks to the similar effects of the neutrino charge radius and the anapole moment, and of the neutrino magnetic and electric moments, on neutrino interactions. Therefore, these are the three neutrino electromagnetic properties (charge, effective charge radius and effective magnetic moment) measured in experiments.

The neutrino electric charge is primarily constrained through measurements of the neutrality of matter and through cosmological observations, which provide much better constraints than neutrino oscillation experiments [195]. On the other hand, the neutrino charge radius would manifest as an increase in the size of the  $\nu$ -on-e elastic scattering coupling constants, allowing it to be studied in neutrino oscillation experiments such as NOvA. Additionally, the value of the neutrino charge radius in the SM is only an order of magnitude smaller than the current world-leading limits [52] and measuring it could either confirm the validity of neutrino interactions in the SM, or open possibilities to non-standard contributions to neutrino scattering [195]. However, measurement of the neutrino charge radius is not part of this analysis, but may be included in the future re-analysis of the  $\nu$ -on-e interactions in the NOvA ND.

### 4.1.1 Neutrino electric and magnetic dipole moments

The size and effect of neutrino electromagnetic properties depend on the specific [BSM](#) theory applied. Evaluating one loop diagrams in the minimally extended [SM](#) with three right-handed Dirac neutrinos, as described in Sec. 1.4, gives the first approximation of the electric and magnetic moments, which are now  $3 \times 3$  matrices with elements:

$$\left. \begin{aligned} \mu_{kj}^D \\ i\epsilon_{kj}^D \end{aligned} \right\} \simeq \frac{3eG_F}{16\sqrt{2}\pi^2} (m_k \pm m_j) \left( \delta_{kj} - \frac{1}{2} \sum_{l=e,\mu,\tau} U_{lk}^\star U_{lj} \frac{m_l^2}{m_W^2} \right), \quad (4.5)$$

where  $m_k, m_j$  are the neutrino masses and  $m_l$  are the masses of charged leptons which appear in the loop diagrams [195]. The  $D$  superscript denotes Dirac neutrinos and  $M$  denotes Majorana neutrinos throughout this section. Also,  $e$  is the electron charge,  $G_F$  is the Fermi coupling constant,  $U$  is the [PMNS](#) neutrino oscillation matrix, and  $m_W$  is the mass of the  $W$  boson. Higher order electromagnetic corrections were neglected, but can also have a significant contribution, depending on the theory.

It can be seen that Dirac neutrinos have no diagonal electric moments ( $\epsilon_{kk}^D = 0$ ) and their diagonal magnetic moments are approximately

$$\mu_{kk}^D \simeq \frac{3eG_F m_k}{8\sqrt{2}\pi^2} \simeq 3.2 \times 10^{-19} \left( \frac{m_k}{\text{eV}} \right) \mu_B, \quad (4.6)$$

where  $\mu_B$  is the Bohr magneton which represents the value of the electron magnetic moment [195]. Neutrino magnetic moments are therefore strongly suppressed by the smallness of neutrino masses, with theoretical predictions in Eq. 4.6 several orders of magnitude below the reach of current experiments [198].

The transition magnetic moments in the minimally extended [SM](#) from Eq. 4.5 are suppressed with respect to the largest of the diagonal magnetic moments by at least a factor of  $10^{-4}$  due to the  $m_W^2$  in the denominator. The transition electric moments are even smaller due to the mass difference in Eq. 4.5. Therefore an experimental observation of a magnetic moment larger than in Eq. 4.6 would indicate physics beyond the minimally extended [SM](#) [195, 199].

The suppression of the neutrino magnetic moment by the smallness of its mass can be also expressed in a general case [199]. The ‘natural’ upper limits on the size of

the neutrino magnetic moment for any **BSM** theory that has **NP** generated at a scale  $\Lambda_{NP}$  can be expressed as [200]

$$\mu_\nu^D(\mu_B) \lesssim 3 \times 10^{-15} \frac{m_\nu^D \text{ (eV)}}{[\Lambda_{NP} \text{ (TeV)}]^2}. \quad (4.7)$$

Therefore for  $\Lambda_{NP} \simeq 1 \text{ TeV}$  and  $m_\nu^D \lesssim 1 \text{ eV}$  the limit becomes  $\mu_\nu^D \lesssim 3 \times 10^{-15} \mu_B$ , well below the current experimental capabilities. However, these upper bounds only apply if **NP** is generated well above the electroweak scale  $\Lambda_{EW} \sim 100 \text{ GeV}$  [195].

For Majorana neutrinos, the magnetic and electric form factors (and therefore the magnetic and electric moment matrices) are antisymmetric, thus Majorana neutrinos only have transition moments. The simplest extension of the **SM** that includes Majorana neutrinos requires either the addition of a Higgs triplet, or right-handed neutrinos together with a Higgs singlet [195]. Neglecting the Feynman diagrams which depend on the model of the scalar sector, the magnetic and electric dipole moments are

$$\left. \begin{aligned} \mu_{kj}^M \\ \epsilon_{kj}^D \end{aligned} \right\} \simeq \mp \frac{3ieG_F}{16\sqrt{2}\pi^2} (m_k \pm m_j) \sum_{l=e,\mu,\tau} \text{Im/Re} [U_{lk}^\star U_{lj}] \frac{m_l^2}{m_W^2}, \quad (4.8)$$

where **Im** is for  $\mu_{kj}^M$  and **Re** is for  $\epsilon_{kj}^D$ . These are difficult to compare to the Dirac case, due to possible presence of Majorana phases in the **PMNS** matrices, but it is clear that they have the same order of magnitude as Dirac transition dipole moments. However, the neglected model dependent contributions can enhance the transition dipole moments for Majorana neutrinos [195].

The natural upper bound on the Majorana magnetic moment is less strict compared to the Dirac neutrinos, due to the antisymmetric nature of Majorana magnetic moment, which requires additional Yukawa couplings in the **BSM** theory compared to Dirac neutrinos, which can enhance the maximal possible magnetic moment [199]. The limit for Majorana neutrinos can be expressed as

$$\mu_{\alpha\beta}^M(\mu_B) \leq 4 \times 10^{-9} \frac{[m_\nu^M]_{\alpha\beta} \text{ (eV)}}{[\Lambda_{NP} \text{ (TeV)}]^2} \frac{m_\tau^2}{|m_\alpha^2 - m_\beta^2|}, \quad \alpha, \beta \in \{e, \mu, \tau\}. \quad (4.9)$$

Here, the neutrino magnetic moment is expressed in the flavour basis instead of the mass basis, since the charged lepton masses are diagonal here. The two bases are

related by

$$\mu_{ij} = \sum_{\alpha\beta} \mu_{\alpha\beta} U_{\alpha i}^* U_{\beta j}. \quad (4.10)$$

and the effect of the neutrino magnetic moment on neutrino interactions does not depend on the choice of the basis[62].

These considerations imply, that if a magnetic moment  $\mu \gtrsim 10^{-15} \mu_B$  were measured, neutrinos are almost certainly Majorana particles [199].

### Effective neutrino magnetic moment

As mentioned above, the neutrino magnetic moment measured in experiments is the so-called effective neutrino magnetic moment, which is a combination of electric and magnetic dipole moments and depends on the neutrino source and oscillations. In the ultra-relativistic limit, the effective neutrino magnetic moment is

$$\mu_{\nu_l}^2 (L, E_\nu) = \sum_j \left| \sum_k U_{lk}^* e^{\mp i \Delta m_{kj}^2 L / 2E_\nu} (\mu_{jk} - i\epsilon_{jk}) \right|^2, \quad (4.11)$$

where the minus sign in the exponent is for neutrinos and the plus sign for antineutrinos [195]. Therefore, the only difference between the effective neutrino and antineutrino magnetic moment is in the phase induced by neutrino oscillations. For experiments with baselines short enough that neutrino oscillations would not have time to develop ( $\Delta m^2 L / 2E_\nu \ll \sim 1$ ), such as the NOvA ND, the effective magnetic moment is the same for neutrinos and antineutrinos and is independent of the neutrino energy.

Since the effective magnetic moment depends on the initial neutrino flavour, it is different for experiments studying neutrinos from different sources. Additionally, experiments such as solar neutrino experiments, need to include matter effects on the neutrino oscillations. Therefore the reports on the value (or upper limit) of the effective neutrino magnetic moment are not directly comparable between different types of neutrino experiments.

### 4.1.2 Measuring the neutrino magnetic moment

The most sensitive method to measure the neutrino magnetic moment is the low energy elastic scattering of (anti)neutrinos on electrons [195]. The schematic diagram for this interaction is shown in Fig. 4.2, where the recoil electron's kinetic energy is defined as ( $T_e = E_{e'} - m_e$ ) and the recoil angle with respect to the incoming neutrino beam ( $\theta$ ) is shown.

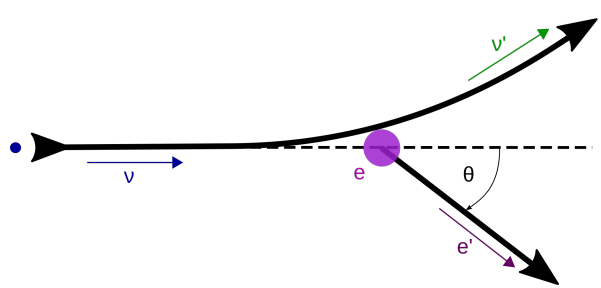


Figure 4.2: Neutrino-on-electron elastic scattering diagram

Since the  $\nu$ -on- $e$  interaction is governed by simple  $2 \rightarrow 2$  kinematics, it can be shown that

$$(P_\nu - P_{e'})^2 = (P_{\nu'} - P_e)^2, \quad (4.12)$$

$$m_\nu^2 + m_e^2 - 2E_\nu E_{e'} + 2E_\nu p_{e'} \cos \theta = m_\nu^2 + m_e^2 - 2E_{\nu'} m_e. \quad (4.13)$$

From the energy conservation

$$E_\nu + m_e = E_{\nu'} + E_{e'} = E_{\nu'} + T_e + m_e \Rightarrow E_{\nu'} = E_\nu - T_e \quad (4.14)$$

it follows that

$$E_\nu p_{e'} \cos \theta = E_\nu E_{e'} - E_{\nu'} m_e = E_\nu (T_e + m_e) - (E_\nu - T_e) m_e = T_e (E_\nu + m_e), \quad (4.15)$$

$$\cos \theta = \frac{E_\nu + m_e}{E_\nu} \sqrt{\frac{T_e^2}{E_{e'}^2 - m_e^2}} = \frac{E_\nu + m_e}{E_\nu} \sqrt{\frac{T_e^2}{T_e^2 + 2T_e m_e}}. \quad (4.16)$$

And finally

$$\cos \theta = \frac{E_\nu + m_e}{E_\nu} \sqrt{\frac{T_e}{T_e + 2m_e}}. \quad (4.17)$$

Which can be rearranged to get

$$T_e = \frac{2m_e E_\nu^2 \cos^2 \theta}{(E_\nu + m_e)^2 - E_\nu^2 \cos^2 \theta}. \quad (4.18)$$

The electron's kinetic energy is therefore constrained as

$$T_e \leq \frac{2E_\nu^2}{2E_\nu + m_e}, \quad (4.19)$$

which corresponds to the limit  $\cos \theta \rightarrow 1$  when the recoil electron goes exactly forward in the incident neutrino direction, as depicted in Fig. 4.3.

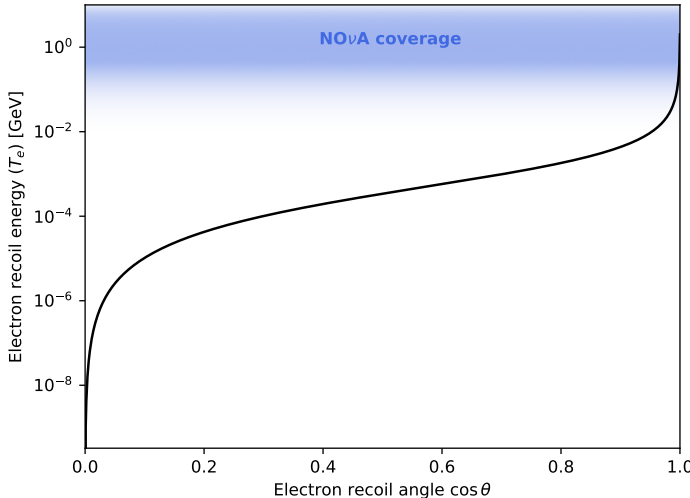


Figure 4.3: Relation between the recoil electron's kinetic energy and angle for the  $\nu$ -on-e elastic scattering. The coverage of the NOvA detectors for measuring the electron recoil energy is shown in blue. Only very forward electrons are therefore recorded in NOvA.

Considering  $E_\nu \sim \text{GeV}$ , it is useful to approximate  $\frac{m_e^2}{E_\nu^2} \rightarrow 0$ . Additionally, considering only very small electron recoil angles, meaning  $\theta^2 \cong (1 - \cos^2 \theta)$ , applied to Eq. 4.17 results in

$$T_e \theta^2 \cong T_e \left( 1 - \left( \frac{E_\nu + m_e}{E_\nu} \right)^2 \frac{T_e}{T_e + 2m_e} \right) = T_e \left( 1 - \left( 1 + \frac{2m_e}{E_\nu} \right) \frac{T_e}{T_e + 2m_e} \right), \quad (4.20)$$

therefore

$$T_e \theta^2 \cong \frac{2m_e T_e}{T_e + 2m_e} \left( 1 - \frac{T_e}{E_\nu} \right) = 2m_e \left( \frac{1}{1 + \frac{2m_e}{T_e}} \right) \left( 1 - \frac{T_e}{E_\nu} \right), \quad (4.21)$$

and finally

$$T_e \theta^2 \cong 2m_e \left( 1 - \frac{T_e}{E_\nu} \right) < 2m_e. \quad (4.22)$$

This is a strong limit that very clearly distinguishes the  $\nu$ -on-e elastic scattering events from other similar interactions involving single electron (mainly the  $\nu_e$ CC interactions).

### Neutrino magnetic moment cross section

In the ultra-relativistic limit, the neutrino magnetic moment interaction flips the neutrino helicity, while the SM weak interaction conserves it, which means it is possible to add the two contributions to the total  $\nu$ -on-e cross section incoherently (without interference terms) [195]:

$$\frac{d\sigma_{\nu\text{-on-e}}}{dT_e} = \left( \frac{d\sigma_{\nu\text{-on-e}}}{dT_e} \right)_{\text{SM}} + \left( \frac{d\sigma_{\nu\text{-on-e}}}{dT_e} \right)_{\text{MAG}}. \quad (4.23)$$

The SM contribution can be expressed as [16, 195]:

$$\left( \frac{d\sigma_{\nu\text{-on-e}}}{dT_e} \right)_{\text{SM}} = \frac{2G_F^2 m_e}{\pi} \left\{ g_1^2 + g_2^2 \left( 1 - \frac{T_e}{E_\nu} \right)^2 - g_1 g_2 \frac{m_e T_e}{E_\nu^2} \right\}, \quad (4.24)$$

where the coupling constants  $g_1$  and  $g_2$  differ between neutrino flavours and between neutrinos and antineutrinos. Their values are:

$$g_1^{\nu_e} = g_2^{\bar{\nu}_e} = \sin^2 \theta_W + 1/2, \quad g_2^{\nu_e} = g_1^{\bar{\nu}_e} = \sin^2 \theta_W, \quad (4.25)$$

$$g_1^{\nu_{\mu,\tau}} = g_2^{\bar{\nu}_{\mu,\tau}} = \sin^2 \theta_W - 1/2, \quad g_2^{\nu_{\mu,\tau}} = g_1^{\bar{\nu}_{\mu,\tau}} = \sin^2 \theta_W, \quad (4.26)$$

where  $\sin^2 \theta_W \cong 0.23$ .

The total SM cross section, and therefore the number of SM  $\nu$ -on-e interactions, depends on the neutrino energy and the minimum measured electron recoil energy. However, in general the cross section for  $\nu_e$  is about 2.5 times larger than for the  $\bar{\nu}_e$ , about 6 times larger than for  $\nu_{\mu/\tau}$  and about 7 times larger than for  $\bar{\nu}_{\mu/\tau}$ .

The neutrino magnetic moment contribution is [195, 201]:

$$\left( \frac{d\sigma_{\nu\text{-on-e}}}{dT_e} \right)_{\text{MAG}} = \frac{\pi \alpha^2}{m_e^2} \left( \frac{1}{T_e} - \frac{1}{E_\nu} \right) \left( \frac{\mu_{\nu_l}}{\mu_B} \right)^2, \quad (4.27)$$

where  $\alpha$  is the fine structure constant and  $\mu_{\nu_l}$  is the effective magnetic moment of  $\nu_l$ . The total cross section now only depends on the neutrino energy and on the effective magnetic moment, but is the same for neutrinos and antineutrinos.

The comparison of the SM and the neutrino magnetic moment differential cross sections is shown in Fig.4.4. Whereas the SM cross section is approximately uniform for  $T_e \rightarrow 0$ , the neutrino magnetic moment cross section rises to infinity. However, this reach is limited by the experimental capabilities of detecting electrons with very low energies. The (possible) NOvA coverage is shown with a shaded blue region, with current capability reaching  $T_e = 0.5$  GeV. Future analyses might extend this reach to lower  $T_e$ , with the lowest possible detectable electron recoil energy  $T_{e,min} \approx 0.01$  GeV, as discussed in Sec. 2.2.

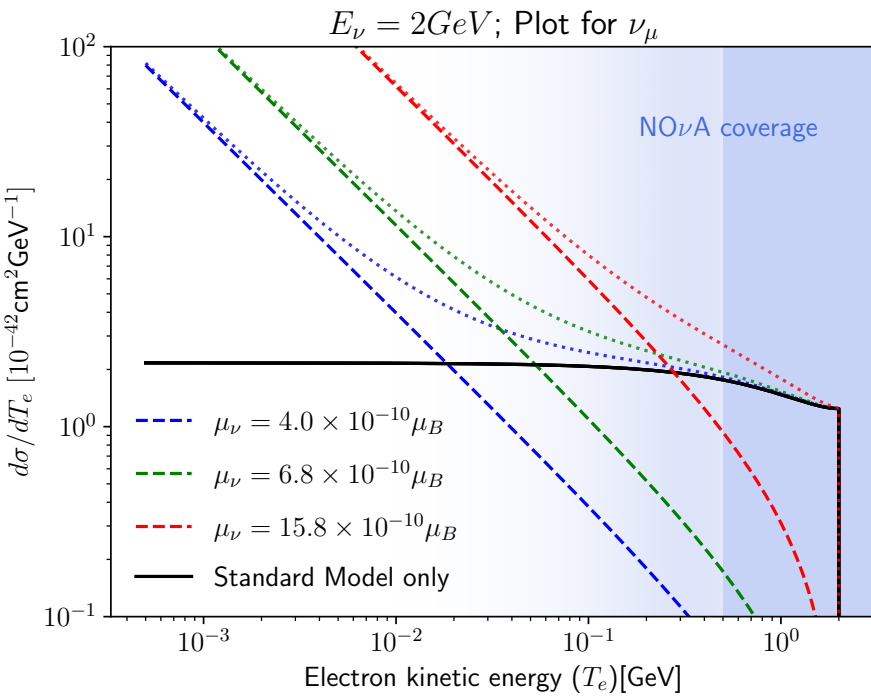


Figure 4.4: Comparison of the neutrino magnetic moment (coloured) and the SM (black) cross sections for the  $\nu$ -on-e elastic scattering. Different colours depict different values of the neutrino magnetic moment, with red corresponding to the previous NOvA measurement, green the LSND result, and blue a possible ultimate NOvA sensitivity, as discussed in the introduction to this chapter. Dashed lines are the individual cross sections and dotted lines are the added total cross section with the standard model contribution. NOvA coverage of electron recoil energies is shown in shaded blue.

Calculating the ratio of the neutrino magnetic moment and the SM cross sections, as shown in Fig. 4.5, can serve as a proxy to estimate the number of neutrino magnetic

moment events in relation to the predicted number of **SM** events, if the  $E_\nu$  and  $T_e$  are known. Additionally, comparing the ratio of the total cross sections can reveal the expected total number of neutrino magnetic moment events as a function of the predicted number of **SM** events. Considering  $E_\nu = 2 \text{ GeV}$ ,  $\mu_\nu = 6.8 \times 10^{-10} \mu_B$  (current best limit for  $\nu_\mu$  from LSND), and integrating differential cross sections for  $\nu_\mu$  in Eq. 4.24 and 4.27 from  $T_{e,min}$  to  $T_{e,max} \rightarrow 2 \text{ GeV}$  results in

$$\frac{\sigma_{\text{MAG}}}{\sigma_{\text{SM}}} \approx \begin{cases} 0.035 & T_{e,min} = 0.5 \text{ GeV}, \\ 0.14 & T_{e,min} = 0.01 \text{ GeV}. \end{cases} \quad (4.28)$$

Therefore, at the current **NOvA** detection capabilities, there are about 0.035 times as many neutrino magnetic moment  $\nu$ -on-e events than **SM** ones. This can be compared with the expected statistical uncertainty on the **SM** background, which in the case of Poisson distributed events is the square root of the number of predicted events. Consequently, it is possible to assess the minimal number of **SM**  $\nu$ -on-e events necessary for the magnetic moment signal to be detected above the **SM** background (without considering systematic uncertainties) as

$$N_{\text{SM}} > 1/0.035^2 \approx 816. \quad (4.29)$$

However, this approximation is calculated only for one value of  $E_\nu$ , but can be used to assess the sensitivity of the experiment.

As can be seen in Fig. 4.4 and Fig. 4.5, the magnetic moment contribution exceeds the **SM** contribution for low enough  $T_e$ . This can be approximated as [195]:

$$T_e \lesssim \frac{\pi^2 \alpha^2}{G_F^2 m_e^3} \left( \frac{\mu_\nu}{\mu_B} \right)^2 \simeq 2.9 \times 10^{19} \left( \frac{\mu_\nu}{\mu_B} \right)^2 [\text{MeV}], \quad (4.30)$$

which does not depend on the neutrino energy. Therefore, experiments sensitive to lower energetic electrons are significantly more sensitive to the neutrino magnetic moment.

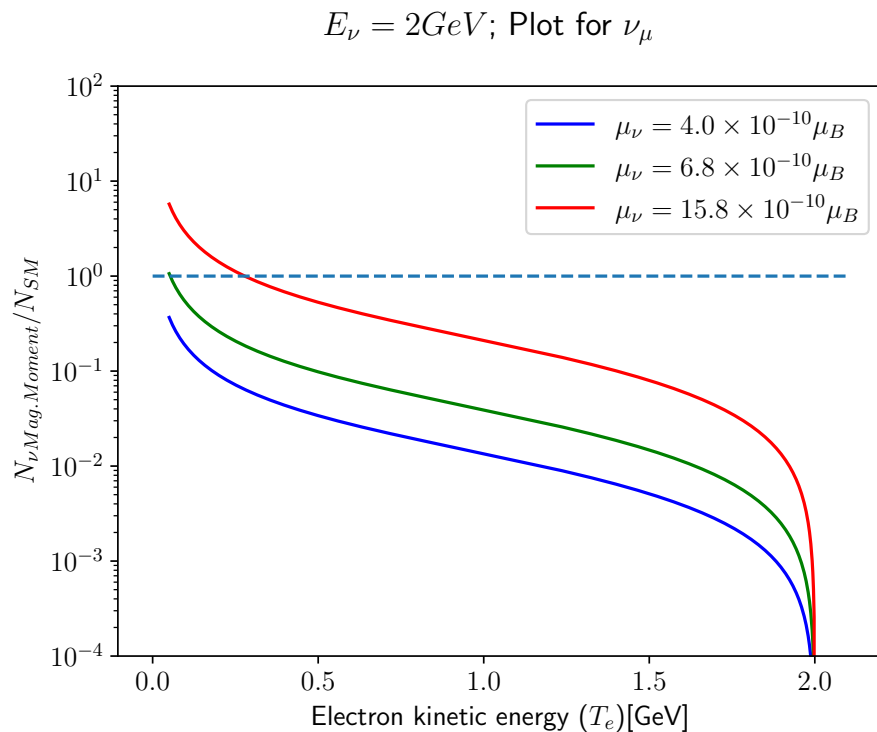


Figure 4.5: Ratio of the neutrino magnetic moment cross section to the SM cross section for the  $\nu$ -on-e elastic scattering of 2 GeV  $\nu_\mu$ . Different colours depict different effective muon neutrino magnetic moment values, with red corresponding to the previous NOvA measurement, green the LSND result, and blue a possible ultimate NOvA sensitivity, as discussed in the introduction to this chapter.

## 4.2 Analysis overview

Our analysis strategy for measuring the effective muon neutrino magnetic moment in the [NOvA ND](#) is based on comparing the total number of reconstructed and selected events in data with the prediction. The predicted events consist of the signal, which depends on the size of the effective muon neutrino magnetic moment, and of the background, which corresponds to the [SM](#)-only (null) hypothesis without any neutrino magnetic moment. We define the signal as true  $\nu\text{-on-e}$  elastic scattering interactions, created with the use of the neutrino magnetic moment cross section instead of the [SM](#) cross section, as described in Sec. 4.1.2. Additionally, the signal events are required to have their true interaction vertex contained within the [ND](#) to exclude events originating from outside of the detector.

The data used in this analysis were collected from the start of [NOvA ND](#) data taking on the August 22<sup>nd</sup>, 2014, until February 3<sup>rd</sup>, 2021. This is the [ND](#) data that were used in the latest [NOvA](#) neutrino oscillations result [54], with an additional year. Although more data have been collected since February 2021, they are still being processed and are not available at the time of writing this thesis. The total exposure of the data sample is approximately  $13.8 \times 10^{20}$  [POT](#). This exposure is used throughout this chapter to scale the predicted distributions and number of events.

This analysis uses the standard [NOvA](#) simulation and reconstruction tools, as were discussed in Sec. 2.4 and 2.5. The simulation was created with approximately four times larger statistics than the data to limit statistical uncertainties from simulation. The total exposure for the simulation is approximately  $55.4 \times 10^{20}$  [POT](#). For the systematic uncertainty studies only a portion of this full sample is used, specifically  $19.3 \times 10^{20}$  [POT](#).

Corrections for known limitations in the simulation are applied in the form of analysis weights applied to each event based on how it is affected by specific variations in the simulation. This includes the corrections for the neutrino beam prediction based on the external measurements used by the [PPFX](#) (Sec. 2.4), and, for the non- $\nu\text{-on-e}$  background only, also the internal and external measurements that constrain the neutrino interaction prediction inside [GENIE](#).

The cross section corrections are not applied to the  $\nu\text{-on-e}$  events, as they are assumed to be known precisely from theory. However, the [GENIE](#) [MC](#) simulation

only considers tree-level SM  $\nu$ -on-e interactions [192], as described in Sec. 4.1.2, and doesn't account for any higher order terms, which are described by radiative corrections. Radiative corrections can be expressed by two adjustments to the tree-level SM  $\nu$ -on-e cross section [202]. First, the values of the weak coupling constants are changed as [203]

$$g_1^{\nu e} \rightarrow 0.7276, \quad g_1^{\nu \mu} \rightarrow -0.2730, \quad g_2 \rightarrow 0.2334. \quad (4.31)$$

Second, there are additional terms added to the cross section equation. Considering only one-loop corrections, the full  $\nu$ -on-e cross section can be expressed as<sup>1</sup> [204]

$$\left( \frac{d\sigma_{\nu\text{-on-e}}}{dy} \right)_{\text{Rad. Corr.}} = \frac{G_F^2 s}{\pi} \left\{ g_1^2 \left( 1 + \frac{\alpha}{\pi} X_1 \right) + g_2^2 (1-y)^2 \left( 1 + \frac{\alpha}{\pi} X_2 \right) - g_1 g_2 \frac{m_e y}{E_\nu} \right\}, \quad (4.32)$$

where

$$y = \frac{T_e + E_\gamma}{E_\nu}, \quad (4.33)$$

$s = 2E_\nu m_e + m_e^2$  is the Mandelstam variable,

$$X_1 = -\frac{2}{3} \log \left( \frac{2yE_\nu}{m_e} \right) + \frac{y^2}{24} - \frac{5y}{12} - \frac{\pi^2}{6} + \frac{23}{72} \quad (4.34)$$

and

$$X_2 = -\frac{2}{3} (1-y)^2 \log \left( \frac{2yE_\nu}{m_e} \right) - \frac{y^2}{18} - \frac{\pi^2}{6} (1-y)^2 - \frac{2y}{9} + \frac{23}{72}. \quad (4.35)$$

In practice, radiative corrections can be implemented as a weight, where each true  $\nu$ -on-e event is weighted by a ratio

$$\text{weight}_{\text{Rad. Corr.}}(E_\nu, T_e) = \left( \frac{d\sigma_{\nu\text{-on-e}}}{dy} \right)_{\text{Rad. Corr.}} / \left( \frac{d\sigma_{\nu\text{-on-e}}}{dy} \right)_{\text{GENIE 3}} ; \quad (4.36)$$

Analogically to the radiative correction weight, it is possible to create a neutrino magnetic moment weight as a ratio between the neutrino magnetic moment and the SM differential cross sections for the  $\nu$ -on-e interactions. This can then serve to predict the number of  $\nu$ -on-e events created by the neutrino magnetic moment interac-

---

<sup>1</sup>There is technically a third correction term  $X_3$  by the  $g_1 g_2$  term, which is however negligible for  $E_\nu \sim \text{GeV}$ .

tion (which make up the signal), without the need for an additional simulation. This is possible thanks to the theoretically very well understood properties of the  $\nu$ -on-e interaction, as described in Sec. 4.1.2. Therefore, the signal sample is created from the true  $\nu$ -on-e sample, with the magnetic moment weight applied. The weight has a form:

$$\text{weight}_{\nu\text{-Mag. Mom.}}(E_\nu, T_e) = \left( \frac{d\sigma_{\nu\text{-on-e}}}{dy} \right)_{\nu\text{-Mag. Mom.}} \Bigg/ \left( \frac{d\sigma_{\nu\text{-on-e}}}{dy} \right)_{\text{GENIE 3}}, \quad (4.37)$$

where

$$\left( \frac{d\sigma_{\nu\text{-on-e}}}{dy} \right)_{\nu\text{-Mag. Mom.}} = E_\nu \left( \frac{d\sigma_{\nu\text{-on-e}}}{dT_e} \right)_{\nu\text{-Mag. Mom.}}. \quad (4.38)$$

Due to the relatively low cross section of the  $\nu$ -on-e interaction, the nominal simulation sample contains very few  $\nu$ -on-e events, which could result in a significant statistical uncertainty from simulation. To avoid this, we created a  $\nu$ -on-e-enhanced simulation sample, which is mainly made up of  $\nu$ -on-e events with a total exposure of  $1.72 \times 10^{24}$  POT. There are a few non- $\nu$ -on-e background events overlaid on top of the  $\nu$ -on-e events to properly account for the possible reconstruction effects of the pileup of neutrino interactions in a single spill [192], since in the real detector, the hits from the true  $\nu$ -on-e interaction can be clustered together into another interaction, or additional hits can be clustered together into the  $\nu$ -on-e event. To save up on unnecessary disk space and processing usage, the enhanced  $\nu$ -on-e sample does not include any cross section related parameters and variables, as the  $\nu$ -on-e interaction is assumed to be known exactly from theory. Therefore, we do not apply cross section weights or account for cross section systematic uncertainties for  $\nu$ -on-e events.

The cross section tuning procedure in NOvA (Sec. 2.4) applies large weights to MEC events in some parts of the parameter space. However, after the full event selection (Sec. 4.3) only a small number of MEC events remain in the detector. This was shown to be an issue especially for the  $\nu_e$ CC MEC events [192]. Applying large tuning corrections to a small number of events results in large statistical fluctuations. To avoid this, we created another special sample with enhanced number of  $\nu_e$ CC MEC events, following the same procedure as for the  $\nu$ -on-e-enhanced sample, with an exposure of  $1.99 \times 10^{24}$  POT.

A summary of the simulation samples and analysis weights for the four different

types of signal and background components is shown in Tab. 4.1. In the following chapter, the  $\nu_e$ CC MEC background is added into the ‘Other background’ sample, even though it is created from a separate simulation.

Table 4.1: Overview of the simulation samples and analysis weight used for the different signal and background components.

Signal type	Sample	Weight
Signal	Enhanced $\nu$ -on-e	Flux & $\nu$ Mag. Moment
$\nu$ -on-e background	Enhanced $\nu$ -on-e	Flux & Rad. Corr.
$\nu_e$ CC MEC background	Enhanced $\nu_e$ CC MEC	Flux & Cross Sec.
Other background	Nominal ND	Flux & Cross Sec.

## 4.3 Event selection

We are searching for  $\nu$ -on-e elastic scattering events, characterised by a single very forward going electron shower, specifically focusing on low electron recoil energies. The main backgrounds for our analysis come from  $\nu_e$ CC interactions, which produce an electron with additional activity, and interactions that produce  $\pi^0$ , which decays into two photons producing electromagnetic showers, where each can look similar to the  $\nu$ -on-e signal. Additionally, there are  $\nu_\mu$ CC interactions, which are generally easy to distinguish from our signal, however, their very high abundance in the NOvA ND makes them a dominant background nevertheless.

I explain the motivation behind each cut of the event selection and discuss their effect on the neutrino magnetic moment events below. I also consider possible improvements to the event selection for a future (re-)analysis.

The strategy for event selection is as follows. First, I remove events that failed reconstruction or data collection, described in Sec. 4.3.1 and 4.3.2. Then, I apply pre-selection cuts that remove obvious background (Sec. 4.3.3), while limiting the reduction of the signal efficiency to about 0.25 %. Following this, I apply the containment cuts (Sec. 4.3.4) that remove events that are either not fully contained within the detector, or events that originate from outside of the detector, such as rock muons. Afterwards, I perform a cut-based Multi Variate Analysis (MVA) on a selection of variables useful for distinguishing the signal from the background, discussed in Sec. 4.3.5,

and evaluate their combined performance on the signal selection. I choose the cut values that result in the best statistical significance, based on a chosen Figure Of Merit (FOM). Given that we are searching for a very limited number of signal events on top of a large background, I chose a simple statistics-only FOM

$$\text{FOM} = \frac{\text{Signal}}{\sqrt{\text{Background}}}. \quad (4.39)$$

The summary of the cut values for the event selection of neutrino magnetic moment signal is presented in Tab. 4.2, showing the label for the event selection variable, its description and the cut value chosen. After the full event selection, the predicted number of signal events for  $\mu_\nu = 10^{-9}\mu_B$  is 56.80 and the total number of background events under the SM hypothesis is 700.33.

### 4.3.1 Data collection quality

To ensure good data quality, we apply the following criteria to data (not applied to simulation) [205]. A cut on the time of each spill relative to other spills and on the exposure of each spill, where every spill is required to have at least  $2^{12}$  POT. Additionally, the current in the focusing horn is required to be within  $-202\text{ kA} < I_{Horn} < -196.4\text{ kA}$ , the position of the beam to be within  $\pm 2\text{ cm}$  in both x and y axis, and that the width of the beam to be within 0.57 and 1.58 cm. Furthermore, incomplete events, or events with issues in one or more DCMs are removed.

### 4.3.2 Reconstruction quality

As described in Sec. 2.5, electrons are reconstructed by slicing, followed by vertexing, then clustering into prongs. To identify electrons we require a valid reconstructed vertex and at least one reconstructed prong. Even though electrons only consist of a single shower, we don't reject events with more than one prong in a slice, as the reconstruction can wrongly assign noise hits as a separate prong. These false secondary prongs can be removed later in the event selection.

Figure 4.6 and Tab. 4.3 show that about 68 % of signal events do not have a valid reconstructed vertex. This is due to the concentration of signal events at very low electron recoil energies, which results in events that can consist of a small number

of hits, or even a single hit. As can be seen in the bottom plot in Fig. 4.6, events with small true electron recoil energies have much smaller vertex reconstruction efficiency than the higher energetic electrons. However, ongoing work is improving the vertex reconstruction in the NOvA detectors with a use of ML instead of the currently used Hough transform combined with Elastic Arms [206]. Improving NOvA vertex reconstruction at low energies can enhance our event selection in the future.

Table 4.2: Summary of the variables and their cut values for the event selection of neutrino magnetic moment signal. Showing the category of the event selection variable, its label, description and the cut value chosen.

	<b>Label</b>	<b>Description</b>	<b>Cut</b>
<b>Reco Qual.</b>	<b>Valid Vtx</b>	Valid reconstructed vertex	$> 0$
	<b>Nº Prongs</b>	Number of reconstructed prongs	$> 0$
	<b>Hits / Plane</b>	Number of hits per plane	$< 6$
	<b>Low <math>E_{Shower}</math></b>	Low cut on calorimetric energy of the most energetic shower	$> 0.5 \text{ GeV}$
<b>Pre-selection</b>	<b>Nº Hits Loose</b>	Preliminary cut on the total number of hits for all prongs in a slice	$< 280$
	<b>Prong Length</b>	Length of the longest prong	$< 640 \text{ cm}$
	<b><math>E\theta^2</math> Loose</b>	Preliminary cut on the product of the calorimetric energy and angle squared of the leading shower	$< 0.064 \text{ GeV} \times \text{rad}^2$
<b>Fiducial</b>	<b>Vertex</b>	x position	$> -177 \text{ cm}$
		y position	$< 177 \text{ cm}$
		z position	$> -177 \text{ cm}$ $< 177 \text{ cm}$ $> 50 \text{ cm}$ $< 1170 \text{ cm}$
	<b>Containment</b>	Minimum hit position in x Maximum hit position in x Minimum hit position in y Maximum hit position in y Minimum hit position in z Maximum hit position in z	$> -177 \text{ cm}$ $< 177 \text{ cm}$ $> -185 \text{ cm}$ $< 177 \text{ cm}$ $> 55 \text{ cm}$ $< 1270 \text{ cm}$
<b>Selection</b>	<b><math>E_{Shower}/E_{Tot}</math></b>	Fraction of energy contained in the most energetic shower	$> 0.91$
	<b>Nº Hits</b>	Total number of hits for all prongs in a slice	$< 116$
	<b>High <math>E_{Shower}</math></b>	Calorimetric energy of the most energetic shower	$< 1.4 \text{ GeV}$
	<b><math>\nu\text{-on-e ID}</math></b>	CVN-based $\nu\text{-on-e}$ identifier	$> 0.65$
	<b><math>E\pi^0</math> ID</b>	CVN-based $\nu\text{-on-e}$ and $\pi^0$ identifier	$> 0.63$
	<b><math>E\theta^2</math></b>	Product of the calorimetric energy and angle squared of the leading shower	$< 0.0048 \text{ GeV} \times \text{rad}^2$

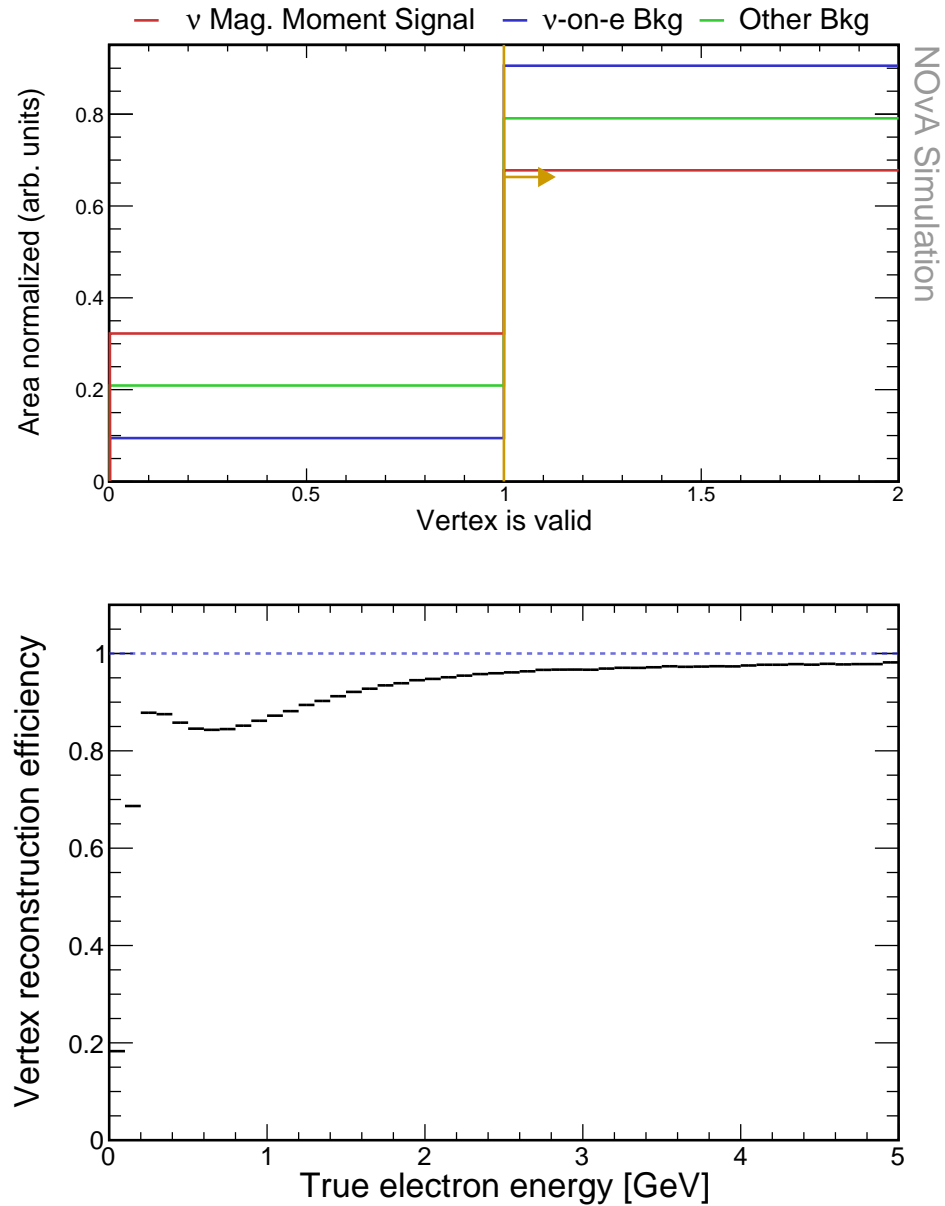


Figure 4.6: Top: Relative comparison of the signal (red),  $\nu$ -on-e background (blue), and other background (green) events for the vertex reconstruction quality selection. Each histogram is area-normalised and the first bin corresponds to events without a valid vertex and second bin to events with correctly reconstructed vertex. The yellow line indicates the chosen cut value, where all events have to have a valid reconstructed vertex. Bottom: profile histogram of the ‘vertex is valid’ variable as a function of the true electron energy for the true signal events, showing the significant drop in vertex reconstruction efficiency at low electron recoil energies. No selection was applied prior to making these plots.

Additionally, we limit the number of hits per plane to  $< 6$ . This is to remove the so-called ‘FEB flashers’, which are caused by such a high energy deposit in one cell, that it affects all the other channels on the same APD [207]. The cut value was chosen so that it removes approximately 0.25 % signal events, which is the same criterion as is used for the pre-selection cuts described below. Relative comparisons between signal and background for the number of prongs and the number of hits per plane are shown in Fig. 4.7.

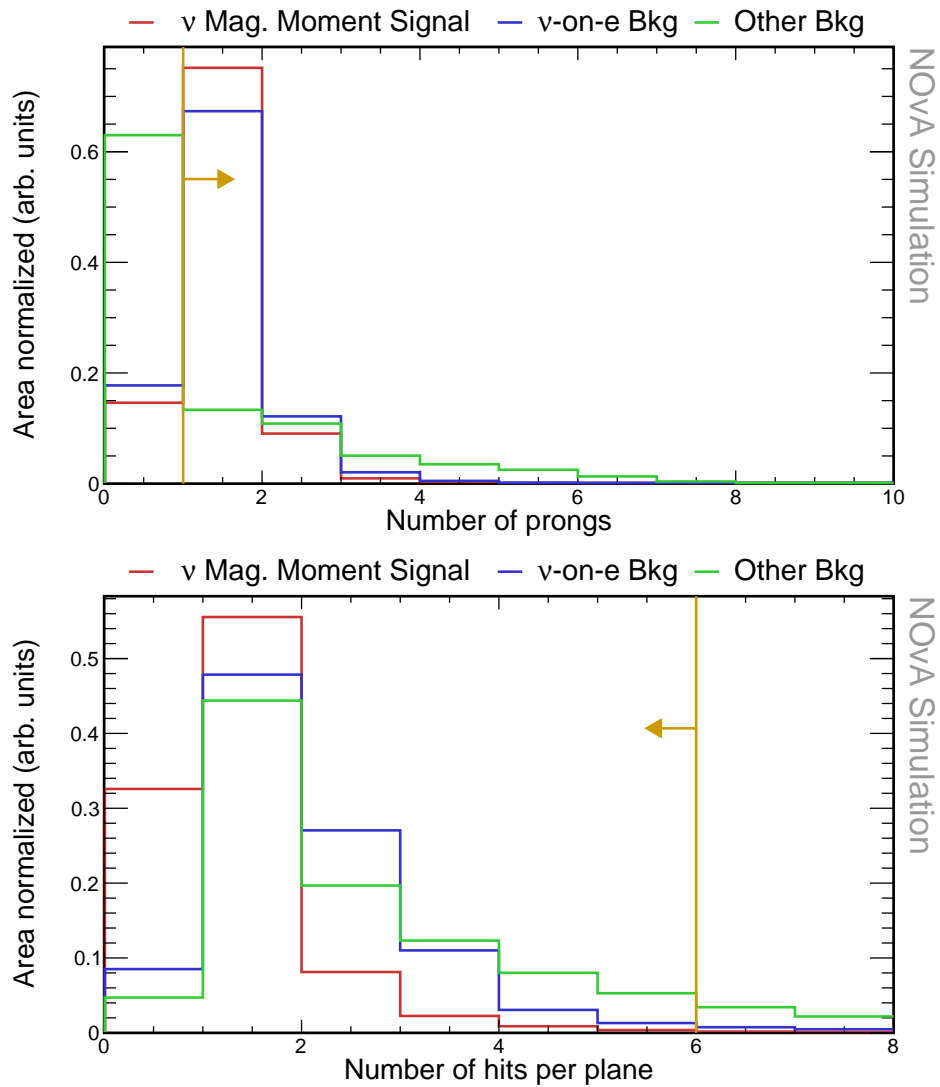


Figure 4.7: Relative comparison of signal (red),  $\nu$ -on-e background (blue), and other background (green) events in the number of prongs (top) and the number of hits per plane (bottom) distributions. Events in both plots are required to have a valid reconstructed vertex and in the bottom plot also at least one reconstructed prong. Yellow lines indicate the cut values for the shown variables, with arrows pointing towards the preserved events. All histograms are area-normalised.

Furthermore, the reconstructed calorimetric energy of the primary shower is re-

quired to be  $E_{cal} > 0.5 \text{ GeV}$  as shown in Fig. 4.8. This is primarily due to the limitations of the currently used **CVN**-based  $\nu\text{-on-e}$  identifiers described in Sec. 4.3.5, which were developed and validated for  $\nu\text{-on-e}$  events with energies above this limit, to avoid the large background at low energies. However, due to the nature of the neutrino magnetic moment signal, which is concentrated at low electron recoil energies, this cut also removes a majority of our signal events, specifically 66.8 %. This large reduction severely impacts the significance of our measurement. On the other hand, it also marks potentially the most impactful improvement available in a future re-analysis. There are other event identifying algorithms available in **NOvA** that could be explored for  $\nu\text{-on-e}$  events to leverage the low energy sample. Additionally, it is possible to develop a purpose-built  $\nu\text{-on-e}$  identifier focusing on low electron recoil energies.

Table 4.3: Event selection cutflow table for the reconstruction quality cuts showing the number of events and the relative efficiency of each cut for each signal sample. The relative efficiency is calculated as number of events remaining after applying the corresponding cut divided by number of events for all the previous cuts. All the cuts are listed in sequence as they are applied.

<b>Selection</b>	<b>Signal</b>		<b><math>\nu\text{-on-e}</math> bkg</b>		<b>Other bkg</b>	
	$N_{evt}$	$\epsilon_{rel} (\%)$	$N_{evt}$	$\epsilon_{rel} (\%)$	$N_{evt}$	$\epsilon_{rel} (\%)$
<b>No Cut</b>	817.34	100	$6.82 \times 10^3$	100	$2.96 \times 10^8$	100
<b>Valid Vtx</b>	553.86	67.76	$6.17 \times 10^3$	90.55	$2.34 \times 10^8$	79.10
<b>Nº Prongs</b>	472.90	85.38	$5.08 \times 10^3$	82.25	$8.66 \times 10^7$	37.00
<b>Hits / Plane</b>	471.14	99.63	$4.97 \times 10^3$	97.85	$7.32 \times 10^7$	89.56
<b>Low <math>E_{Shower}</math></b>	156.37	33.19	$3.53 \times 10^3$	71.09	$4.06 \times 10^7$	55.12

### 4.3.3 Pre-selection

Pre-selection aims to remove obvious background events without significantly affecting the signal. The criterion we chose for the selection of these cuts is determined by the reduction of the signal efficiency by approximately 0.25 % with each cut. This results in the total pre-selection reduction of the signal efficiency by approximately 1 %.

The first two variables used for our pre-selection are the same as were used in the event selection for the  $\nu_e$  appearance **ND** constraint for the three flavour neutrino oscillation measurements [54]. As we are searching for single electron showers, we

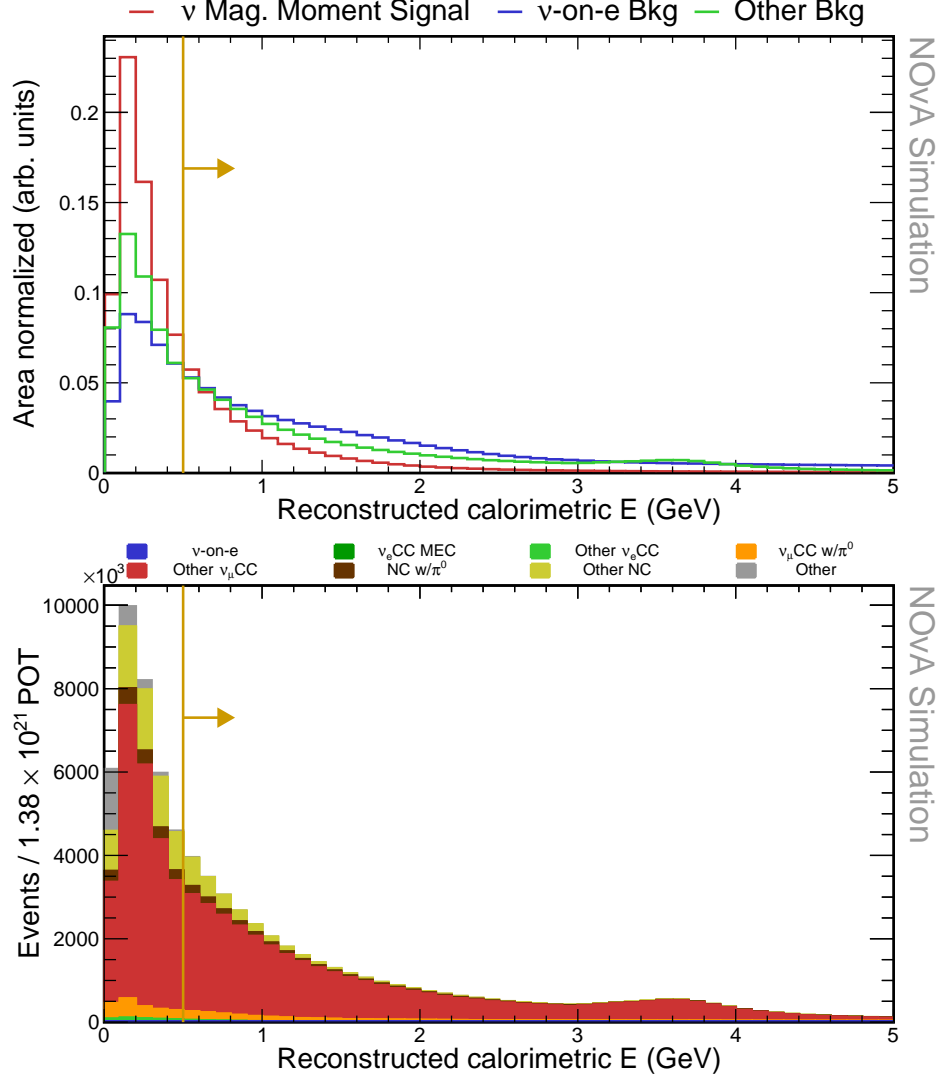


Figure 4.8: Top: Relative comparison of signal (red),  $\nu$ -on-e background (blue), and other background (green) events in the reconstructed calorimetric energy distribution. All histograms are area-normalised. Bottom: Decomposition of background into various sub-samples, normalised to the data POT exposure. Events in both plots are required to have a valid reconstructed vertex, at least one reconstructed prong and less than 6 hits per plane. Yellow lines indicate the cut value for the reconstructed calorimetric energy, with arrows pointing towards the preserved events.

can reduce backgrounds with multiple final state particles by limiting the total activity in the detector. Specifically, we require that the total number of hits assigned to all the reconstructed prongs is  $< 280$ . This is shown in Fig. 4.9. In general, the main background in NOvA consists of the  $\nu_\mu$ CC interactions, which are characterised by long muon tracks. We therefore limit the length of the longest reconstructed prong to be  $< 640$  cm, as shown in Fig. 4.10.

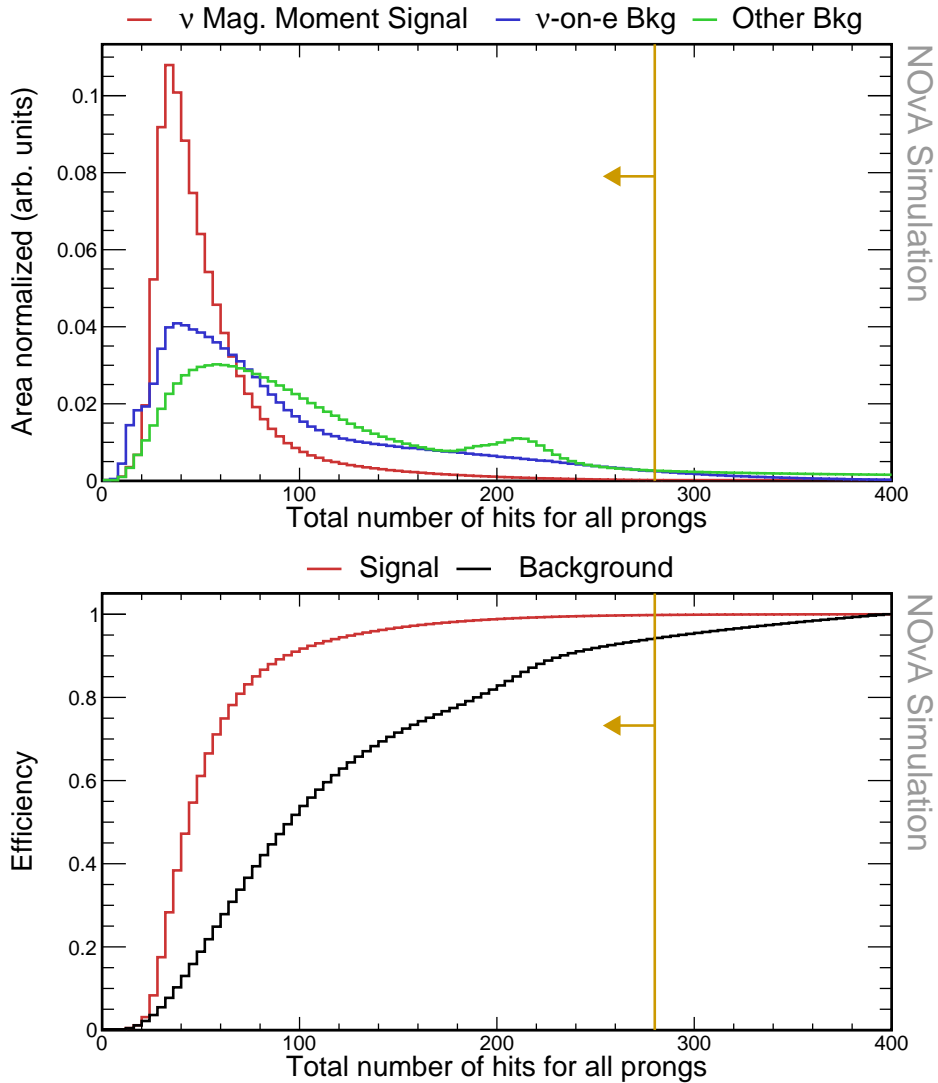


Figure 4.9: Top: Relative comparison of signal (red),  $\nu$ -on-e background (blue), and other background (green) events in the distribution of total number of hits from all reconstructed prongs in the slice. All histograms are area-normalised. Bottom: Cumulative signal (red) and background (black) efficiency calculated as number of signal/background events left of the bin divided by the total number of signal/background events. Yellow lines indicate the cut value for the maximum number of hits, with arrows pointing towards the preserved events. The reconstruction quality cuts were applied before making these plots.

Additionally, as discussed in Sec. 4.1.2, simple  $2 \rightarrow 2$  kinematics dictate that

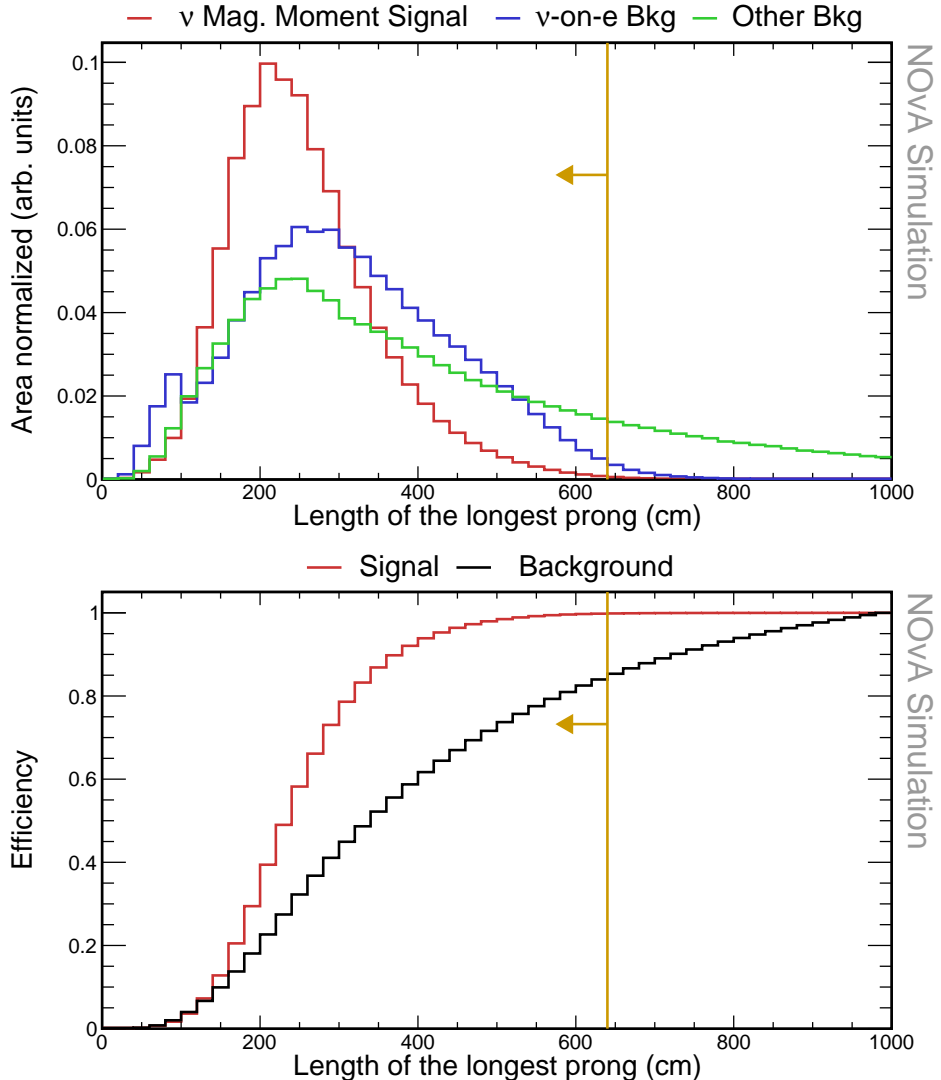


Figure 4.10: Top: Relative comparison of signal (red),  $\nu$ -on-e background (blue), and other background (green) events in the distribution of the length of the longest reconstructed prong in slice. All histograms are area-normalised. Bottom: Cumulative signal (red) and background (black) efficiency calculated as number of signal/background events left of the bin divided by the total number of signal/background events. Yellow lines indicate the cut value for the maximum length of the longest prong, with arrows pointing towards the preserved events. The reconstruction quality cuts and the number of hits cut were applied before making these plots.

the true electron recoil energy and angle for the  $\nu$ -on-e interaction are limited by  $E\theta^2 < 2m_e$ . This can be used to distinguish  $\nu$ -on-e elastic scattering from  $\nu_e$ CC interactions, which also have an electron in the final state. However, due to unavoidable reconstruction deficiencies, the reconstructed  $E\theta^2$  does not have such a strict cut-off value, and we are placing the pre-selection cut at  $E\theta^2 < 0.064$ , as can be seen in Fig. 4.11. Furthermore, some of the signal events can be reconstructed with the opposite direction with respect to the beam, which would result in  $\theta \approx \pi$  rad. However, this reconstruction failure likely does not impact other reconstructed qualities and these events should be preserved for the final sample. For that reason, we are calculating the angle between the outgoing electron and the neutrino beam direction as  $\arccos(\text{abs}(\cos \theta))$ , which gives the same value whether the shower is reconstructed forward or backwards.

The effect of the pre-selection cuts on the signal and background samples are summarised in Tab. 4.4, where the first row lists the number of events after applying all the reconstruction quality cuts from Sec. 4.3.2. All three of the variables used for the pre-selection are employed again in the MVA, as described in Sec. 4.3.5.

Table 4.4: Pre-selection cutflow table showing the number of events and the relative efficiency of each cut for each signal sample. The relative efficiency is calculated as number of events remaining after applying the corresponding cut divided by number of events for all the previous cuts. All the cuts are listed in sequence as they are applied. The top row corresponds to the sample after applying the reconstruction quality cuts.

<b>Selection</b>	<b>Signal</b>		<b><math>\nu</math>-on-e bkg</b>		<b>Other bkg</b>	
	$N_{\text{evt}}$	$\epsilon_{\text{rel}} (\%)$	$N_{\text{evt}}$	$\epsilon_{\text{rel}} (\%)$	$N_{\text{evt}}$	$\epsilon_{\text{rel}} (\%)$
<b>Reco Quality</b>	156.37	100	$3.53 \times 10^3$	100	$4.28 \times 10^7$	100
<b>No Hits Loose</b>	156.05	99.79	$3.41 \times 10^3$	96.46	$3.61 \times 10^7$	84.35
<b>Prong Length</b>	155.7	99.78	$3.37 \times 10^3$	98.85	$2.61 \times 10^7$	72.36
<b><math>E\theta^2</math> Loose</b>	155.14	99.64	$3.33 \times 10^3$	98.83	$8.83 \times 10^6$	33.82

#### 4.3.4 Fiducial and containment cuts

To ensure all the deposited energy of the recoil electron is contained within the detector and to remove events originating outside of the detector (such as rock muons for the ND), we constrain the position of the reconstructed vertex and all the prongs in the slice. The decision on where to place the exact cut values is made based on the maximum FOM value.

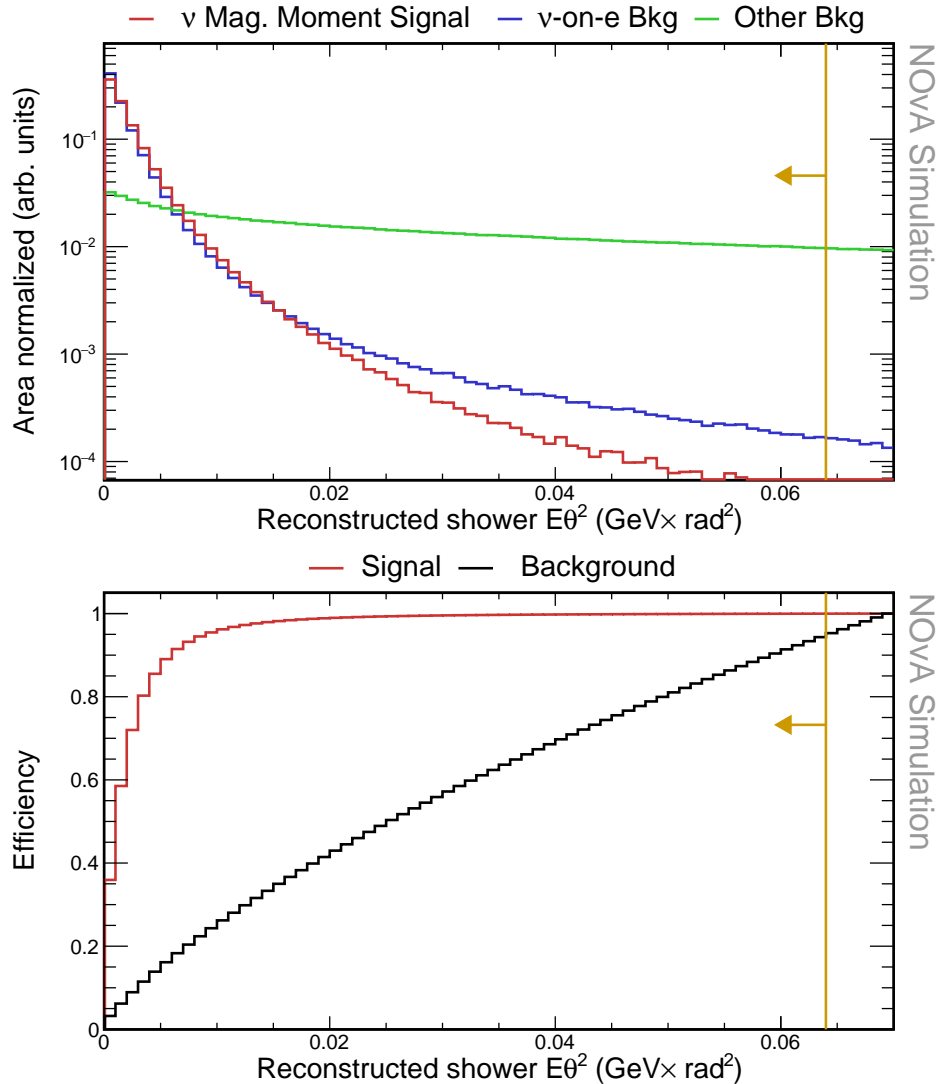


Figure 4.11: Top: Relative comparison of signal (red),  $\nu$ -on-e background (blue), and other background (green) events in the distribution of the reconstructed energy of the leading shower multiplied by its angle from the incoming neutrino beam direction squared. All histograms are area-normalised with logarithmic y axis. Bottom: Cumulative signal (red) and background (black) efficiency calculated as number of signal/background events left of the bin divided by the total number of signal/background events. Yellow lines indicate the cut value for the depicted variable, with arrows pointing towards the preserved events. The reconstruction quality cuts, the number of hits cut, and the length of the longest prong cuts were applied before making both of these plots.

The reconstructed vertex is required to be within the fiducial volume, which represents a well-understood volume of the detector. To select the fiducial volume, we investigate distributions of the reconstructed vertex in the x, y and z direction, shown in Fig. 4.12, 4.13 and 4.14 respectively. Basic reconstruction quality and pre-selection cuts are applied to make these distributions. Additionally, for the x and y position distributions, we require that the vertex is not placed inside of the Muon Catcher by requiring  $Vtx_Z < 1270$  cm, as it can significantly affect these distributions. The slanted distributions in x and y are caused by the off-axis nature of the NuMI beam and the periodic peaks are due to a combination of the detector structure and the choice of binning.

The reconstructed vertex is required to be contained within the following volume:

$$-175 \text{ cm} < Vtx_X < 175 \text{ cm}, \quad (4.40)$$

$$-175 \text{ cm} < Vtx_Y < 175 \text{ cm}, \quad (4.41)$$

$$95 \text{ cm} < Vtx_Z < 1170 \text{ cm}. \quad (4.42)$$

Furthermore, we constrain the extreme positions (minimum and maximum) of all the hits within the most energetic prong, which is assumed to represent the electron shower for the signal events. We apply the reconstruction quality, pre-selection and fiducial (vertex position) cuts to their distributions, shown in Fig. 4.15-4.20. The extreme hit positions are required to be within the following volume:

$$-175 \text{ cm} < \min_X, \max_X < 175 \text{ cm}, \quad (4.43)$$

$$-175 \text{ cm} < \min_Y, \max_Y < 175 \text{ cm}, \quad (4.44)$$

$$105 \text{ cm} < \min_Z, \max_Z < 1270 \text{ cm}. \quad (4.45)$$

### 4.3.5 Multivariate analysis cuts

Following the removal of obvious backgrounds and events not contained within the detector, we aim to optimise the event selection to achieve the highest significance for measuring the effective muon neutrino magnetic moment. This goal is equivalent to maximising our FOM from Eq. 4.39.

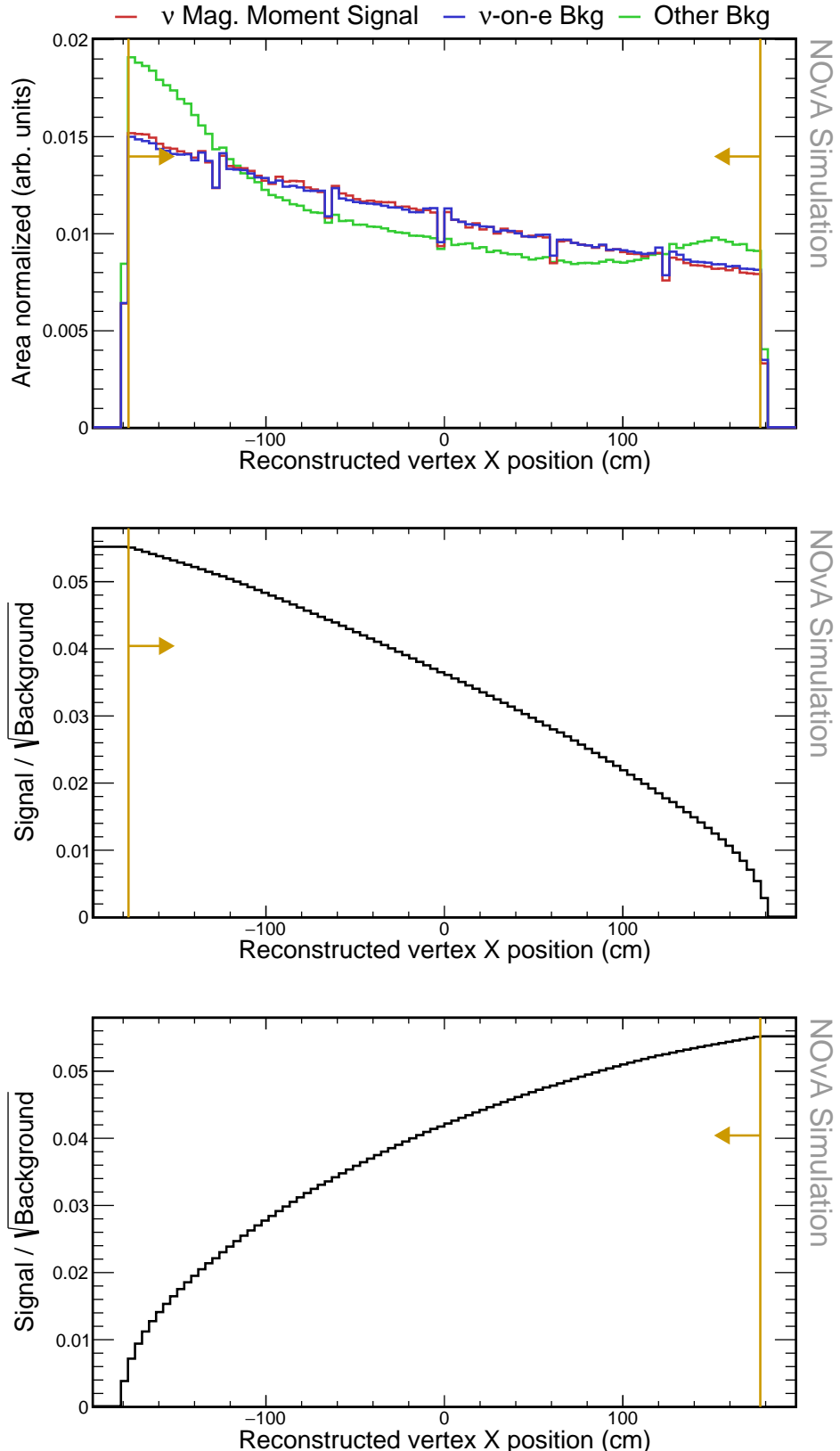


Figure 4.12: Top: Relative comparison of signal (red),  $\nu$ -on-e background (blue), and other background (green) events in the distribution of the x position of the reconstructed vertex. All histograms are area-normalized. Middle and bottom: Cumulative FOM calculated as the number of signal events, divided by the number of background events from that bin until the end of the plot to the right (middle) or left (bottom). The reconstruction quality and pre-selection cuts were applied prior to making these plots. Additionally, vertex is required to be within the active region of the detector ( $Vtx_Z < 1270$  cm). Yellow lines show the cut values that create the fiducial volume, with arrows pointing towards the preserved events.

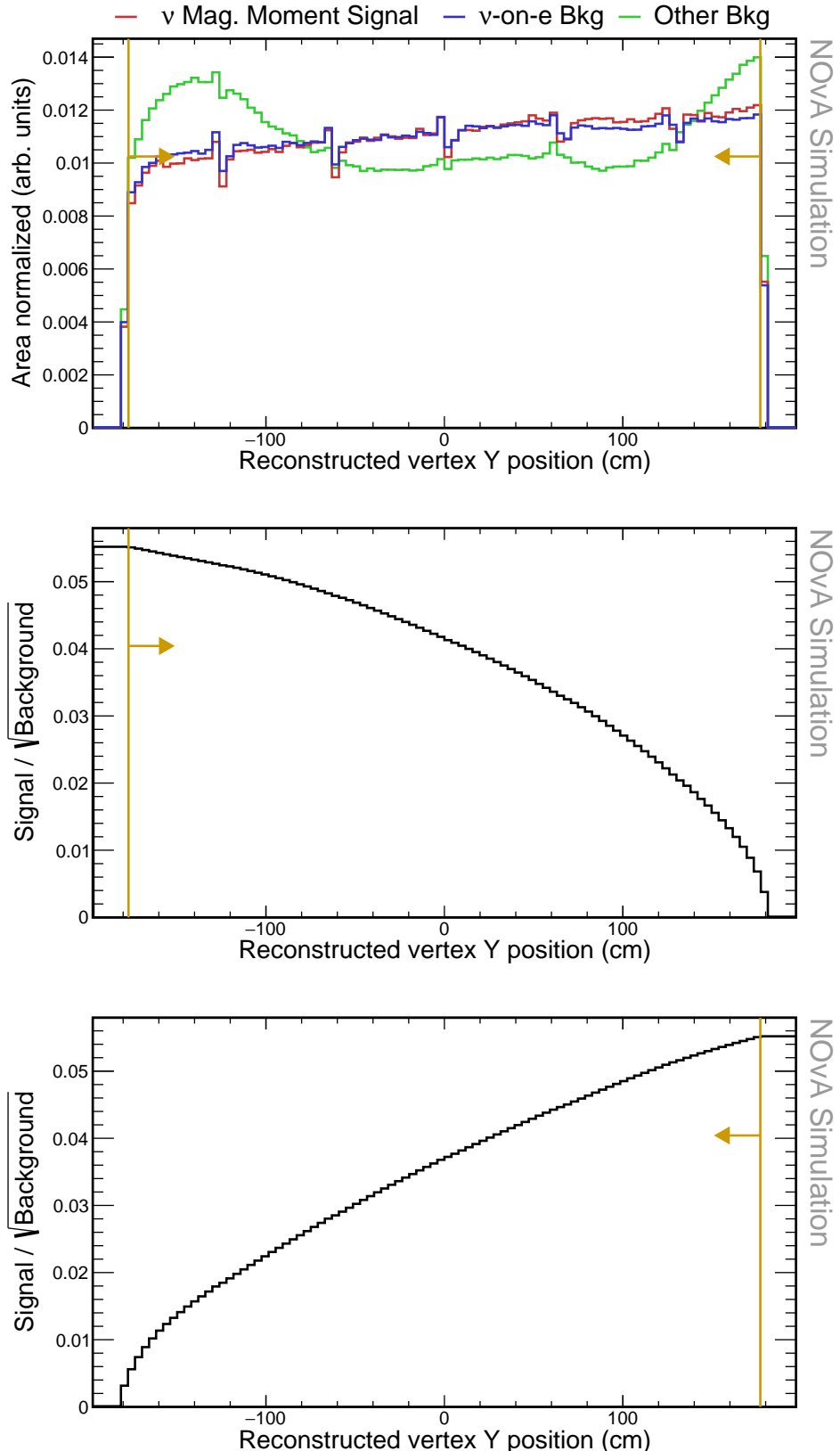


Figure 4.13: Top: Relative comparison of signal (red),  $\nu$ -on-e background (blue), and other background (green) events in the distribution of the y position of the reconstructed vertex. All histograms are area-normalized. Middle and bottom: Cumulative FOM calculated as the number of signal events, divided by the number of background events from that bin until the end of the plot to the right (middle) or left (bottom). The reconstruction quality and pre-selection cuts were applied prior to making these plots. Additionally, vertex is required to be within the active region of the detector ( $Vtx_Z < 1270$  cm). Yellow lines show the cut values that create the fiducial volume, with arrows pointing towards the preserved events.

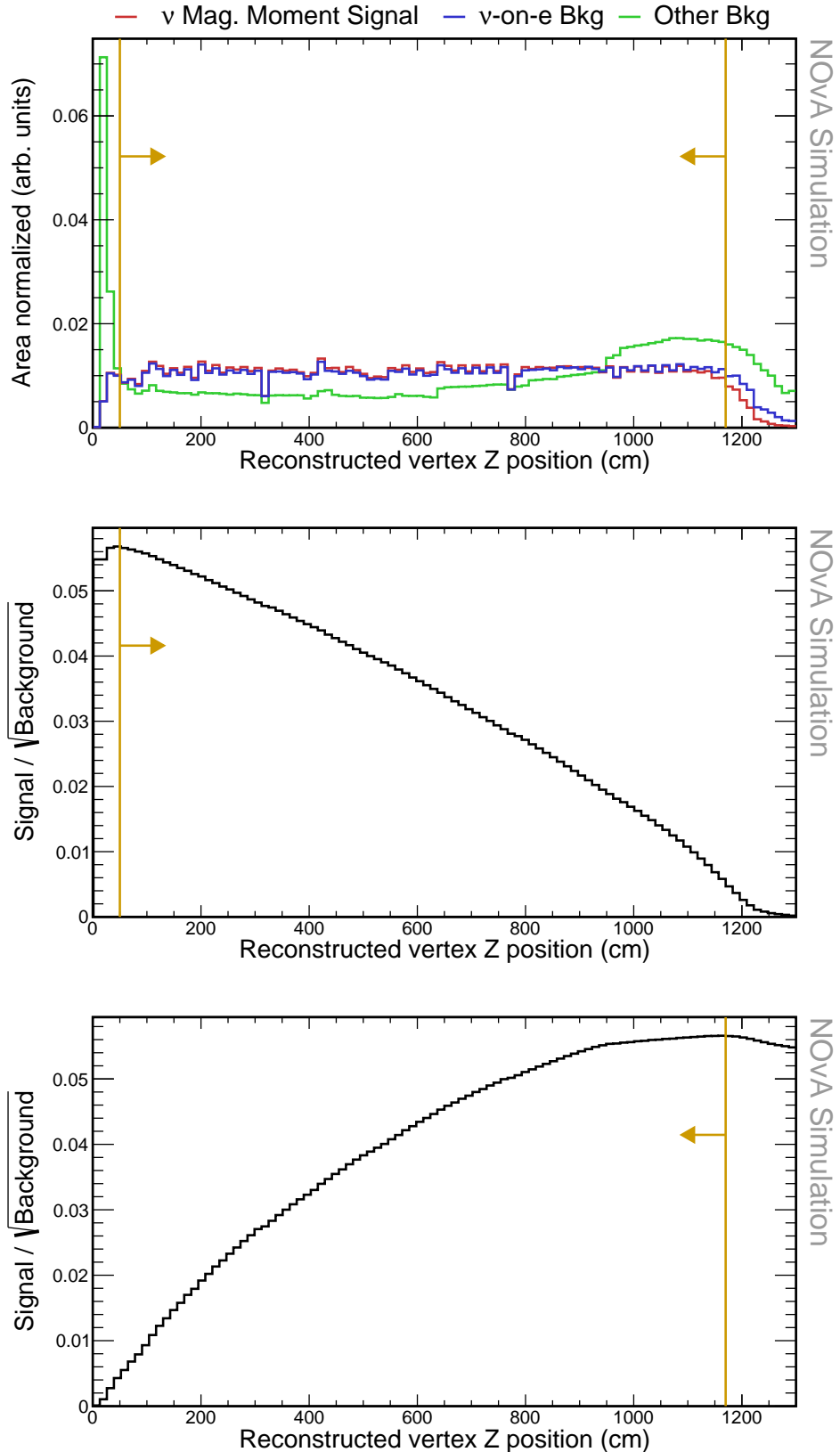


Figure 4.14: Top: Relative comparison of signal (red),  $\nu$ -on-e background (blue), and other background (green) events in the distribution of the z position of the reconstructed vertex. All histograms are area-normalized. Middle and bottom: Cumulative FOM calculated as the number of signal events, divided by the number of background events from that bin until the end of the plot to the right (middle) or left (bottom). The reconstruction quality and pre-selection cuts were applied prior to making these plots. Yellow lines show the cut values that create the fiducial volume, with arrows pointing towards the preserved events.

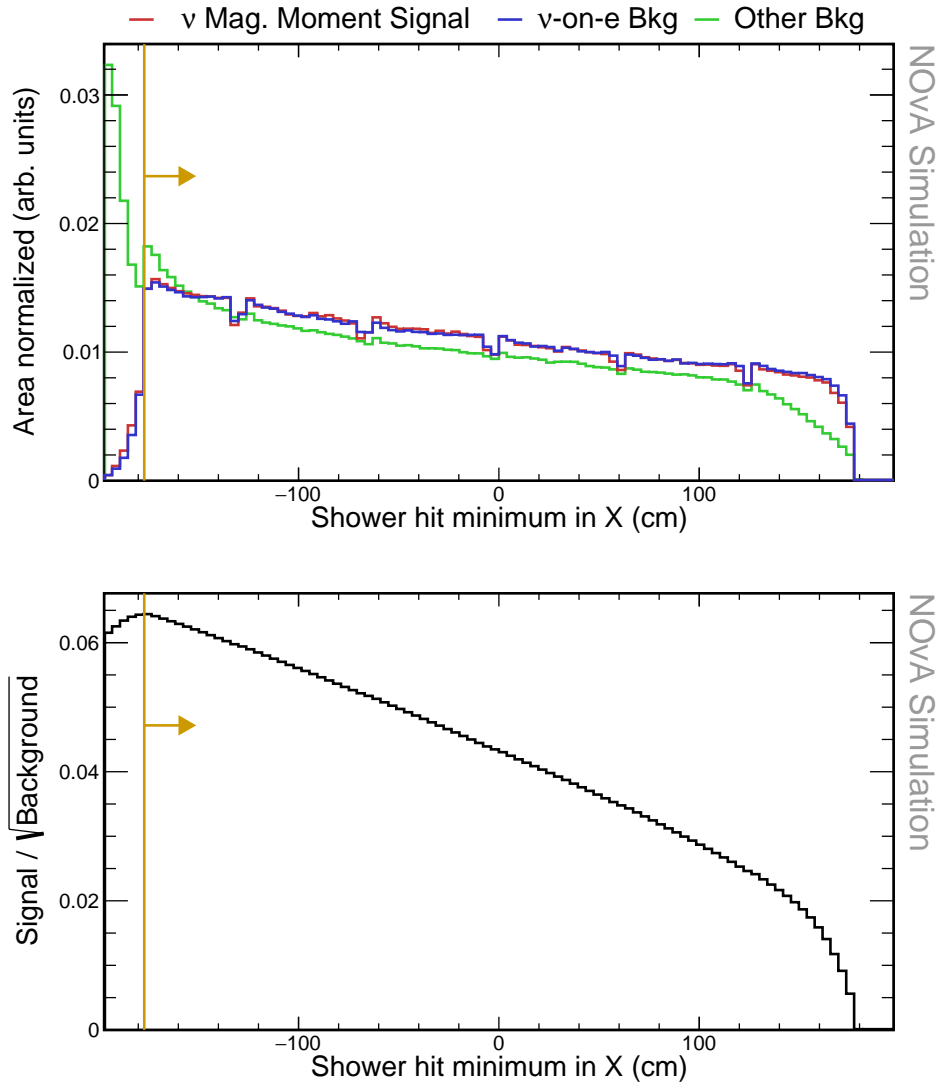


Figure 4.15: Top: Relative comparison of signal (red),  $\nu$ -on-e background (blue), and other background (green) events in the distribution of the minimum hit position of the most energetic prong along the x axis. All histograms are area-normalized. Bottom: Cumulative FOM calculated as the number of signal events, divided by the number of background events from that bin until the end of the plot in the direction of the yellow arrow. The reconstruction quality, pre-selection and fiducial cuts were applied prior to making these plots. Yellow lines show the cut values that create the containment volume, with arrows pointing towards the preserved events.

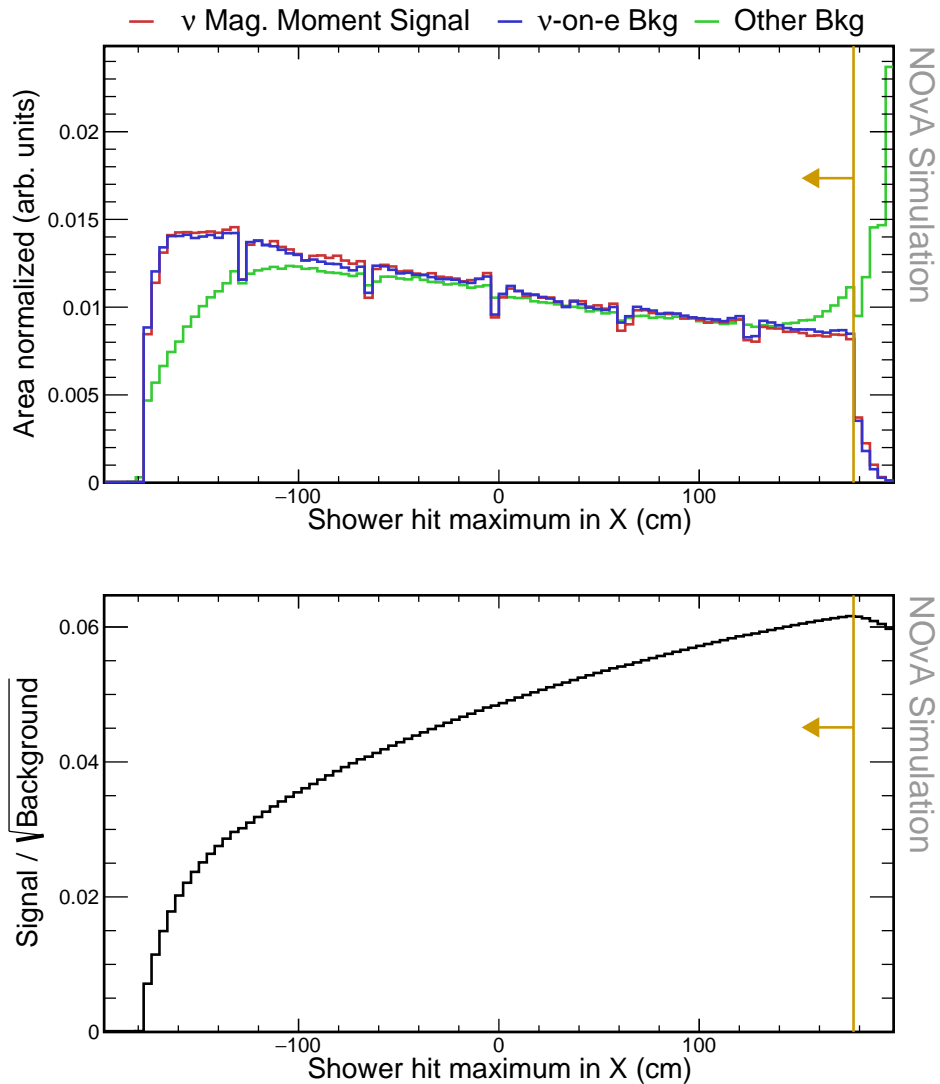


Figure 4.16: Top: Relative comparison of signal (red),  $\nu$ -on-e background (blue), and other background (green) events in the distribution of the maximum hit position of the most energetic prong along the x axis. All histograms are area-normalized. Bottom: Cumulative FOM calculated as the number of signal events, divided by the number of background events from that bin until the end of the plot in the direction of the yellow arrow. The reconstruction quality, pre-selection and fiducial cuts were applied prior to making these plots. Yellow lines show the cut values that create the containment volume, with arrows pointing towards the preserved events.

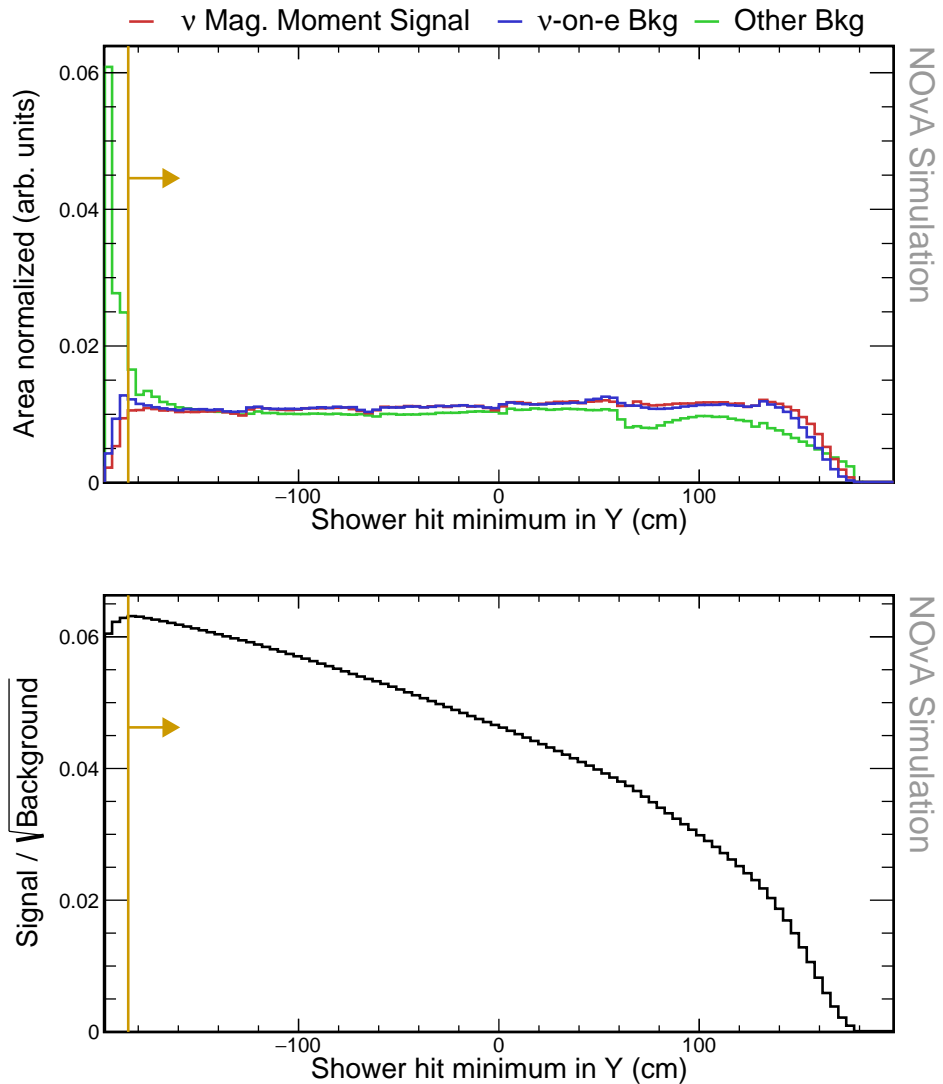


Figure 4.17: Top: Relative comparison of signal (red),  $\nu$ -on-e background (blue), and other background (green) events in the distribution of the minimum hit position of the most energetic prong along the y axis. All histograms are area-normalized. Bottom: Cumulative FOM calculated as the number of signal events, divided by the number of background events from that bin until the end of the plot in the direction of the yellow arrow. The reconstruction quality, pre-selection and fiducial cuts were applied prior to making these plots. Yellow lines show the cut values that create the containment volume, with arrows pointing towards the preserved events.

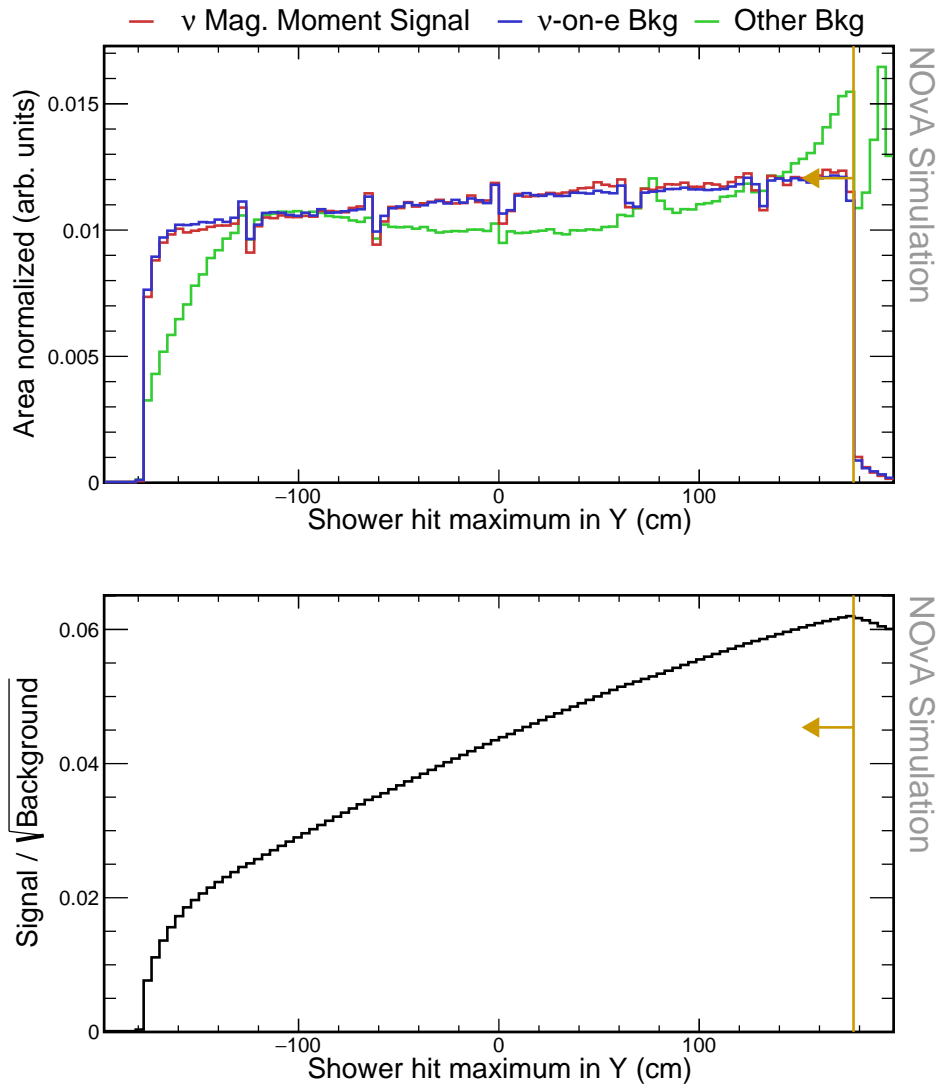


Figure 4.18: Top: Relative comparison of signal (red),  $\nu$ -on-e background (blue), and other background (green) events in the distribution of the maximum hit position of the most energetic prong along the y axis. All histograms are area-normalized. Bottom: Cumulative FOM calculated as the number of signal events, divided by the number of background events from that bin until the end of the plot in the direction of the yellow arrow. The reconstruction quality, pre-selection and fiducial cuts were applied prior to making these plots. Yellow lines show the cut values that create the containment volume, with arrows pointing towards the preserved events.

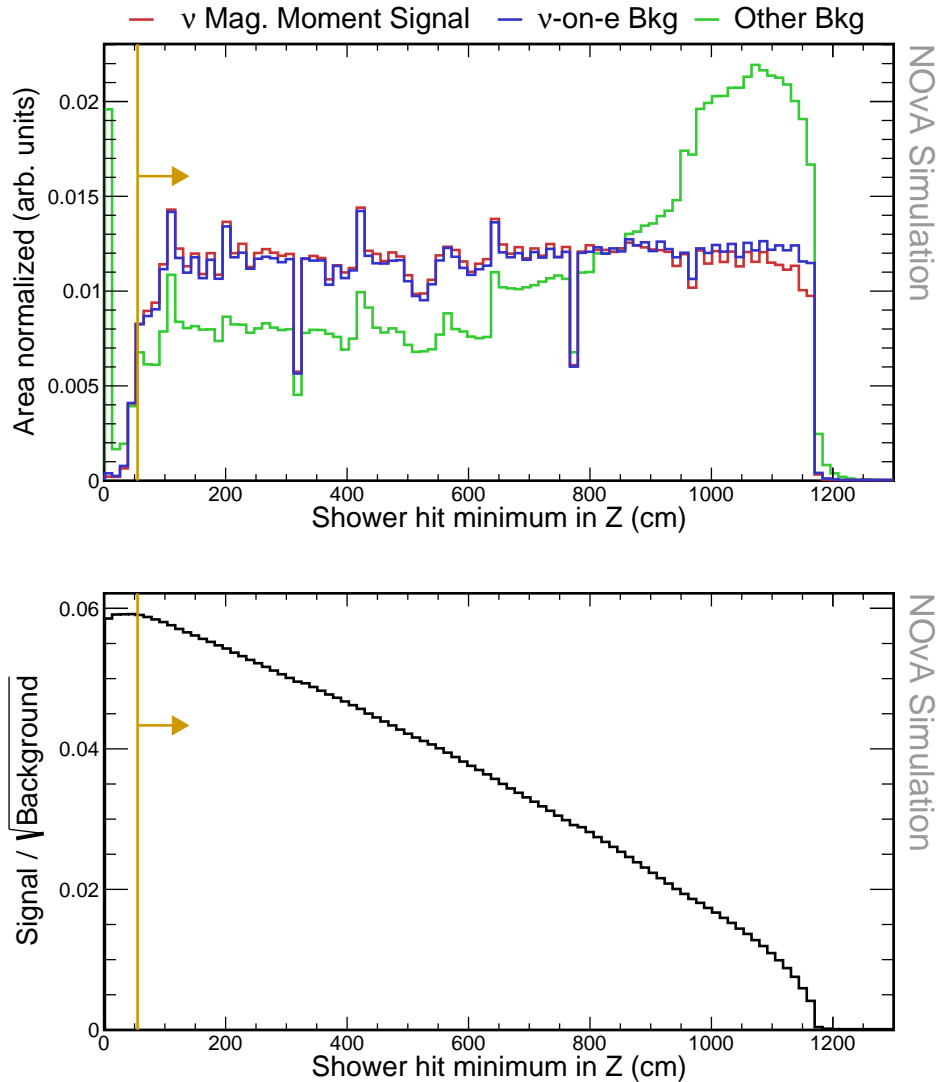


Figure 4.19: Top: Relative comparison of signal (red),  $\nu$ -on-e background (blue), and other background (green) events in the distribution of the minimum hit position of the most energetic prong along the z axis. All histograms are area-normalized. Bottom: Cumulative FOM calculated as the number of signal events, divided by the number of background events from that bin until the end of the plot in the direction of the yellow arrow. The reconstruction quality, pre-selection and fiducial cuts were applied prior to making these plots. Yellow lines show the cut values that create the containment volume, with arrows pointing towards the preserved events.

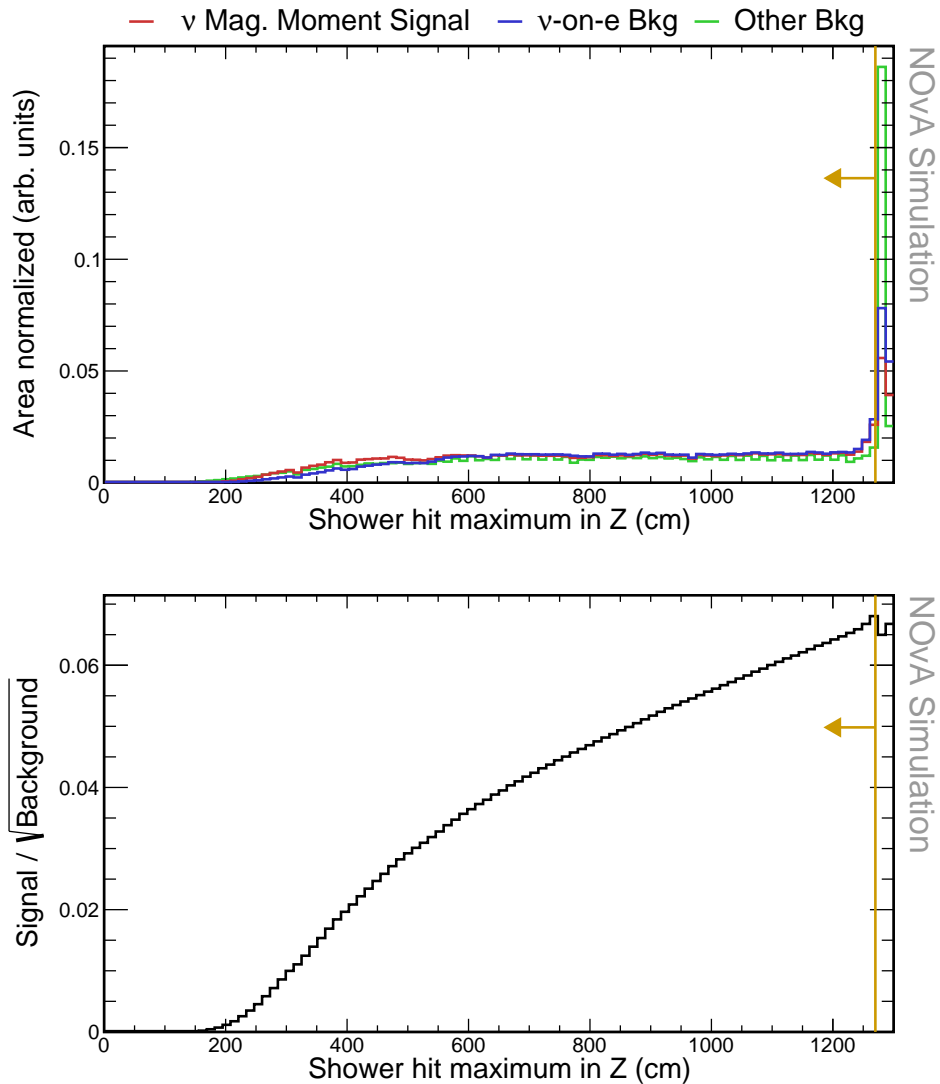


Figure 4.20: Top: Relative comparison of signal (red),  $\nu$ -on-e background (blue), and other background (green) events in the distribution of the maximum hit position of the most energetic prong along the z axis. All histograms are area-normalized. Bottom: Cumulative FOM calculated as the number of signal events, divided by the number of background events from that bin until the end of the plot in the direction of the yellow arrow. The reconstruction quality, pre-selection and fiducial cuts were applied prior to making these plots. Yellow lines show the cut values that create the containment volume, with arrows pointing towards the preserved events.

For this purpose, we utilised ROOT’s [208] Tool for MVA (MVA) [209]. Specifically, we employed the rectangular cut optimisation method, which uses multivariate parameter fitters to maximise background rejection across the full range of signal efficiencies. We used the MC sampling fitting method, assuming that for each input variable, there is a single cut value (maximum or minimum) that optimally discriminates between signal and background.

TMVA generally performs better with a limited number of input variables that have strong discriminating power. Therefore, we investigated several input variables and selected only those that achieved significant background rejection. There are additional variables not mentioned here that might achieve better final results, providing opportunities for future re-analyses. Additionally, we do not apply any transformations to the input variables prior to optimisation, which might also improve the final result after dedicated study.

The variables considered include those already used in the pre-selection: the total number of hits for all prongs in slice, the length of the longest prong, and  $E\theta^2$ , as discussed in Sec. 4.3.3. During the TMVA optimisation, we found that the length of the longest prong did not significantly enhance discriminating power and thus removed it from the set of input variables. Additionally, we included the reconstructed energy of the most energetic shower, as used for reconstruction quality selection in Sec. 4.3.2, intending to restrict events with higher energies, since our signal is concentrated at low electron recoil energies.

Additionally, we considered all the variables used for the NOvA  $\nu$ -on-e analysis for the neutrino flux constraint [192]. The first is the fraction of the reconstructed

Table 4.5: Event selection cutflow table for the containment cuts showing the number of events and the relative efficiency of each cut for each signal sample. The relative efficiency is calculated as number of events remaining after applying the corresponding cut divided by number of event for all the previous cuts. All the cuts are listed in sequence as they are applied. The top row corresponds to the sample after applying the reconstruction quality and pre-selection cuts.

<b>Selection</b>	<b>Signal</b>		<b><math>\nu</math>-on-e bkg</b>		<b>Other bkg</b>	
	$N_{evt}$	$\epsilon_{rel}$ (%)	$N_{evt}$	$\epsilon_{rel}$ (%)	$N_{evt}$	$\epsilon_{rel}$ (%)
<b>Pre-selection</b>	155.14	100	$3.33 \times 10^3$	100	$8.83 \times 10^6$	100
<b>Fiducial</b>	143.02	92.19	$2.88 \times 10^3$	85.60	$5.96 \times 10^6$	67.57
<b>Containment</b>	117.41	82.09	$2.08 \times 10^3$	72.12	$1.10 \times 10^6$	18.38

energy of the most energetic shower ( $E_{Shower}$ ) to the total energy of all the reconstructed prongs in the entire slice ( $E_{Tot}$ ). This variable distinguished our signal events, which only have a single shower, from events with multiple showers or additional activity. The second is the gap between the vertex and the most energetic shower, which can distinguish between electron and  $\pi^0$  events, as the latter should have a characteristic gap several cells long. Additionally, we examined the amount of energy contained within  $\pm 8$  planes away from the vertex, besides the energy associated with the most energetic prong, which should distinguish the purely leptonic signal from backgrounds with significant hadronic activity. However, the gap and the vertex energy variables underperformed compared to others and were ultimately not used within the TMVA.

We also utilised two CNN-based event classifiers developed for the NOvA  $\nu$ -on-e analysis for the neutrino flux constraint [192, 193]. These classifiers are specifically designed to identify  $\nu$ -on-e interactions. The first, named  $\nu$ -on-e ID, is trained to select  $\nu$ -on-e events from the primary  $\nu_\mu$ CC background, while the second, named  $E\pi^0$  ID, is trained on events passing the  $\nu$ -on-e ID selection to reject the remaining background with a  $\pi^0$ . These classifiers use a pixel map of the entire slice as input and are designed with the same CNN architecture as ProngCVN and EventCVN described in Sec. 2.5.

The result of the TMVA is a set of cuts on each of the input variables that maximises the FOM. The input variables and the cuts that were selected for them are shown in Fig. 4.21, 4.22, and 4.23. The effect of these cuts is summarised in Tab. 4.6. Applying the TMVA cuts reduces the signal by 51.62 %, the  $\nu$ -on-e background by 75.03 % and other background by 99.98 %. The specific values of the cuts resulting

from the TMVA are

$$E_{Shower}/E_{Tot} > 0.91, \quad (4.46)$$

$$\text{Total } N^o \text{ hits for all prongs} < 116, \quad (4.47)$$

$$E_{Shower} < 1.4 \text{ GeV}, \quad (4.48)$$

$$E\theta^2 < 0.0048 \text{ GeV} \times \text{rad}^2, \quad (4.49)$$

$$\nu - on - eID > 0.65, \quad (4.50)$$

$$E\pi^0 ID > 0.63. \quad (4.51)$$

Table 4.6: Event selection cutflow table for the results of the cut-based Multivariate analysis, showing the number of events and the relative efficiency of each cut for each signal sample. The relative efficiency is calculated as number of events remaining after applying the corresponding cut divided by number of event for all the previous cuts. All the cuts are listed in sequence as they are applied. The top row corresponds to the sample after applying the reconstruction quality, pre-selection, fiducial and containment cuts.

<b>Selection</b>	<b>Signal</b>		<b><math>\nu</math>-on-e bkg</b>		<b>Other bkg</b>	
	$N_{evt}$	$\epsilon_{rel} (\%)$	$N_{evt}$	$\epsilon_{rel} (\%)$	$N_{evt}$	$\epsilon_{rel} (\%)$
<b>Contained</b>	117.41	100	$2.08 \times 10^3$	100	$1.10 \times 10^6$	100
$E_{Shower}/E_{Tot}$	113.03	96.28	$2.02 \times 10^3$	97.32	$4.53 \times 10^5$	41.30
<b>N<sup>o</sup> Hits</b>	106.48	94.20	$1.45 \times 10^3$	71.53	$4.02 \times 10^5$	88.78
<b>High <math>E_{Shower}</math></b>	85.51	80.31	777.91	53.76	$3.01 \times 10^5$	74.84
<b><math>\nu</math>-on-e ID</b>	72.23	84.47	652.32	83.86	$4.40 \times 10^3$	1.46
<b><math>E\pi^0</math> ID</b>	67.35	93.24	608.19	93.23	$2.83 \times 10^3$	64.34
<b><math>E\theta^2</math></b>	56.80	84.33	519.09	85.35	181.24	6.40

After the full event selection, the predicted number of signal events for  $\mu_\nu = 10^{-9} \mu_B$  is 56.80, and the total number of background events under the SM hypothesis is 700.33. The decomposition of background into interaction types is shown in Fig. 4.24 and listed in Tab. 4.7. The event selection results in

$$\text{Signal Purity} = \frac{\text{Signal}}{\text{Signal+Background}} = 7.50 \%, \quad (4.52)$$

$$\text{Signal Efficiency} = \frac{\text{Signal}}{\text{Signal}_{\text{No Cut}}} = 6.95 \%. \quad (4.53)$$

Also,

$$\frac{\text{Signal}}{\sqrt{\text{Background}}} = 2.15 \quad (4.54)$$

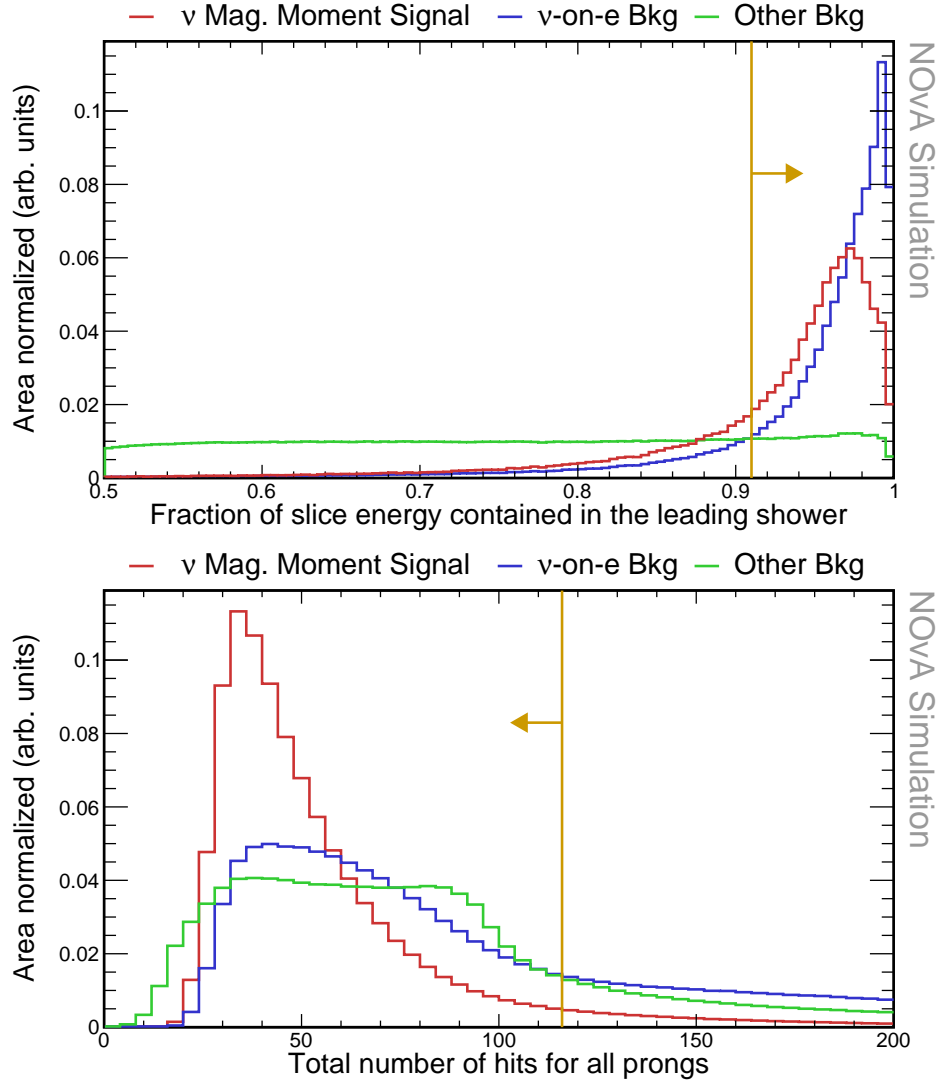


Figure 4.21: Relative comparison of signal (red),  $\nu$ -on-e background (blue), and other background (green) events in the distribution of the fraction of the total energy contained in the primary shower (top) and of the total number of hits in the slice (bottom). All histograms are area-normalized. The reconstruction quality, pre-selection, fiducial and containment cuts were applied prior to making these plots. Yellow lines show the cut values on the depicted variables, with arrows pointing towards the preserved events.

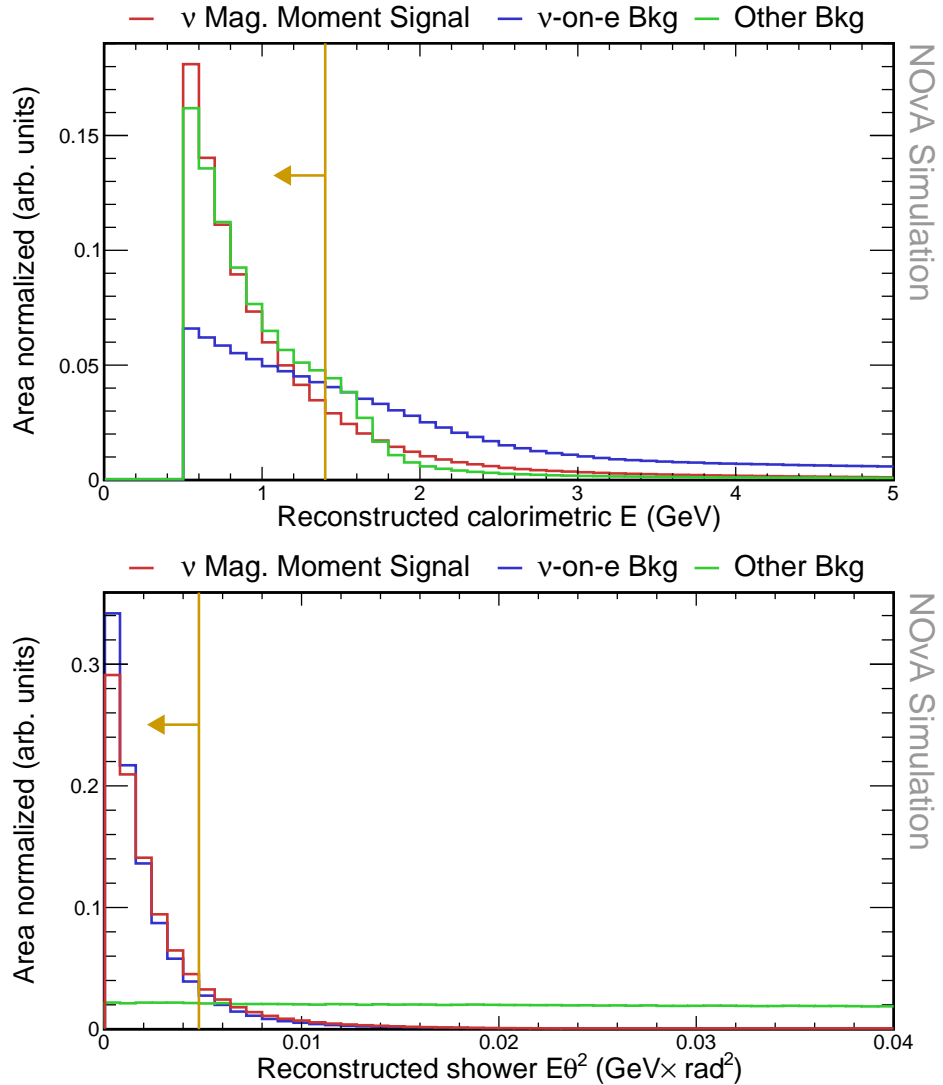


Figure 4.22: Relative comparison of signal (red),  $\nu$ -on-e background (blue), and other background (green) events in the distribution of the reconstructed energy of the primary shower (top) and of the reconstructed energy multiplied by the angle from the incoming neutrino beam direction squared.(bottom). All histograms are area-normalized. The reconstruction quality, pre-selection, fiducial and containment cuts were applied prior to making these plots. Yellow lines show the cut values on the depicted variables, with arrows pointing towards the preserved events.

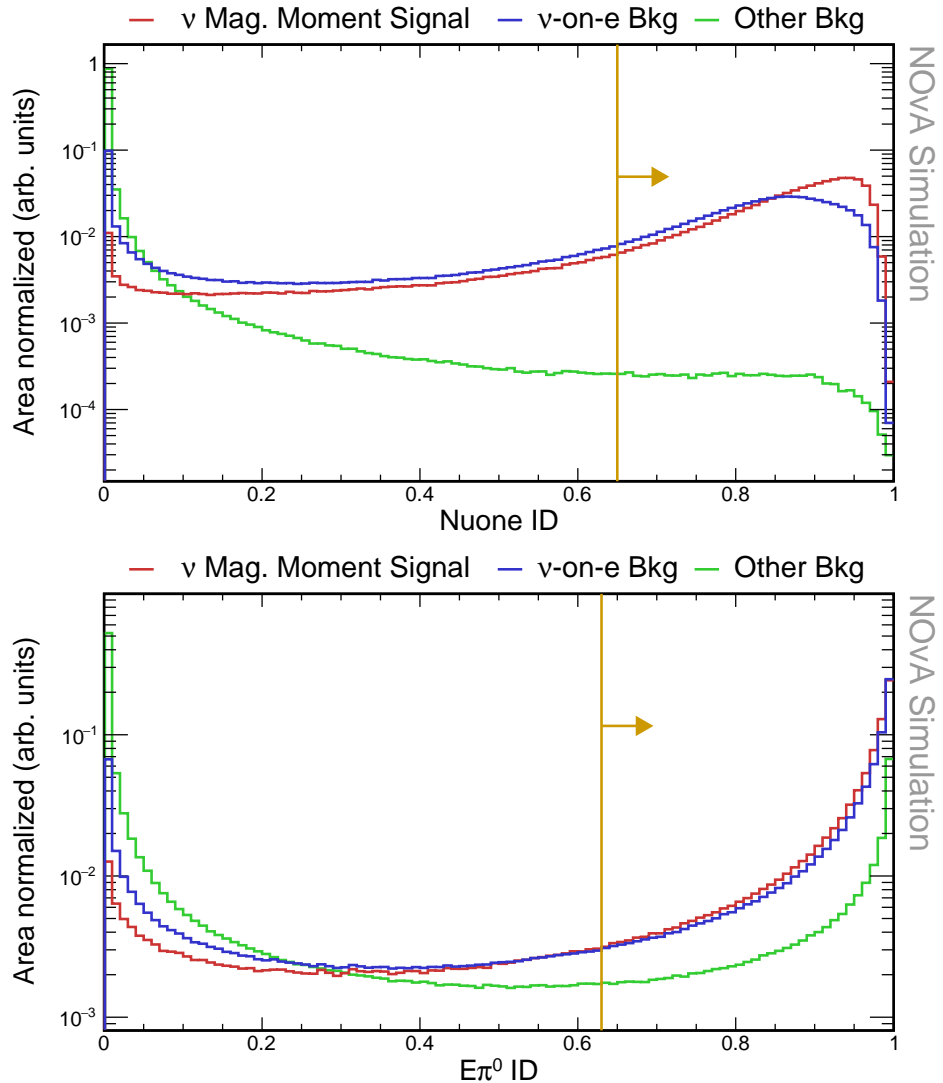


Figure 4.23: Relative comparison of signal (red),  $\nu$ -on-e background (blue), and other background (green) events in the distribution of the NuoneID (top) and EPi0ID (bottom) event identifiers. All histograms are area-normalized and logarithmic in the y axis. The reconstruction quality, pre-selection, fiducial and containment cuts were applied prior to making these plots. Yellow lines show the cut values on the depicted variables, with arrows pointing towards the preserved events.

and

$$\text{FOM} = \frac{\text{Signal}}{\sqrt{\text{Signal+Background}}} = 2.06. \quad (4.55)$$

Table 4.7: Interaction types contributing to the SM background after full event selection. Interactions with/without  $\pi^0$  in the final state are specifically selected due to their significant contribution to the  $\nu$ -on-e background.

<b>Interaction</b>	<b>Number of events</b>
$\nu$ -on-e .....	519.09
NC w/ $\pi^0$ .....	72.96
NC w/o $\pi^0$ .....	21.51
$\nu_\mu$ CC w/ $\pi^0$ .....	28.07
$\nu_\mu$ CC w/o $\pi^0$ .....	25.67
$\nu_e$ CCMEC .....	2.22
Other $\nu_e$ CC .....	9.83
Other .....	20.98
<b>Total</b> .....	700.33

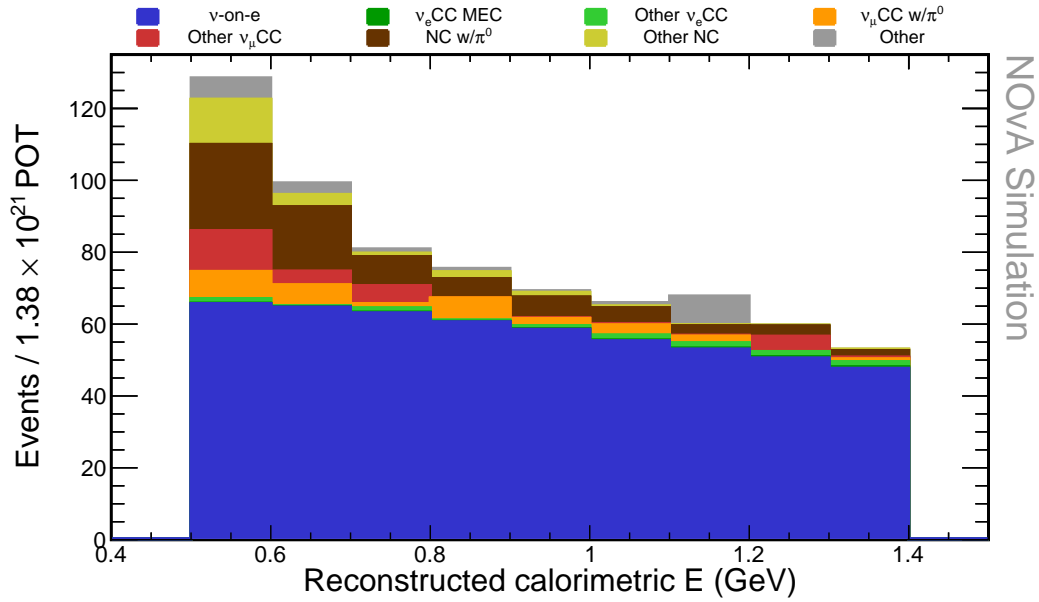


Figure 4.24: Background composition of events passing the full event selection as a function of the reconstructed energy of the leading shower - electron for  $\nu$ -on-e events. Events are scaled to the data exposure. Origin of the "Other" background events between 1.1 – 1.2 GeV is not known.

## 4.4 Systematic uncertainties

We consider all the standard NOvA systematic uncertainties described in Sec. 2.8, grouped into four categories: neutrino flux, detector calibration, detector modelling,

and neutrino interaction systematic uncertainties. Summary of the effects of both systematic and statistical uncertainties on the predicted number of SM background events is shown in Fig. 4.25. The four categories of systematic uncertainties are assumed to be uncorrelated between each other, allowing to calculate their combined effect by adding their individual contribution in quadrature. The statistical uncertainty is calculated as  $\sqrt{N_{SM}}$  since the number of predicted events follows the Poisson distribution. The total prediction of the number of SM background events can be expressed as

$$N_{SM} = 700.33 \pm 26.46 \text{ (stat.)}_{-62.99}^{+72.48} \text{ (syst.)}. \quad (4.56)$$

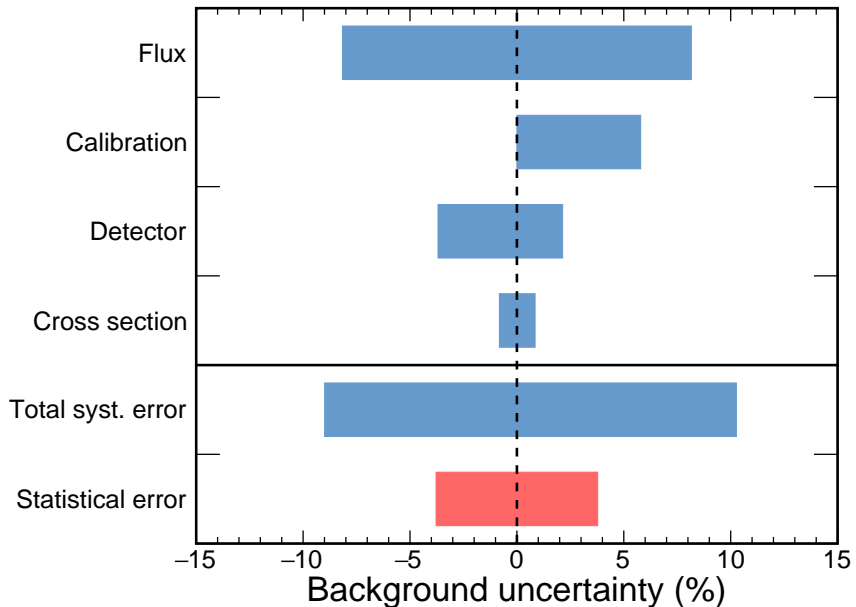


Figure 4.25: Relative effect of systematic and statistical uncertainties on the number of SM background events. The total systematic uncertainty (blue bottom bar) is calculated as a square root of the sum of squares of the four categories of systematic uncertainties, shown ordered by the size of their effect. These are the neutrino flux, detector calibration, detector modelling, and neutrino cross section systematic uncertainties.

To assess the effect of the neutrino flux systematic uncertainty, we use 8 ND-only principal components. Figure 4.26 shows their combined effect on the predicted SM background as a function of the primary shower's reconstructed energy. Since the principal components are uncorrelated by construction, the total systematic uncertainty for each bin is calculated by adding the effect of all the principal components in quadrature. The effect of the neutrino flux systematic uncertainty does not depend

on the primary shower's calorimetric energy and altering the neutrino flux prediction can be represented by a normalization shift. The final effect of the neutrino flux systematic uncertainty on the total number of SM background events is  $\pm 8.16\%$  and is symmetric around the nominal prediction.

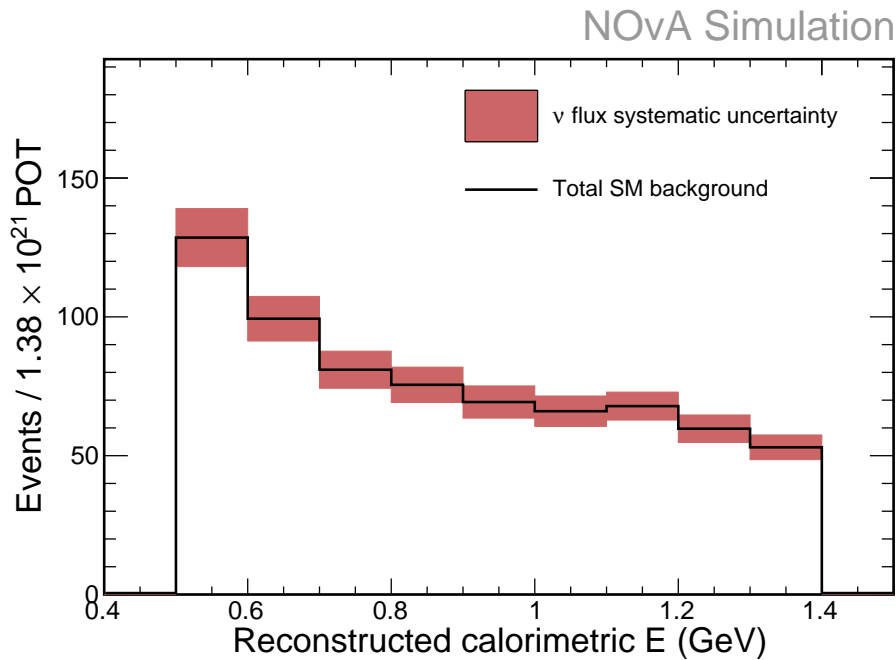


Figure 4.26: Effect of the total neutrino flux systematic uncertainty on the primary shower energy distribution of the SM background events.

The effect of the total detector modelling and calibration systematic uncertainties on the number of SM background events is asymmetrical, increasing the number of events by  $+6.17\%$  and decreasing by  $3.69\%$ . The effect of these uncertainties depends on the energy of the primary shower (which is the recoil electron for  $\nu$ -on-e events), as can be seen in Fig. 4.27. This means that the energy distribution of the SM background events can be significantly altered due to the detector uncertainties. The largest contribution comes from the absolute energy scale uncertainty, which has a one-sided effect of  $+5.72\%$ . This is due to both the positive and the negative shift in the absolute energy scale increasing the total number of SM background events. The light level and Cherenkov systematic uncertainties are asymmetrical and alter the number of SM background events in both directions by  $^{+1.13\%}_{-3.39\%}$  and  $^{+1.82\%}_{-1.46\%}$  respectively. The detector ageing and calibration shape systematic uncertainties are one sided by default and increase the number of the SM background events by  $+0.55\%$  and  $+0.69\%$  respectively.

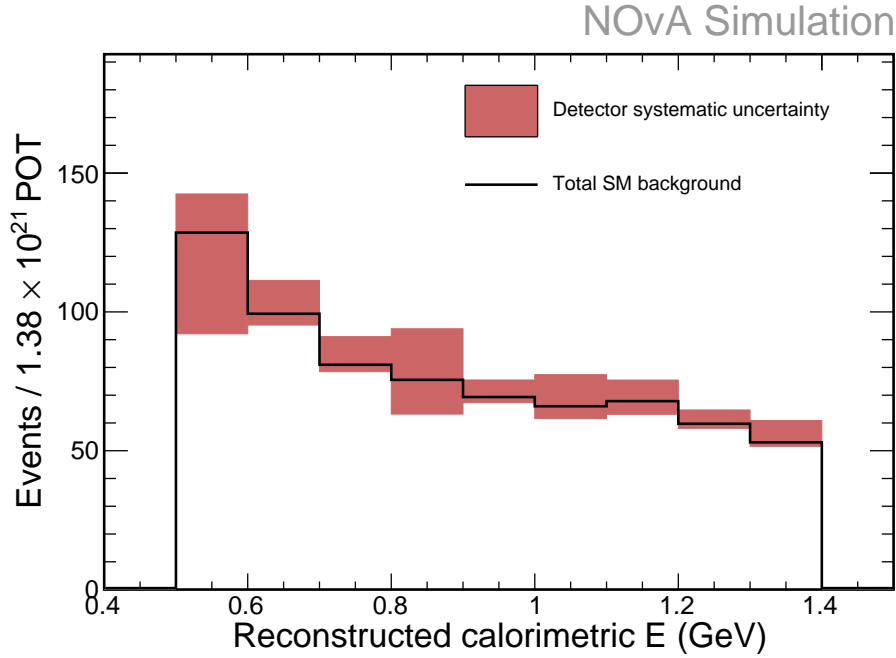


Figure 4.27: Effect of the total detector systematic uncertainty on the primary shower energy distribution of the SM background. The detector uncertainty consists of the absolute calibration, calibration shape, detector ageing, light level, and Cherenkov systematic uncertainties.

Since we assume that the  $\nu$ -on-e interaction is known precisely, the dominant  $\nu$ -on-e component of the SM background has no systematic uncertainty from neutrino interactions. Therefore, the neutrino interaction systematic uncertainty affects only the 181 "Other background" events, which make up 34.9 % of the total SM background. Consequently, the total neutrino interaction uncertainty on the SM background is relatively small, with a combined effect on the number of SM background events of  $^{+1.54\%}_{-1.49\%}$ . The most dominant neutrino interaction systematic uncertainties are related to interactions with  $\pi^0$  in the final state, such as the axial mass ( $^{+0.97\%}_{-0.90\%}$ ) and the vector mass ( $^{+0.41\%}_{-0.35\%}$ ) of the NCRes interactions, the scaling of the COH $\pi$ NC interactions ( $^{+0.85\%}_{-0.85\%}$ ), or the mean free path of pions before they undergo an interaction ( $^{+0.30\%}_{-0.43\%}$ ). Other neutrino interaction systematic uncertainties have only a marginal ( $< 0.3\%$ ) effect on the number of SM background events.

## 4.5 Statistical analysis

Our analysis compares the total observed number of events,  $N_O$ , with the expected (predicted) number of events,  $N_E(\mu_\nu)$ , which in general depends on the value of the

effective neutrino magnetic moment,  $\mu_\nu$ , and is equal to the sum of the expected signal and background events:

$$N_E(\mu_\nu) = N_S(\mu_\nu) + N_B. \quad (4.57)$$

The number of background events is equal to  $N_{SM}$  from Eq. 4.56 and the number of signal events can be expressed as

$$N_S = 56.80 \times \left( \frac{\mu_\nu}{10^{-9} \mu_B} \right)^2, \quad (4.58)$$

as described in Sec. 4.3.

The number of recorded events within a fixed time interval follows the Poisson distribution with the likelihood (probability) of observing  $N_O$  events given a hypothesis predicting  $N_E$  events defined as [52]:

$$L(N_O; N_E(\mu_\nu)) = \frac{N_E(\mu_\nu)^{N_O}}{N_O!} e^{-N_E(\mu_\nu)}. \quad (4.59)$$

To estimate and constrain  $\mu_\nu$ , we employ a frequentist approach using the Poisson-distributed likelihood ratio [210]

$$\lambda = \frac{L(N_O; N_E(\mu_\nu))}{L_{sat}(N_O; N_O)}. \quad (4.60)$$

Here,  $L_{sat}$  is the so-called saturated model, for which  $N_E = N_O$  and is constant with respect to  $\mu_\nu$  [52]. Maximising the likelihood with respect to  $\mu_\nu$  is equivalent to minimising the ‘log-likelihood ratio’ described as:

$$-2 \ln \lambda(\mu_\nu) = -2 \ln \left( \frac{L(N_O; N_E(\mu_\nu))}{L(N_O; N_O)} \right) \quad (4.61)$$

$$= 2 \left[ N_E(\mu_\nu) - N_O + N_O \ln \frac{N_O}{N_E(\mu_\nu)} \right]. \quad (4.62)$$

According to Wilk’s theorem [211], under the assumptions that the hypothesis is correct, the sample size is sufficiently large, and certain regularity conditions (which are met in our case) are satisfied, the log-likelihood ratio follows a chi-squared ( $\chi^2$ ) distribution. Therefore, the log-likelihood ratio serves not only to find the maximum likelihood estimators of  $\mu_\nu$  but also to provide a statistic usable for a goodness-of-fit test [52].

### 4.5.1 Treatment of systematic uncertainties

Systematic uncertainties are incorporated into the fitting framework as nuisance parameters that multiply the likelihood function in Eq. 4.59. Each systematic uncertainty is modelled according to the normal distribution centred at zero, with a standard deviation corresponding to its respective  $1\sigma$  variation. Systematic uncertainties are treated as mutually uncorrelated, justifying their independent treatment.

Incorporating the nuisance parameters into the log-likelihood ratio function in Eq. 4.61 results in so-called ‘*penalty terms*’. These terms are proportional to the square of each systematic pull’s variation in units of  $\sigma$ , thereby increasing the log-likelihood ratio for solutions that favour non-zero systematic shifts:

$$-2 \ln \lambda(\mu_\nu, \vec{\eta}) = -2 \left[ E(\mu_\nu, \vec{\eta}) - O + O \ln \frac{O}{E(\mu_\nu, \vec{\eta})} \right] + \sum_{i=1}^M \left( \frac{\eta_i}{\sigma} \right)^2. \quad (4.63)$$

Here,  $\vec{\eta}$  is a vector of  $M$  nuisance parameters representing the effect of systematic uncertainties.

In practice, we produce systematically shifted predictions for each systematic uncertainty with shifts at fixed integer  $\sigma$  values. Due to the computationally expensive nature of reproducing the detector simulation, variations in detector and calibration systematic uncertainties are estimated only at  $\pm 1\sigma$  values. However, for beam and cross section uncertainties, variations are estimated at  $\pm 1\sigma$ ,  $\pm 2\sigma$ , and  $\pm 3\sigma$  levels. These systematically shifted predictions are then interpolated using cubic spline-based fit. For one-sided systematic uncertainties, such as detector ageing and calibration shape uncertainties, the fit is fixed at zero for the excluded side [142].

### 4.5.2 Hypothesis testing and confidence limits

To evaluate whether the observed number of events can be described solely using the SM prediction, we perform a hypothesis test for the ‘*null hypothesis*’,  $H_0$ , for which  $\mu_\nu = 0$ ,  $E_S = 0$ , and hence the expected number of events is  $N_E = N_B$ . The log-likelihood ratio is in this case

$$-2 \ln \lambda_{H_0} = 2 \left[ N_B - N_O + N_O \ln \frac{N_O}{N_B} \right] + \sum_{k=1}^M \eta_k^2 \quad (4.64)$$

and its minimum follows a  $\chi^2$  distribution with one degree of freedom. This allows us to calculate the p-value of the goodness-of-fit of the null hypothesis. We reject the null hypothesis if the statistical test yields a p-value below a critical value - significance level. We set the significance level at  $\alpha = 0.10$ , which is a common threshold in other measurements of the neutrino magnetic moment, as discussed in the introduction to this chapter.

If we fail to reject the null hypothesis, defined as  $p > \alpha$ , we establish an upper limit on the value of the effective muon neutrino magnetic moment. We consider our results to represent only the  $\nu_\mu$  thanks their high purity in our neutrino beam, as described in Sec. 2.1.

The upper limit is calculated by iterating over a fixed range of neutrino magnetic moment values and calculating the minimum log likelihood from Eq. 4.63 at each iteration, while profiling over the nuisance parameters (systematic variations). This means that at each iteration, the value of the neutrino magnetic moment is fixed, and the log-likelihood function is minimised with respect to the systematic shifts. The minimisation of the log-likelihood ratio is done using a MIGRAD-based algorithm in ROOT [208].

The minimum of the log-likelihood, as a function of the neutrino magnetic moment, follows a  $\chi^2$  distribution with one degree of freedom and is often denoted as

$$-2 \ln \lambda \left( \theta, \hat{\vec{\eta}} \right) \equiv \Delta\chi^2(\mu_\nu). \quad (4.65)$$

Here  $\hat{\vec{\eta}}$  denotes the vector of systematic shifts that minimise the log-likelihood for that specific  $\mu_\nu$ . We determine the 90% C.L. limit on the neutrino magnetic moment (equal to  $1 - \alpha$ ) as the range of  $\mu_\nu$  values for which

$$\Delta\chi^2 < 2.71. \quad (4.66)$$

This is calculated as the integral of the right tail of the  $\chi^2$  distribution with one degree of freedom.

## 4.6 Results

To avoid biasing our decisions based on the number and distribution of the observed data events, we performed the event selection, studied systematic uncertainties, and decided on the statistical analysis methods prior to revealing the data samples in a so-called blinded analysis. We first validated the selected analysis methods using fake data, which were generated by applying a random fluctuation to the predicted number of events based on the Poisson distribution.

After investigating results from the fake data studies we unblinded the data sample and obtained the total number of observed events passing our selection. The number of selected events recorded in the NOvA ND corresponding to exposure  $1.38 \times 10^{21}$  POT is

$$N_O = 773. \quad (4.67)$$

Since we are only comparing the total number of predicted and observed events, the Best Fit (BF) point for the number of signal events can be simply calculated as

$$N_{S,BF} = N_O - N_B = 72.67. \quad (4.68)$$

From Eq. 4.58 we get the BF for the neutrino magnetic moment as

$$\mu_{\nu_\mu, BF} = \sqrt{\frac{72.67}{56.80}} \times 10^{-9} \mu_B = 1.13 \times 10^{-9} \mu_B. \quad (4.69)$$

The final distribution of the predicted SM background events, predicted signal events corresponding to  $\mu_\nu = 10^{-9} \mu_B$ , and the observed data events as a function of the primary shower's reconstructed calorimetric energy is shown in Fig. 4.28. We do not use this energy distribution of events for hypothesis testing or parameter estimation, only to validate whether our simulation predicts the observation with sufficient precision. As can be seen, the observed data are within the systematic and statistical uncertainty for all the displayed bins with the only exception being the bin between (0.9 GeV, 1.0 GeV). The discrepancy between data and simulation in this bin is however still within two standard variations from the accepted values and therefore we conclude that the simulation predicts the observed data satisfactorily well.

We calculated the minimum log likelihood for the null hypothesis, as described in

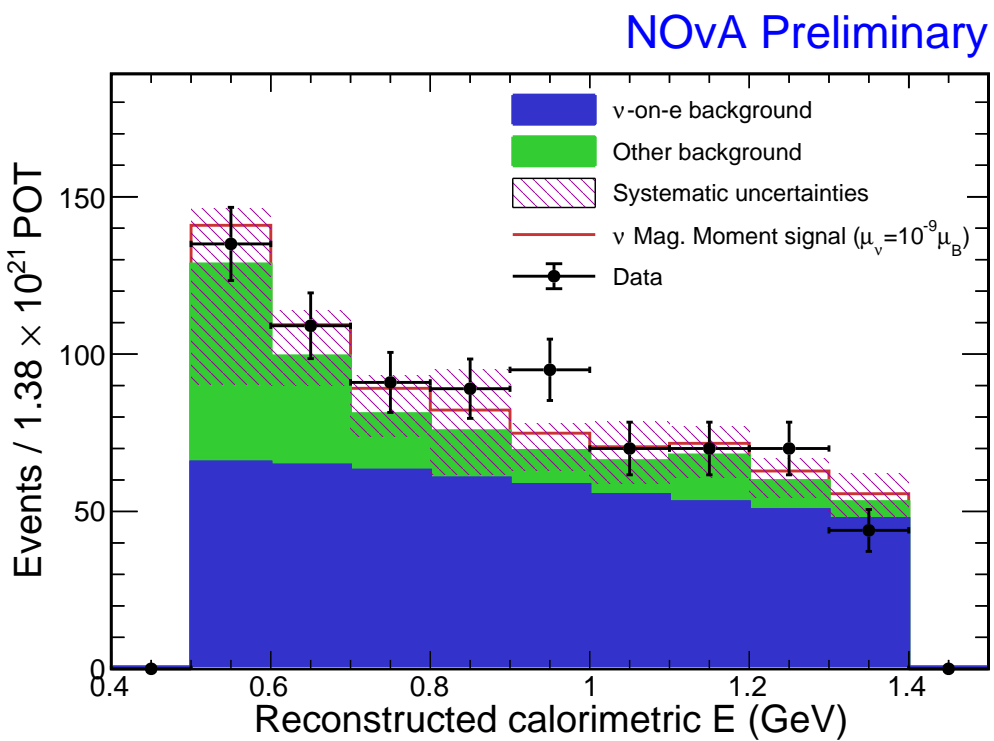


Figure 4.28: Comparison of the observed data to the prediction of the neutrino magnetic moment signal corresponding to  $\mu_\nu = 10^{-9} \mu_B$  (red line) and the SM background (filled area) as a function of the reconstructed calorimetric energy of the most energetic shower. The SM background is divided into the  $\nu$ -on- $e$  component in blue and the rest in green, with the associated systematic uncertainty on the SM background shown in shaded purple. Data is shown with statistical uncertainty based on Poisson distribution. All samples are scaled to the true data exposure  $1.38 \times 10^{21}$  POT.

Eq. 4.64, as

$$-2 \ln \lambda_{H_0, \min} = 1.02964, \quad (4.70)$$

which corresponds to the double sided p-value of 0.31. Since this value is larger than our pre-determined significance level of 0.1, we are not able to reject the null hypothesis. This means that we did not observe an excess of  $\nu$ -on-e events above the SM background.

As described in Sec. 4.5.2, we can determine the limit on the value of the effective muon neutrino magnetic moment by calculating  $\Delta\chi^2$  for a range of  $\mu_\nu$  value as shown in Fig. 4.29. From this distribution we calculate the limit as

$$\mu_{\nu_\mu} < 1.91 \times 10^{-9} \mu_B \text{ at } 90\% \text{ C.L..} \quad (4.71)$$

We can also estimate the systematic uncertainty on the best fit point from the  $\Delta\chi^2$  distribution shown in Fig. 4.29 by taking the  $1\sigma$  range ( $\Delta\chi^2 = 1$ ) of the full systematic uncertainty distribution. The  $1\sigma$  range for all systematics is  $(0.14, 1.63) \times 10^{-9} \mu_B$ , which is equivalent to the best fit point having an uncertainty:

$$\mu_{\nu_\mu, BF} = (1.13^{+0.50}_{-0.99}) \times 10^{-9} \mu_B. \quad (4.72)$$

## 4.7 Summary

We analysed a selection of events recorded in the NOvA ND and compared it to the prediction, searching for an excess of  $\nu$ -on-e interaction over the SM background, corresponding to a signal of an effective muon neutrino magnetic moment. We found the BF value of  $\mu_{\nu_\mu, BF} = (1.13^{+0.50}_{-0.99}) \times 10^{-9} \mu_B$ . We failed to reject the null hypothesis that the observed events can be described by SM interactions only and placed an upper limit on the effective muon neutrino magnetic moment of  $\mu_{\nu_\mu} < 19.1 \times 10^{-10} \mu_B$  at 90% C.L..

The uncertainty on the background prediction is dominated by systematic uncertainties, particularly those related to the neutrino flux prediction, effect of which is evident in Fig. 4.29. Detector-related systematic uncertainties are the second-largest contributor, with neutrino interaction uncertainties having only a limited impact.

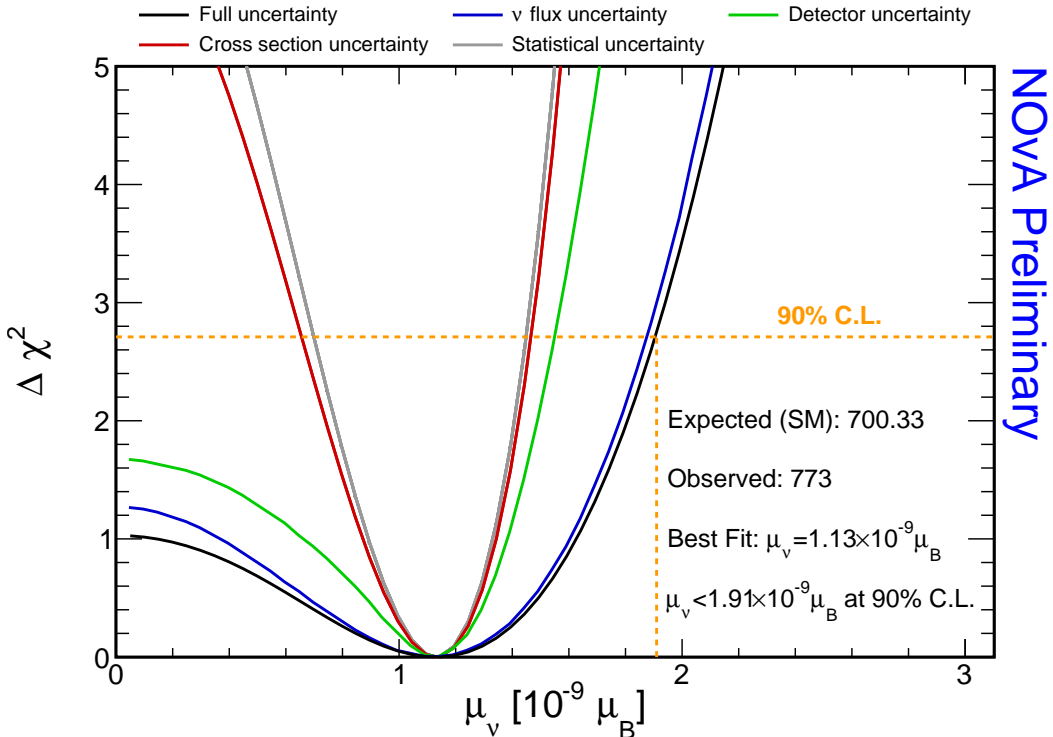


Figure 4.29: Distribution of the minimum log likelihood ratio, equal to  $\Delta\chi^2$ , as a function of the neutrino magnetic moment as determined from a fit of the prediction to the observed data. The minimum is calculated by profiling over systematic uncertainties, as explained in text. Various selections of systematic uncertainties included in the fit are shown, with no systematic uncertainties included in gray (statistics-only result), neutrino flux, detector, and neutrino cross section systematic uncertainties in blue, green, and red respectively. The black line shows the distribution with the full range of systematic uncertainties included in the fit. This distribution is used to determine the 90% C.L. limit on the value of the effective muon neutrino magnetic moment, by calculating the value corresponding to  $\Delta\chi^2 = 2.71$ , as described in text.

However, the signal process’s low cross-section results in significant statistical uncertainty, as the number of neutrino magnetic moment signal events is much smaller than the SM background.

Our 90% C.L. limit is less strict than the current world-leading limit [52] for muon neutrinos of  $\mu_{\nu_\mu} < 6.8 \times 10^{-10} \mu_B$  at 90 % C.L. [187]. It is also less strict than the previous NOvA limit of  $\mu_{\nu_\mu} < 15.8 \times 10^{-10} \mu_B$  at 90 % C.L. [191], which however does not account for the effect of systematic uncertainties.

There are several possibilities for improvements in future iterations of the analysis. The simplest enhancement is to increase the size of the dataset, as NOvA is expected to continue running through 2026, more than doubling the available FHC data. Additionally, including RHC data, either by simply using them together with the FHC data, or through a separate analysis, would help improve the reach of our analysis. It could also help disentangle some of the backgrounds and systematic uncertainties, given that the neutrino magnetic moment should affect neutrinos and antineutrinos equally, while the backgrounds can be affected variously.

Further improvements could come from enhancements to the detector simulation, calibration, and event reconstruction, particularly for single-electron events. The ongoing analysis of data from the NOvA Test Beam detector will be instrumental in these upgrades, as discussed in Chapter 3, reducing the effect of detector-related systematic uncertainties. Additionally, implementing the new hadron production data from NA61 and EMPHATIC experiments will significantly improve the neutrino flux prediction and reduce the associated systematic uncertainty, as discussed in Sec. 2.4.

It is also possible to further improve the event selection, either by enhancing the signal-to-background ratio of the signal sample by tuning the employed cuts, or by devising one or multiple control samples. Control samples are regions dominated by a specific type of background with little to no signal events. Simultaneously fitting these control regions alongside the signal region would help constrain both the background levels and their associated systematic uncertainties. In the signal sample, we applied a low energy cut at 0.5 GeV due to limited time for investigating low-energy backgrounds and corresponding systematic uncertainties. In the future it might be possible to extend the event selection to lower energies improving our signal-to-background ratio. However, as can be seen in Fig. 4.24, there are significant

backgrounds at low energies with a similar shape to the signal, therefore it would be imperative to properly study these background before extending the low energy cut to lower energies.

Another potential improvement involves transitioning from a single-bin fit to a multi-bin fit, using the reconstructed calorimetric energy of the leading shower. The NOvA light dark matter analysis employs template fitting for this purpose, which assumes the prediction accurately describes the shapes of the signal and background distributions while allowing their normalisations to vary. This reduces the number of free parameters in the fit while enhancing sensitivity to the shape differences. This is especially relevant for our analysis since the magnetic moment signal sharply rises at lower energies, while the dominant  $\nu$ -on-e background has a more uniform distribution. On the other hand, this technique assumes no prior knowledge on the normalisation. Therefore, a combination of template-only and normalisation-only fit might be the best solution.

# CHAPTER 5

## Conclusion

In this thesis we presented results of the search for the muon neutrino magnetic moment by searching for an excess of  $\nu$ -on-e events above the SM background. We used muon-neutrino dominated data from the NOvA ND collected between 2014 and 2021, corresponding to an exposure of  $13.8 \times 10^{20}$  POT. We did not find any excess of  $\nu$ -on-e events with a goodness-of-fit test for the Standard Model-only hypothesis yielding a p-value of 0.31. We placed an upper limit on the effective muon neutrino magnetic moment at  $\mu_{\nu_\mu} < 19.1 \times 10^{-10} \mu_B$  at 90% C.L..

Multitude possibilities of improvements for the future iterations of this analysis will allow NOvA to provide competitive results on the effective muon neutrino magnetic moment.

The uncertainties in this analysis are dominated by systematic uncertainties for neutrino beam prediction and detector modelling, as well as the statistical uncertainty of the predicted signal over the predicted background. The systematic uncertainties on the neutrino beam prediction are being tackled by improving the neutrino beam prediction with a novel set of data from the NA61 and EMPHATIC experiments.

The improvements for the systematic uncertainties on the detector modelling are relying on the results from the NOvA Test Beam experiment. We presented an overview of the Test Beam detector and its calibration, which is an essential step in ensuring the applicability of the Test Beam detector data. We described the first full calibration of the NOvA Test Beam detector, including generating a novel prediction of cosmic muons, as well as numerous improvements and future possibilities for the NOvA calibration procedures.



# Acronyms

**$\nu$ -on-e** neutrino-on-electron (interaction). 111, 112, 114, 118–127, 129–137, 139–154, 156, 157, 162, 163, 166, 167

**2p2h** two particle - two hole. 5, 6, 22

**ADC** Analog-to-Digital Converter. 19, 26, 29, 30, 66, 67, 77

**APD** Avalanche Photodiode. 16, 18, 19, 22, 29, 30, 66, 67, 69, 73, 79, 84, 131

**ASIC** Application-Specific Integrated Circuit. 19

**BDT** Boosted Decision Tree. 26

**BF** Best Fit. 161, 163

**BPF** Break Point Fitter. 24, 45–53, 55–60

**BSM** Beyond Standard Model. 10–12, 111–113, 115, 116

**C.L.** Confidence Level. 111, 112, 160, 163–165, 167

**CC** Charged Current. 1, 2, 4–6, 8, 9, 22, 23, 36, 120, 126, 127, 134, 136, 149, 154

**CEvNS** Coherent Elastic  $\nu$ -Nucleus Scattering. 6

**CMC** Comprehensive Model Configuration. 22

**CNN** Convolutional Neural Network. 25, 149

**COH $\pi$**  Coherent  $\pi$  (production). 6, 22, 36, 157

**CP** Charge conjugation - Parity (symmetry). 1, 8, 10, 13

**CRY** Cosmic-Ray Shower Generator. 22, 26, 44

**CVN** Convolutional Visual Network. 25, 129, 132

**DAQ** Data Acquisition. 19, 23, 28

**DCM** Data Concentration Module. 19, 128

**DIS** Deep Inelastic Scattering. 5, 22, 35, 36

**DUNE** Deep Underground Neutrino Experiment. 10, 13, 21

**FB** Fibre Brightness. 29, 30, 61–63, 71, 72, 106, 107, 109

**FD** Far Detector. 15–19, 22, 23, 29–31, 35, 38, 39, 41–43, 46, 48, 51, 54, 59, 61, 64, 66, 97, 102, 103, 109

**FEB** Front End Board. 18–20, 29, 43, 44, 66, 67, 70, 73, 74, 76, 79–82, 84–86, 89, 102, 106, 107, 109, 131

**Fermilab** Fermi National Accelerator Laboratory. 13, 16, 21, 41, 42

**FHC** Forward Horn Current (neutrino mode). 14, 15, 165

**FOM** Figure Of Merit. 128, 136, 138–147, 149, 154

**FPGA** Field Programmable Gate Array. 19

**FSI** Final State Interaction. 6, 22, 36

**FTBF** Fermilab Test Beam Facility. 39

**HK** Hyper-Kamiokande. 10

**HNL** Heavy Neutral Lepton. 12

**LBL** Long Baseline. 10

**LDM** Light Dark Matter. 112

**LOWESS** Locally Weighted Scatter plot Smoothing. 31, 32, 71

**MC** Monte Carlo. 20–22, 26, 44, 124, 148

**MEC** Meson Exchange Current. 6, 22, 36, 126, 127, 154

**MEU** Muon Energy Unit. 33, 95, 96, 98

**MI** Main Injector. 13, 14, 20

**MIP** Minimum Ionising Particle. 26, 30, 33, 99–101, 103

**MIPP** Main Injector Particle Production (experiment). 21

**ML** Machine Learning. 25, 26, 129

**MSW** Mikheyev-Smirnov-Wolfenstein. 9

**MVA** Multi Variate Analysis. 127, 136, 148, 170

**MWPC** Multiwire Proportional Chamber. 40

**NC** Neutral Current. 1–4, 6, 8, 9, 23, 25, 154, 157

**ND** Near Detector. 13–17, 19, 23, 24, 34–36, 38, 39, 41–43, 46, 48, 51, 52, 54, 59, 61, 66, 97, 102, 103, 109, 111, 112, 114, 117, 124, 127, 132, 136, 155, 161, 163, 167

**NDOS** Near Detector on the Surface. 16, 41–43, 88

**NOvA** NuMI Off-axis  $\nu_e$  Appearance (experiment). 10, 13–26, 28–36, 38–42, 44, 45, 52, 59, 63, 67, 77, 79, 86, 94, 95, 97, 101, 103, 108–112, 114, 117, 119, 121–124, 126, 127, 129, 132, 134, 148, 149, 154, 161, 163, 165–167

**NP** New Physics. 11, 116

**NuMI** Neutrinos from the Main Injector. 13–16, 20, 21, 23, 40, 138

**PCA** Principal Component Analysis. 35

**PE** Photo Electron. 18, 19, 27, 29–31, 66–68, 94, 98

**PECorr** Corrected Photo Electrons. 31, 33, 94–96

**PID** Particle Identification. 25

**PMNS** Pontecorvo-Maki-Nakagawa-Sakata. 7, 8, 115, 116

**POT** Protons On Target. 13, 124, 126, 128, 133, 161, 162, 167

**PPFX** Package to Predict the Flux. 21, 35, 124

**PVC** Polyvinyl chloride. 16–18, 34

**QE** Quasi Elastic (interaction). 4–6, 22, 35, 36

**ReMId** Reconstructed Muon Identifier. 26

**Res** Resonant baryon production. 5, 22, 35, 36, 157

**RHC** Reverse Horn Current (antineutrino mode). 14, 15, 165

**SK** Super-Kamiokande. 9

**SM** Standard Model. 1, 2, 10–12, 111, 113–116, 120–125, 128, 150, 154–159, 161–163, 165, 167

**SNO** Sudbury Neutrino Observatory. 9

**T2K** Tokai to Kamioka (experiment). 10

**TMVA** Tool for MVA. 148–150

**ToF** Time of Flight. 40

**WLS** Wavelength Shifting (fibre). 16–18, 22, 26, 28, 30, 33, 69, 77

# Bibliography

- [1] Wolfgang Pauli. Pauli letter collection: letter to Lise Meitner. Typed copy. URL <http://cds.cern.ch/record/83282>.
- [2] L. M. Brown. The idea of the neutrino. *Physics Today*, 31(9):23–28, September 1978. doi:[10.1063/1.2995181](https://doi.org/10.1063/1.2995181). (Including translation of W. Pauli, Aufsdtze und Vortrdge u’ber Physik und Erkenntnistheorie, Braunschweig (1961)).
- [3] H. A. Bethe. Ionization power of a neutrino with magnetic moment. *Mathematical Proceedings of the Cambridge Philosophical Society*, 31(1):108–115, 1935. doi:[10.1017/S0305004100012998](https://doi.org/10.1017/S0305004100012998).
- [4] Enrico Fermi. Tentativo di una teoria dei raggi  $\beta$ . *Il Nuovo Cimento (1924-1942)*, 11(1):1–19. ISSN 1827-6121. doi:[10.1007/BF02959820](https://doi.org/10.1007/BF02959820).
- [5] Fred L. Wilson. Fermi’s theory of beta decay. *American Journal of Physics*, 36(12):1150–1160, 1968. doi:[10.1119/1.1974382](https://doi.org/10.1119/1.1974382). (A complete English translation of E.Fermi, Zeitschrift fur Physik 88, 161 (1934)).
- [6] Sheldon L. Glashow. Partial-symmetries of weak interactions. *Nuclear Physics*, 22(4):579–588. ISSN 0029-5582. doi:[10.1016/0029-5582\(61\)90469-2](https://doi.org/10.1016/0029-5582(61)90469-2). URL <https://www.sciencedirect.com/science/article/pii/0029558261904692>.
- [7] Steven Weinberg. A model of leptons. *Phys. Rev. Lett.*, 19:1264–1266, Nov 1967. doi:[10.1103/PhysRevLett.19.1264](https://doi.org/10.1103/PhysRevLett.19.1264).
- [8] Abdus Salam. *Weak and electromagnetic interactions*, pages 244–254. doi:[10.1142/9789812795915\\_0034](https://doi.org/10.1142/9789812795915_0034).
- [9] L. Landau. On the conservation laws for weak interactions. *Nuclear Physics*, 3(1):127–131. ISSN 0029-5582. doi:[10.1016/0029-5582\(57\)90061-5](https://doi.org/10.1016/0029-5582(57)90061-5). URL <https://www.sciencedirect.com/science/article/pii/0029558257900615>.
- [10] T. D. Lee and C. N. Yang. Parity nonconservation and a two-component theory of the neutrino. *Phys. Rev.*, 105:1671–1675, Mar 1957. doi:[10.1103/PhysRev.105.1671](https://doi.org/10.1103/PhysRev.105.1671).

- [11] Abdus Salam. On parity conservation and neutrino mass. *Nuovo Cim.*, 5:299–301, 1957. doi:[10.1007/BF02812841](https://doi.org/10.1007/BF02812841).
- [12] Peter W. Higgs. Broken symmetries and the masses of gauge bosons. *Phys. Rev. Lett.*, 13:508–509, Oct 1964. doi:[10.1103/PhysRevLett.13.508](https://doi.org/10.1103/PhysRevLett.13.508).
- [13] F. Englert and R. Brout. Broken symmetry and the mass of gauge vector mesons. *Phys. Rev. Lett.*, 13:321–323, Aug 1964. doi:[10.1103/PhysRevLett.13.321](https://doi.org/10.1103/PhysRevLett.13.321).
- [14] G. S. Guralnik, C. R. Hagen, and T. W. B. Kibble. Global conservation laws and massless particles. *Phys. Rev. Lett.*, 13:585–587, Nov 1964. doi:[10.1103/PhysRevLett.13.585](https://doi.org/10.1103/PhysRevLett.13.585).
- [15] Steven Weinberg. A model of leptons. *Phys. Rev. Lett.*, 19:1264–1266, Nov 1967. doi:[10.1103/PhysRevLett.19.1264](https://doi.org/10.1103/PhysRevLett.19.1264).
- [16] Carlo Giunti and Chung W. Kim. *Fundamentals of Neutrino Physics and Astrophysics*. 2007. ISBN 978-0-19-850871-7.
- [17] F. Reines and C. L. Cowan. Detection of the free neutrino. *Phys. Rev.*, 92:830–831, Nov 1953. doi:[10.1103/PhysRev.92.830](https://doi.org/10.1103/PhysRev.92.830).
- [18] Cowan Jr. C.L., Reines F., Harrison F.B., Kruse H.W., and McGuire A.D. Detection of the free neutrino: A confirmation. *Science*, 124(3212):103–104, July 1956. doi:[10.1126/science.124.3212.103](https://doi.org/10.1126/science.124.3212.103).
- [19] F. Reines and C.L. Cowan. Neutrino physics. *Physics Today*, 10(8):12–18, 1957. doi:[10.1063/1.3060455](https://doi.org/10.1063/1.3060455).
- [20] B. Adeva et al. Measurement of  $Z^0$  decays to hadrons and a precise determination of the number of neutrino species. *Phys. Lett. B*, 237:136–146, 1990. doi:[10.1016/0370-2693\(90\)90476-M](https://doi.org/10.1016/0370-2693(90)90476-M).
- [21] S. Schael et al. Precision electroweak measurements on the  $Z$  resonance. *Phys. Rept.*, 427:257–454, 2006. doi:[10.1016/j.physrep.2005.12.006](https://doi.org/10.1016/j.physrep.2005.12.006).
- [22] M. C. Goodman. Resource letter anp-1: Advances in neutrino physics. *American Journal of Physics*, 84:309–319, 2016. doi:[10.1119/1.4962228](https://doi.org/10.1119/1.4962228).

- [23] M. Schwartz. Feasibility of using high-energy neutrinos to study the weak interactions. *Phys. Rev. Lett.*, 4:306–307, Mar 1960. doi:[10.1103/PhysRevLett.4.306](https://doi.org/10.1103/PhysRevLett.4.306).
- [24] K. Kodama et al. Observation of tau neutrino interactions. *Phys. Lett. B*, 504: 218–224, 2001. doi:[10.1016/S0370-2693\(01\)00307-0](https://doi.org/10.1016/S0370-2693(01)00307-0).
- [25] K. Kodama et al. Final tau-neutrino results from the DONuT experiment. *Phys. Rev. D*, 78:052002, 2008. doi:[10.1103/PhysRevD.78.052002](https://doi.org/10.1103/PhysRevD.78.052002).
- [26] William J Marciano and Zohreh Parsa. Neutrino–electron scattering theory\*. *Journal of Physics G: Nuclear and Particle Physics*, 29(11):2629. doi:[10.1088/0954-3899/29/11/013](https://doi.org/10.1088/0954-3899/29/11/013).
- [27] J. A. Formaggio and G. P. Zeller. From ev to eev: Neutrino cross sections across energy scales. *Rev. Mod. Phys.*, 84:1307–1341, Sep 2012. doi:[10.1103/RevModPhys.84.1307](https://doi.org/10.1103/RevModPhys.84.1307).
- [28] *Fundamental Physics at the Intensity Frontier*, 5 2012. doi:[10.2172/1042577](https://doi.org/10.2172/1042577).
- [29] D. Casper. The Nuance neutrino physics simulation, and the future. *Nucl. Phys. B Proc. Suppl.*, 112:161–170, 2002. doi:[10.1016/S0920-5632\(02\)01756-5](https://doi.org/10.1016/S0920-5632(02)01756-5).
- [30] Jr. Davis, Raymond, Don S. Harmer, and Kenneth C. Hoffman. Search for neutrinos from the sun. *Phys. Rev. Lett.*, 20:1205–1209, 1968. doi:[10.1103/PhysRevLett.20.1205](https://doi.org/10.1103/PhysRevLett.20.1205).
- [31] G. Danby, J-M. Gaillard, K. Goulianos, L. M. Lederman, N. Mistry, M. Schwartz, and J. Steinberger. Observation of high-energy neutrino reactions and the existence of two kinds of neutrinos. *Phys. Rev. Lett.*, 9:36–44, Jul 1962. doi:[10.1103/PhysRevLett.9.36](https://doi.org/10.1103/PhysRevLett.9.36).
- [32] A. A. Aguilar-Arevalo et al. First measurement of the muon neutrino charged current quasielastic double differential cross section. *Phys. Rev. D*, 81:092005, May 2010. doi:[10.1103/PhysRevD.81.092005](https://doi.org/10.1103/PhysRevD.81.092005).
- [33] M. Sajjad Athar, A. Fatima, and S. K. Singh. Neutrinos and their interactions with matter. *Prog. Part. Nucl. Phys.*, 129:104019, 2023. doi:[10.1016/j.ppnp.2022.104019](https://doi.org/10.1016/j.ppnp.2022.104019).

- [34] M. Martini, M. Ericson, G. Chanfray, and J. Marteau. Unified approach for nucleon knock-out and coherent and incoherent pion production in neutrino interactions with nuclei. *Phys. Rev. C*, 80:065501, Dec 2009. doi:[10.1103/PhysRevC.80.065501](https://doi.org/10.1103/PhysRevC.80.065501).
- [35] M. Martini, M. Ericson, G. Chanfray, and J. Marteau. Neutrino and antineutrino quasielastic interactions with nuclei. *Phys. Rev. C*, 81:045502, Apr 2010. doi:[10.1103/PhysRevC.81.045502](https://doi.org/10.1103/PhysRevC.81.045502).
- [36] M. Martini, M. Ericson, and G. Chanfray. Neutrino quasielastic interaction and nuclear dynamics. *Phys. Rev. C*, 84:055502, Nov 2011. doi:[10.1103/PhysRevC.84.055502](https://doi.org/10.1103/PhysRevC.84.055502).
- [37] D. Akimov et al. Observation of coherent elastic neutrino-nucleus scattering. *Science*, 357(6356):1123–1126. doi:[10.1126/science.aao0990](https://doi.org/10.1126/science.aao0990).
- [38] B Pontecorvo. Mesonium and antimesonium. *Sov. Phys. JETP*, 33:549–551, 8 1957.
- [39] B. Pontecorvo. Inverse beta processes and nonconservation of lepton charge. *Sov. Phys. JETP*, 7:172–173, 1958.
- [40] Ziro Maki, Masami Nakagawa, and Shoichi Sakata. Remarks on the unified model of elementary particles. *Prog. Theor. Phys.*, 28:870–880, 1962. doi:[10.1143/PTP.28.870](https://doi.org/10.1143/PTP.28.870).
- [41] V. Gribov and B. Pontecorvo. Neutrino astronomy and lepton charge. *Physics Letters B*, 28(7):493–496. ISSN 0370-2693. doi:[10.1016/0370-2693\(69\)90525-5](https://doi.org/10.1016/0370-2693(69)90525-5). URL <https://www.sciencedirect.com/science/article/pii/0370269369905255>.
- [42] M.C. Gonzalez-Garcia and Yosef Nir. Neutrino Masses and Mixing: Evidence and Implications. *Rev. Mod. Phys.*, 75:345–402, 2003. doi:[10.1103/RevModPhys.75.345](https://doi.org/10.1103/RevModPhys.75.345).
- [43] L. Wolfenstein. Neutrino oscillations in matter. *Phys. Rev. D*, 17:2369–2374, May 1978. doi:[10.1103/PhysRevD.17.2369](https://doi.org/10.1103/PhysRevD.17.2369).

- [44] S.P. Mikheyev and A.Yu. Smirnov. Resonance Amplification of Oscillations in Matter and Spectroscopy of Solar Neutrinos. *Sov. J. Nucl. Phys.*, 42:913–917, 1985.
- [45] M. Aglietta et al. Experimental study of atmospheric neutrino flux in the NUSEX experiment. *Europhysics Letters (EPL)*, 8(7):611–614, 04 1989. doi:[10.1209/0295-5075/8/7/005](https://doi.org/10.1209/0295-5075/8/7/005).
- [46] K. Daum et al. Determination of the atmospheric neutrino spectra with the Fréjus detector. *Zeitschrift für Physik C Particles and Fields*, 66(3):417–428, 1995. ISSN 1431-5858. doi:[10.1007/BF01556368](https://doi.org/10.1007/BF01556368).
- [47] R. Becker-Szendy et al. Electron- and muon-neutrino content of the atmospheric flux. *Phys. Rev. D*, 46:3720–3724, Nov 1992. doi:[10.1103/PhysRevD.46.3720](https://doi.org/10.1103/PhysRevD.46.3720).
- [48] Y. Fukuda et al. Atmospheric muon-neutrino / electron-neutrino ratio in the multiGeV energy range. *Phys. Lett. B*, 335:237–245, 1994. doi:[10.1016/0370-2693\(94\)91420-6](https://doi.org/10.1016/0370-2693(94)91420-6).
- [49] Y. Fukuda et al. Evidence for oscillation of atmospheric neutrinos. *Phys. Rev. Lett.*, 81:1562–1567, 1998. doi:[10.1103/PhysRevLett.81.1562](https://doi.org/10.1103/PhysRevLett.81.1562).
- [50] Q.R. Ahmad et al. Direct evidence for neutrino flavor transformation from neutral current interactions in the Sudbury Neutrino Observatory. *Phys. Rev. Lett.*, 89:011301, 2002. doi:[10.1103/PhysRevLett.89.011301](https://doi.org/10.1103/PhysRevLett.89.011301).
- [51] Patrick Huber et al. Snowmass Neutrino Frontier Report. In *Snowmass 2021*, 11 2022.
- [52] R. L. Workman and Others. Review of Particle Physics. *PTEP*, 2022:083C01, 2022. doi:[10.1093/ptep/ptac097](https://doi.org/10.1093/ptep/ptac097).
- [53] Ivan Esteban, M. C. Gonzalez-Garcia, Michele Maltoni, Thomas Schwetz, and Albert Zhou. The fate of hints: updated global analysis of three-flavor neutrino oscillations. *JHEP*, 09:178, 2020. doi:[10.1007/JHEP09\(2020\)178](https://doi.org/10.1007/JHEP09(2020)178).

- [54] M. A. Acero et al. Improved measurement of neutrino oscillation parameters by the NOvA experiment. *Phys. Rev. D*, 106(3):032004, 2022. doi:[10.1103/PhysRevD.106.032004](https://doi.org/10.1103/PhysRevD.106.032004).
- [55] K. Abe et al. Measurements of neutrino oscillation parameters from the T2K experiment using  $3.6 \times 10^{21}$  protons on target. *Eur. Phys. J. C*, 83(9):782, 2023. doi:[10.1140/epjc/s10052-023-11819-x](https://doi.org/10.1140/epjc/s10052-023-11819-x).
- [56] B. Abi et al. Volume I. Introduction to DUNE. *Journal of Instrumentation*, 15 (08):T08008. doi:[10.1088/1748-0221/15/08/T08008](https://doi.org/10.1088/1748-0221/15/08/T08008).
- [57] K. Abe et al. Hyper-Kamiokande Design Report. 5 2018.
- [58] M. Aker et al. Direct neutrino-mass measurement with sub-electronvolt sensitivity. *Nature Phys.*, 18(2):160–166, 2022. doi:[10.1038/s41567-021-01463-1](https://doi.org/10.1038/s41567-021-01463-1).
- [59] Aghanim, N. et al. Planck 2018 results - vi. cosmological parameters. *Astron. Astrophys.*, 641:A6. doi:[10.1051/0004-6361/201833910](https://doi.org/10.1051/0004-6361/201833910).
- [60] A. Aguilar et al. Evidence for neutrino oscillations from the observation of  $\bar{\nu}_e$  appearance in a  $\bar{\nu}_\mu$  beam. *Phys. Rev. D*, 64:112007, Nov 2001. doi:[10.1103/PhysRevD.64.112007](https://doi.org/10.1103/PhysRevD.64.112007).
- [61] A.A. Aguilar-Arevalo et al. Significant Excess of ElectronLike Events in the MiniBooNE Short-Baseline Neutrino Experiment. *Phys. Rev. Lett.*, 121(22): 221801, 2018. doi:[10.1103/PhysRevLett.121.221801](https://doi.org/10.1103/PhysRevLett.121.221801).
- [62] M.C. Gonzalez-Garcia and Michele Maltoni. Phenomenology with Massive Neutrinos. *Phys. Rept.*, 460:1–129, 2008. doi:[10.1016/j.physrep.2007.12.004](https://doi.org/10.1016/j.physrep.2007.12.004).
- [63] Rabindra N. Mohapatra and Goran Senjanovic. Neutrino Mass and Spontaneous Parity Nonconservation. *Phys. Rev. Lett.*, 44:912, 1980. doi:[10.1103/PhysRevLett.44.912](https://doi.org/10.1103/PhysRevLett.44.912).
- [64] Ettore Majorana. Teoria simmetrica dell'elettrone e del positrone. *Nuovo Cim.*, 14:171–184, 1937. doi:[10.1007/BF02961314](https://doi.org/10.1007/BF02961314). Translated by Luciano Maiani in “Soryushiron Kenkyu”, 63 (1981) 149-462.

- [65] Nova experiments official website. URL <https://novaexperiment.fnal.gov>. Cited February 2024.
- [66] Fermi national accelerator laboratory official website. URL <https://fnal.gov>. Cited February 2024.
- [67] Gary Feldman for the NOvA Collaboration. Physics of the nova experiment. White paper, 2012. URL <https://nova-docdb.fnal.gov/cgi-bin>ShowDocument?docid=7733>. Public NOvA document: NOVA-doc-7733-v1, cited on 05.2020.
- [68] R.B. Patterson. The NOvA Experiment: Status and Outlook. *Nucl. Phys. B Proc. Suppl.*, 235-236:151–157, 2013. doi:[10.1016/j.nuclphysbps.2013.04.005](https://doi.org/10.1016/j.nuclphysbps.2013.04.005).
- [69] P. Adamson et al. First measurement of muon-neutrino disappearance in NOvA. *Phys. Rev. D*, 93(5):051104, 2016. doi:[10.1103/PhysRevD.93.051104](https://doi.org/10.1103/PhysRevD.93.051104).
- [70] M.A. Acero et al. First Measurement of Neutrino Oscillation Parameters using Neutrinos and Antineutrinos by NOvA. *Phys. Rev. Lett.*, 123(15):151803, 2019. doi:[10.1103/PhysRevLett.123.151803](https://doi.org/10.1103/PhysRevLett.123.151803).
- [71] M. A. Acero et al. Measurement of neutrino-induced neutral-current coherent  $\pi^0$  production in the NOvA near detector. *Phys. Rev. D*, 102(1):012004, 2020. doi:[10.1103/PhysRevD.102.012004](https://doi.org/10.1103/PhysRevD.102.012004).
- [72] M. A. Acero et al. Measurement of the double-differential muon-neutrino charged-current inclusive cross section in the NOvA near detector. *Phys. Rev. D*, 107(5):052011, 2023. doi:[10.1103/PhysRevD.107.052011](https://doi.org/10.1103/PhysRevD.107.052011).
- [73] M. A. Acero et al. Measurement of the  $\nu_e$ –Nucleus Charged-Current Double-Differential Cross Section at  $\langle E_\nu \rangle = 2.4$  GeV using NOvA. *Phys. Rev. Lett.*, 130 (5):051802, 2023. doi:[10.1103/PhysRevLett.130.051802](https://doi.org/10.1103/PhysRevLett.130.051802).
- [74] M. A. Acero et al. Measurement of  $\nu_\mu$  charged-current inclusive  $\pi^0$  production in the NOvA near detector. *Phys. Rev. D*, 107(11):112008, 2023. doi:[10.1103/PhysRevD.107.112008](https://doi.org/10.1103/PhysRevD.107.112008).
- [75] P. Adamson et al. Search for active-sterile neutrino mixing using neutral-current interactions in NOvA. *Phys. Rev. D*, 96(7):072006, 2017. doi:[10.1103/PhysRevD.96.072006](https://doi.org/10.1103/PhysRevD.96.072006).

- [76] M. A. Acero et al. Search for Active-Sterile Antineutrino Mixing Using Neutral-Current Interactions with the NOvA Experiment. *Phys. Rev. Lett.*, 127(20):201801, 2021. doi:[10.1103/PhysRevLett.127.201801](https://doi.org/10.1103/PhysRevLett.127.201801).
- [77] M. A. Acero et al. Supernova neutrino detection in NOvA. *JCAP*, 10:014, 2020. doi:[10.1088/1475-7516/2020/10/014](https://doi.org/10.1088/1475-7516/2020/10/014).
- [78] M. A. Acero et al. Extended search for supernovalike neutrinos in NOvA coincident with LIGO/Virgo detections. *Phys. Rev. D*, 104(6):063024, 2021. doi:[10.1103/PhysRevD.104.063024](https://doi.org/10.1103/PhysRevD.104.063024).
- [79] M. A. Acero et al. Search for slow magnetic monopoles with the NOvA detector on the surface. *Phys. Rev. D*, 103(1):012007, 2021. doi:[10.1103/PhysRevD.103.012007](https://doi.org/10.1103/PhysRevD.103.012007).
- [80] Peter N. Shanahan and Patricia LaVern Vahle. Physics with NOvA: a half-time review. *Eur. Phys. J. ST*, 230(24):4259–4273, 2021. doi:[10.1140/epjs/s11734-021-00285-9](https://doi.org/10.1140/epjs/s11734-021-00285-9).
- [81] Peter Shanahan and Patricia Vahle. The NOvA Physics Program through 2025. Snowmass 2021 Letters of Interest NF, 135. URL [https://www.snowmass21.org/docs/files/summaries/NF/SNOWMASS21-NF1\\_NF3\\_Patricia\\_Vahle-145.pdf](https://www.snowmass21.org/docs/files/summaries/NF/SNOWMASS21-NF1_NF3_Patricia_Vahle-145.pdf).
- [82] P. Adamson et al. The NuMI Neutrino Beam. *Nucl. Instrum. Meth. A*, 806:279–306, 2016. doi:[10.1016/j.nima.2015.08.063](https://doi.org/10.1016/j.nima.2015.08.063).
- [83] Records. URL <https://operations.fnal.gov/records/>. Performance records achieved by the Fermilab accelerators. Cited May 2024.
- [84] Katsuya Yonehara. Megawatt upgrade of numi target system. 1 2022. URL <https://www.osti.gov/biblio/1844332>.
- [85] Leonidas Aliaga Soplin. *Neutrino Flux Prediction for the NuMI Beamline*. PhD thesis, William-Mary Coll., 2016.
- [86] Leonidas Aliaga Soplin. 2017-2018 Beam Plots. NOVA Document 20843. URL <https://nova-docdb.fnal.gov/cgi-bin/sso>ShowDocument?docid=20843>. NOvA internal document.

- [87] D. S. Ayres et al. The nova technical design report. *NOvA Collaboration*, 2007. doi:[10.2172/935497](https://doi.org/10.2172/935497).
- [88] Yury Kudenko. Neutrino detectors for oscillation experiments. *JINST*, 12(06):C06003, 2017. doi:[10.1088/1748-0221/12/06/C06003](https://doi.org/10.1088/1748-0221/12/06/C06003).
- [89] S. Mufson et al. Liquid scintillator production for the NOvA experiment. *Nucl. Instrum. Meth. A*, 799:1–9, 2015. doi:[10.1016/j.nima.2015.07.026](https://doi.org/10.1016/j.nima.2015.07.026).
- [90] Alex Sousa. Density of NOvA Liquid Scintillator at 69° F. NOVA Document 11886, . URL <https://nova-docdb.fnal.gov/cgi-bin/sso>ShowDocument?docid=11886>. NOvA internal document.
- [91] M.J. Berger, J.S. Coursey, M.A. Zucker, and J. Chang. ESTAR, PSTAR, and ASTAR: Computer Programs for Calculating Stopping-Power and Range Tables for Electrons, Protons, and Helium Ions (version 1.2.3). URL <http://physics.nist.gov/Star>.
- [92] Luke Vinton. Calorimetric Energy Scale Calibration of the NOvA Detectors. NOVA Document 13579, document FA\_Calorimetric\_energy\_scale.pdf. URL <https://nova-docdb.fnal.gov/cgi-bin/sso>ShowDocument?docid=13579>. NOvA Technical Note.
- [93] Xinchun Tian. NOvA Data Acquisition Software System. In *Meeting of the APS Division of Particles and Fields*, 9 2011.
- [94] Joao Coelho, Barnali Chowdhury, and Ryan Murphy. Tech note: Good data selection. NOVA Document 13546. URL <https://nova-docdb.fnal.gov/cgi-bin/sso>ShowDocument?docid=13546>. NOvA technical note.
- [95] Jonathan M. Paley. BadChannels Technical Note. NOVA Document 12771. URL <https://nova-docdb.fnal.gov/cgi-bin/sso>ShowDocument?docid=12771>. NOvA technical note.
- [96] A. Aurisano, C. Backhouse, R. Hatcher, N. Mayer, J. Musser, R. Patterson, R. Schroeter, and A. Sousa. The NOvA simulation chain. *J. Phys. Conf. Ser.*, 664(7):072002, 2015. doi:[10.1088/1742-6596/664/7/072002](https://doi.org/10.1088/1742-6596/664/7/072002).

- [97] S. Agostinelli et al. GEANT4—a simulation toolkit. *Nucl. Instrum. Meth. A*, 506: 250–303, 2003. doi:[10.1016/S0168-9002\(03\)01368-8](https://doi.org/10.1016/S0168-9002(03)01368-8).
- [98] Zarko Pavlovic. *Observation of Disappearance of Muon Neutrinos in the NuMI Beam*. PhD thesis, Texas U., 2008.
- [99] L. Aliaga et al. Neutrino Flux Predictions for the NuMI Beam. *Phys. Rev. D*, 94(9):092005, 2016. doi:[10.1103/PhysRevD.94.092005](https://doi.org/10.1103/PhysRevD.94.092005). [Addendum: Phys.Rev.D 95, 039903 (2017)].
- [100] C. Alt et al. Inclusive production of charged pions in p+C collisions at 158-GeV/c beam momentum. *Eur. Phys. J. C*, 49:897–917, 2007. doi:[10.1140/epjc/s10052-006-0165-7](https://doi.org/10.1140/epjc/s10052-006-0165-7).
- [101] Gemma Maria Tinti. *Sterile neutrino oscillations in MINOS and hadron production in pC collisions*. PhD thesis, 2010.
- [102] B Baatar, G Barr, J Bartke, L Betev, O Chvala, J Dolejsi, V Eckardt, HG Fischer, Z Fodor, A Karev, et al. Inclusive production of protons, anti-protons, neutrons, deuterons and tritons in p+ c collisions at 158 gev/c beam momentum. *The European Physical Journal C*, 73:1–66, 2013. doi:[10.1140/epjc/s10052-013-2364-3](https://doi.org/10.1140/epjc/s10052-013-2364-3).
- [103] D. S. Barton et al. Experimental study of the  $a$  dependence of inclusive hadron fragmentation. *Phys. Rev. D*, 27:2580–2599, Jun 1983. doi:[10.1103/PhysRevD.27.2580](https://doi.org/10.1103/PhysRevD.27.2580).
- [104] Andrey V. Lebedev. *Ratio of Pion Kaon Production in Proton Carbon Interactions*. PhD thesis, 2007.
- [105] T.T. Böhlen, F. Cerutti, M.P.W. Chin, A. Fassò, A. Ferrari, P.G. Ortega, A. Mairani, P.R. Sala, G. Smirnov, and V. Vlachoudis. The fluka code: Developments and challenges for high energy and medical applications. *Nuclear Data Sheets*, 120:211–214. ISSN 0090-3752. doi:[10.1016/j.nds.2014.07.049](https://doi.org/10.1016/j.nds.2014.07.049).
- [106] Alfredo Ferrari, Paola R. Sala, Alberto Fasso, and Johannes Ranft. FLUKA: A multi-particle transport code (Program version 2005). 10 2005. doi:[10.2172/877507](https://doi.org/10.2172/877507).

- [107] A. Aduszkiewicz et al. Measurements of production and inelastic cross sections for p+C , p+Be , and p+Al at 60 GeV/c and p+C and p+Be at 120 GeV/c. *Phys. Rev. D*, 100(11):112001, 2019. doi:[10.1103/PhysRevD.100.112001](https://doi.org/10.1103/PhysRevD.100.112001).
- [108] H. Adhikary et al. Measurements of  $\pi^+$ ,  $\pi^-$ ,  $p$ ,  $\bar{p}$ ,  $K^+$  and  $K^-$  production in 120 GeV/c p + C interactions. *Phys. Rev. D*, 108:072013, 2023. doi:[10.1103/PhysRevD.108.072013](https://doi.org/10.1103/PhysRevD.108.072013).
- [109] H. Adhikary et al. Measurements of KS0,  $\Lambda$ , and  $\Lambda^-$  production in 120 GeV/c p+C interactions. *Phys. Rev. D*, 107(7):072004, 2023. doi:[10.1103/PhysRevD.107.072004](https://doi.org/10.1103/PhysRevD.107.072004).
- [110] A. Aduszkiewicz et al. Measurements of hadron production in  $\pi^+ + C$  and  $\pi^+ + Be$  interactions at 60 GeV/c. *Phys. Rev. D*, 100(11):112004, 2019. doi:[10.1103/PhysRevD.100.112004](https://doi.org/10.1103/PhysRevD.100.112004).
- [111] Matej Pavin. Hadron production measurements for neutrino experiments, 2020. URL [https://indico.fnal.gov/event/43209/contributions/187869/attachments/130502/159028/HadronProduction\\_neutrino2020.pdf](https://indico.fnal.gov/event/43209/contributions/187869/attachments/130502/159028/HadronProduction_neutrino2020.pdf). Presented on Neutrino 2020 conference.
- [112] T. Akaishi et al. EMPHATIC: A Proposed Experiment to Measure Hadron Scattering and Production Cross Sections for Improved Neutrino Flux Predictions. 12 2019.
- [113] C. Andreopoulos et al. The GENIE Neutrino Monte Carlo Generator. *Nucl. Instrum. Meth. A*, 614:87–104, 2010. doi:[10.1016/j.nima.2009.12.009](https://doi.org/10.1016/j.nima.2009.12.009).
- [114] J. Nieves, J. E. Amaro, and M. Valverde. Inclusive quasielastic charged-current neutrino-nucleus reactions. *Phys. Rev. C*, 70:055503, Nov 2004. doi:[10.1103/PhysRevC.70.055503](https://doi.org/10.1103/PhysRevC.70.055503).
- [115] Aaron S. Meyer, Minerba Betancourt, Richard Gran, and Richard J. Hill. Deuterium target data for precision neutrino-nucleus cross sections. *Phys. Rev. D*, 93:113015, Jun 2016. doi:[10.1103/PhysRevD.93.113015](https://doi.org/10.1103/PhysRevD.93.113015).

- [116] J. Nieves, I. Ruiz Simo, and M. J. Vicente Vacas. Inclusive charged-current neutrino-nucleus reactions. *Phys. Rev. C*, 83:045501, Apr 2011. doi:[10.1103/PhysRevC.83.045501](https://doi.org/10.1103/PhysRevC.83.045501).
- [117] R. Gran, J. Nieves, F. Sanchez, and M. J. Vicente Vacas. Neutrino-nucleus quasi-elastic and 2p2h interactions up to 10 gev. *Phys. Rev. D*, 88:113007, Dec 2013. doi:[10.1103/PhysRevD.88.113007](https://doi.org/10.1103/PhysRevD.88.113007).
- [118] Ch. Berger and L. M. Sehgal. Lepton mass effects in single pion production by neutrinos. *Phys. Rev. D*, 76:113004, Dec 2007. doi:[10.1103/PhysRevD.76.113004](https://doi.org/10.1103/PhysRevD.76.113004).
- [119] Ch. Berger and L. M. Sehgal. Partially conserved axial vector current and coherent pion production by low energy neutrinos. *Phys. Rev. D*, 79:053003, Mar 2009. doi:[10.1103/PhysRevD.79.053003](https://doi.org/10.1103/PhysRevD.79.053003).
- [120] A Bodek and U. K. Yang. Higher twist, xi(omega) scaling, and effective LO PDFs for lepton scattering in the few GeV region. *J. Phys. G*, 29:1899–1906, 2003. doi:[10.1088/0954-3899/29/8/369](https://doi.org/10.1088/0954-3899/29/8/369).
- [121] T. Yang, C. Andreopoulos, H. Gallagher, K. Hoffmann, and P. Kehayias. A Hadronization Model for Few-GeV Neutrino Interactions. *Eur. Phys. J. C*, 63:1–10, 2009. doi:[10.1140/epjc/s10052-009-1094-z](https://doi.org/10.1140/epjc/s10052-009-1094-z).
- [122] L.L. Salcedo, E. Oset, M.J. Vicente-Vacas, and C. Garcia-Recio. Computer simulation of inclusive pion nuclear reactions. *Nuclear Physics A*, 484(3):557–592. ISSN 0375-9474. doi:[10.1016/0375-9474\(88\)90310-7](https://doi.org/10.1016/0375-9474(88)90310-7).
- [123] Chris Hagmann, David Lange, and Douglas Wright. Cosmic-ray shower generator (cry) for monte carlo transport codes. volume 2, pages 1143 – 1146. ISBN 978-1-4244-0922-8. doi:[10.1109/NSSMIC.2007.4437209](https://doi.org/10.1109/NSSMIC.2007.4437209).
- [124] C. N. Chou. The nature of the saturation effect of fluorescent scintillators. *Phys. Rev.*, 87:904–905, Sep 1952. doi:[10.1103/PhysRev.87.904](https://doi.org/10.1103/PhysRev.87.904).
- [125] M. Baird, J. Bian, M. Messier, E. Niner, D. Rocco, and K. Sachdev. Event Reconstruction Techniques in NOvA. *J. Phys. Conf. Ser.*, 664(7):072035, 2015. doi:[10.1088/1742-6596/664/7/072035](https://doi.org/10.1088/1742-6596/664/7/072035).

- [126] Martin Ester, Hans-Peter Kriegel, Jörg Sander, and Xiaowei Xu. A density-based algorithm for discovering clusters in large spatial databases with noise. In *Proceedings of the Second International Conference on Knowledge Discovery and Data Mining*, KDD'96, page 226–231. AAAI Press, 1996. doi:[10.5555/3001460.3001507](https://doi.org/10.5555/3001460.3001507).
- [127] Leandro A. F. Fernandes and Manuel Menezes de Oliveira Neto. Real-time line detection through an improved hough transform voting scheme. *Pattern Recognit.*, 41:299–314, 2008. doi:[10.1016/j.patcog.2007.04.003](https://doi.org/10.1016/j.patcog.2007.04.003). URL <https://api.semanticscholar.org/CorpusID:5996185>.
- [128] Mattias Ohlsson, Carsten Peterson, and Alan L. Yuille. Track finding with deformable templates — the elastic arms approach. *Computer Physics Communications*, 71(1):77–98. ISSN 0010-4655. doi:[10.1016/0010-4655\(92\)90074-9](https://doi.org/10.1016/0010-4655(92)90074-9). URL <https://www.sciencedirect.com/science/article/pii/0010465592900749>.
- [129] R. Krishnapuram and J.M. Keller. A possibilistic approach to clustering. *IEEE Transactions on Fuzzy Systems*, 1(2):98–110, 1993. doi:[10.1109/91.227387](https://doi.org/10.1109/91.227387).
- [130] Miin-Shen Yang and Kuo-Lung Wu. Unsupervised possibilistic clustering. *Pattern Recognition*, 39(1):5–21. ISSN 0031-3203. doi:[10.1016/j.patcog.2005.07.005](https://doi.org/10.1016/j.patcog.2005.07.005). URL <https://www.sciencedirect.com/science/article/pii/S0031320305002943>.
- [131] Jianming Bian, Hongyue Duyang, and Alexander Radovic. Blessing package for Neutrino-Electron Scattering and Coherent Pi0. NOVA Document 13862. URL <https://nova-docdb.fnal.gov/cgi-bin/sso>ShowDocument?docid=13862>. NOvA internal document.
- [132] Nicholas Jacob Raddatz. *Measurement of Muon Neutrino Disappearance with Non-Fiducial Interactions in the NOvA Experiment*. PhD thesis, Minnesota U., 2016.
- [133] Michael David Baird. *An Analysis of Muon Neutrino Disappearance from the NuMI Beam Using an Optimal Track Fitter*. PhD thesis, Indiana U., 2015.
- [134] G. Lutz. Optimum track fitting in the presence of multiple scattering. *NIM*

- A*, 273(1):349–361. ISSN 0168-9002. doi:10.1016/0168-9002(88)90836-4. URL <https://www.sciencedirect.com/science/article/pii/0168900288908364>.
- [135] Brian Rebel. Window tracking algorithm for cosmic ray muons. NOVA Document 15977-v1. URL <https://nova-docdb.fnal.gov/cgi-bin/sso>ShowDocument?docid=15977>. NOvA internal document.
- [136] Christian Szegedy, Wei Liu, Yangqing Jia, Pierre Sermanet, Scott Reed, Dragomir Anguelov, Dumitru Erhan, Vincent Vanhoucke, and Andrew Rabinovich. Going Deeper with Convolutions. *arXiv e-prints*, art. arXiv:1409.4842. doi:[10.48550/arXiv.1409.4842](https://doi.org/10.48550/arXiv.1409.4842).
- [137] A. Aurisano, A. Radovic, D. Rocco, A. Himmel, M.D. Messier, E. Niner, G. Pawloski, F. Psihas, A. Sousa, and P. Vahle. A Convolutional Neural Network Neutrino Event Classifier. *JINST*, 11(09):P09001, 2016. doi:[10.1088/1748-0221/11/09/P09001](https://doi.org/10.1088/1748-0221/11/09/P09001).
- [138] Fernanda Psihas. Measurement of long baseline neutrino oscillations and improvements from deep learning. 1 2018. doi:[10.2172/1437288](https://doi.org/10.2172/1437288). URL <https://www.osti.gov/biblio/1437288>.
- [139] Prabhjot Singh. *Extraction of Neutrino Oscillation Parameters using a Simultaneous Fit of  $\nu_\mu$  Disappearance and  $\nu_e$  Appearance data with the NOvA Experiment*. PhD thesis, University of Delhi, Dept. of Physics and Astrophysics, India, Delhi U., 9 2019.
- [140] Ryan J. Nichol. Fibre brightness from cosmic muon data. NOVA Document 34909. URL <https://nova-docdb.fnal.gov/cgi-bin/sso>ShowDocument?docid=34909>. NOvA technical note.
- [141] Prabhjot Singh. Attenuation Calibration of the NOvA Detectors. In *The 38th International Conference on High Energy Physics (ICHEP 2016)*, 2024. URL <https://nova-docdb.fnal.gov/cgi-bin/sso>ShowDocument?docid=15840>. (cited on 03.2024).
- [142] Nitish Nayak. *A Joint Measurement of  $\nu_\mu$ -Disappearance and  $\nu_e$ -Appearance in*

- the NuMI beam using the NOvA Experiment.* PhD thesis, UC, Irvine (main), UC, Irvine, 2021.
- [143] M. A. Acero et al. Adjusting neutrino interaction models and evaluating uncertainties using NOvA near detector data. *Eur. Phys. J. C*, 80(12):1119, 2020. doi:[10.1140/epjc/s10052-020-08577-5](https://doi.org/10.1140/epjc/s10052-020-08577-5).
  - [144] M. Valverde, J.E. Amaro, and J. Nieves. Theoretical uncertainties on quasielastic charged-current neutrino–nucleus cross sections. 638(4):325–332. ISSN 0370-2693. doi:[10.1016/j.physletb.2006.05.053](https://doi.org/10.1016/j.physletb.2006.05.053).
  - [145] Richard Gran. Model Uncertainties for Valencia RPA Effect for MINERvA. *arXiv e-prints*, 5 2017. URL <https://arxiv.org/abs/1705.02932>.
  - [146] M. Tzanov et al. Precise measurement of neutrino and antineutrino differential cross sections. *Phys. Rev. D*, 74:012008, Jul 2006. doi:[10.1103/PhysRevD.74.012008](https://doi.org/10.1103/PhysRevD.74.012008).
  - [147] M. Kordosky. Ramifications of intranuclear re-scattering in MINOS. 159:223–228. ISSN 0920-5632. doi:[10.1016/j.nuclphysbps.2006.08.040](https://doi.org/10.1016/j.nuclphysbps.2006.08.040). URL <https://www.sciencedirect.com/science/article/pii/S0920563206005342>. Proceedings of the 4th International Workshop on Neutrino-Nucleus Interactions in the Few-GeV Region.
  - [148] A. Mislicvec et al. Measurement of total and differential cross sections of neutrino and antineutrino coherent  $\pi^\pm$  production on carbon. *Phys. Rev. D*, 97(3):032014, 2018. doi:[10.1103/PhysRevD.97.032014](https://doi.org/10.1103/PhysRevD.97.032014).
  - [149] E. S. Pinzon Guerra et al. Using world  $\pi^\pm$ -nucleus scattering data to constrain an intranuclear cascade model. *Phys. Rev. D*, 99:052007, Mar 2019. doi:[10.1103/PhysRevD.99.052007](https://doi.org/10.1103/PhysRevD.99.052007).
  - [150] K. Abe et al. Measurement of neutrino and antineutrino oscillations by the t2k experiment including a new additional sample of  $\nu_e$  interactions at the far detector. *Phys. Rev. D*, 96:092006, Nov 2017. doi:[10.1103/PhysRevD.96.092006](https://doi.org/10.1103/PhysRevD.96.092006).
  - [151] Erika Catano-Mur, V Hewes, and Lisa Koerner. NOvA Production 5.1 Detector Systematics Executive Summary. NOVA Document 53225. URL <https://nova.fnal.gov/documents/53225>

- //nova-docdb.fnal.gov/cgi-bin/sso>ShowDocument?docid=53225. NOvA technical note.
- [152] Juan Miguel Carceller. Calibration shape systematic: middle region and final parameterizations. NOVA Document 49986, April 2021. URL <https://nova-docdb.fnal.gov/cgi-bin/sso>ShowDocument?docid=49986>. NOvA internal document.
- [153] V Hewes Oleg Samoylov. NOvA Production 5 Detector Simulation Changes and Systematics. NOVA Document 43935. URL <https://nova-docdb.fnal.gov/cgi-bin/sso>ShowDocument?docid=43935>. NOvA technical note.
- [154] Michael Wallbank. The NOvA Test Beam Program. *PoS*, ICHEP2020:188, . doi:[10.22323/1.390.0188](https://doi.org/10.22323/1.390.0188).
- [155] Alex Sousa. Test Beam Plenary Update - FNAL September 2018. NOVA Document 33012, . URL <https://nova-docdb.fnal.gov/cgi-bin/sso>ShowDocument?docid=33012>. NOvA internal document.
- [156] Alex Sousa, Ryan Nichol, Karol Lang, and Jeff Nelson. NOvA Test Beam Task Force Report. NOVA Document 15750. URL <https://nova-docdb.fnal.gov/cgi-bin/sso>ShowDocument?docid=15750>. NOvA technical note.
- [157] Alex Sousa. NOvA Test Beam Status and Plans - Support Documentation. NOVA Document 22172-v2, . URL <https://nova-docdb.fnal.gov/cgi-bin/sso>ShowDocument?docid=22172>. NOvA technical note.
- [158] Fermilab test beam facility official website. URL <https://ftbf.fnal.gov/>. Cited March 2024.
- [159] Alex Sousa. NOvA Test Beam Plenary @ IU Collaboration Meeting. NOVA Document 29543, . URL <https://nova-docdb.fnal.gov/cgi-bin/sso>ShowDocument?docid=29543>. NOvA internal document.
- [160] Michael Wallbank. Final Test Beam Updates (Geometry and Other!). NOVA Document 58388, . URL <https://nova-docdb.fnal.gov/cgi-bin/sso>ShowDocument?docid=58388>. NOvA internal document.

- [161] Michael Wallbank. Understanding, Improving, Validating the Test Beam Geometry. NOVA Document 57955, February 2023. URL <https://nova-docdb.fnal.gov/cgi-bin/sso>ShowDocument?docid=57955>. NOvA internal document.
- [162] Robert Kralik. Test beam calibration update. NOVA Document 57516-v2. URL <https://nova-docdb.fnal.gov/cgi-bin/sso>ShowDocument?docid=57516>. NOvA internal document.
- [163] Alex Sousa. Test Beam Plenary Update - Jun. 6, 2019. NOVA Document 38349, . URL <https://nova-docdb.fnal.gov/cgi-bin/sso>ShowDocument?docid=38349>. NOvA internal document.
- [164] Miniboone experiments official website. URL <https://www-boone.fnal.gov/>. Cited March 2024.
- [165] Alex Sousa. Filling System and Scintillator Status. NOVA Document 34067, . URL <https://nova-docdb.fnal.gov/cgi-bin/sso>ShowDocument?docid=34067>. NOvA internal document.
- [166] Junting Huang, Will Flanagan, and Beatriz Tapia Oregui. Test Beam: Light Yield of the Liquid Scintillator Drained from the NDOS Detector. NOVA Document 38740. URL <https://nova-docdb.fnal.gov/cgi-bin/sso>ShowDocument?docid=38740>. NOvA internal document.
- [167] Dung Phan. Test Beam: Tintometer Measurement of Texas A&M oil. NOVA Document 39088. URL <https://nova-docdb.fnal.gov/cgi-bin/sso>ShowDocument?docid=39088>. NOvA internal document.
- [168] Alex Sousa. Test Beam Scintillator Fill Plan. NOVA Document 34196, . URL <https://nova-docdb.fnal.gov/cgi-bin/sso>ShowDocument?docid=34196>. NOvA internal document.
- [169] Alex Sousa. 2nd Block Filling Status - Nov. 18, 2019. NOVA Document 41961, . URL <https://nova-docdb.fnal.gov/cgi-bin/sso>ShowDocument?docid=41961>. NOvA internal document.
- [170] Teresa Megan Lackey. *Proton Scattering in NOvA Test Beam*. PhD thesis, .

- [171] David Northacker, Alex Sousa, and Yagmur Torun. Test Beam - Overfilling Horizontal Planes. NOVA Document 49439. URL <https://nova-docdb.fnal.gov/cgi-bin/sso>ShowDocument?docid=49439>. NOvA internal document.
- [172] Mark Messier and Teresa Lackey. Data driven cosmic generation. NOVA Document 51327-v3. URL <https://nova-docdb.fnal.gov/cgi-bin/sso>ShowDocument?docid=51327&version=3>. NOvA internal document.
- [173] Leon M. Mualem. Hamamatsu QC data for ND APD arrays. NOVA Document 5239. URL <https://nova-docdb.fnal.gov/cgi-bin/sso>ShowDocument?docid=5239>. NOvA internal document.
- [174] Hayes D Merritt. DAQChannelMap Terms and Definitions. NOVA Document 11570. URL <https://nova-docdb.fnal.gov/cgi-bin/sso>ShowDocument?docid=11570>. NOvA internal document.
- [175] Tian Xin. Technote for data-driven threshold and shadow correction. NOVA Document 15223. URL <https://nova-docdb.fnal.gov/cgi-bin/sso>ShowDocument?docid=15223>. NOvA technical note.
- [176] Matthew Strait. Update on light level tuning. NOVA Document 43249. URL <https://nova-docdb.fnal.gov/cgi-bin/sso>ShowDocument?docid=43249>. NOvA internal document.
- [177] Artur Sztuc. DCM/FEB Shut-Off Studies. NOVA Document 53658. URL <https://nova-docdb.fnal.gov/cgi-bin/sso>ShowDocument?docid=53658>. NOvA internal document.
- [178] Adam Lister. Period 12-14 Calibration Validation Document. NOVA Document 60709. URL <https://nova-docdb.fnal.gov/cgi-bin/sso>ShowDocument?docid=60709>. NOvA technical note.
- [179] Adam Lister and Jozef Trokan-Tenorio. Calibration of Periods 12-14 Data in the NOvA Near and Far Detectors. NOVA Document 60838. URL <https://nova-docdb.fnal.gov/cgi-bin/sso>ShowDocument?docid=60838>. NOvA technical note.

- [180] Randeeth L Dasanayaka. TB response with UnixTime(S). NOVA Document 59591. URL <https://nova-docdb.fnal.gov/cgi-bin/sso>ShowDocument?docid=59591>. NOvA internal document.
- [181] E. Aprile et al. Excess electronic recoil events in XENON1T. *Phys. Rev. D*, 102: 072004, . doi:[10.1103/PhysRevD.102.072004](https://doi.org/10.1103/PhysRevD.102.072004).
- [182] E. Aprile et al. Search for New Physics in Electronic Recoil Data from XENONnT. *Phys. Rev. Lett.*, 129:161805, . doi:[10.1103/PhysRevLett.129.161805](https://doi.org/10.1103/PhysRevLett.129.161805).
- [183] M. Atzori Corona, W. M. Bonivento, M. Cadeddu, N. Cargioli, and F. Dordei. New constraint on neutrino magnetic moment and neutrino millicharge from LUX-ZEPLIN dark matter search results. *Phys. Rev. D*, 107:053001. doi:[10.1103/PhysRevD.107.053001](https://doi.org/10.1103/PhysRevD.107.053001).
- [184] M. Agostini et al. Limiting neutrino magnetic moments with Borexino Phase-II solar neutrino data. *Phys. Rev. D*, 96:091103. doi:[10.1103/PhysRevD.96.091103](https://doi.org/10.1103/PhysRevD.96.091103).
- [185] Amir N. Khan. Light new physics and neutrino electromagnetic interactions in XENONnT. *Physics Letters B*, 837:137650. ISSN 0370-2693. doi:[10.1016/j.physletb.2022.137650](https://doi.org/10.1016/j.physletb.2022.137650). URL <https://www.sciencedirect.com/science/article/pii/S0370269322007845>.
- [186] K. S. Babu, Sudip Jana, and Manfred Lindner. Large Neutrino Magnetic Moments in the Light of Recent Experiments. *JHEP*, 10:040. doi:[10.1007/JHEP10\(2020\)040](https://doi.org/10.1007/JHEP10(2020)040).
- [187] L. B. Auerbach et al. Measurement of electron-neutrino electron elastic scattering. *Phys. Rev. D*, 63:112001. doi:[10.1103/PhysRevD.63.112001](https://doi.org/10.1103/PhysRevD.63.112001).
- [188] D. A. Krakauer et al. Limits on the neutrino magnetic moment from a measurement of neutrino - electron elastic scattering. 252:177–180. doi:[10.1016/0370-2693\(90\)91100-P](https://doi.org/10.1016/0370-2693(90)91100-P).
- [189] L. A. Ahrens et al. Determination of electroweak parameters from the elastic scattering of muon neutrinos and antineutrinos on electrons. *Phys. Rev. D*, 41: 3297–3316, Jun 1990. doi:[10.1103/PhysRevD.41.3297](https://doi.org/10.1103/PhysRevD.41.3297).

- [190] P. Vilain et al. Experimental study of electromagnetic properties of the muon-neutrino in neutrino - electron scattering. *Phys. Lett. B*, 345:115–118, 1995. doi:[10.1016/0370-2693\(94\)01678-6](https://doi.org/10.1016/0370-2693(94)01678-6).
- [191] Biao Wang. *Muon-Neutrino Electron Elastic Scattering and a Search for the Muon-Neutrino Magnetic Moment in the NOvA Near Detector*. PhD thesis. URL [https://scholar.smu.edu/hum\\_sci\\_physics\\_etds/1](https://scholar.smu.edu/hum_sci_physics_etds/1).
- [192] Wenjie Wu and Yiwen Xiao. Constraint of the Integrated Neutrino Flux from Neutrino-Electron Elastic Scattering in the NOvA Near Detector. NOVA Document 56383. URL <https://nova-docdb.fnal.gov/cgi-bin/sso>ShowDocument?docid=56383>. NOvA technical note.
- [193] Athula Wickremasinghe, Wenjie Wu, and Yiwen Xiao. Status of the Measurement of Neutrino-Electron Elastic Scattering in the NOvA Near Detector. In *Neutrino 2022*. URL <https://indico.kps.or.kr/event/30/contributions/738/>.
- [194] Barnali Brahma, Tyler Horoho, and Mu Wei. TechNote: Light Dark Matter Search with NOvA Near Detector. NOVA Document 59439. URL <https://nova-docdb.fnal.gov/cgi-bin/sso>ShowDocument?docid=59439>. NOvA technical note.
- [195] Carlo Giunti and Alexander Studenikin. Neutrino electromagnetic interactions: A window to new physics. *Rev. Mod. Phys.*, 87:531–591, Jun 2015. doi:[10.1103/RevModPhys.87.531](https://doi.org/10.1103/RevModPhys.87.531).
- [196] Boris Kayser. Majorana neutrinos and their electromagnetic properties. *Phys. Rev. D*, 26:1662–1670, Oct 1982. doi:[10.1103/PhysRevD.26.1662](https://doi.org/10.1103/PhysRevD.26.1662).
- [197] José F. Nieves. Electromagnetic properties of majorana neutrinos. *Phys. Rev. D*, 26:3152–3158, Dec 1982. doi:[10.1103/PhysRevD.26.3152](https://doi.org/10.1103/PhysRevD.26.3152).
- [198] Carlo Giunti, Julieta Gruszko, Benjamin Jones, Lisa Kaufman, Diana Parno, and Andrea Pocar. Report of the Topical Group on Neutrino Properties for Snowmass 2021. 9 2022.

- [199] Nicole F. Bell, Mikhail Gorchtein, Michael J. Ramsey-Musolf, Petr Vogel, and Peng Wang. Model independent bounds on magnetic moments of Majorana neutrinos. *Phys. Lett. B*, 642:377–383, 2006. doi:[10.1016/j.physletb.2006.09.055](https://doi.org/10.1016/j.physletb.2006.09.055).
- [200] Nicole F. Bell, Vincenzo Cirigliano, Michael J. Ramsey-Musolf, Petr Vogel, and Mark B. Wise. How magnetic is the Dirac neutrino? *Phys. Rev. Lett.*, 95:151802, 2005. doi:[10.1103/PhysRevLett.95.151802](https://doi.org/10.1103/PhysRevLett.95.151802).
- [201] P. Vogel and J. Engel. Neutrino electromagnetic form factors. *Phys. Rev. D*, 39: 3378–3383, Jun 1989. doi:[10.1103/PhysRevD.39.3378](https://doi.org/10.1103/PhysRevD.39.3378).
- [202] E. Valencia et al. Constraint of the MINER $\nu$ a medium energy neutrino flux using neutrino-electron elastic scattering. *Phys. Rev. D*, 100:092001, Nov 2019. doi:[10.1103/PhysRevD.100.092001](https://doi.org/10.1103/PhysRevD.100.092001).
- [203] Jens Erler and Shufang Su. The weak neutral current. 71:119–149. ISSN 0146-6410. doi:[10.1016/j.ppnp.2013.03.004](https://doi.org/10.1016/j.ppnp.2013.03.004). URL <https://www.sciencedirect.com/science/article/pii/S0146641013000239>. Fundamental Symmetries in the Era of the LHC.
- [204] D.Yu Bardin and V.A. Dokuchaeva. On one-loop electroweak corrections to neutrino-electron elastic scattering. 246(2):221–230. ISSN 0550-3213. doi:[10.1016/0550-3213\(84\)90293-1](https://doi.org/10.1016/0550-3213(84)90293-1). URL <https://www.sciencedirect.com/science/article/pii/0550321384902931>.
- [205] Teresa Lackey. Data Quality Technical Note Prod5.1/2023. NOVA Document 59876, . URL <https://nova-docdb.fnal.gov/cgi-bin/sso>ShowDocument?docid=59876>. NOvA technical note.
- [206] Erin Ewart. Primary and Secondary Vertexing Update for February 2024 Collaboration Meeting. NOVA Document 61190, February 2024. URL <https://nova-docdb.fnal.gov/cgi-bin/sso>ShowDocument?docid=61190>. NOvA internal document.
- [207] Leonidas Aliaga, Derek Doyle, Matthew Judah, Norm Buchanan, Linda Cremonesi, Mat Muether, and Jon Paley. Measurement of the Double-Differential Inclusive Electron-Neutrino Charged-Current Cross Section in the NOvA Near

- Detector. NOVA Document 37668, 04 2020. URL <https://nova-docdb.fnal.gov/cgi-bin/sso>ShowDocument?docid=37668>. NOvA technical note.
- [208] Rene Brun et al. root-project/root: v6.22/08. URL <https://doi.org/10.5281/zenodo.3895860>.
- [209] Andreas Hoecker, Peter Speckmayer, Joerg Stelzer, Jan Therhaag, Eckhard von Toerne, and Helge Voss. TMVA: Toolkit for Multivariate Data Analysis. *PoS*, ACAT:040, 2007.
- [210] Roger Barlow. Extended maximum likelihood. 297(3):496–506. ISSN 0168-9002. doi:[10.1016/0168-9002\(90\)91334-8](https://doi.org/10.1016/0168-9002(90)91334-8). URL <https://www.sciencedirect.com/science/article/pii/0168900290913348>.
- [211] S. S. Wilks. The Large-Sample Distribution of the Likelihood Ratio for Testing Composite Hypotheses. *Annals Math. Statist.*, 9(1):60–62, 1938. doi:[10.1214/aoms/1177732360](https://doi.org/10.1214/aoms/1177732360).

## APPENDIX A

# Test Beam calibration validation plots

### A.1 Distributions for stopping muons

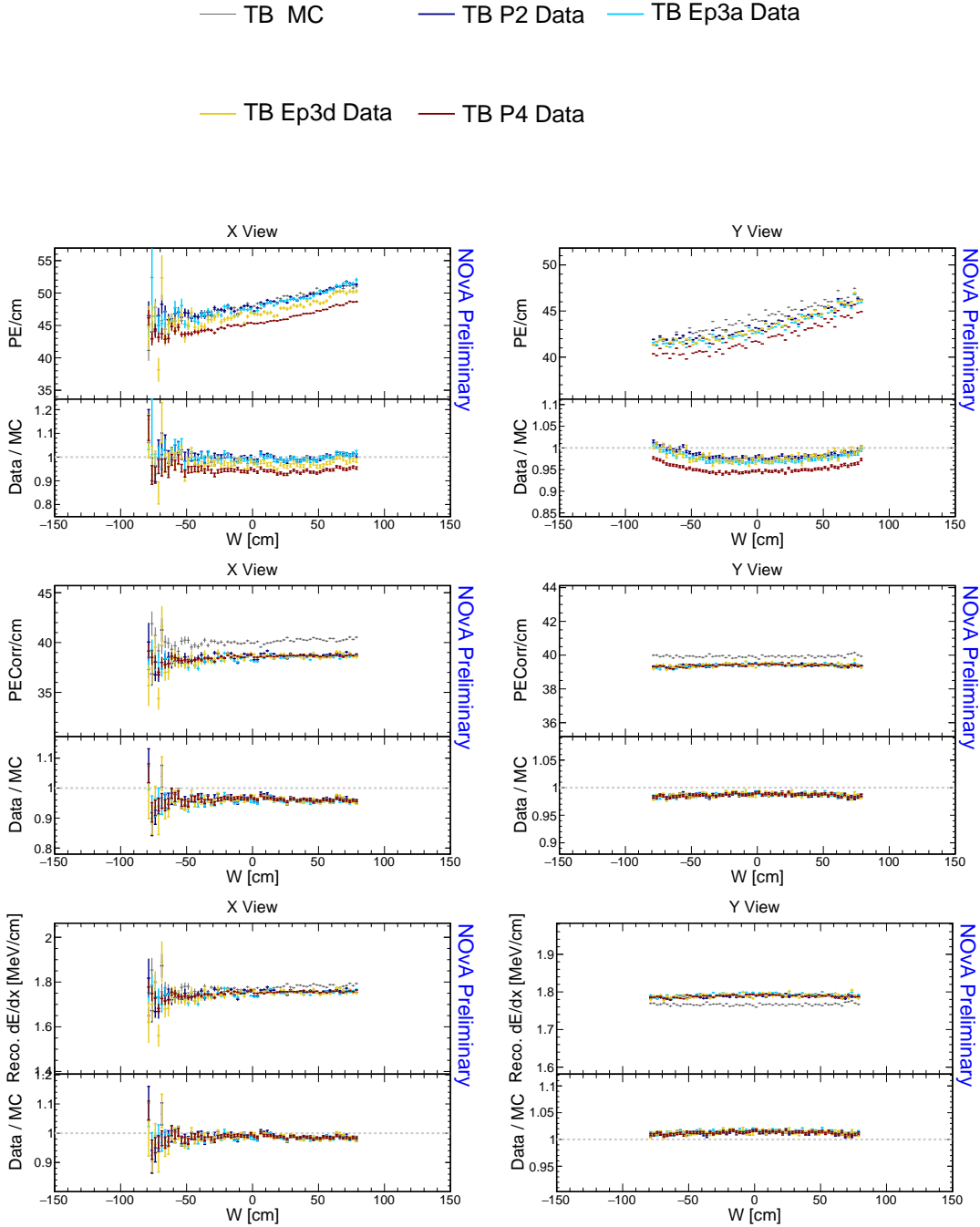


Figure A.1: Distributions of stopping muons within a 1-2 m track window from the end of their tracks across the position within a cell for simulation (gray) and all the Test Beam data samples. The top row shows the energy deposition before any correction, middle row after relative calibration corrections and bottom row after full calibration corrections. The left column shows the X view (vertical planes) and right column the Y view (horizontal planes).

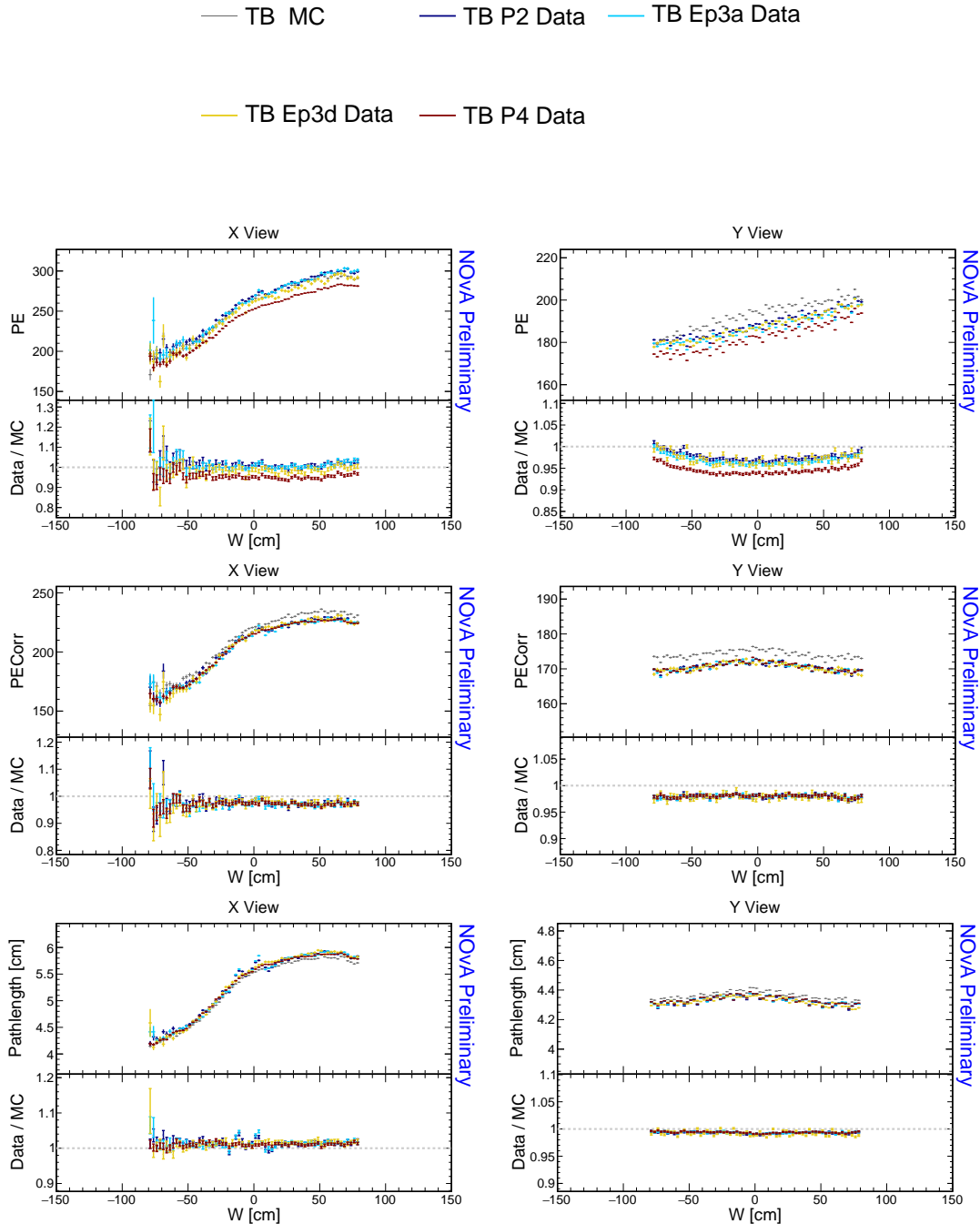


Figure A.2: Distributions of stopping muons within a 1-2 m track window from the end of their tracks across the position within a cell for simulation (gray) and all the Test Beam data samples. The top row shows the number of recorded photo electrons before any corrections, middle row shows the same after relative calibration corrections and bottom row shows the path length through the cell. The left column shows the X view (vertical planes) and right column the Y view (horizontal planes).

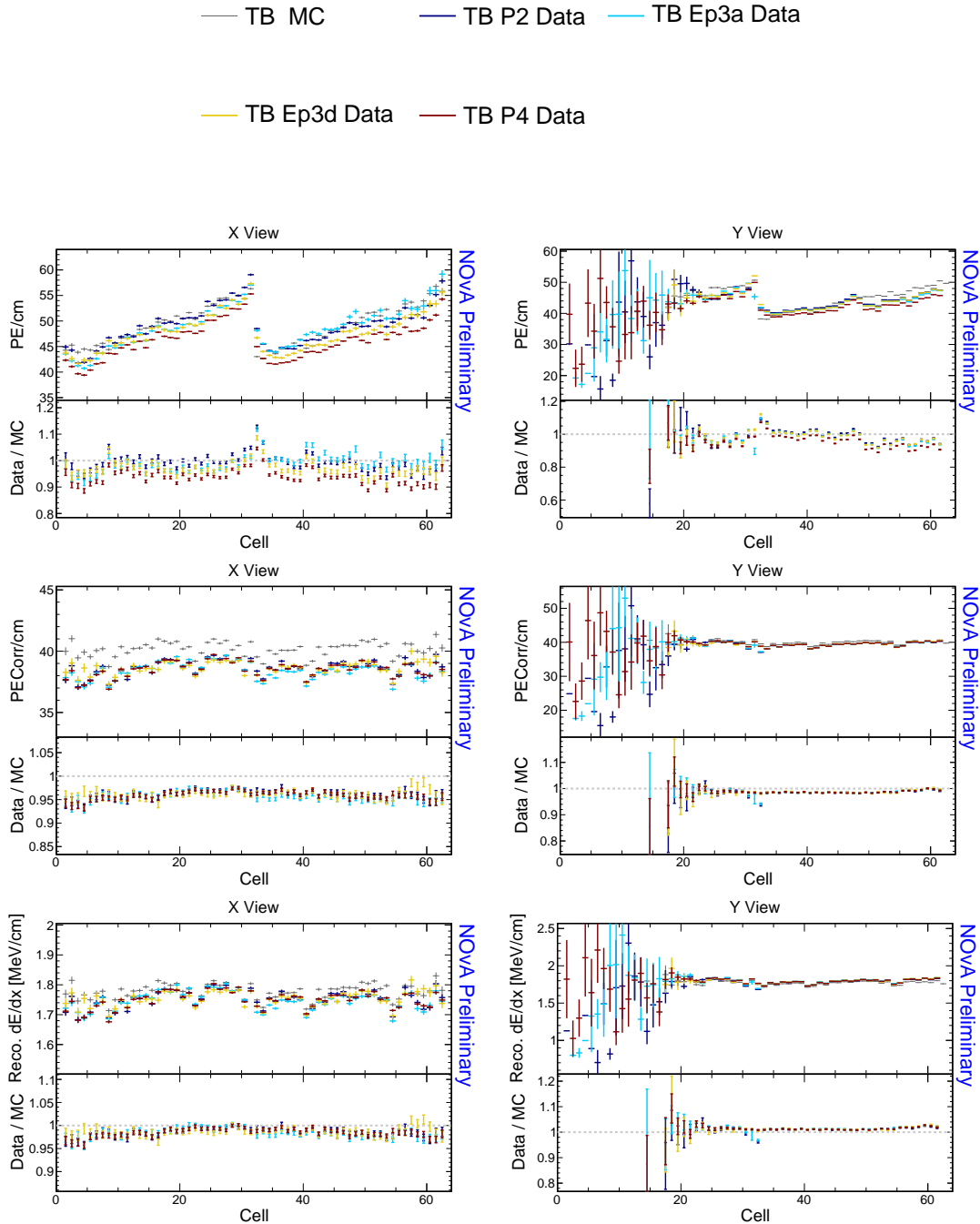


Figure A.3: Distributions of stopping muons within a 1-2 m track window from the end of their tracks across the cells for simulation (gray) and all the Test Beam data samples. The top row shows the energy deposition before any correction, middle row after relative calibration corrections and bottom row after full calibration corrections. The left column shows the X view (vertical planes) and right column the Y view (horizontal planes).

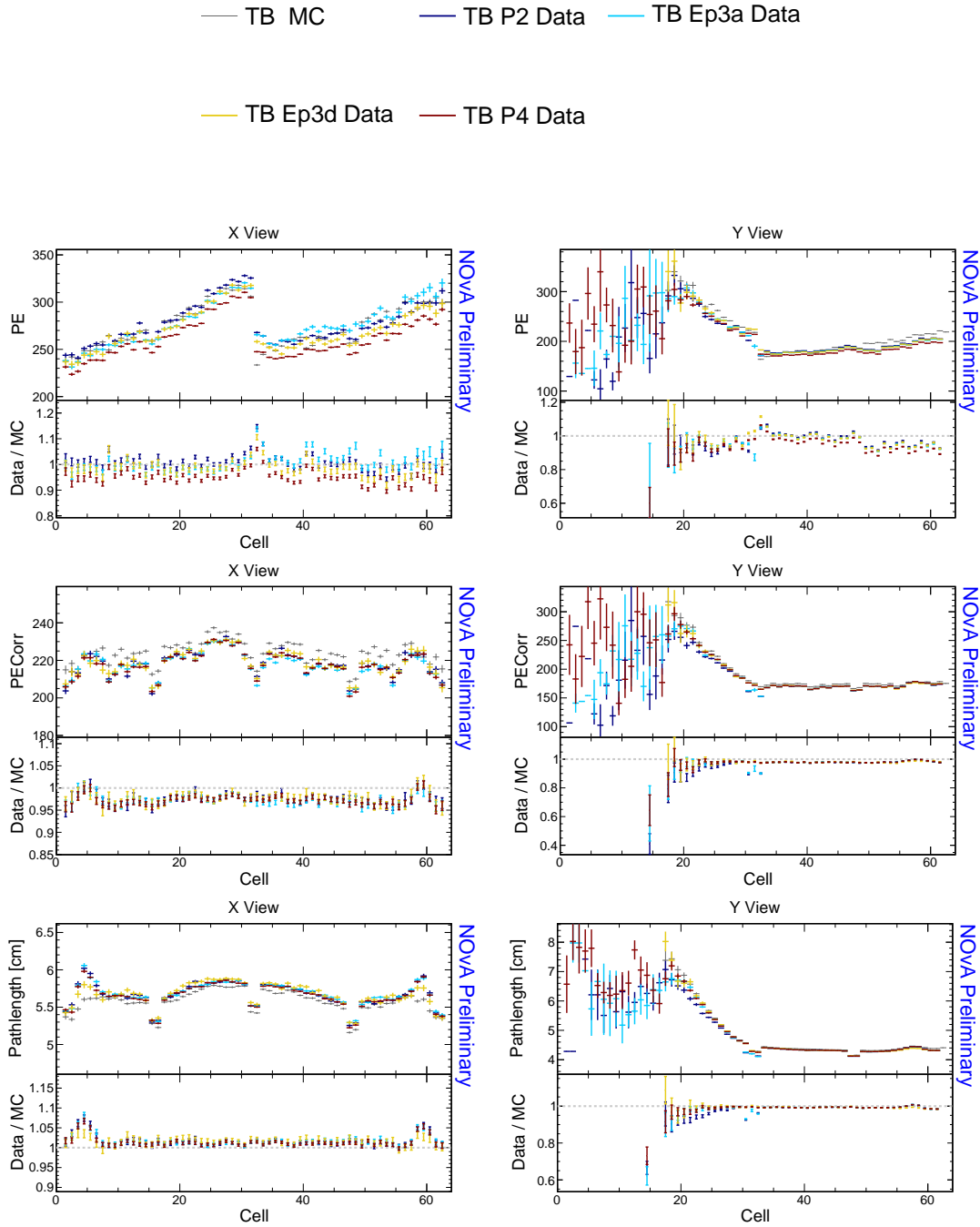


Figure A.4: Distributions of stopping muons within a 1-2 m track window from the end of their tracks across the detector cells for simulation (gray) and all the Test Beam data samples. The top row shows the number of recorded photo electrons before any corrections, middle row shows the same after relative calibration corrections and bottom row shows the path length through the cell. The left column shows the X view (vertical planes) and right column the Y view (horizontal planes).

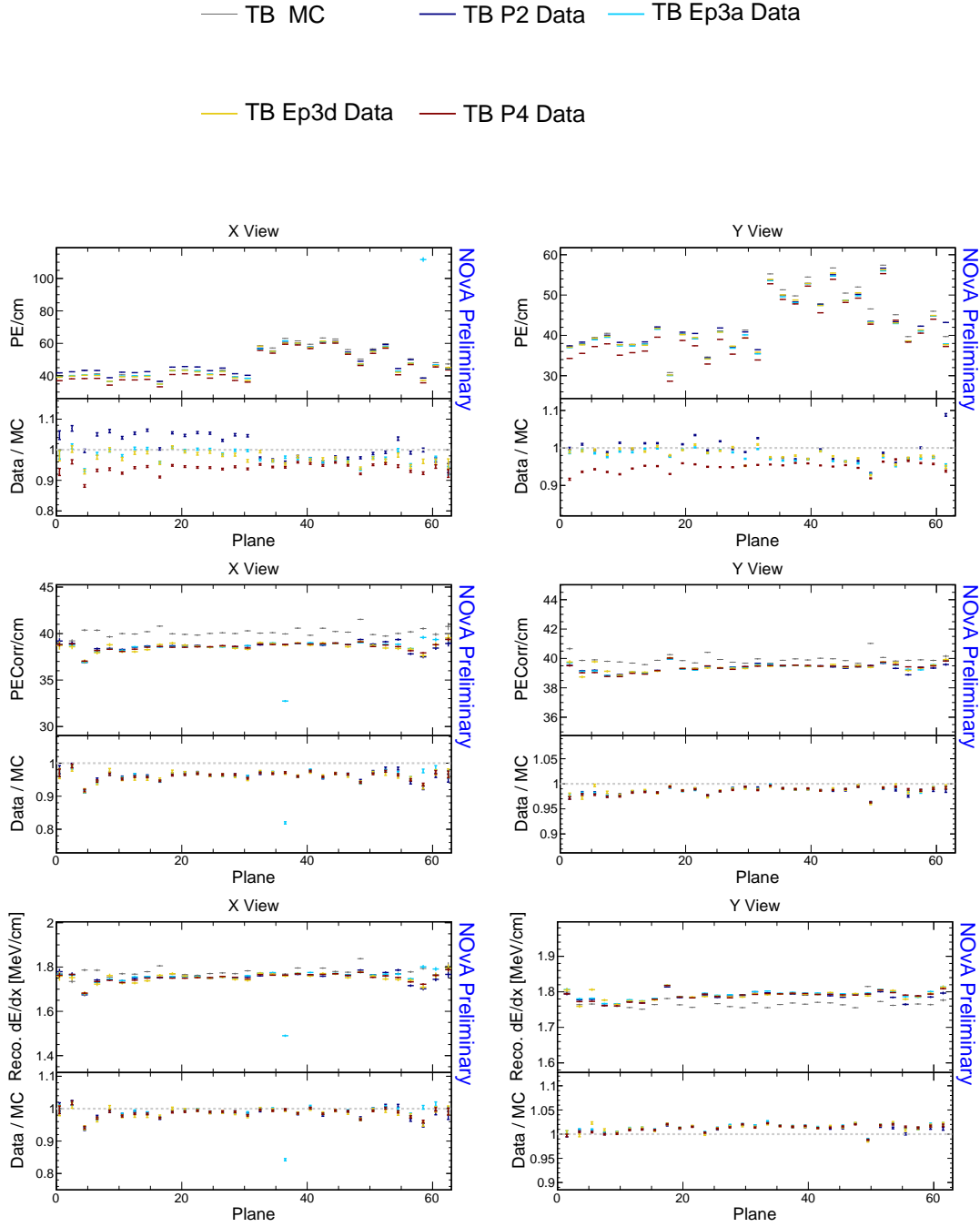


Figure A.5: Distributions of stopping muons within a 1-2 m track window from the end of their tracks across the detector planes for simulation (gray) and all the Test Beam data samples. The top row shows the energy deposition before any correction, middle row after relative calibration corrections and bottom row after full calibration corrections. The left column shows the X view (vertical planes) and right column the Y view (horizontal planes).

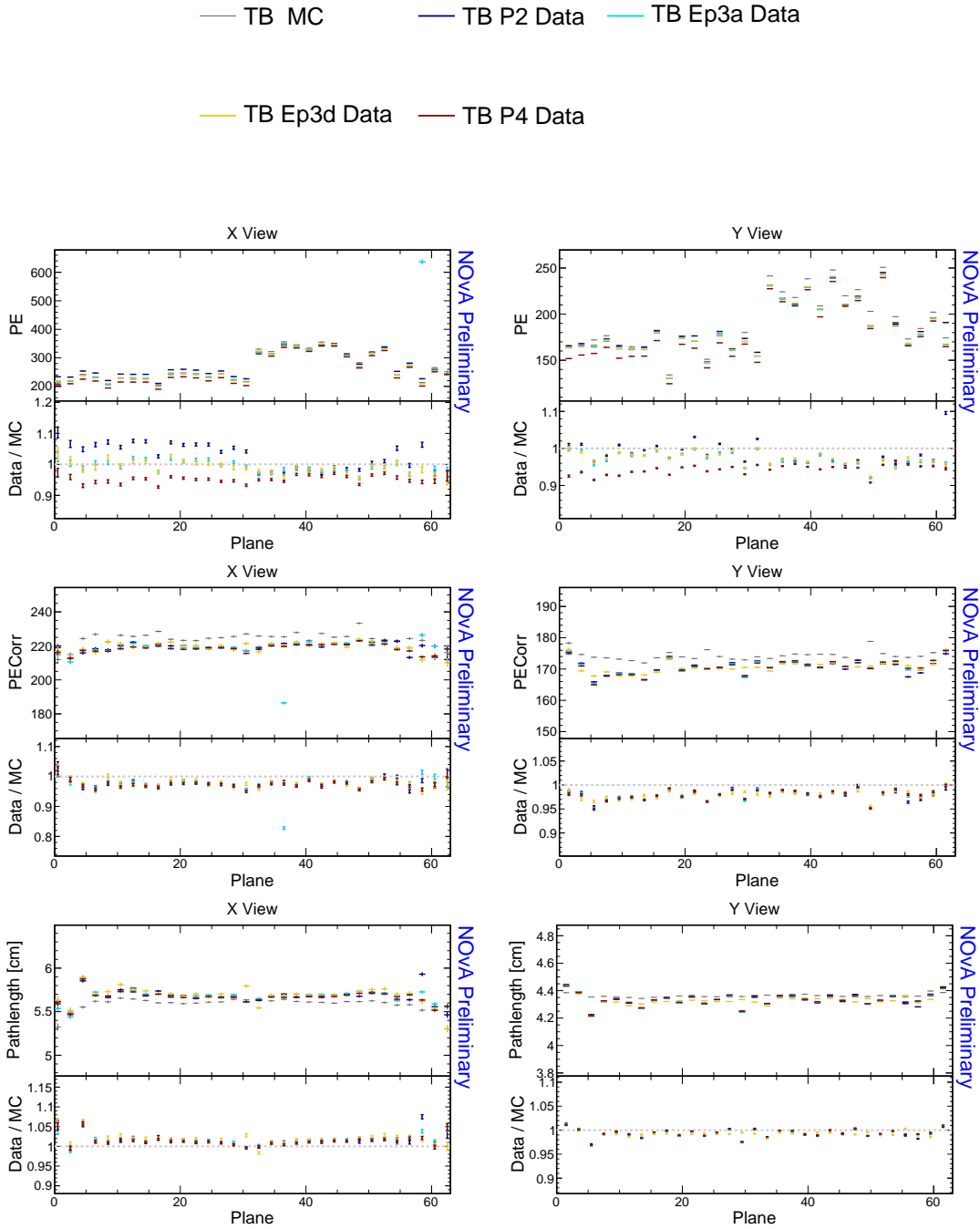


Figure A.6: Distributions of stopping muons within a 1-2 m track window from the end of their tracks across the detector planes for simulation (gray) and all the Test Beam data samples. The top row shows the number of recorded photo electrons before any corrections, middle row shows the same after relative calibration corrections and bottom row shows the path length through the cell. The left column shows the X view (vertical planes) and right column the Y view (horizontal planes).

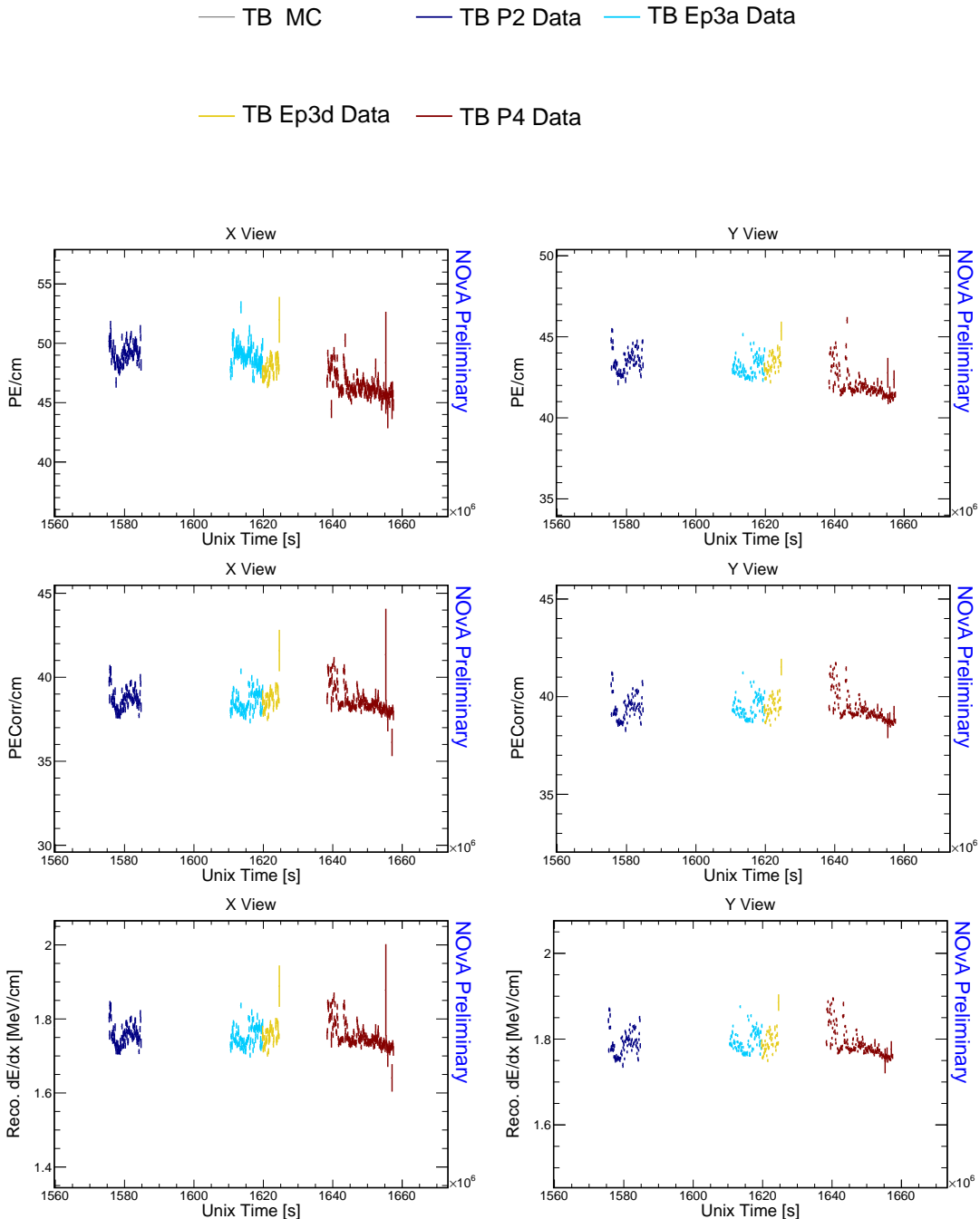


Figure A.7: Distributions of stopping muons within a 1-2 m track window from the end of their tracks as a function of time for the Test Beam data samples. The top row shows the energy deposition before any correction, middle row after relative calibration corrections and bottom row after full calibration corrections. The left column shows the X view (vertical planes) and right column the Y view (horizontal planes).

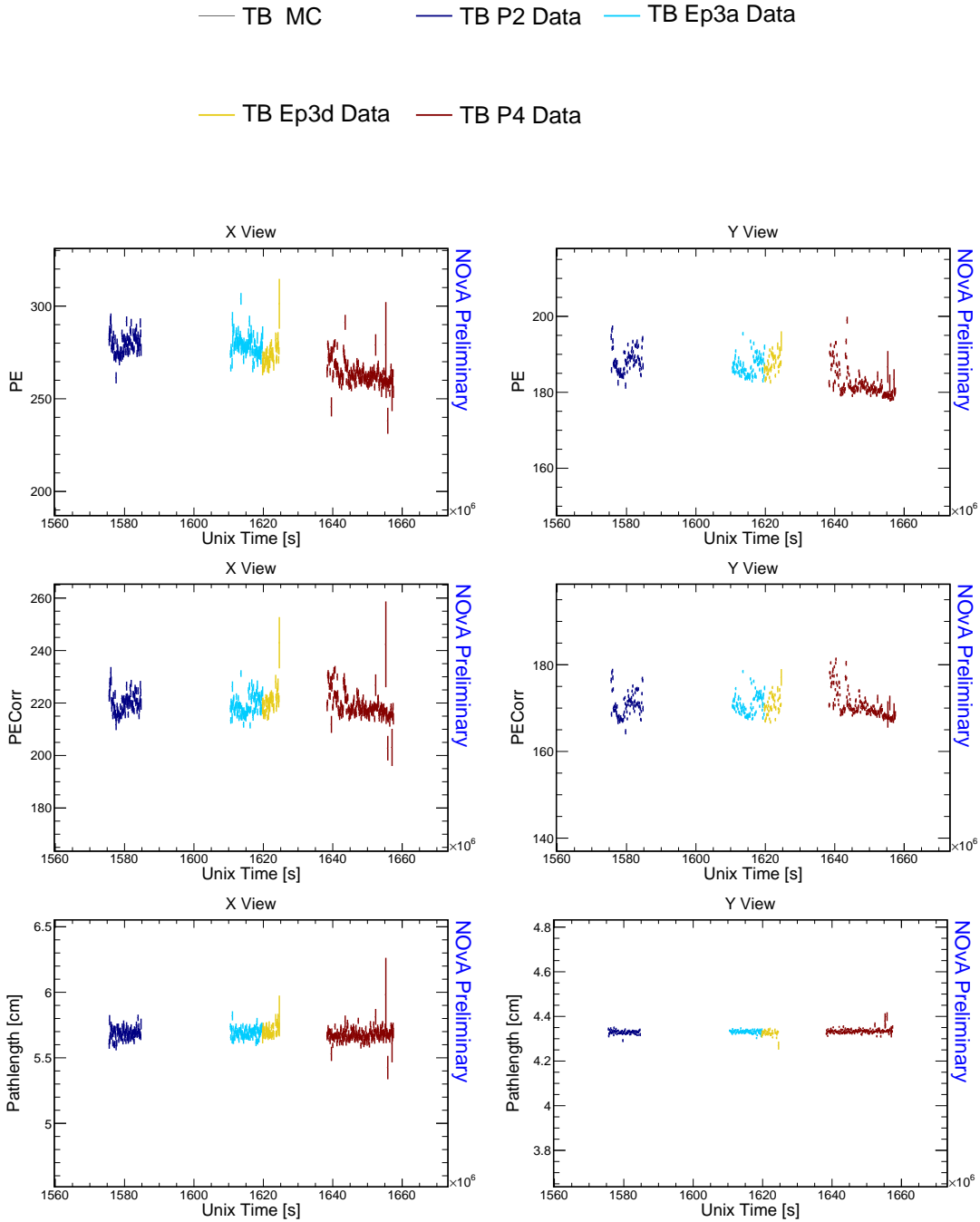


Figure A.8: Distributions of stopping muons within a 1-2 m track window from the end of their tracks as a function of time for simulation (gray) and all the Test Beam data samples. The top row shows the number of recorded photo electrons before any corrections, middle row shows the same after relative calibration corrections and bottom row shows the path length through the cell. The left column shows the X view (vertical planes) and right column the Y view (horizontal planes).

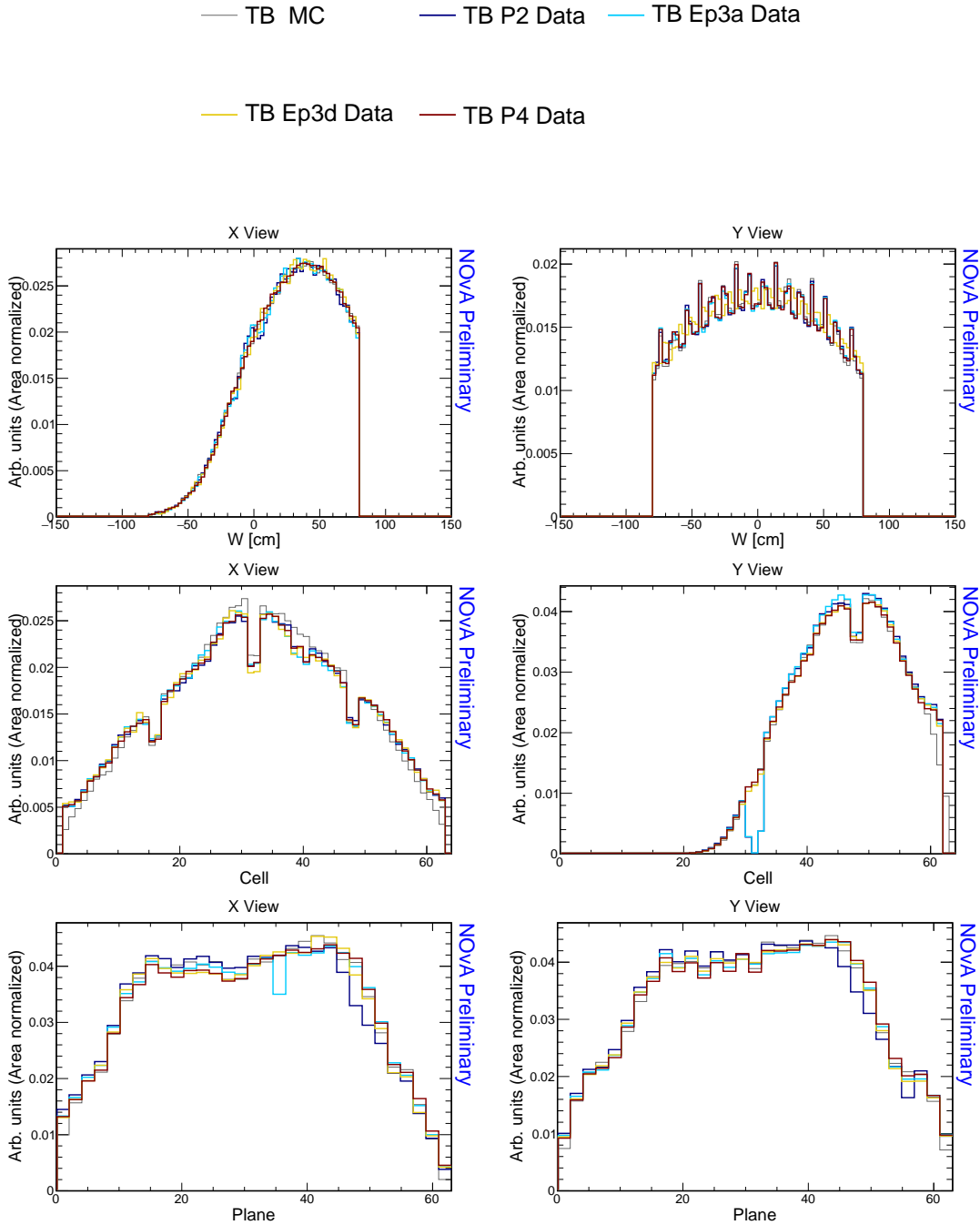


Figure A.9: Distributions of the variables used in the calibration of stopping muons within a 1-2 m track window from the end of their tracks for simulation (gray) and all the Test Beam data samples. The top row shows the position within a cell, middle row the cell number and bottom row the plane number. The left column shows the X view (vertical planes) and right column the Y view (horizontal planes).

## A.2 Distributions for through-going muons

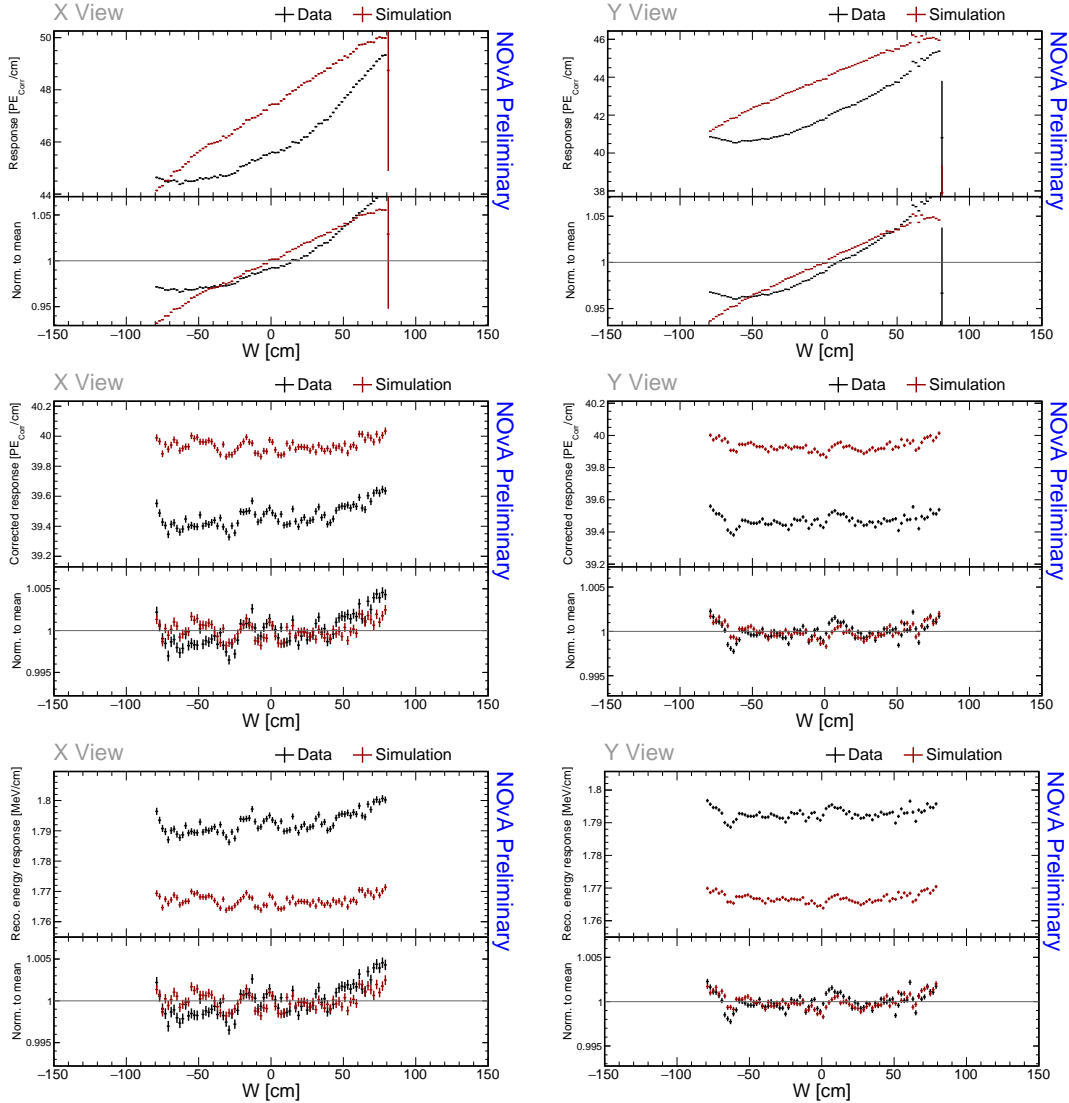


Figure A.10: Distributions of through-going cosmic muons with  $w \in (-80, 80)$  cm as a function of  $w$  for stable runs in the Test Beam period 4 data (black) and data-based simulation (red). Bottom panel of each plot shows the ratio of each bin and the mean y axis, separately for data and simulation. Discrepancy in the right-most bin is solely due to binning.

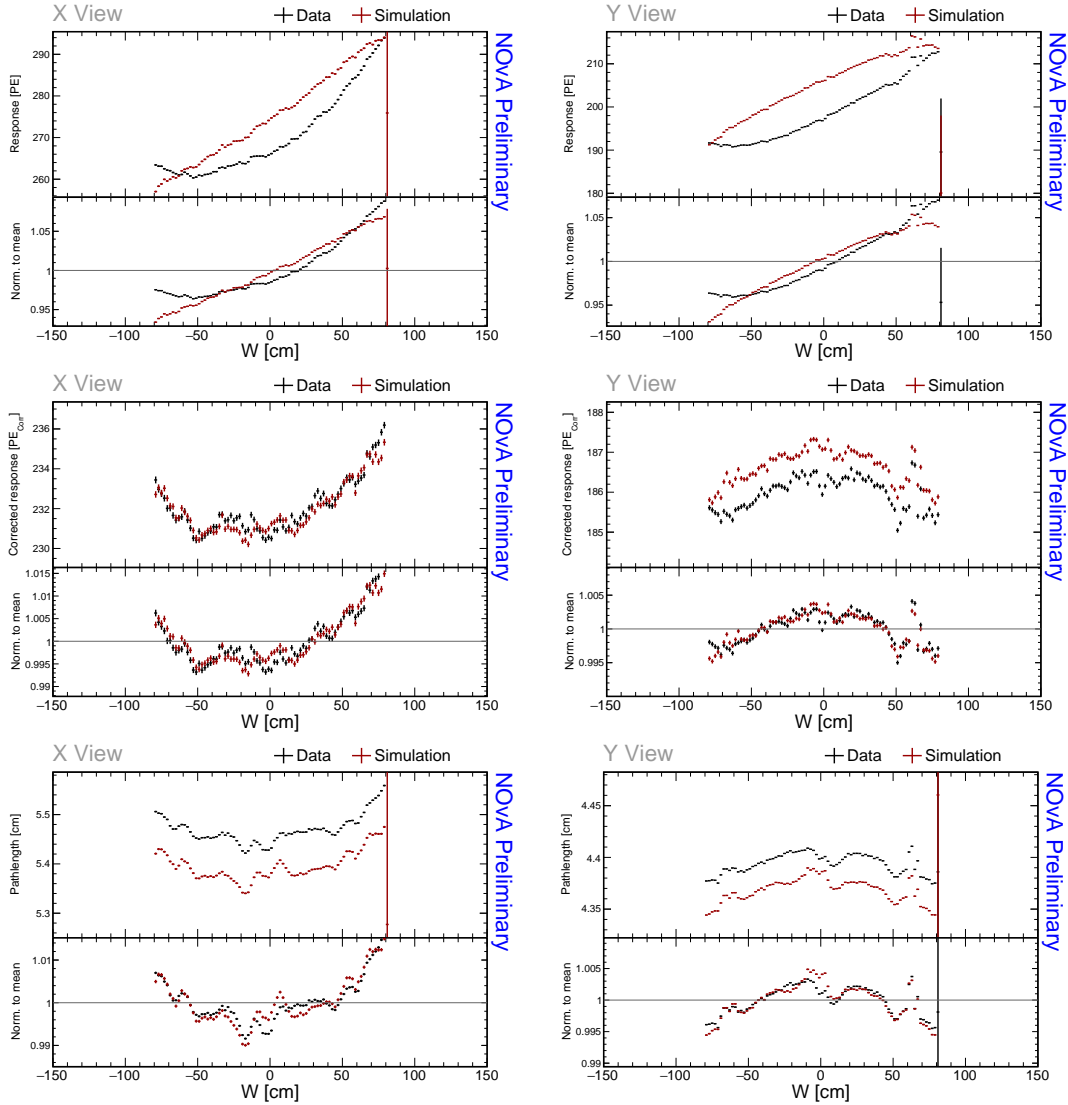


Figure A.11: Distributions of through-going cosmic muons with  $w \in (-80, 80)$  cm as a function of  $w$  for stable runs in the Test Beam period 4 data (black) and data-based simulation (red). Bottom panel of each plot shows the ratio of each bin and the mean y axis, separately for data and simulation. Discrepancy in the right-most bin is solely due to binning.

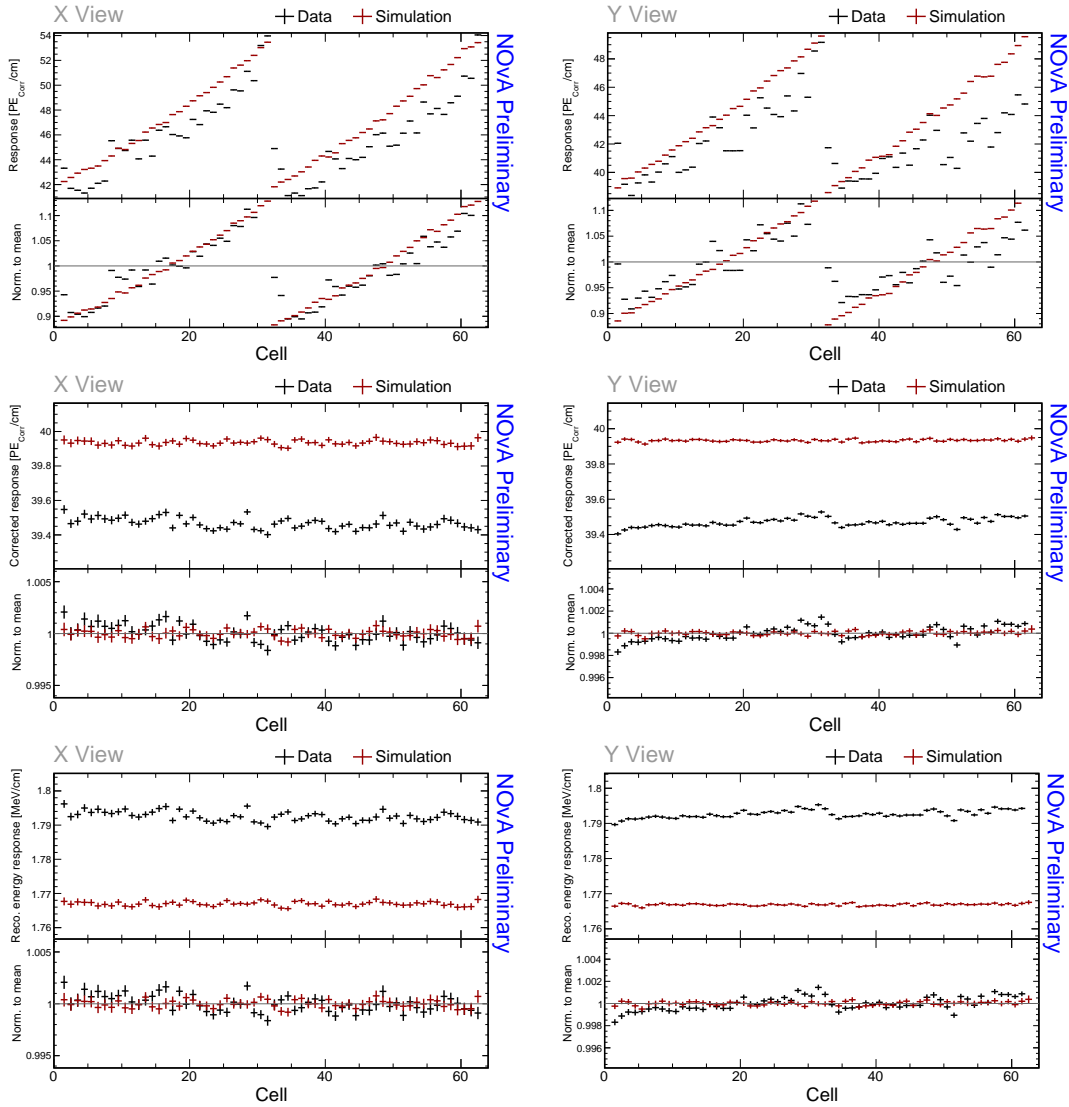


Figure A.12: Distributions of through-going cosmic muons with  $w \in (-80, 80)$  cm as a function of cell number for stable runs in the Test Beam period 4 data (black) and data-based simulation (red). Bottom panel of each plot shows the ratio of each bin and the mean y axis, separately for data and simulation.

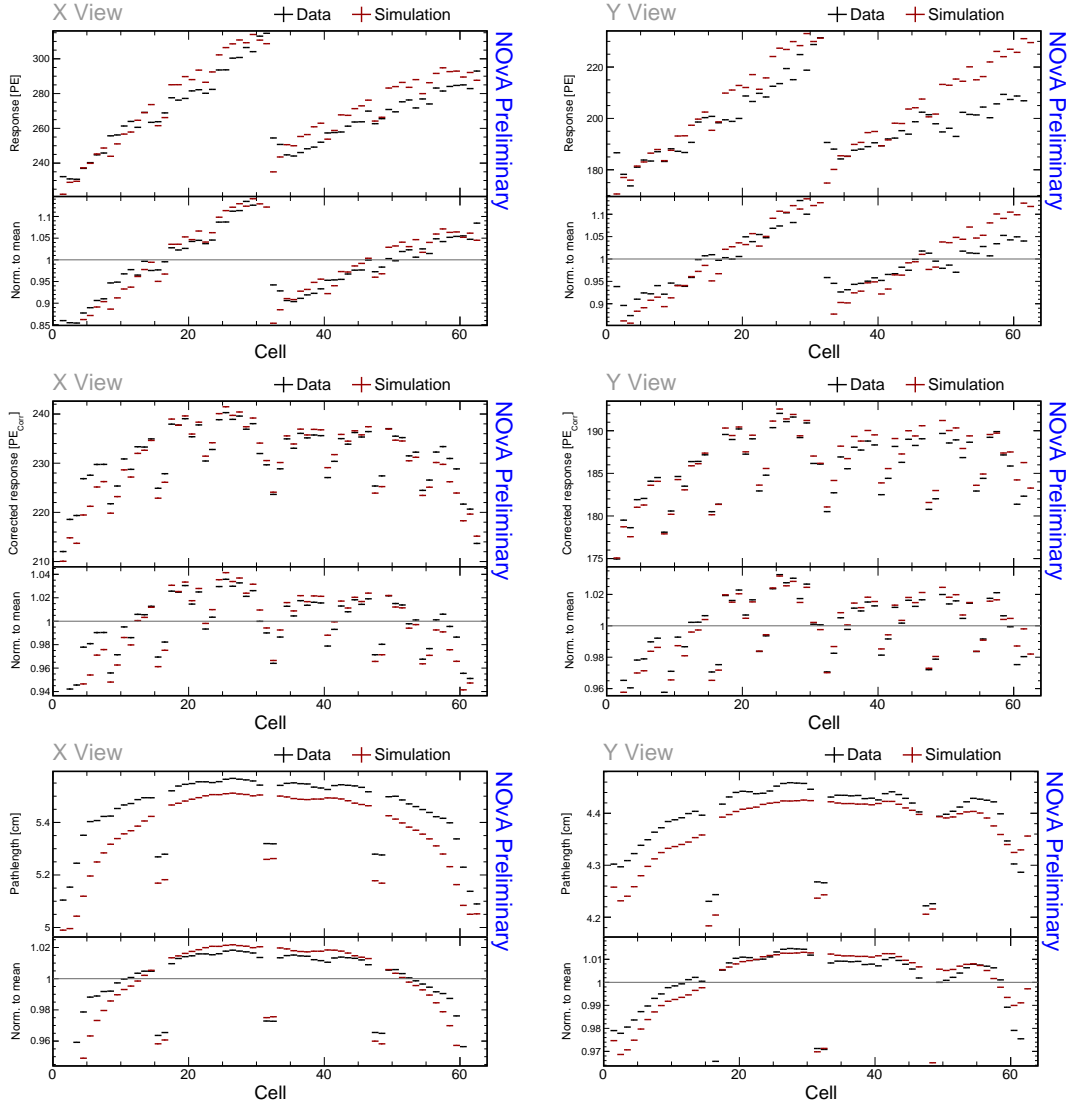


Figure A.13: Distributions of through-going cosmic muons with  $w \in (-80, 80)$  cm as a function of cell number for stable runs in the Test Beam period 4 data (black) and data-based simulation (red). Bottom panel of each plot shows the ratio of each bin and the mean y axis, separately for data and simulation.

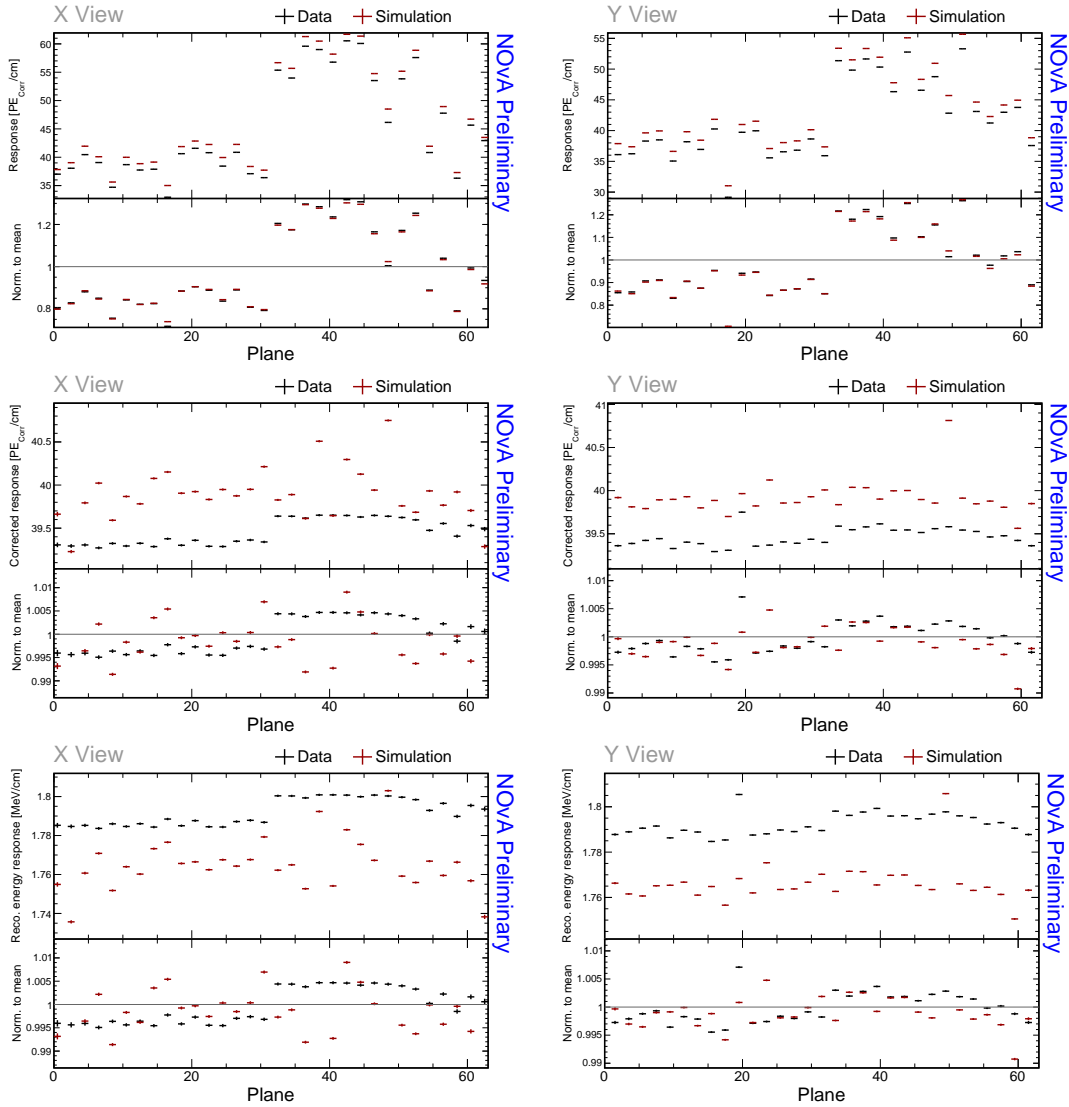


Figure A.14: Distributions of through-going cosmic muons with  $w \in (-80, 80)$  cm as a function of plane number for stable runs in the Test Beam period 4 data (black) and data-based simulation (red). Bottom panel of each plot shows the ratio of each bin and the mean y axis, separately for data and simulation.

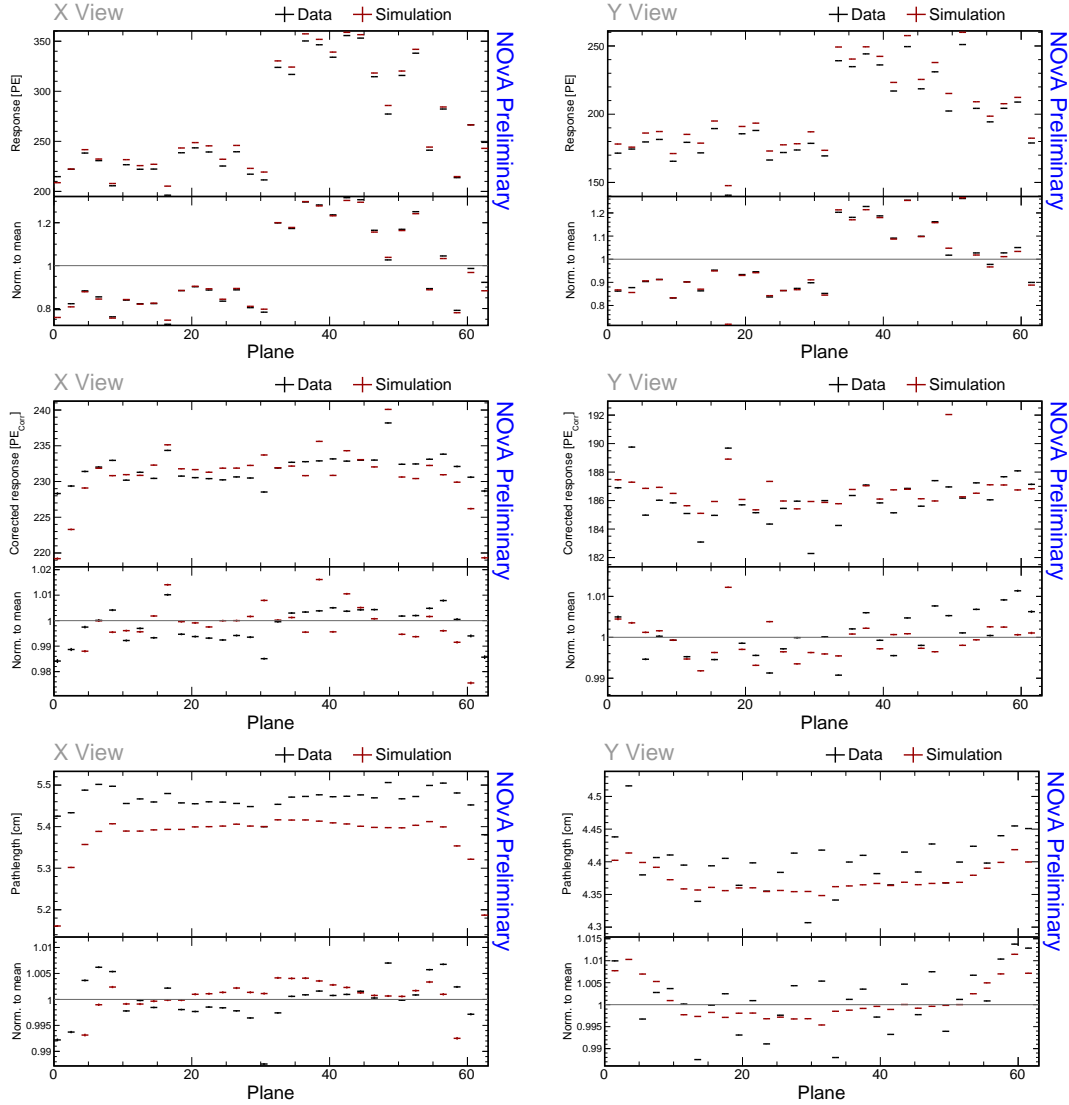


Figure A.15: Distributions of through-going cosmic muons with  $w \in (-80, 80)$  cm as a function of plane number for stable runs in the Test Beam period 4 data (black) and data-based simulation (red). Bottom panel of each plot shows the ratio of each bin and the mean y axis, separately for data and simulation.

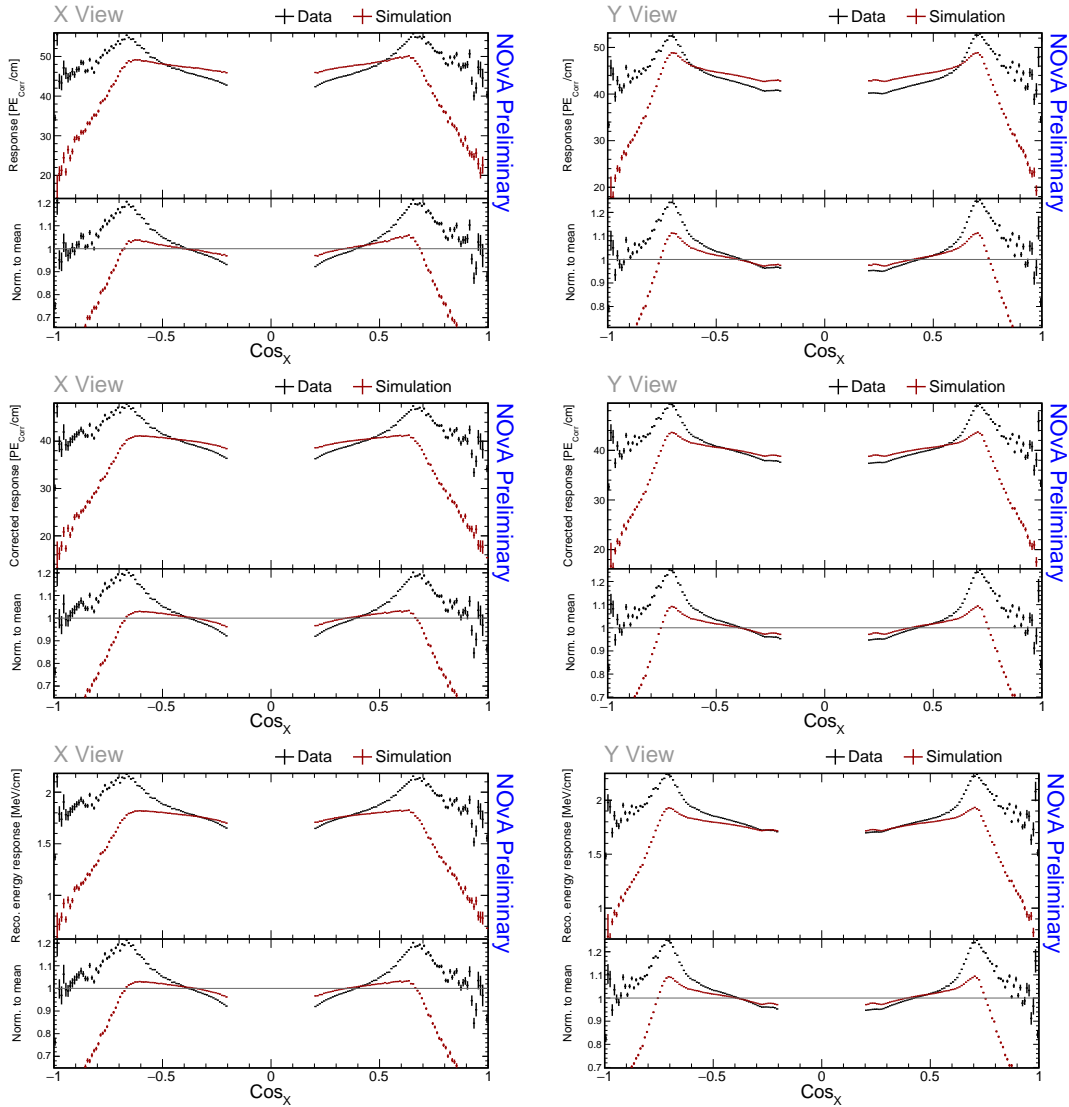


Figure A.16: Distributions of through-going cosmic muons with  $w \in (-80, 80)$  cm as a function of the cosine of the angle from the x axis for stable runs in the Test Beam period 4 data (black) and data-based simulation (red). Bottom panel of each plot shows the ratio of each bin and the mean y axis, separately for data and simulation.

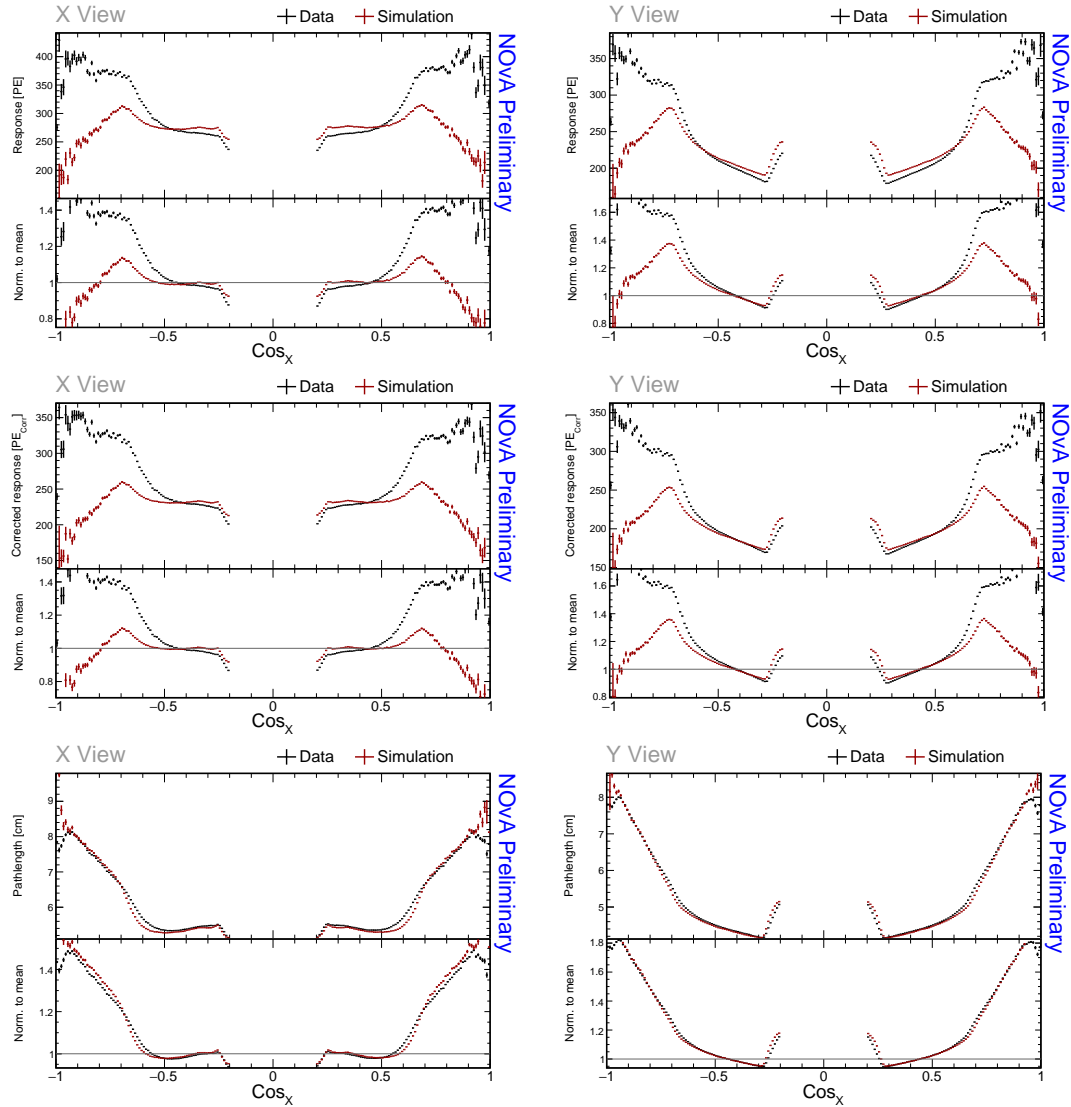


Figure A.17: Distributions of through-going cosmic muons with  $w \in (-80, 80)$  cm as a function of the cosine of the angle from the x axis for stable runs in the Test Beam period 4 data (black) and data-based simulation (red). Bottom panel of each plot shows the ratio of each bin and the mean y axis, separately for data and simulation.

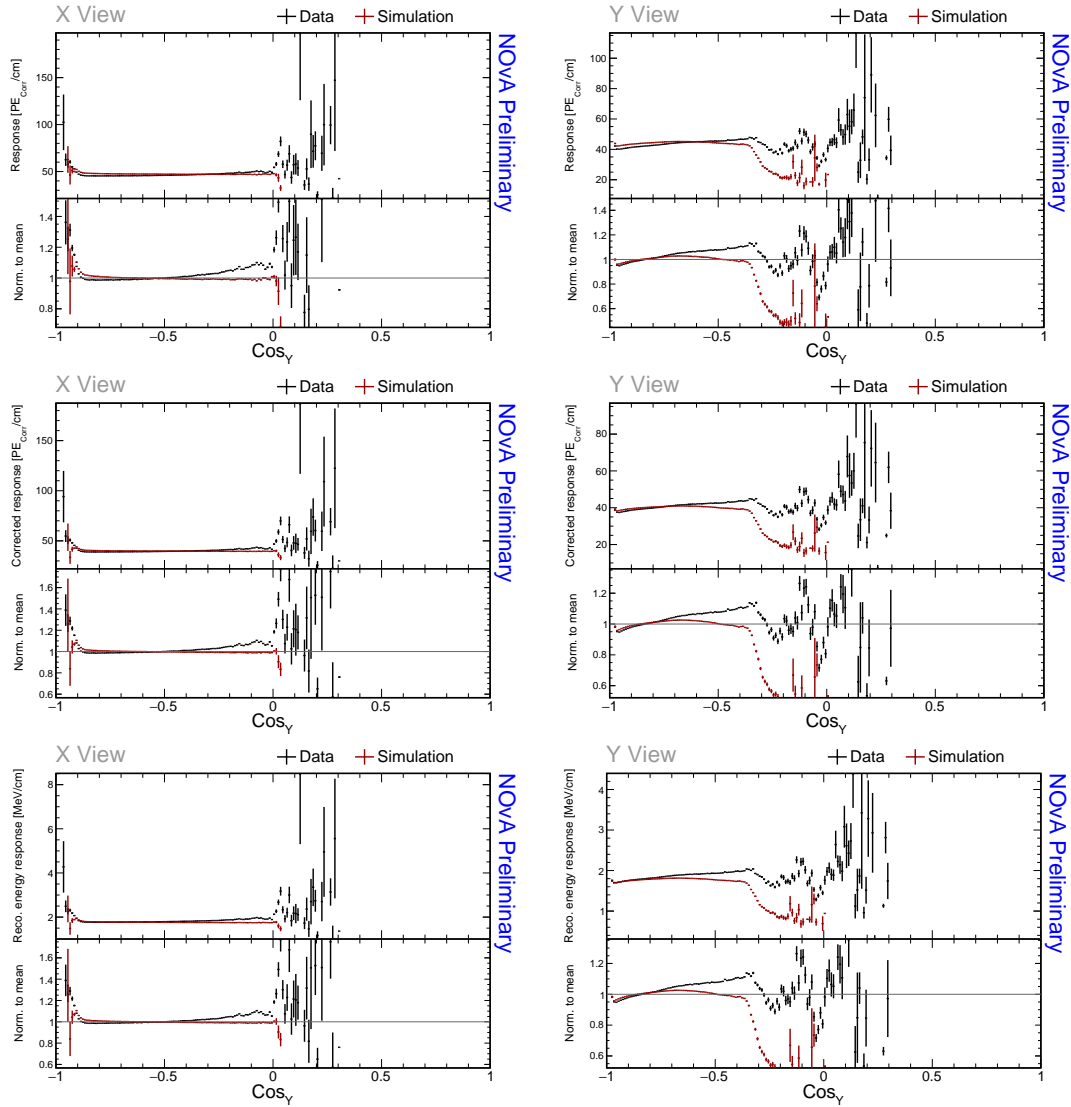


Figure A.18: Distributions of through-going cosmic muons with  $w \in (-80, 80)$  cm as a function of the cosine of the angle from the y axis for stable runs in the Test Beam period 4 data (black) and data-based simulation (red). Bottom panel of each plot shows the ratio of each bin and the mean y axis, separately for data and simulation.

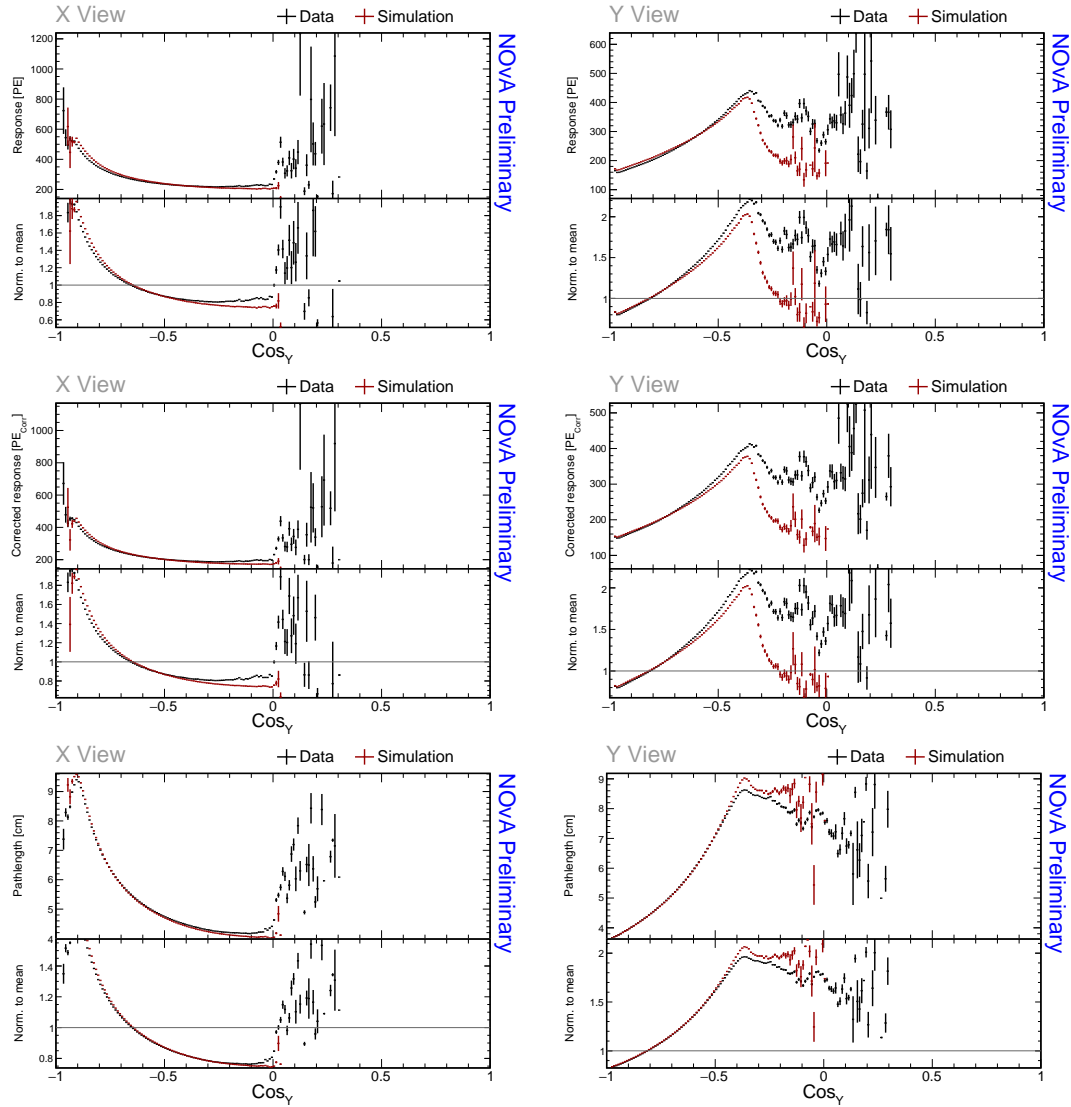


Figure A.19: Distributions of through-going cosmic muons with  $w \in (-80, 80)$  cm as a function of the cosine of the angle from the y axis for stable runs in the Test Beam period 4 data (black) and data-based simulation (red). Bottom panel of each plot shows the ratio of each bin and the mean y axis, separately for data and simulation.

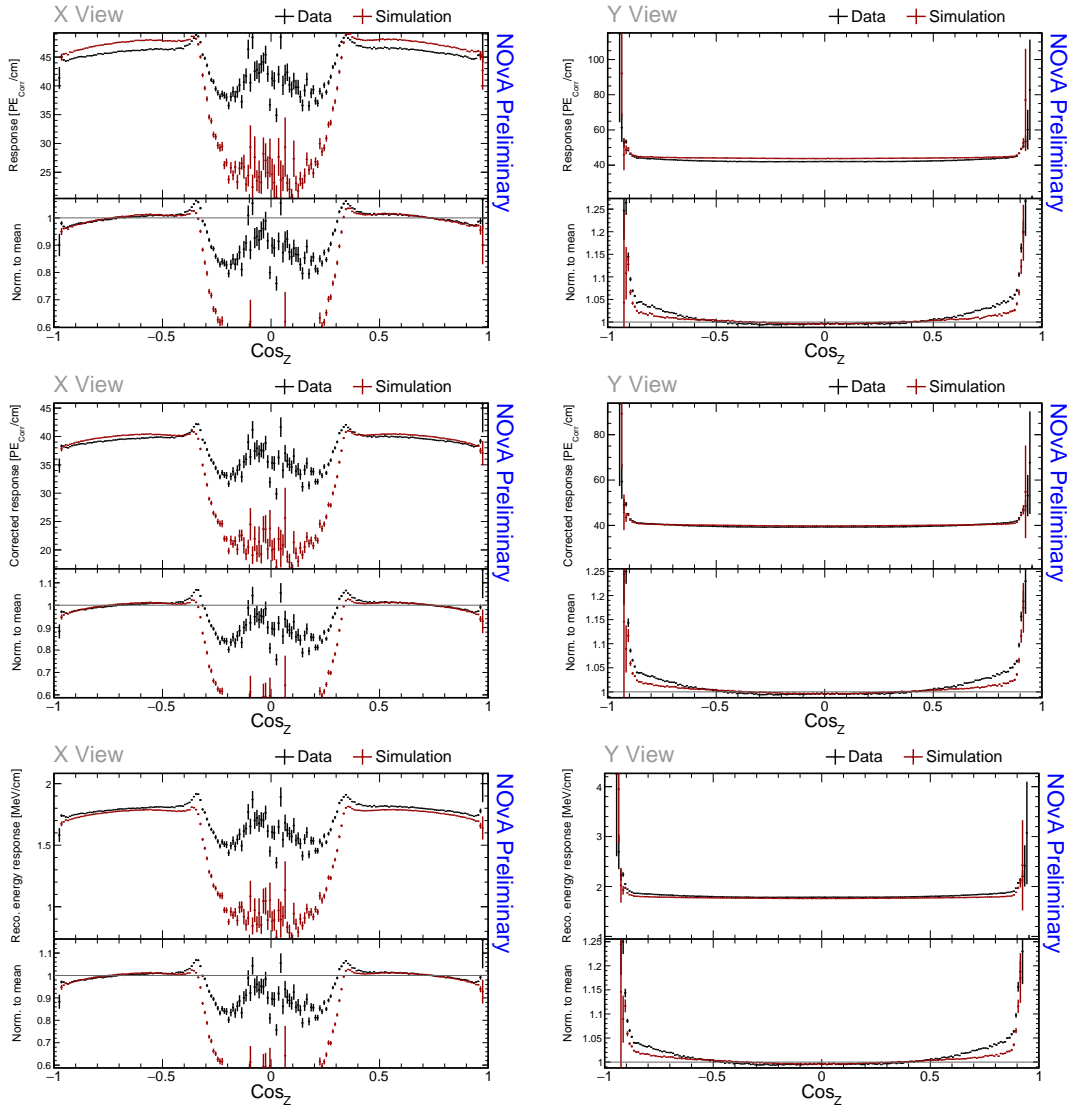


Figure A.20: Distributions of through-going cosmic muons with  $w \in (-80, 80)$  cm as a function of the cosine of the angle from the z axis for stable runs in the Test Beam period 4 data (black) and data-based simulation (red). Bottom panel of each plot shows the ratio of each bin and the mean y axis, separately for data and simulation.

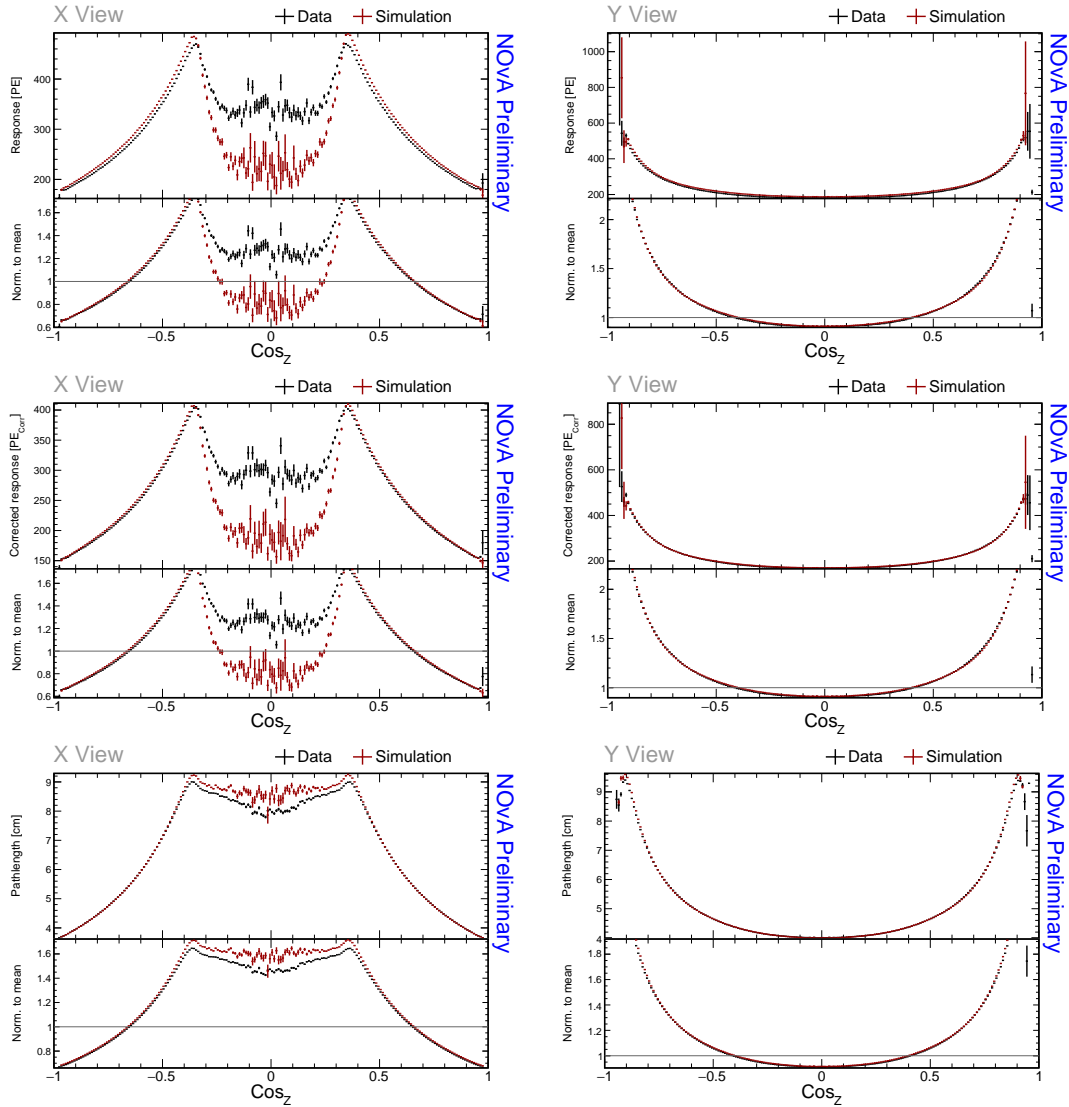


Figure A.21: Distributions of through-going cosmic muons with  $w \in (-80, 80)$  cm as a function of the cosine of the angle from the x axis for stable runs in the Test Beam period 4 data (black) and data-based simulation (red). Bottom panel of each plot shows the ratio of each bin and the mean y axis, separately for data and simulation.